Aerosols and Chemistry in the Planetary Atmospheres

Thesis by

Xi Zhang

In Partial Fulfillment of the Requirements for the

Degree of

Doctor of Philosophy

CALIFORNIA INSTITUTE OF TECHNOLOGY

Pasadena, California

2013

(Defended November 29, 2012)

To my parents

and

my sister and her family

ACKNOWLEDGEMENTS

Following Chinese tradition, I would first like to thank my parents, my sister, and her family. Their endless love reached across the Pacific Ocean and has never ceased to comfort me and cure me of my homesickness in the last five and a half years. It is to them that this dissertation is dedicated.

I owe my most sincere gratitude to my Ph.D. advisor Yuk Yung. Without him, this thesis is not possible. Two thousand years ago, Confucius described a Chinese gentleman as having "*three varying aspects: seen from afar, he looks severe, when approached he is found to be mild, when heard speaking he turns out to be incisive.*" Yuk is a gentleman. He is the most sincere person I have ever met. As far as I know, he is the only Ph.D. advisor who takes students to the supermarket to shop for groceries (please ask Mike Wong for details) and fixes their cars (please ask me for details). He cares about the students. Thus, he not only passes on to them his scientific knowledge and research methods, but he also inspires and encourages them through his everyday life as a unity of knowledge and practice. I believe the latter is inherited from the traditional Chinese scholars that came after Confucius. He taught me not only how to accelerate but also how to break, and why the most important attributes are judgment and vision. Also, I must thank Shaumay, Yuk's wife, for her delicious dishes that she shared with us every year when we had parties at their house.

I would also like to thank John Seinfeld. His aerosol class might be my most productive class at Caltech, as my class project was quickly published and eventually became the first chapter of my thesis. I learned a lot from his efficiency and physical insights during my collaboration with him.

I was privileged to have benefited from working with many other scientists during my time at Caltech as well. In my first year, with virtually no research experience, David Stevenson knocked me out of my idealized theoretical world. Conor Nixon helped me understand the

information mined from planetary data in a reasonable way. Robert West and his insistence on the research approach finally led me to the light at the end of the tunnel, although at the beginning I thought it was an impossible task. Run-lie Shia's physical intuition and insightful comments are always appreciated. A complete list is not possible, although I would like to thank as many as I can. They are Mark Allen, Adam Showman, Spyros Pandis, Patrick Irwin, Donald Shemansky, Mao-Chang Liang, Franklin Mills, Denis Belyaev, Raul Morales-Juberias, Timothy Dowling, Christopher Parkinson, Joseph Ajello, Julie Moses, Leigh Fletcher, Glenn Orton, Roger Yelle, Frank Montmessin, Jean-Loup Bertaux, Oded Aharonson, Victoria Meadows, Javier Martin-Torres, Don Banfield, as well as the young rising stars: Mike Line, Peter Gao, Joshua Kammer, and Cheng Li. Clearly, the US planetary science community is a good example of a mature scientific field.

I am also grateful for the support from the planetary science option staff, especially from Irma Black and Margaret Carlos. Special thanks also go to Mike Black and Scott Dungan for having resolved my numerous computer problems. I must also thank Shawn Ewald for his advice on IDL programming, Mimi Gerstell for having corrected the grammar errors in my papers, and Irene Chen for having translated my LaTex manuscript into the Microsoft Word format.

When I was hanging out with the planets in space, my friends dragged me back down to Earth and gave color to my everyday life. I must thank Wendy for having opened up a whole new sweet world for me with her dessert magic; Peter and David for teaching me the Hao-style Tai-Chi and martial arts; Cheng, Qiong, Jinqiang, and Yi, for being the only ones I know with cooking skills rivaling their research skills; Le, Da, Mike, Peter, Zan, Ke, Xuan, Zhan, Lingsen, Yihe, Yingdi, Dunzhu, King-Fai, Tan, and Yi-Chun for sharing their joys and sorrows with me during the last several years, and the hikers Zhihong, Wendian, Tong, Junle, Yubing, Daiqi, and Yan for leading me all across Southern California. Where the wind blows, where we will occupy. Next stop, Mt. Whitney.

I would like to thank the friends who shared the joys of their family with me: Runqiang and Yu, Zhaoyan and Tian, Na and Pengcheng, Wei and Rui, Guanglei and Mingyuan (and their beautiful twins!), Hank and Eileen, Ting and Fan, and Lijun and Yun. May their love shine warmly forever.

I devote my thesis to Haogang Xiao, my dearest brother in the heavens; I will stop blaming you for leaving us alone. Yunfeng and Jiayu, let us carry on his unfinished dreams together.

Finally, I would like to thank my undergraduate advisor in Peking University, Zuo Xiao, who guided me though the scientific field and encouraged me to pursue my Ph.D. degree at Caltech. He excels at writing Chinese poems, just like my Ph.D. advisor Yuk Yung. Maybe I should also learn how to write them one day.

ABSTRACT

This dissertation is devoted to studying aerosols and their roles in regulating chemistry, radiation, and dynamics of planetary atmospheres. In chapter I, we provided a fundamental mathematical basis for the quasi-equilibrium growth assumption, a well-accepted approach to representing formation of secondary organic aerosols (SOAs) in microphysical simulations in the Earth's atmosphere. Our analytical work not only explains the quasi-equilibrium growth, which emerges as a limiting case in our theory, but also predicts the other types of condensational growth, confirmed by the recent laboratory and field experiments. In chapter II, we presented a new photochemical mechanism in which the evaporation of the aerosols composed of sulfuric acid or polysulfur on the nightside of Venus could provide a sulfur source above 90 km. Our model results imply the enhancements of sulfur oxides such as SO, SO_2, and SO_3. This is inconsistent with the previous model results but in agreement with the recent ground-based and spacecraft observations. In chapters III and IV, we developed a nonlinear optimization approach to retrieve the aerosol and cloud structure on Jupiter from the visible and ultraviolet images acquired by the Cassini spacecraft, combined with the ground-based near-infrared observations. We produced the first realistic spatial distribution of Jovian stratospheric aerosols in latitudes and altitudes. We also retrieved the stratospheric temperature and hydrocarbon species based on the mid-infrared spectra from the Cassini and Voyager spacecrafts. Based on the above information, the accurate and detailed maps of the instantaneous radiative forcing in Jovian stratosphere are

obtained, revealing a significant heating effect from the polar dark aerosols in the high latitude region and therefore a strong modulation on the global meridional circulation in the stratosphere of Jupiter. In chapter V, we study the transport of passive tracers, such as aerosols, acetylene (C_2H_2) and ethane (C_2H_6) in the Jovian stratosphere, using both analytical and numerical approaches. We established several benchmark analytical solutions for the coupled photochemical-advective-diffusive system to understand its basic behaviors under different assumptions. A numerical two-dimensional chemical transport model is applied to Jupiter, and the effects of eddy mixing process and meridional circulation on the distributions of stratospheric species are discussed.

Table of Contents

List of Figures

List of Tables

Preface

In the revolution of the universe are comprehended all the four elements, and this being circular and having a tendency to come together, compresses everything and will not allow any place to be left void. Wherefore, also, fire above all things penetrates everywhere, and air next, as being next in rarity of the elements; and the two other elements in like manner penetrate according to their degrees of rarity. For those things which are composed of the largest particles have the largest void left in their compositions, and those which are composed of the smallest particles have the least. And the contraction caused by the compression thrusts the smaller particles into the interstices of the larger. And thus, when the small parts are placed side by side with the larger, and the lesser divide the greater and the greater unite the lesser, all the elements are borne up and down and hither and thither towards their own places; for the change in the size of each changes its position in space. And these causes generate an inequality which is always maintained, and is continually creating a perpetual motion of the elements in all time.

—*Timaeus, Plato, 427~347 BC*

Thus begins with the ancient view of the elements of our universe. I had not studied any modern science when I first read it in the middle school. Surprisingly, this picture still looks inspiring and intuitively helpful for me after more than a decade of training in modern physics and chemistry. Is it another evidence of the "footnote to Plato"? Instead, I would rather attribute it to my special interest in planetary atmospheric sciences. In this field the classical sciences are still more or less applicable. The four elements: fire, air, water and earth, not only represent the existence of possible phases of matters (such as plasma, gas, liquid and solid phases) in the atmosphere, but also the metaphors of several important interactive processes in the atmosphere, such as radiation, fluid dynamics, photochemistry and aerosol microphysics, etc. It is always interesting to think as the great masters in ancient Greece, although nowadays we have more powerful tools available to study the details of our hypotheses.

In this dissertation, I selected several publications related to aerosols and their roles in planetary atmospheres. Aerosols are the condensed phases in the atmospheres. They could be solid (e.g., ice crystals and dusts on Mars) or liquid (e.g., sulfuric acid droplets on Venus), or some semi solid phase between them (e.g., polysulfur on Venus). Aerosols could come from many sources. For example, the primary aerosols on Earth are directly emitted from the surface (e.g., sea salt), while the secondary aerosols in the atmosphere are produced by the gas-phase chemical processes. The formation mechanisms of aerosols and their interactions with gas and radiation field are very complicated. Readers are encouraged to consult chapters 8~15 in Seinfeld and Pandis (2006) for our current understanding on aerosols. Aerosols are not only a challenging problem on many planets, but also, or more importantly, aerosol radiative forcing contributes the greatest uncertainty to the Earth's climate predictions according to the recent 2007 IPCC (Intergovernmental Panel on Climate Change) report.

This dissertation is multidisciplinary, trying to elaborate on different aspects on aerosol sciences for different planetary atmospheres. In the following chapters, I focus on several key questions, including how do they form on Earth (chapter I), how do they interact with other atmospheric species on Venus (chapter II), how to determine their properties and distributions on Jupiter (chapter IV), how do they influence the radiative energy distributions on Jupiter (chapter III and IV), and how do the atmospheric circulation and mixing processes shape the tracer (including aerosols) distributions in general and specifically on Jupiter (chapter V). The supplementary materials of chapter II and III are summarized in Appendices A and B, respectively.

In terms of the research approach, chapter I and chapter V are mostly theoretical work, with help of minor numerical simulations. chapter II is a large photochemical simulation study. chapters III and IV mix data analysis, information retrieval and computationally expensive radiative transfer modeling, although some simple approximate theories are also introduced.

Chapter I

Diffusion-Limited versus Quasi-Equilibrium Aerosol Growth*

That is Dao of heaven; it depletes those who abound, and completes those who lack.

— *Lao Tsu, Ancient China*

Summary

Condensation of gas-phase material onto particulate matter is the predominant route by which atmospheric aerosols evolve. The traditional approach to representing formation of secondary organic aerosols (SOAs) is to assume instantaneous partitioning equilibrium of semivolatile organic compounds between gas and particle phases. Growth occurs as the vapor concentration of the species increases owing to gas-phase chemistry. The fundamental mathematical basis of such a condensation growth mechanism (quasi-equilibrium growth) has been lacking. Analytical solutions for the evolution of an organic aerosol size distribution undergoing quasi-equilibrium growth and irreversible diffusion-limited growth are obtained for open and closed systems. The quasi-equilibrium growth emerges as a limiting case for semivolatile species condensation when the rate of change of the ambient vapor concentration is slow compared with the rate of establishment of local gas-aerosol equilibrium. The results suggest that the growth mechanism in a particular situation might be inferred from the characteristics of the evolving size distribution. In certain conditions, a bimodal size distribution can occur during the condensation of a single species on an initially unimodal distribution.

* Appeared as: Zhang, X., Pandis, S.N., Seinfeld, J.H., 2012. Diffusion-limited versus quasi-equilibrium aerosol growth. Aerosol Science and Technology 46, 8, 874-885.

1.1. Introduction

The size distribution of atmospheric aerosols is controlled largely by gas-to-particle conversion, and the characteristics of the evolution of the size distribution are indicative of the nature of the gas-to-particle conversion process. The mode of condensation of gas-phase organic species onto ambient aerosols is of particular interest. In theory, the rate of condensation of a vapor molecule on a particle is controlled by the difference between the ambient partial pressure of the substance and its equilibrium vapor pressure over the particle surface (Seinfeld and Pandis 2006). Under typical atmospheric conditions, the characteristic timescale for gas-phase diffusion to establish a steady-state profile around a particle is generally less than 10^{-3} s (Seinfeld and Pandis 2006). Therefore, at any instant of time, the concentration profile of the species in the vicinity of the particle is established by steady-state molecular diffusion. Once the equilibrium vapor pressure of the condensing species over the particle surface becomes equal to the ambient partial pressure, equilibrium is established between the gas and aerosol phases. If the ambient partial pressure changes slowly relative to the timescale over which the gas-aerosol equilibrium is established, the particle grows (or evaporates) accordingly. The rate of particle growth in this situation is then controlled by the (slower in general) rate of change of the equilibrium vapor pressure over the particle surface. This situation can be referred to as volume-limited or quasi-equilibrium growth. The traditional rate of condensation that depends on the difference between the ambient partial pressure and the vapor pressure over the particle surface can be termed diffusion-limited (or kinetic) condensation. If the equilibrium vapor pressure of the condensing species is zero or practically zero, then the diffusion-limited growth is irreversible.

Riipinen et al. (2011) studied the effect of the mode of condensation on the evolution of the atmospheric size distribution of organic aerosol. They considered both irreversible diffusion-limited growth, that is, irreversible mass transfer with the assumption of a zero vapor pressure at the particle surface (Spracklen et al. 2010), and an approach that assumes that the formation of the organic mass transferred to each particle group is proportional to

its volume fraction (as compared with the total particle volume) of this group. In this application, it was assumed that the particles were mainly organic, so the organic fraction is similar to the total volume fraction. Riipinen et al. (2011) evaluated both approaches to representing organic condensation on the evolution of ambient aerosol size distributions, by comparing predicted versus observed growth rate of freshly nucleated particles. They assumed that the organic species consisted of a low-volatility species that condenses kinetically on the surface area distribution and a semivolatile species that instantaneously reaches gas-particle equilibrium with the aerosol volume distribution. In a comparison of predicted and observed growth rates, the best agreement was achieved when at least 50% of the organic aerosol was assumed to condense via the irreversible kinetic route. Thus, the work of Riipinen et al. (2011) work suggested that the evolution of atmospheric aerosol size distribution owing to organic species condensation exhibits features characteristic of both traditional irreversible diffusion-limited mass transfer and a process in which growth depends on the volume of condensed species. A characteristic of the latter mechanism is that the greater the amount of condensed absorbing material, the greater is the capacity for absorption of vapor.

Recent work illustrated the potential role of different mechanisms of particle growth in the formation of secondary organic aerosol (SOA). Perraud et al. (2012) reported studies of particles formed in the simultaneous oxidation of α-pinene by O_3 and NO_3. The NO_3 reaction with α-pinene led to organic nitrates, which typically are more volatile than the products of ozonolysis. In separate experiments, organic nitrate vapor products from the reaction of α-pinene and NO_3 are exposed to liquid polyethylene glycol (PEG) particles. Uptake by the PEG droplets was shown to be consistent with gas-particle partitioning equilibrium. Uptake of the same nitrate products by the SOA formed by the ozonolysis of α-pinene, however, was shown to behave consistent with a nonequilibrium, kinetically limited mechanism. Moreover, such behavior indicates that re evaporation of the organic nitrates back to the gas phase is negligible on the timescale of the experiments, as would be consistent with the SOA material being highly viscous. Other recent studies showed that SOA particles behave as semisolid material (Virtanen et al. 2010, 2011; Vaden et al. 2011).

The properties of SOA (formed by the ozonolysis of α-pinene) inferred by Perraud et al. (2012) were also observed by Cappa and Wilson (2011) as evidenced by much slower rates of thermal evaporation than expected for liquid droplets.

Up to this point, a mathematical analysis of a particle growth mechanism depending on particle volume has been lacking. We investigate here the fundamental aspects of this growth mechanism and we contrast it to the irreversible diffusion-limited condensation case. These two approaches have been used in regional and global chemical transport models to describe the formation of SOA (Lane et al. 2008; Spracklen et al. 2010).

The present work is structured as follows. In section 1.2, we present both the condensation equation that governs the time-dependent growth (or evaporation) of the aerosol size distribution and the general form of the growth law that governs the rate of change of the size of a particle under customary diffusion-limited conditions. The volatility of the condensing species is characterized by its pure component vapor pressure; a "non-volatile" species has essentially a zero vapor pressure, whereas a "semi-volatile" species has a vapor pressure such that at equilibrium the species exists appreciably in both gas and particle phases. In order to illustrate the two cases, we consider a situation in which the ambient partial pressure of the species begins increasing at a given rate at $t = 0$, at which time the particles commence growing.

In a so-called "open system," the vapor is continually replenished so that the loss of vapor to growing particles can be neglected. In a "closed system," vapor loss to growing particles must be accounted for. We obtain analytical solutions for the evolution of aerosol size distribution in an open system in the two cases of diffusion-limited and quasi-equilibrium growth. The inherent timescale for growth in the open system is that at which the ambient partial pressure is changing. In the case of quasi-equilibrium growth, as might occur with a semivolatile species, equilibrium between the gas and particle phases is established rapidly relative to the timescale at which the partial pressure is changing. Particles then grow as the equilibrium continually shifts to respond to the increasing partial pressure of the

condensing species. Condensation of a nonvolatile species is simply described by diffusion-limited growth. In the closed system, an equilibrium state of the entire gas–particle system is eventually reached at which the equilibrium vapor pressure over all particles is the same.

We show explicitly that in the usual case of formation of semivolatile SOA in which the ambient vapor generation rate is slow compared with the vapor absorption rate by the particles, the particles reach a quasi-equilibrium state, which characterizes gas-particle partitioning equilibrium across the entire size spectrum. Both diffusion-limited and quasi-equilibrium growth are illustrated by numerical simulations in section 1.3.

1.2. Condensation Equation

The general dynamic equation governing the size distribution of aerosols undergoing condensation and evaporation processes is (Seinfeld and Pandis 2006) as follows:

$$\frac{\partial n_D(D_p,\ t)}{\partial t} + \frac{\partial [I_D(D_p,\ t) n_D(D_p t)]}{\partial D_p} = 0, \tag{1.1}$$

where $n_D(D_p,\ t)$ is the particle number distribution as function of diameter D_p and the time t. Here $I_D(D_p,\ t) = dD_p/dt$ is the rate of change of the diameter of a single particle due to condensation or evaporation. The traditional initial and boundary conditions for equation (1.1) are

$$n_D(D_p, 0) = n_0(D_p), \tag{1.2}$$

$$n_D(0, t) = 0. \tag{1.3}$$

The condensation equation implies conservation of the total number of particles. We neglect here all other processes that could lead to an increase or decrease in the total number of particles, such as coagulation, new particle formation, particle loss, etc.

Because D_p is a monotonic function of D_0, where D_0 is the initial diameter, the number of particles in each size bin is conserved:

$$n_D(D_p, t)dD_p(t) = n_0(D_0)dD_0. \quad (1.4)$$

The size distribution $n_D(D_p, t)$ at time t can be expressed as

$$n_D(D_p, t) = \frac{\partial D_0(D_p,\ t)}{\partial D_p} n_0(D_0(D_p, t)), \quad (1.5)$$

where $D_0(D_p,\ t)$ is the initial diameter of a particle that has a diameter D_p at time *t*. That equation (1.5) is the general solution of equation (1.1) is demonstrated by substitution and using the equation:

$$\frac{dD_0}{dt} = \frac{\partial D_0(D_p, t)}{\partial t} + \frac{\partial D_0(D_p, t)}{\partial D_p}\frac{dD_p}{dt} = 0. \quad (1.6)$$

One needs to solve the characteristic curve of equation (1.1), i.e., the growth rate equation $I_D(D_p, t) = dD_p/dt$ with the boundary condition $D_p(0) = D_0$.

In diffusion-limited condensation, the general growth law can be expressed as (Seinfeld and Pandis 2006) follows:

$$I_D(D_P, t) = \frac{4D_i M_i}{RTD_p\rho_p}\left(p_i(t) - p_{eq,i}(D_p)\right) f(K_n, \alpha), \quad (1.7)$$

where *Di* is the molecular diffusion coefficient for species *i* in air, *T* is the temperature, *R* is the gas constant, ρ_p is the density of the particle, M_i is the molecular weight of the condensing species, $f(Kn, \alpha)$ is the correction factor for noncontinuum conditions, and α is the accommodation coefficient. The Knudsen number Kn is $Kn = \lambda_i/D_p$, where λ_i is the mean free path of condensable species i; $p_i(t)$ is the partial pressure of i far from the particle surface and $p_{eq,i}(D_p)$ is the equilibrium vapor pressure of i over the particle surface. Also $p_{eq,i}(D_p)$ depends on particle size and composition through Raoult's law and the Kelvin effect in an ideal solution:

$$p_{eq,i}(D_p) = \chi_i p^0_{eq,i}\, exp\left(\frac{4\sigma M_i}{RT\rho_p D_p}\right), \quad (1.8)$$

where $p^0_{eq,i}$ is the equilibrium vapor pressure of the pure component i and χ_i is the mole fraction of the species i in the particle phase (an ideal solution is assumed for simplicity). The exponential term expresses the Kelvin effect; σ is the particle surface tension.

In this work, we consider only the case with one condensable species. Conclusions will hold for the multicomponent case as well. Let us assume that at $t = 0$, the particle consists of a nonvolatile "solvent," for convenience with molecular weight M_i. To simplify the derivation, we assume that the density of the condensable species is the same as that of the nonvolatile solvent. From mass conservation of the solvent,

$$\frac{\pi}{6}\rho_p D_p^3(1-\chi_i) = \frac{\pi}{6}\rho_p D_0^3(1-\chi_{i0}), \tag{1.9}$$

where χ_{i0} is the initial mole fraction of i in the particle, if any, and D_0 is its initial diameter. From equations (1.8) and (1.9), we obtain

$$p_{eq.i}(D_p) = p_{eq.i}^0\left[1-\left(\frac{D_0}{D_p}\right)^3(1-\chi_{i0})\right]exp\left(\frac{4\sigma M_i}{RT\rho_p D_p}\right), \tag{1.10}$$

from which the growth law can be expressed as

$$I_D(D_P,t) = \frac{dD_p}{dt}$$
$$= \frac{4D_i M_i}{RTD_p\rho_p}\left\{p_i(t) - p_{eq.i}^0\left[1-\left(\frac{D_0}{D_p}\right)^3\times(1-\chi_{i0})\right]exp\left(\frac{4\sigma M_i}{RT\rho_p D_p}\right)\right\}f(Kn,\alpha). \tag{1.11}$$

1.2.1. Open System

We begin with an idealized case of an open system in which the partial pressure $p_i(t)$ linearly increases with time: $p_i(t) = \gamma t$, and the initial mole fraction of i in the particle $\chi_{i0} = 0$. The general conclusions of this work will apply for a nonzero initial mole fraction χ_{i0}. The effect of the uptake of i by growing particles on $p_i(t)$ is neglected. With the general growth law of equation (1.11), the condensation equation must be solved numerically. In the following two special cases, an analytical solution of equation (1.1) is possible.

1.2.1.1. Analytical Solution of Irreversible Diffusion-Limited Growth

Consider first the case in which the condensing species is essentially nonvolatile (i.e., $p_{eq.i}^0$

≈ 0). If the rate of increases of $p_i(t)$ is sufficiently rapid, then the initial period during which $\gamma t \approx p^0_{eq.i}$ can be neglected with respect to growth since at this point $D_p \approx D_0$. The partial pressure gradient can simply be approximated by

$$\gamma t - p^0_{eq.i}\left[1 - \left(\frac{D_0}{D_p}\right)^3\right] exp\left(\frac{4\sigma M_i}{RT\rho_p D_p}\right) \approx \gamma t. \tag{1.12}$$

In the diffusion-limited growth case, the growth rate can be expressed as $I_D\big(D_p, t\big) = A(t)G\big(D_p\big)$, where $A(t) = A_1 t$ with $A_1 = 4D_i M_i \gamma / RT\rho_p$ and $G\big(D_p\big) = f(Kn, \alpha)/D_p$.

Instead of solving the growth rate equation and using equation (1.5), here it is useful to define

$$F_D(D_{p,}t) = G\big(D_p\big)n_D\big(D_p, t\big), \tag{1.13}$$

and equation (1.1) becomes

$$\frac{\partial F_D(D_p, t)}{\partial t} + I_D\big(D_p, t\big)\frac{\partial F_D(D_p, t)}{\partial D_p} = 0, \tag{1.14}$$

the characteristic curves of which are

$$\frac{dD_p}{dt} = I_D\big(D_p, t\big). \tag{1.15}$$

Along the characteristic curves, $F_D(D_p, t)$ is constant. Therefore,

$$F_D\big(D_p, t\big) = F_D(D_0, 0) = G(D_0)n_0(D_0). \tag{1.16}$$

Here $D_0 = D_p(t = 0)$ and is expressed as $D_0 = D_0\big(D_p, t\big)$. From equations (1.13) and (1.16), we obtain

$$n_D\big(D_p, t\big) = \frac{G(D_0)}{G\big(D_p\big)}n_0(D_0) = \frac{D_p}{D_0}\frac{f(Kn(D_0), \alpha)}{f\big(Kn\big(D_p\big), \alpha\big)}n_0(D_0). \tag{1.17}$$

where $D_0 = D_0\big(D_p, t\big)$ is found from equation (1.15). Note that equation (1.17) is essentially a special case of equation (1.5). Equation (1.15) may not always be amenable to analytical solution. Here, we present the solutions for the continuum, free-molecule, and transition regimes, respectively. In the first two cases, we can obtain an explicit expression of the final distribution, $n_D(D_p, t)$. For the transition regime, the solution depends on the functional form of $f(Kn, \alpha)$.

• ***Continuum Regime***

In the continuum regime $(Kn \ll 1), f(Kn, \alpha) = 1,$ and equation (1.15) becomes $D_p dD_p = A(t)dt,$ from which we obtain $D_0 = (D_p^2 - A_1 t^2)^{1/2}$, and the solution of the condensation equation is

$$n_D(D_p, t) = \frac{D_p}{(D_p^2 - A_1 t^2)^{1/2}} n_0 \left[\left(D_p^2 - A_1 t^2 \right)^{1/2} \right]. \tag{1.18}$$

This is similar to equation (13.25) in Seinfeld and Pandis (2006).

• ***Free-molecule Regime***

In the free-molecule regime $(Kn \gg 1), f\left(Kn(D_p), \alpha\right) = \alpha D_p / 2\lambda_i.$ Equation (1.15) becomes $(2\lambda_i/\alpha) dD_p = A(t)dt.$ We obtain $D_0 = D_p - \alpha A_1 t^2 / 4\lambda_i,$ and the solution is

$$n_D(D_p, t) = n_0 \left(D_p - \frac{\alpha A_1}{4\lambda_i} t^2 \right). \tag{1.19}$$

We note that in the free-molecule regime, the entire distribution evolves toward larger diameters, with its shape preserved.

• ***Transition Regime***

There are several available expressions for the flux-matching factor $f(Kn, \alpha)$ in the transition regime (Seinfeld and Pandis 2006). Park and Lee (2000) showed that the harmonic mean expression for $f(Kn, \alpha)$ is the only form for which $D_p(t)$ can be solved explicitly. Here $f(Kn, \alpha)$ in the harmonic mean approach is

$$f(Kn, a) = \frac{1}{1 + \frac{2K_n}{\alpha}}, \tag{1.20}$$

for which the characteristic curves are given by

$$D_p^2 - D_0^2 + \frac{4\lambda_i}{\alpha} (D_p - D_0) - A_1 t^2 = 0. \tag{1.21}$$

and we obtain

$$D_0 = -\frac{2\lambda_i}{\alpha} + \left[\left(D_p + \frac{2\lambda_i}{\alpha} \right)^2 - A_1 t^2 \right]^{\frac{1}{2}}. \tag{1.22}$$

The analytical solution for the size distribution in this case is

$$n_D(D_p,t)=\frac{D_p+\frac{2\lambda_i}{\alpha}}{[(D_p+\frac{2\lambda_i}{\alpha})^2-A_1t^2]^{1/2}}\times n_0\left\{-\frac{2\lambda_i}{\alpha}+\left[\left(D_p+\frac{2\lambda_i}{\alpha}\right)^2-A_1t^2\right]^{1/2}\right\}. \quad (1.23)$$

For the Dahneke (1983) flux-matching formula for $f(Kn,\alpha)$,

$$f(Kn,\alpha)=\frac{1+Kn}{1+2Kn(1+Kn)/\alpha}, \quad (1.24)$$

one can insert equation (1.24) into equation (1.15), from which we obtain

$$D_p^2-D_0^2+\left(\frac{4\lambda_i}{\alpha}-2\right)(D_p-D_0)+2\lambda_i^2\ln\frac{D_p+\lambda_i}{D_0+\lambda_i}-A_1t^2=0. \quad (1.25)$$

Although $D_p(t)$ cannot be expressed in terms of D_0 and t explicitly, this formula can be evaluated numerically and used in equation (1.18).

1.2.1.2. Analytical Solution of Quasi-Equilibrium Growth

In this case, we assume that quasi-equilibrium between the gas and particle phases can be established in a relatively short timescale. Note that this approximation may be valid only for particles for which the timescale to reach gas-particle equilibrium is sufficiently short (Meng and Seinfeld 1996). The quasi-equilibrium state implies

$$\gamma t\approx p_{eq.i}^0\left[1-\left(\frac{D_0}{D_p}\right)^3\right]exp\left(\frac{4\sigma M_i}{RT\rho_pD_p}\right). \quad (1.26)$$

In the case of quasi-equilibrium growth, each particle is assumed at all times to be in quasi-equilibrium with the gas-phase partial pressure. From equation (1.26),

$$D_0(D_p,t)=D_p\left[1-\frac{t}{B}exp\left(-\frac{K}{D_p}\right)\right]^{1/3}, \quad (1.27)$$

where B is the characteristic timescale for the change of the partial pressure of the ambient vapor and K is the Kelvin effect factor:

$$B=\frac{p_{eq.i}^0}{\gamma},\qquad K=\frac{4\sigma M_i}{RT\rho_p}. \quad (1.28)$$

By differentiating equation (1.27), we obtain

$$\frac{\partial D_0(D_p,t)}{\partial D_p} = \left[1 - \frac{K}{3D_p}\frac{t}{Bexp(K/D_p) - t}\right] \times \left[1 - \frac{t}{B}exp\left(-\frac{K}{D_p}\right)\right]^{1/3}. \quad (1.29)$$

Substituting into equation (1.5), we obtain the general solution for the quasi-equilibrium growth:

$$n_D(D_p,t) = \left[1 - \frac{K}{3D_p}\frac{t}{Bexp\left(\frac{K}{D_p}\right) - t}\right] \times \left[1 - \frac{t}{B}exp\left(-\frac{K}{D_p}\right)\right]^{1/3} \times n_0\left[D_p\left[1 - \frac{t}{B}exp\left(-\frac{K}{D_p}\right)\right]^{1/3}\right]. \quad (1.30)$$

The time evolution of the total volume and the mean diameter can also be obtained. If the Kelvin effect can be neglected (equivalent to setting $K = 0$ in equation (1.30)), the expressions are

$$V(t) = \frac{V_0}{1 - t/B}, \quad (1.31)$$

$$D(t) = \frac{D_0}{(1 - t/B)^{1/3}}. \quad (1.32)$$

where V_0 and D_0 are, respectively, the total volume and the mean diameter of the initial size distribution (pure solvent). Equations (1.31) and (1.32) show that both quantities accelerate in the long time range (larger t), as a consequence of the assumed continuing increase of the partial pressure in the gas phase. As the vapor pressure of the condensing species approaches its equilibrium value, the volume concentration increases dramatically. Equilibrium of the binary particles with the vapor at its pure component saturation concentration requires a molar fraction equal to unity and therefore infinite condensation of the semivolatile component resulting in infinite dilution of the preexisting absorbing material.

1.2.2. Closed System

In the closed system, we assume that the initial ambient partial pressure of the vapor is p_0. Let us assume that initially there is no condensed species i in the particle. At $t = 0$,

regardless of vapor pressure, all particles begin growing by diffusion-limited condensation. According to equation (1.11), initially smaller particles will grow faster. If the species vapor pressure is so small that the compound is essentially nonvolatile, then particles simply grow by diffusion-limited condensation until the vapor is exhausted. The ultimate aerosol size distribution is that predicted by diffusion-limited growth. For semivolatile species, as the ambient partial pressure decreases owing to uptake by particles, at some point the smaller size particles reach equilibrium with the ambient vapor. The Kelvin effect accelerates this process. As the larger particles continue to grow, the ambient partial pressure continues to decrease, leading to evaporation of the smaller particles. The competition among particles of different sizes for the available vapor will eventually result in an overall equilibrium state of the entire system in which the equilibrium vapor pressure over all particles is the same.

Although the time evolution of the particle size distribution has to be obtained numerically, the equilibrium state of the system can be derived analytically. The final equilibrium vapor pressure over each particle is the same and can be expressed as $\zeta p_{eq.i}^0$:

$$\chi_{eq}(D_p) p_{eq.i}^0 \, exp\left(\frac{K}{D_p}\right) = \zeta p_{eq.i}^0 , \tag{1.33}$$

where $0 < \zeta < 1$. From equation (1.9), we obtain

$$D_0 = D_p \left[1 - \zeta exp\left(-\frac{K}{D_p}\right)\right]^{1/3} . \tag{1.34}$$

The final equilibrium partial pressure in equations (1.33) and (1.34) is expressed as a fraction ζ of $p_{eq.i}^0$. The fraction ζ can be related to the mole fraction χ_∞ of the condensed species in particles at the large end of the size distribution, where the Kelvin effect is expected to be smallest.

The ultimate change of each diameter δD:

$$\delta D = D_p - D_0 = D_p \left[1 - \left[1 - \chi_\infty \exp\left(-\frac{K}{D_p}\right)\right]^{\frac{1}{3}}\right], \tag{1.35}$$

increases with D_p, such that, in reaching the equilibrium state, larger particles experience larger diameter change during the evolution. This behavior is fundamentally different from that in diffusion-limited growth, where the small particles exhibit a proportionately larger size change. This behavior, as shown in section 1.2.1.2, is characteristic of "equilibrium growth," or "volume growth," in which larger particles absorb more vapor and thus grow preferentially.

From equation (1.34),

$$\frac{dD_0}{dD_p} = \left[1 - \frac{K}{3D_p}\frac{\chi_\infty}{exp\,(K/D_p) - \chi_\infty}\right] \times \left[1 - \chi_\infty exp\left(-\frac{K}{D_p}\right)\right]^{1/3}, \qquad (1.36)$$

and from the conservation law, i.e., equation (1.4), the equilibrium size distribution $n_{eq}(D_p)$ is obtained:

$$n_{eq}(D_p) = \left[1 - \frac{K}{3D_p}\frac{\chi_\infty}{\exp\left(\frac{K}{D_p}\right) - \chi_\infty}\right] \times \left[1 - \chi_\infty exp\left(-\frac{K}{D_p}\right)\right]^{\frac{1}{3}} \times$$

$$n_0\left[D_p\left[1 - \chi_\infty exp\left(-\frac{K}{D_p}\right)\right]^{1/3}\right]. \qquad (1.37)$$

Now we can derive χ_∞. In the equilibrium state, the partial pressure of the ambient gas is equal to the equilibrium vapor pressure over the particle surface: $\chi_\infty p^0_{eq.i}$. Therefore, the total mass loss in the gas phase during the condensation process (per unit volume of air) is

$$\delta m_{i,g} = \frac{(p_0 - \chi_\infty p^0_{eq.i})M_i}{RT}. \qquad (1.38)$$

On the other hand, the total mass of the condensed species in the particle phase (per unit volume of air) is

$$\delta m_{i,p} = \rho_p(V_{eq} - V_0) = \int_0^\infty \rho_p\,\chi_\infty exp\left(-\frac{K}{D_p}\right)\frac{\pi}{6}D_p^3 n_{eq}(D_p)dD_p, \qquad (1.39)$$

where V_{eq} and V_0 are the total volumes for the equilibrium state and the initial state, respectively. In a closed system, the total mass is conserved, i.e., $\delta m_{i,p} = \delta m_{i,g}$:

$$\rho_p\left(V_{eq} - V_0\right) = \frac{\left(p_0 - \chi_\infty p^0_{eq.i}\right)M_i}{RT}. \tag{1.40}$$

One can insert equation (1.37) into equation (1.39) and solve for χ_∞ numerically by equating the right-hand sides of equations (1.39) and (1.40).

In the special case in which the Kelvin effect can be neglected, each particle will have the same equilibrium mole fraction therefore $V_{eq} = V_0/(1 - \chi_\infty)$. Equation (1.40) becomes

$$\frac{(p_0 - \chi_\infty p^0_{eq.i})M_i}{RT} = \frac{\chi_\infty}{1 - \chi_\infty}\rho_p V_0 \tag{1.41}$$

from which

$$\chi_\infty = \frac{p_0 + p^0_{eq.i} + \eta - \sqrt{(p_0 + p^0_{eq.i} + \eta)^2 - 4p_0 p^0_{eq.i}}}{2p^0_{eq.i}},$$

$$\text{where } \eta = \rho_p RTV_0/M_i. \tag{1.42}$$

Therefore, three factors determine χ_∞: $p_0, p^0_{eq.i}$, and η. We note that χ_∞ increases as p_0 increases, $p^0_{eq.i}$ decreases, and η decreases. When the initial partial pressure of the vapor is large, more vapor will condense so that the ultimate mole fraction is higher. The final mole fraction is lower if there is more initial solvent (larger V_0) or the temperature is higher.

1.3. Size Distribution Dynamics

In this section, we illustrate the foregoing theory by analyzing the size distribution evolution over a range of conditions of condensing species volatility. For numerical evaluation of the solutions, we choose the following parameter values: $D_i = 0.1\ \text{cm}^2\ \text{s}^{-1}, M_i = 100\ \text{g mol}^{-1},\ T = 298\ \text{K}, \rho_p = 1\ \text{g cm}^{-3}, \alpha = 1,$ and $\lambda_i = 0.06\ \mu\text{m}$; $p^0_{eq.i}$ and γ are varied in different cases. (A value of $p^0_{eq.i} = 10^{-9}$ atm corresponds to a gas-phase saturation mass concentration, $c_i^* \approx 4\ \mu g\ m^{-3}$.) We consider an initially lognormally distributed aerosol population consisting of nonvolatile solvent:

$$n_D\left(D_p, 0\right) = n_0(D_0) = \frac{N_0}{\sqrt{2\pi}D_0 \ln\sigma_g} exp\left(-\frac{\ln^2(D_0/\overline{D}_{pg}}{2\ln^2\sigma_g}\right). \tag{1.43}$$

For these illustrative examples, we assume that $N_0 = 10^4\ cm^{-3}, \overline{D}_{pg} = 0.05\ \mu m$, and $\sigma_g = 1.5$.

1.3.1. Open System

A balance on the vapor in an open system, in which the loss of vapor owing to condensation is accounted for, is

$$\frac{dp_i(t)}{dt} = \gamma - \frac{\rho_p RT}{M_i}\int_0^\infty \frac{\pi}{2} D_p^2 \frac{dD_p}{dt} n(D_p, t) dD_p, \tag{1.44}$$

or

$$\frac{dp_i(t)}{dt} = \gamma - 2\pi D_i \times \int_0^\infty D_p \left\{ p_i(t) - p_{eq.i}^0 \left[1 - \left(\frac{D_0}{D_p} \right)^3 (1 - \chi_{i0}) \right] \times exp\left(\frac{4\sigma M_i}{RT\rho_p D_p} \right) \right\} f(Kn, \alpha) n(D_p, t) dD_p. \tag{1.45}$$

If the volatility of i is sufficiently low, and $p_i(t) \gg p_{eq.i}$, the solution for diffusion-limited condensation, in which it is assumed that $p_{eq.i}$ is constant ($p_{eq.i}^0$), can be viewed as providing an upper limit for the rate of diffusion growth. The inherent timescale of the growth is governed by the rate at which the partial pressure is assumed to change, γ. Figure 1.1 shows the time evolution of both the number and the volume distributions under diffusion-limited growth using the Dahneke flux-matching formula (equation (1.24)). In this case, $p_{eq.i}^0 = 0$ atm and$\gamma = 10^{-11}$atm min^{-1}. The size distribution exhibits the well-known narrowing characteristics of diffusion-limited growth. On the other hand, a quasi-equilibrium solution can be obtained from equation (1.25). Figure 1.2 shows the time evolution of the aerosol in this regime for the case in which $p_{eq.i}^0 = 10^{-9}$ atm and $\gamma = 10^{-11}$atm min^{-1}. While this regime is idealized, the solution captures the important characteristics of equilibrium growth, i.e., the larger particles grow preferentially.

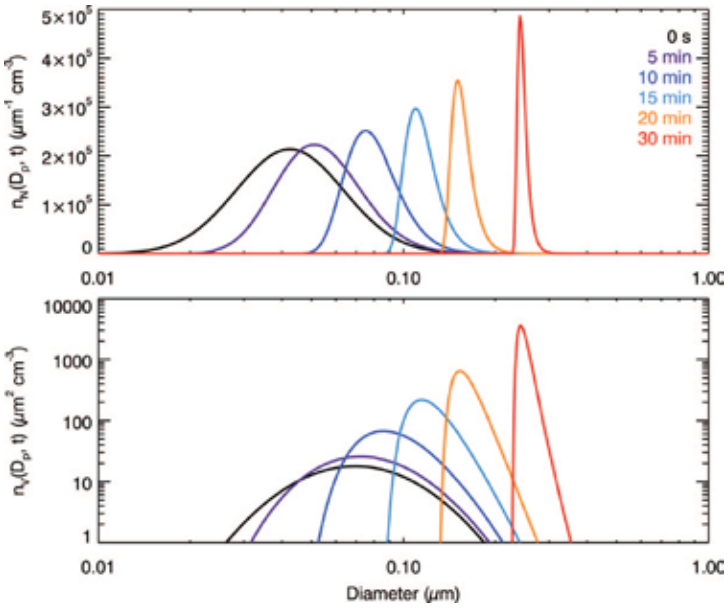

Figure 1.1. Analytical solution of diffusion-limited growth in an open system with flux-matching expressions from Dahneke (1983). Evolution of the aerosol number distribution, $n_N(D_p, t)$, and the volume distribution, $n_V(D_p, t)$; $p^0_{eq.i} = 0$ atm, $\gamma = 10^{-11}$ atm min^{-1}.

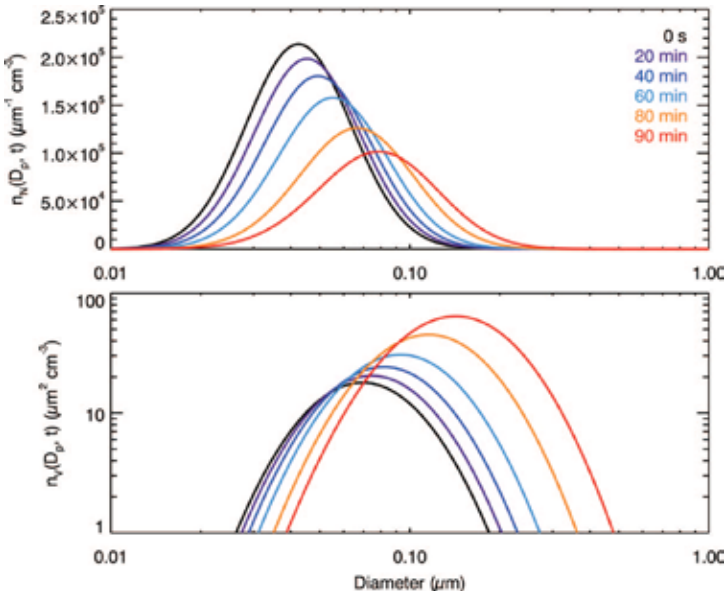

Figure 1.2. Analytical solution of quasi-equilibrium growth in an open system. Evolution of the aerosol number distribution, $n_N(D_p, t)$, and the volume distribution, $n_V(D_p, t)$; $p^0_{eq.i} = 10^{-9}\ atm, \gamma = 10^{-11}\ atm\ min^{-1}$.

1.3.2. Closed System

In the closed system, in the absence of vapor generation, the system will eventually reach equilibrium. The timescale to reach the equilibrium state depends on the initial vapor partial pressure, p_0, the pure component equilibrium pressure, $p_{eq.i}^0$, and the total volume of particles at the initial state, V_0. In the numerical simulations, we assume $\gamma = 0$ and solve equations (1) and (45) together. Figure 1.3 shows the time evolution of the aerosol with $p_0 = 10^{-8}$ atm and $p_{eq.i}^0 = 10^{-9}$ atm. In the first few minutes, the size distribution evolves as in diffusion-limited growth, with the width narrowing and the peak increasing with time. After about 10 min, the peak of the size distribution begins to decrease, and the width increases. The retreat of the peak results from the evaporation of small particles as the partial pressure of the ambient gas decreases, while the large particles continue to grow. After 10 hr, the entire system reaches approximately the equilibrium state, which is predicted by the analytical solution (dashed line, equation (1.37)). For a more volatile species with $p_{eq.i}^0 = 10^{-8}$ atm (Figure 1.4), the system reaches the equilibrium state in about 10 min.

The physical basis of the growth observed in the formation of semivolatile SOA is now evident. The ambient vapor generation rate is slow compared with the vapor absorption rate by the particles, and the particles are able to reach a quasi-equilibrium state. Suppose two different size particles exist with the same initial mole fraction of condensable species. If the vapor supply is unlimited, the partial pressure gradient between the ambient gas and the smaller particles is roughly the same as that between the larger particles at any time, and thus, the smaller particles will always grow faster than the larger particles, i.e., diffusion-limited growth. However, if the vapor supply is limited, the condensed-phase mole fractions adjust accordingly. The smaller particles respond faster so that the partial pressure gradient declines faster, while the larger particles continue to evolve, eventually establishing gas-particle partitioning equilibrium across the entire size spectrum.

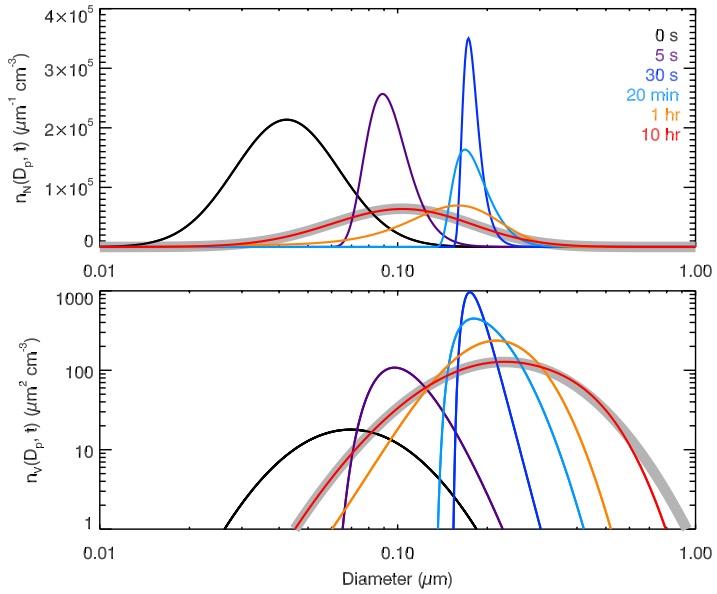

Figure 1.3. Evolution of the aerosol number distribution, $n_N(D_p, t)$, and the volume distribution, $n_V(D_p, t)$, in a closed system; $p_0 = 10^{-8}$ atm, $p^0_{eq.i} = 10^{-9}$ atm. The gray curve shows the analytical solution for the final distribution ($\chi_\infty = 0.9832$).

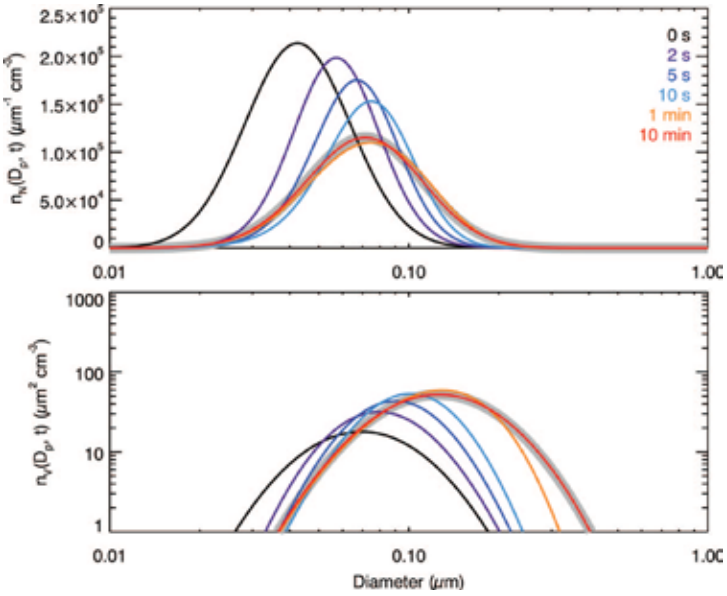

Figure 1.4. Evolution of the aerosol number distribution, $n_N(D_p, t)$, and the volume distribution, $n_V(D_p, t)$, in a closed system; $p_0 = 10^{-8}$ atm, $p^0_{eq.i} = 10^{-8}$ atm. The gray curve shows the analytical solution for the final distribution ($\chi_\infty = 0.8485$).

1.3.3. General System

In the fully general system, there is a constant addition of vapor and at the same time condensation to the particles. One can explore different types of size distribution dynamics by varying the initial distribution (the vapor loss term depends strongly on the total volume of particles), γ, and $p_{eq.i}^0$. In this study, we fix the initial distribution as above and demonstrate typical evolution patterns. The simulation is based on the simultaneous solution of equations (1.11) and (1.45). Different initial distributions will lead to quantitatively different, but qualitatively consistent, conclusions. For instance, for a larger number concentration (N_0 is larger), or aerosol volume ($\overline{D}_{pg}$is larger), the transition time from diffusion-limited growth to equilibrium growth will be shorter.

For $\gamma = 10^{-9}$ atm min^{-1} and $p_{eq.i}^0 = 10^{-10}$ atm, the vapor generation rate is sufficiently large that vapor loss to particles is relatively unimportant. Figure 1.5 shows the standard diffusion-limited growth pattern that results, as we obtained in the open system (Figure 1). Again, the inherent growth timescale is governed by γ.

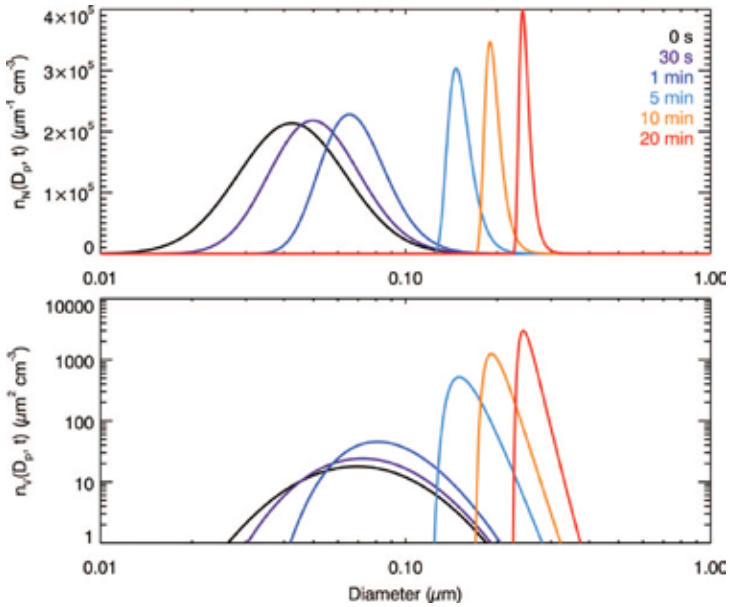

Figure 1.5. Simulated evolution of the aerosol number distribution, $n_N(D_p, t)$, and the volume distribution, $n_V(D_p, t)$, in a fully general system; $p_{eq.i}^0 = 10^{-10}$ atm, $\gamma = 10^{-9}$ atm min^{-1}.

For $\gamma = 10^{-11}$ atm min^{-1} and $p^0_{eq.i} = 10^{-10}$ atm, the vapor generation is sufficiently slow that the equilibrium partial pressure over the particle surface is able to reach the quasi-equilibrium state, and the size distribution exhibits a shape characteristic of equilibrium growth (Figure 1.6). Note that the growth in the full system significantly differs from the quasi-equilibrium case in the open system (Figure 1.2). In the quasi-equilibrium case, if the vapor is generated indefinitely, the maximum value of the vapor pressure over the surface of a particle is that of the pure substance, after which a quasi-equilibrium state does not exist. As the particles grow, the capacity to absorb the ambient vapor increases, and the ambient vapor pressure can achieve a nearly constant level when the rate of vapor absorption by the particles equals the rate of vapor generation. Larger particles have a larger absorption capacity so that they grow faster and lead to a broader size distribution. The growth rate is limited by the rate of change of the ambient partial pressure, γ, which governs the inherent timescale.

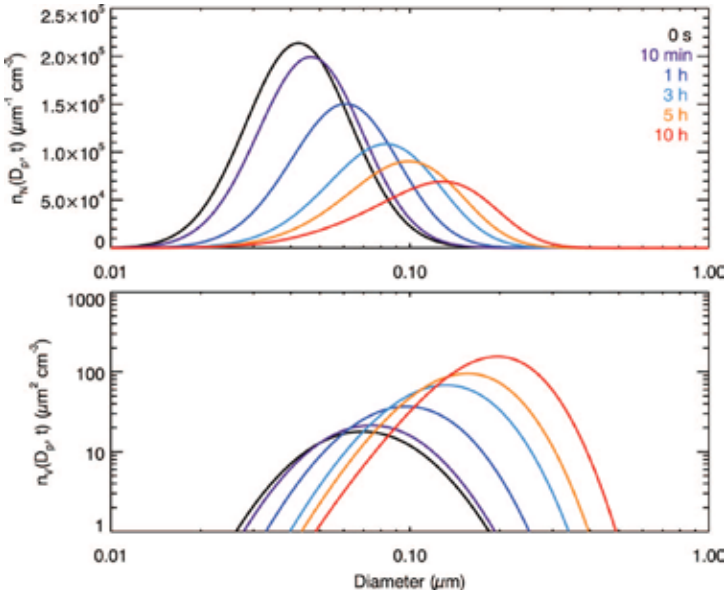

Figure 1.6. Simulated evolution of the aerosol number distribution, $n_N(D_p, t)$ and the volume distribution, $n_V(D_p, t)$, in a fully general system; $p^0_{eq.i} = 10^{-10}$ atm, $\gamma = 10^{-11}$ atm min^{-1}.

In the case of $\gamma = 10^{-9}$ atm min^{-1} and $p^0_{eq.i} = 10^{-9}$ atm, the size evolution pattern demonstrates both equilibrium and diffusion-limited growth (Figure 1.7). In the first few

minutes, when the vapor partial pressure is not large, the evolution behaves like equilibrium growth; after the gas partial pressure is large enough to maintain the partial pressure gradient, the smaller particles grow faster and catch up with the larger particles, i.e., diffusion-limited growth.

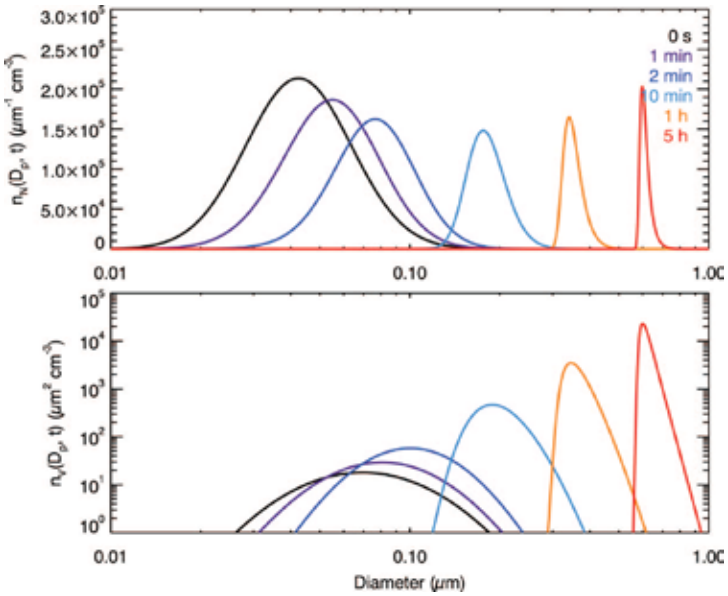

Figure 1.7. Simulated evolution of the aerosol number distribution, $n_N(D_p, t)$ and the volume distribution, $n_V(D_p, t)$, in a fully general system; $p^0_{eq.i} = 10^{-9}$ atm, $\gamma = 10^{-9}$ atm min^{-1}.

A "two-mode case" is shown in Figure 1.8, with $\gamma = 10^{-9}$ atm min^{-1} and $p^0_{eq.i} = 10^{-8}$ atm. This case is same as that in Figure 1.7 except that the condensable species is more volatile. All the particles grow more slowly because they reach equilibrium more readily. An approximate, but quantitative, explanation may be obtained from equations (1.31) and (1.32): when B is larger, $V(t)$ and $D(t)$ are smaller. As the particles grow larger, the rate of vapor absorption by the particles increases, and it will slightly exceed the rate of vapor generation (in this case, it occurs at about 30 min). After that, the partial pressure of the ambient gas gradually decreases for a long period. Small particles partial pressure continues to decrease. However, even larger particles, e.g., > 0.3 μm, continue to grow by diffusion, because the equilibrium vapor pressure over their surface is still low. A divergence in the particle bins occurs around 0.2~0.3 μm. A new particle mode is formed

near 0.1 μm from particles that have partially evaporated. This two-mode feature could persist as long as the partial pressure continues to decrease, until the equilibrium vapor pressure over the large end of the spectrum becomes large enough to reduce the rate of vapor absorption below that of the rate of vapor generation. In the case of Figure 1.7, initially the particles grow faster than the case of Figure 1.8, and the ambient vapor pressure actually starts to decrease much earlier (at about 3 min). However, the small size mode is not obvious because only a tiny fraction of the particles in the small end of the spectrum reach the equilibrium state at that time. By noting this, we can suggest conditions for the occurrence of the two-mode size distribution. (1) A condensable species with an intermediate pure component equilibrium pressure. If $p_{eq.i}^{0}$ is too small, the particles will exhibit diffusion-limited growth. If the species is too volatile, the particles will grow too slowly to suppress the increase of the partial pressure of the ambient vapor, and the size distribution will just behave as an equilibrium growth. (2) Before the rate of vapor absorption by the particles exceeds the rate of vapor generation, there must be sufficient particles in the equilibrium state in order to form a discernible mode. The two-mode pattern could persist for a long period (10 hr or more in the case of Figure 1.8).

1.4. Atmospheric Implications

The present work is directly relevant to the analysis of SOA growth. The traditional approach of assuming instantaneous partitioning equilibrium of semivolatile organic compounds between the gas and particle phases has been consistently verified in the case of liquid aerosol particles. Recent work, as discussed in section 1.1, has shown that in certain cases, the aerosol itself has the properties of semisolid material. In that case, a species once condensed and incorporated into the aerosol phase is essentially trapped in the particle, and the establishment of equilibrium with the vapor phase is significantly retarded. The condensational growth in that case will exhibit the characteristics of diffusion-limited growth. These contrasting modes of growth will be reflected in the character of the resulting aerosol size distributions.

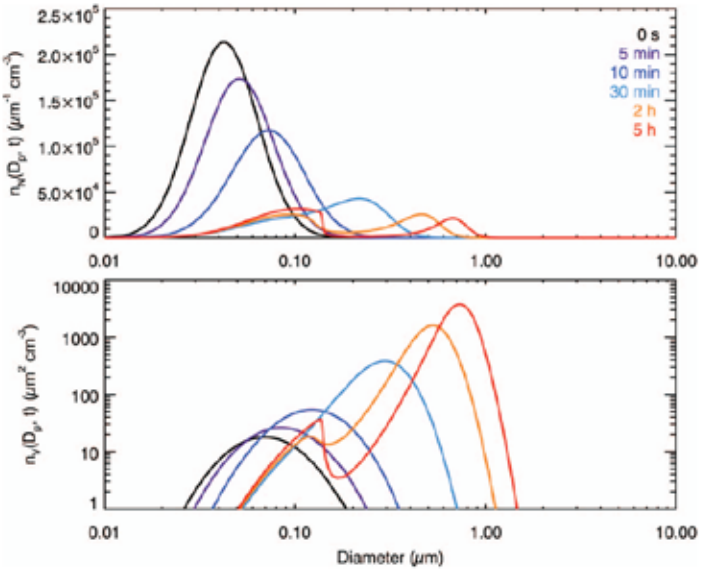

Figure 1.8. Simulated evolution of the aerosol number distribution, $n_N(D_p, t)$ and the volume distribution, $n_V(D_p, t)$, in a fully general system; $p^0_{eq.i} = 10^{-8}$ atm, $\gamma = 10^{-9}$ atm min^{-1}.

Chapter II

Sulfur Chemistry in the Middle Atmosphere of Venus[†]

"In the course of transformation they are produced and extinguished being born and then dying, dying and then being born, in birth after birth, in death after death, the way a torch spun in a circle forms an unbroken wheel of flame."

— The Surangama Sutra, Siddhartha Gautama, 563~483 BC

Summary

Venus Express measurements of the vertical profiles of SO and SO_2 in the middle atmosphere of Venus provide an opportunity to revisit the sulfur chemistry above the Middle cloud tops (~58 km). A one dimensional photochemistry-diffusion model is used to simulate the behavior of the whole chemical system including oxygen-, hydrogen-, chlorine-, sulfur-, and nitrogen-bearing species. A sulfur source is required to explain the SO_2 inversion layer above 80 km. The evaporation of the aerosols composed of sulfuric acid (model A) or polysulfur (model B) above 90 km could provide the sulfur source. Measurements of SO_3 and SO ($a^1\Delta \rightarrow X^3\Sigma^{-1}$) emission at 1.7 μm may be the key to distinguish between the two models.

2.1. Introduction

Venus is a natural laboratory of sulfur chemistry. Due to the difficulty of observing the lower atmosphere, we are still far from unveiling the chemistry at lower altitudes (Mills et al. 2007). On the other hand, the relative abundance of data above the middle cloud tops (~58 km) allows us to test the sulfur chemistry in the middle atmosphere. Mills et al. (2007)

[†] Appeared as: Zhang, X., Liang, M.C., Mills, F.P., Belyaev, D., Yung, Y.L., 2012. Sulfur chemistry in the middle atmosphere of Venus. Icarus 217, 2, 714-739.

summarized the important observations before Venus Express and gave an extensive review of the sulfur chemistry on Venus.

Recently, measurements of Venus Express and ground-based observations have greatly improved our knowledge of the sulfur chemistry. Marcq et al. (2005; 2006; 2008) reported the latitudinal distributions of CO, OCS, SO_2 and H_2O in the 30-40 km region. The anti-correlation of latitudinal profiles of CO and OCS implies the conversion of OCS to CO in the lower atmosphere (Yung et al. 2009). Using the latitudinal and vertical temperature distribution obtained by Pätzold et al. (2007), Piccialli et al. (2008) deduced the dynamic structure, which shows a weak zonal wind pattern above ~70 km. The discovery of the nightside warm layer by the Spectroscopy for Investigation of Characteristics of the Atmosphere of Venus (SPICAV) onboard Venus Express (Bertaux et al. 2007) is a strong evidence of substantial heating in the lower thermosphere (above 90 km). Near the antisolar point, this heating is consistent with the existence of a subsolar-antisolar (SSAS) circulation. However, the nightside warm layer has been reported in SPICAV observations at all observed local times and latitudes and does not appear to be consistent with ground-based submillimeter observations (Clancy et al. 2008). Through the occultation technique, Solar Occultation at Infrared (SOIR) and SPICAV carry out measurements of the vertical profiles of major species above 70 km, including H_2O, HDO, HCl, HF (Bertaux et al. 2007), CO (Vandaele et al. 2008), SO and SO_2 (Belyaev et al. 2008; 2011). Aerosols are found to be in a bimodal distribution above 70 km (Wilquet et al. 2009). These high vertical resolution profiles are obtained mainly in the polar region. Using the SPICAV nadir mode, Marcq et al. (2011a) found large temporal and spatial variations of the SO_2 column densities above the cloud top in the period of 2006-2007, which suggests that the cloud region is dynamically very active. Ground-based measurements also provide valuable information. Krasnolposky (2010a; 2010b) obtained spatially resolved distributions of CO_2, CO, HDO, HCl, HF, OCS, and SO_2 at the cloud tops from the CSHELL spectrograph at NASA/IRTF. Sandor et al. (2010) reported ground-based submillimeter observations of SO and SO_2 inversion layers above 85 km. The submillimeter results are qualitatively consistent with the vertical profiles from Venus

Express (Belyaev et al. 2011). However, only the smallest SO and SO_2 abundances inferred from the SPICAV observations (Belyaev et al. 2011) are quantitatively similar to those inferred from the submillimeter observations (Sandor et al. 2010). Spatial and temporal variability may explain at least some of the differences among the observations (Sandor et al. 2010), but detailed inter-comparisons are required. These measurements and the proposed correlation of upper mesosphere SO_2 abundances with temperature open up new opportunities to study the photochemical and transport processes in the middle atmosphere of Venus.

Sandor et al. (2010) found that SO and SO_2 inversion layers cannot be reproduced by the previous photochemical model (Yung and DeMore 1982). Therefore they suggested that the photolysis of sulfuric acid aerosol might directly produce the gas phase SO_x. A detailed photochemical simulation by Zhang et al. (2010) showed that the evaporation of H_2SO_4 aerosols with subsequent photolysis of H_2SO_4 vapor could provide the major sulfur source in the lower thermosphere if the rate of photolysis of H_2SO_4 vapor is sufficiently high. Their models also predicted supersaturation of H_2SO_4 vapor pressure around 100 km. The latest SO and SO_2 profiles retrieved from the Venus Express measurements agree with their model results (Belyaev et al. 2011). This mechanism reveals the close connection between the gaseous sulfur chemistry and aerosols. Previously sulfuric acid was considered only as the ultimate sink of gaseous sulfur species in the middle atmosphere. If it could also be a source, the thermodynamics and microphysical properties of H_2SO_4 must be examined more carefully. Alternatively, if the polysulfur (S_x) is indeed a significant component of the aerosols as the unknown UV absorber, Carlson (2010) estimated that the elemental sulfur is about 1% of the H_2SO_4 abundance. This might also be enough to produce the sulfur species if there is a steady supply of S_x aerosols to the upper atmosphere.

The purpose of this paper is to use photochemical models to investigate the sulfur chemistry in the middle atmosphere and its relation with aerosols based on our current knowledge of observational evidence and laboratory measurements. We will introduce our model in section 2.2. In section 2.3, we will discuss the two possible sulfur sources above

90 km, H_2SO_4 and S_x, respectively, the roles they play in the sulfur chemistry, their implications and how to distinguish the two sources by the future observations. The last section provides a summary of the chapter and conclusions.

2.2. Model Description

Our photochemistry-diffusion model is based on the one-dimensional Caltech/JPL kinetics code for Venus (Yung and DeMore 1982; Mills 1998) with updated chemical reactions. The model solves the coupled continuity equations with chemical kinetics and diffusion processes, as functions of time and altitude from 58 to 112 km. The atmosphere is assumed to be in hydrostatic equilibrium. We use 32 altitude grids with increments of 0.4 km from 58 to 60 km and 2 km from 60 to 112 km. The diurnally averaged radiation field from 100 to 800 nm is calculated using a modified radiative transfer scheme including gas absorption, Rayleigh scattering by molecules and Mie scattering by aerosols with wavelength-dependent optical properties (see appendix A). The unknown UV absorber is approximated by changing the single scattering albedo of the mode 1 aerosols beyond 310 nm, as suggested by Crisp (1986). Because the SO, SO_2 and aerosol profiles from Venus Express are observed in the polar region during the solar minimum period (2007-2008), our calculations are set at a circumpolar latitude (70°N) and we use the low solar activity solar spectra for the duration of the Spacelab 3 ATMOS experiment with an overlay of Lyman alpha as measured by the Solar Mesospheric Explorer (SME).

In this study we selected 51 species, namely, O, $O(^1D)$, O_2, $O_2(^1\Delta)$, O_3, H, H_2, OH, HO_2, H_2O, H_2O_2, N_2, Cl, Cl_2, ClO, HCl, HOCl, ClCO, $COCl_2$, ClC(O)OO, CO, CO_2 , S, S_2 , S_3, S_4, S_5, S_7, S_8, SO, $(SO)_2$, SO_2, SO_3, S_2O, HSO_3, H_2SO_4, OCS, OSCl, $ClSO_2$, four chlorosulfanes (ClS, ClS_2, Cl_2S, and Cl_2S_2) and eight nitrogen-containing species (N, NO, NO_2, NO_3, N_2O, HNO, HNO_2, and HNO_3). The chlorosulfanes (S_mCl_n) are included because they open an important pathway to form S_2 and polysulfur $S_{x(x=2\rightarrow8)}$ in the region 60~70 km (Mills and Allen 2007), although there are significant uncertainties in their chemistry. The chlorosulfane chemistry is not important for the sulfur cycles above ~80 km

because the S_mCl_n abundances are low. Nitrogen-containing species, especially NO and NO_2, can act as catalysts for converting SO to SO_2 and O to O_2 in the 70~80 km region (Krasnopolsky 2006). A recent study by Sundaram et al. (2011) suggests that the odd nitrogen (NO_x) chemistry might also have significant effects on the abundances of sulfur oxides in the 80~90 km region.

In Zhang et al. (2010), the chemistry was simplified because $(SO)_2$, S_2O and HSO_3 were considered only as the sinks of the sulfur species. This might not be accurate enough for the chemistry below 80 km where there seems to be difficulty in matching the SO_2 observations. Instead, a full set of 41 photodissociation reactions is used here, along with about 300 neutral chemical reactions, as listed in appendix A. We take the ClCO thermal equilibrium constant from the 1-σ model in Mills et al. (2007) so that we can constrain the total O_2 column abundances to ~2×10^{18} cm^{-2}. In addition, we introduce the heterogeneous nucleation processes of elemental sulfur (S, S_2 and polysulfur) because these sulfur species can readily stick to sulfuric acid droplets and may provide the source material for the unknown UV absorber (Carlson 2010). But we neglect all the heterogeneous reactions among the condensed elemental sulfur species on the droplet surface. The calculation of the heterogeneous condensation rates is described in appendix A. The accommodation coefficient α is varied from 0.01 to 1 for the sensitivity study (section 2.4).

The temperature profiles are shown in Figure 2.1 (left panel). The daytime temperature profile below 100 km (solid line) is obtained from the observations of VeRa onboard Venus Express near the polar region (71°N, figure 1 of Pätzold et al. 2007). Above 100 km the temperature is from Seiff (1983). The nighttime temperature profile (dashed line) above 90 km is measured by Venus Express in orbit 104 at latitude 4° S and local time 23:20 h (black curve in the figure 1 of Bertaux et al. 2007). The nighttime temperature profile is used to calculate the H_2SO_4 saturation vapor pressure only.

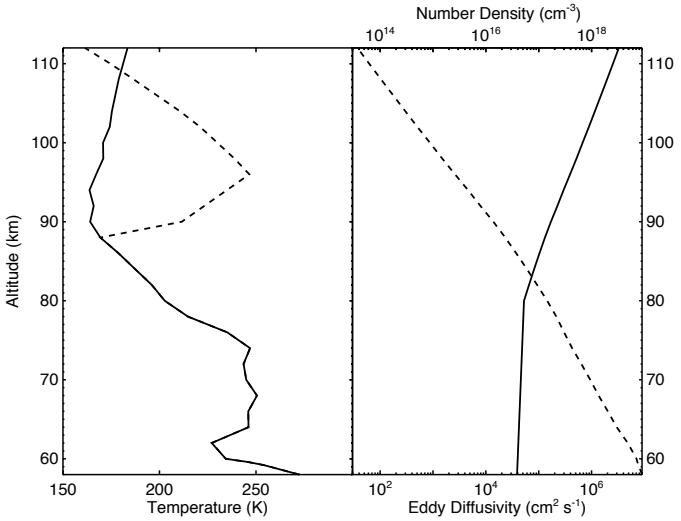

Figure 2.1. Left panel: daytime temperature profile (solid) and nighttime temperature profile (dashed). Right panel: eddy diffusivity profile (solid) and total number density profile (dashed).

In the 1-D model, species are assumed to be mixed vertically by turbulent eddies. Molecular diffusion becomes important above the homopause region (130~135 km). The eddy diffusivity increases with altitude in the Venus mesosphere for reasons discussed later. Since the zonal wind is observed to decrease with altitude above 70 km due to the temperature gradient from pole to equator (Piccialli et al. 2008), we assume that vertical transport of gas species is predominantly due to mixing caused by transient internal gravity waves, as proposed by Prinn (1975). In this case the eddy diffusion coefficient will be inversely proportional to the square root of the number density (Lindzen 1981). Von Zahn et al. (1979) derived the eddy diffusion coefficient $\sim 1.4\times10^{13}$ $[M]^{-0.5}$ $cm^2\ s^{-1}$ from the number density around the homopause region, based on mass spectrometer measurements from *Pioneer Venus*. We use slightly larger values $K_z = 2.0\times10^{13}$ $[M]^{-0.5}$ $cm^2\ s^{-1}$ above 80 km to include an additional contribution of the SSAS circulation. In the region below 80 km, Woo and Ishmaru (1981) estimated the diffusivity $\leq 4.0\times10^4$ $cm^2\ s^{-1}$ at ~60 km from radio signal scintillations. Therefore our eddy diffusivity profile from 58~80 km is estimated by linear interpolation between the values at 80 and 60 km. The eddy diffusion profile is shown in Figure 2.1 (right panel). However, the vertical advection due to the SSAS circulation might be dominant above 90 km. The SPICAV measurements show that

the SO_2 mixing ratio from ~90-100 km is almost constant with altitude, which implies a very efficient transport process.

Since Zhang et al. (2010) has already shown that the model without additional sulfur sources above 90 km cannot explain the observed SO_2 inversion layer, we focus on two models in this study: model A with enhanced H_2SO_4 abundance above 90 km and model B with enhanced S_8 abundance above 90 km. In both models we fix the vertical profiles of N_2, H_2O, and H_2SO_4. The N_2 profile is given by a constant mixing ratio of 3.5%. The H_2O profile (see Figure 2.3) is prescribed on the basis of the Venus Express observations (Bertaux et al. 2007) above 70 km and is assumed to be constant below. The accommodation coefficient of the sulfur nucleation is set to unity (the upper limit) in the standard model.

The H_2SO_4 saturation vapor pressure (SVP) and the photolysis cross sections are discussed in appendix A. appendix A also shows that the H_2SO_4 weight percent profile derived from thermodynamics under the conditions of the Venus mesosphere is consistent with the photometric observations. Model A uses the nighttime H_2SO_4 vapor abundance (Figure A.6) and the H_2SO_4 photolysis cross sections with high UV cross section in the interval 195-330 nm (dashed line in Figure A.7). The H_2SO_4 abundance above 90 km is scaled to reproduce the observed SO and SO_2 data. The day and nighttime S_x saturated mixing ratio profiles based on Lyons (2008) are shown in Figure A.6. The S_8 mixing ratio under nighttime temperature could achieve ppb levels at ~96 km. Based on this, we fix the S_8 profile in model B as the sulfur source. The S_8 profile is composed of two parts: (1) below 90 km, we use the output from model A, which shows the S_8 concentration is undersaturated; (2) above 90 km, we scale the S_8 saturated vapor abundances under nighttime temperature to match the observations. We also adopt the daytime H_2SO_4 vapor abundance and the H_2SO_4 photolysis cross sections with low UV cross section in the interval 195-330 nm (solid line in Figure A.7); therefore the H_2SO_4 photolysis has almost no contribution to the sulfur enhancement in model B.

The SO_2 and OCS mixing ratios at 58 km are set to 3.5 and 1.5 ppm, respectively. The upper and lower boundary conditions for the important species are listed in Table 2.1. We set the HCl mixing ratio as 0.4 ppm at 58 km, which is about a factor of 2 larger than the Venus Express observations (Bertaux et al. 2007). However, other observations support the 0.4 ppm HCl (Connes et al. 1967; Krasnopolsky 2010a). We argue that since ClC(O)OO is the key species to convert CO and O_2 to CO_2 (Mills et al. 2007), 0.4 ppm HCl is needed in our model to constrain the total column abundances of O_2.

Table 2.1. Boundary conditions

Species	Lower Boundary at 58 km	Upper Boundary at 112 km
O	$\mathbf{v} = \mathbf{v_m}$	$\Phi = -5.03\times10^{11}$
O_2	$\mathbf{v} = \mathbf{v_m}$	$\Phi = 9.00\times108$
O_2 ($^1\Delta$)	$\mathbf{v} = \mathbf{v_m}$	$\Phi = 3.00\times10^{8}$
Cl	$\mathbf{v} = \mathbf{v_m}$	$\Phi = -1.00\times10^{7}$
HCl	$\mathbf{f} = 4.00\times10^{-7}$	$\Phi = 1.00\times10^{7}$
CO	$\mathbf{f} = 4.50\times10^{-5}$	$\Phi = -5.03\times10^{11}$
CO_2	$\mathbf{f} = 0.965$	$\Phi = 5.03\times10^{11}$
SO_2	$\mathbf{f} = 3.50\times10^{-6}$	$\Phi = 0$
OCS	$\mathbf{f} = 1.50\times10^{-6}$	$\Phi = 0$
N	$\mathbf{v} = \mathbf{v_m}$	$\Phi = -3.00\times10^{8}$
NO	$\mathbf{f} = 5.50\times10^{-9}$	$\Phi = 0$
Other species	$\mathbf{v} = \mathbf{v_m}$	$\Phi = 0$

Note. The symbols **f,** Φ and **v** refer to the volume mixing ratio, flux ($cm^{-2}\,s^{-1}$), and velocity ($cm\,s^{-1}$), respectively. The positive sign of Φ means the upward flow. The upper boundary fluxes are from Mills (1998). $\Phi = 0$ means the photochemical equilibrium state. At the lower boundary, all other species not listed here are assumed to diffuse downward with the maximum deposition velocity (dry deposition) $\mathbf{v_m} = K/H$, where K and H are the eddy diffusivity and scale height at 58 km, respectively. The lower boundary conditions of CO, HCl and CO_2 are from Yung and DeMore (1982) and Mills (1998). The N and NO boundary conditions are from Krasnopolsky (2006). SO_2 and OCS lower boundary mixing ratios are set to match the observations from Belyaev et al. (2011) and Krasnopolsky (2010b), respectively.

2.3. Model Results

2.3.1. Enhanced H_2SO_4 Case (Model A)

In model A, the saturation ratio of H_2SO_4 is 0.25 (undersaturated H_2SO_4 under nighttime temperature), corresponding to the peak value ~0.2 ppm at 96 km. Figure 2.2-2.8 show the volume mixing ratios of oxygen, hydrogen (including HO_x), chlorine, chlorine-sulfur species, elemental sulfurs, nitrogen species, and sulfur oxides, respectively. The observations of SO, SO_2 and OCS are also plotted in Figure 2.8.

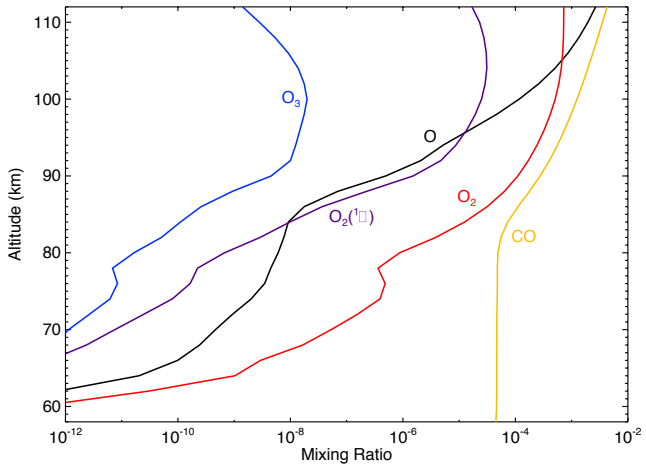

Figure 2.2. Volume mixing ratio profiles of the oxygen species from model A.

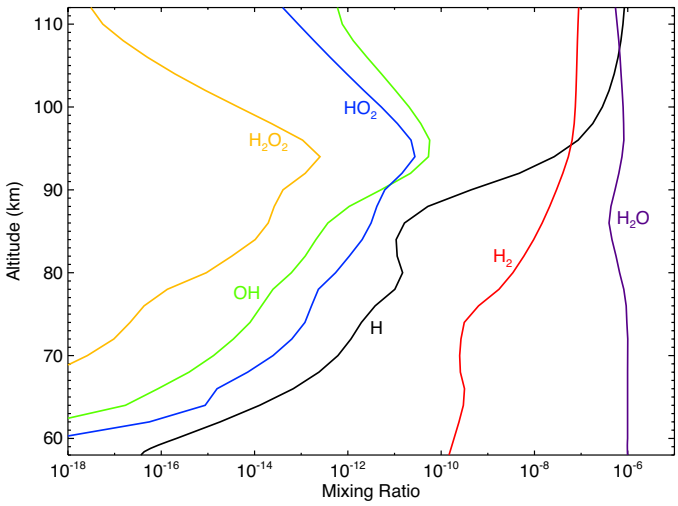

Figure 2.3. Same as Figure 2.2, for hydrogen species.

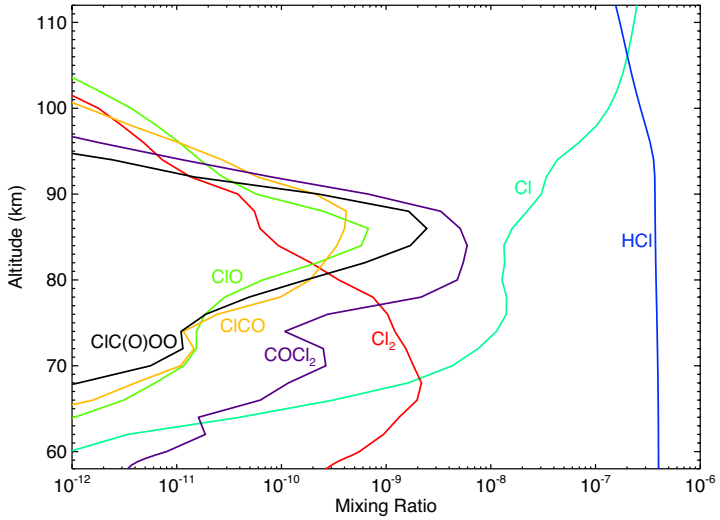

Figure 2.4. Same as Figure 2.2, for chlorine species.

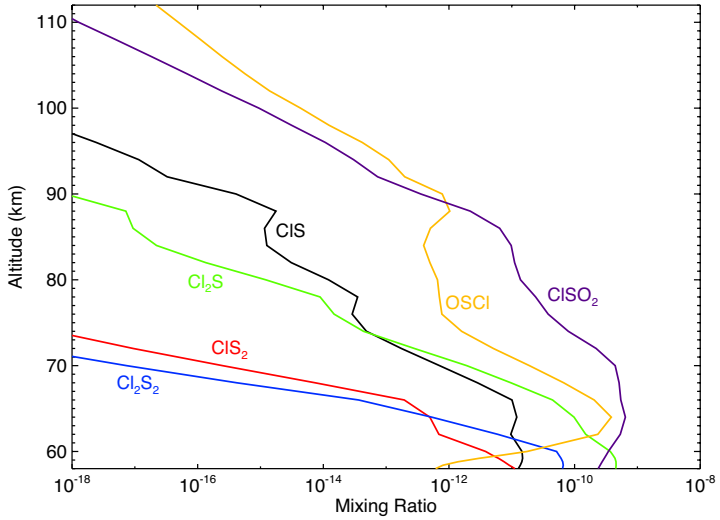

Figure 2.5. Same as Figure 2.2, for chlorine-sulfur species.

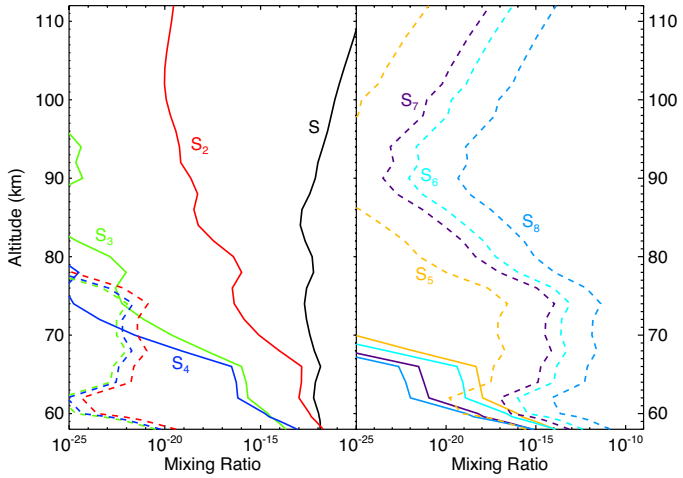

Figure 2.6. Volume mixing ratio profiles (solid) of the elemental sulfur species from model A. The dashed lines are the monoclinic S_x saturated mixing ratio profiles over solid S_x based on Lyons (2008), in equilibrium with the daytime temperatures.

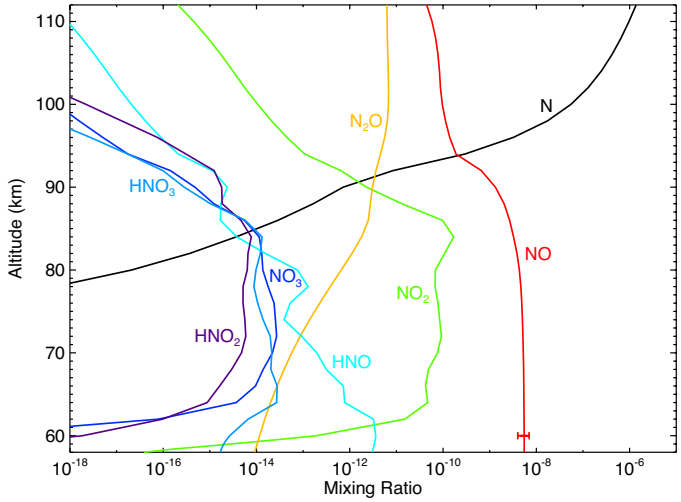

Figure 2.7. Same as Figure 2.2, for nitrogen species. The NO measurement (5.5±1.5 ppb) is from Krasnopolsky (2006).

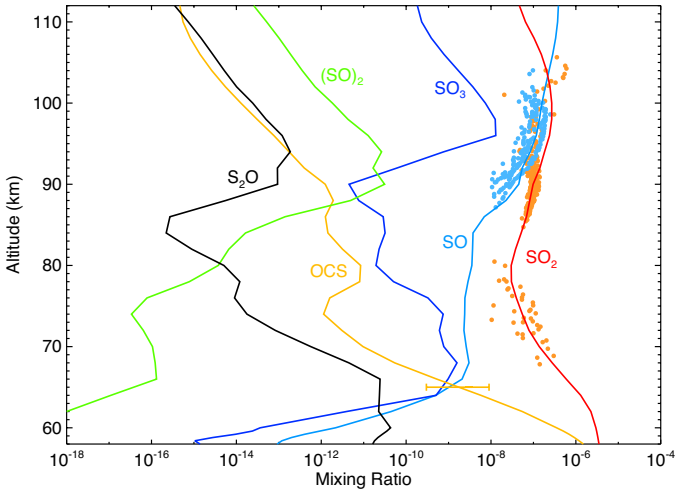

Figure 2.8. Same as Figure 2.2, for the sulfur oxides. The SO_2 and SO observations with error bars are from the Belyaev et al. (2010). The temperature at 100 km is 165~170 K for the observations. The OCS measurement (0.3~9 ppb with the mean value of 3 ppb) is from Krasnopolsky (2010b).

The model outputs of oxygen, hydrogen and chlorine species generally agree with the previous studies (model C in Yung and DeMore 1982; the 1-σ model in Mills 1998). The differences arise mainly from the differences of the temperature profiles and radiation field between the polar region in our model and the midlatitude in the previous models. Compared with the temperature profile from Seiff (1983) used in the previous models, the current profile at 70ºN is colder in the upper cloud layer (58~70 km) but warmer between 70 and 80 km. The O_2 profile is consistent with the one-sigma model in Mills (1998). The concentrations of chlorine species in model A are lower than those in model C of Yung and DeMore (1982) mainly because of the lower boundary values of HCl (0.8 ppm in their model C and 0.4 ppm in our model). The abundances of chlorine-sulfur species in our model are slightly larger than those from Mills (1998) near the lower boundary because there is more OCS at the lower boundary of the model A. The profile for OCS in Figure 2.8 differs significantly from that in Figure 1 of Yung et al. (2009). Although the secondary peak around 80 km is present in both figures, it is much smaller in the present model. The main reason is that the peak is produced by S + CO, where the S atoms are ultimately derived from SO_2 photolysis. The model of Yung et al. (2009) is primarily intended to study the sulfur chemistry in the lower atmosphere, and its SO_2 concentrations above the

cloud tops exceed the observational constraints. We should refer to Figure 2.8 as a more realistic representation of the concentrations of sulfur species in the middle atmosphere. The nitrogen species in our model are less than that in model B of Yung and DeMore (1982) simply because their lower boundary value of NO is 30 ppb, which is about 6 times larger than the observed values, 5.5 ppb on average at 65 km (Krasnopolsky 2006). Since the polysulfur chemistry has been updated based on Moses et al. (2002), model A results are different from those of Mills (1998). But the polysulfur chemistry has large uncertainties and more laboratory measurements of the reaction coefficients are needed (see discussions in section 2.4). Concentrations of sulfur oxides are obviously different from those of early models when we include the sulfur source above 90 km.

The photolysis of the parent species CO_2, OCS, SO_2, H_2O and HCl, which are transported by eddy diffusion from 58 km, provides the sources for the other species. Although the sulfur chemistry is closely coupled with the oxygen and chlorine chemistry in the region 60~70 km, the sulfur species have little effect on the abundances of the oxygen species (including HO_x) and chlorine species above 70 km, but not vice versa. In other words, the model without sulfur chemistry would produce roughly the same amount of oxygen and chlorine species as the model with sulfur species does above 70 km where the sulfur species are less abundant and can no longer tie up the chlorine and oxygen species. The free oxygen and chlorine bearing radicals, such as O, OH, Cl and ClO, are the key catalysts in recycling sulfur species. On the other hand, the sulfur species do not act as catalysts. Therefore, to some extent the sulfur cycle in the mesosphere can be separated from the other cycles above 70 km. Figure 2.9 illustrates the important pathways of the sulfur cycle. For simplicity, the chlorosulfane chemistry and polysulfur chemistry are not shown here. See Mills and Allen (2007) and Yung et al. (2009) for detailed discussions. A fast cycle, including the photodissociation and oxidization processes, exists among the sulfur species. Below 90 km, H_2SO_4 and S_x act as the ultimate sinks rather than the sources of the sulfur species in the region. The total production rate of H_2SO_4 from 58~112 km is 5.6×10^{11} cm^{-2} s^{-1} with a peak value of 1.3×10^{6} cm^{-3} s^{-1} around 64 km, while the total loss rate of gaseous elemental sulfur to aerosol through heterogeneous nucleation processes is 2.6×10^{12} cm^{-2} s^{-1},

when summed across all elemental sulfurs that are lost, equivalent to a sulfur atom loss rate ~3.3×10^{12} cm^{-2} s^{-1}. Therefore, the major sink of sulfur species in model A is the polysulfur aerosols. The polysulfur sink decreases with altitude mainly because both the aerosol and gaseous sulfur species are less abundant at higher altitude (Figure 2.6, also see the discussion in section 2.4). For reference, the Krasnopolsky and Pollack model [1994] requires the H_2SO_4 production rate of 2.2×10^{12} cm^{-2} s^{-1}. Some previous models range from 9×10^{11} to 1×10^{13} cm^{-2} s^{-1} (Yung and DeMore 1982; Krasnopolsky and Pollack 1994). So the H_2SO_4 production rate in model A is lower than those previously modeled values.

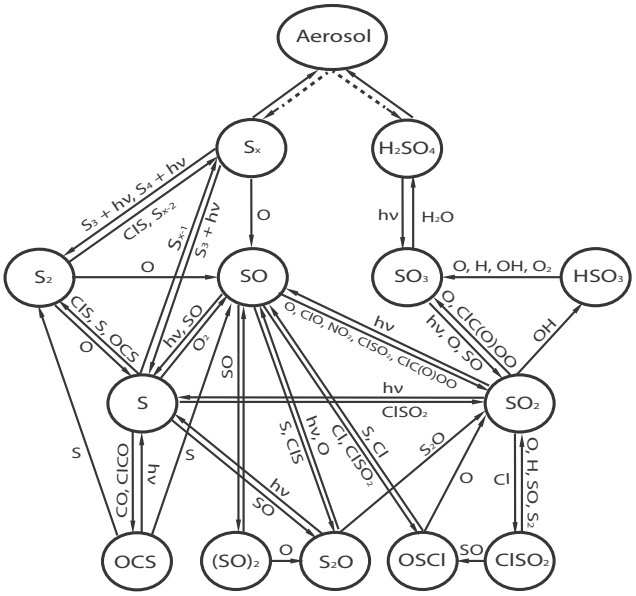

Figure 2.9. Important chemical pathways for sulfur species.

Below ~65 km, $ClSO_2$ is in chemical equilibrium with SO_2. SO_2 reacts with the chlorine radical: $Cl + SO_2 + CO_2 \rightarrow ClSO_2 + CO_2$, and $ClSO_2$ reacts with O, S, S_2, SO, $ClSO_2$, etc. (Reactions R293~R300 in appendix A) to return back SO_2 and produce chlorine species including chlorosulfanes. Above ~65 km, photolysis of SO_2 becomes the dominant sink, with a minor branch of oxidization to SO_3. The three-body reaction O+SO produces more SO_2, and ClO and ClC(O)OO reacting with SO also play important roles in SO_2

production. The major production and loss rates for SO, SO_2 and SO_3 in model A are plotted in Figure 2.10.

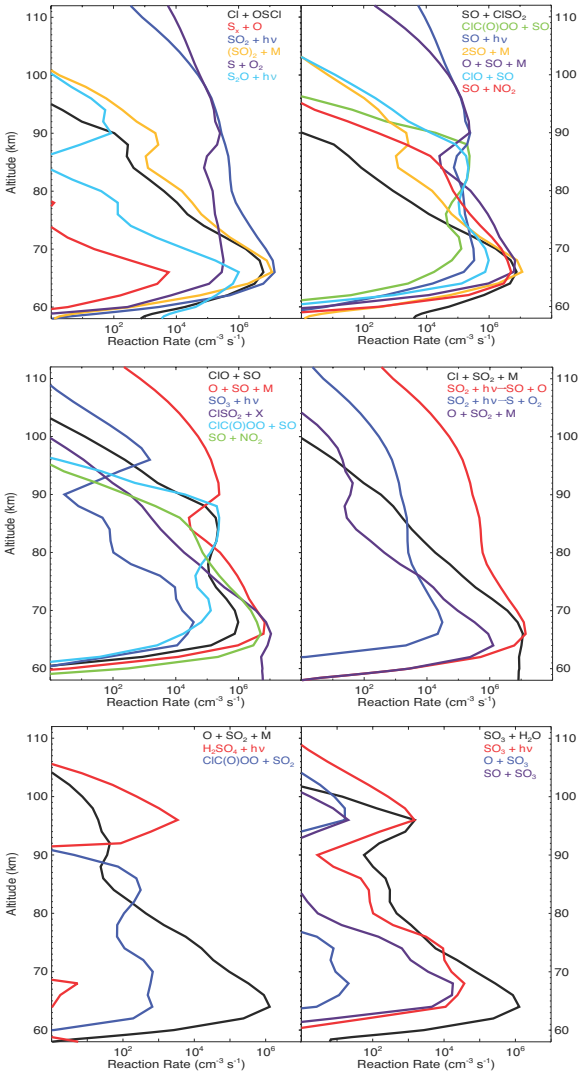

Figure 2.10. Important production and loss rates for SO (upper), SO_2 (middle) and SO_3 (lower) from model A.

The SO and SO_2 inversion layers above 80 km are successfully reproduced in model A (Figure 2.8) although the agreement between the model results and observations is not perfect. We attribute the discrepancy to the constant H_2SO_4 saturation ratio above 90 km. The SO_2 measurements imply that the H_2SO_4 abundance in model A might be

underestimated above 100 km. The chemistry is mainly driven by the photolysis and reactions with O and O_2. The fast recycling between the sulfur species can be seen from the largest production and loss rates in Figure 2.10. At 96 km where the peaks of the reaction rates are, the SO_3 photolysis rate (~1.5×10^3 cm^{-3} s^{-1}) and $SO_3 + H_2O$ rate (~1.5×10^3 cm^{-3} s^{-1}) are roughly comparable, which implies about half of the sulfur in H_2SO_4 goes into SO_x and produces the inversion layers of SO_2 and SO. Model A predicts the existence of an SO_3 inversion layer, with a peak value of ~13 ppb at 96 km. More discussion will be provided in section 2.4.

2.3.2. Enhanced S_x Case (model B)

The S_x aerosol might be another possible sulfur source in the upper region because S_x could react with atomic oxygen to produce SO. But this possibility is more ambiguous because (1) The S_x aerosol has not been identified although it is the most likely UV absorber (Carlson 2010); (2) As shown in the Figure 2.6, the production of S_x is mainly confined to the region below 65 km. So the S_x in the haze layer might not be sufficient to supply the sulfur source; (3) The S_x chemistry has large uncertainty due to the lack of laboratory experiments. The reaction coefficients for S_x + O in our model were estimated by Moses et al. (2002) based on that for S_2 + O.

The required saturation ratio of S_8 is only 3×10^{-4} in order to produce the SO and SO_2 inversion layers (Figure 2.11). That means we need only 0.1 ppt S_x vapor above 90 km. The SO and SO_2 profiles (and other sulfur species) from models A and B are really similar due to the fast sulfur cycle within which the major sulfur species are in quasi-equilibrium (see section 2.4). However, there is a large difference in SO_3 profiles because the SO_3 in model B is derived mainly from SO_2 but not from the photolysis of H_2SO_4 in model A. The SO_3 at 96 km predicted by model B is ~0.1 ppb, which is two orders of magnitude less than that in model A. Therefore, future measurement of SO_3 could distinguish the two mechanisms.

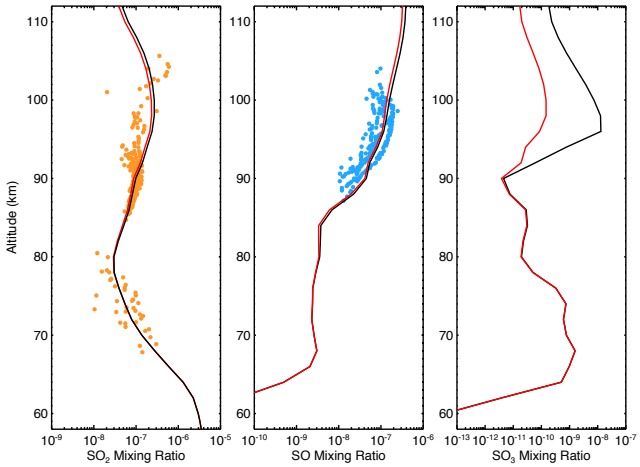

Figure 2.11. Comparison of volume mixing ratio profiles of SO_2 (left), SO (middle) and SO_3 (right) from models A (black) and B (red).

The major production and loss rates for SO, SO_2 and SO_3 in model B are plotted in Figure 2.12. Note that not only S_8 + O produces SO but other S_x derived from S_8 also react with O to produce SO, so in fact one S_8 gas molecule could eventually produce about eight SO molecules. The major differences between models A and B are the SO and SO_3 production mechanisms.

2.4 Discussion

2.4.1 Summary of Chemistry above 80 km

The results of models A and B are summarized in Table 2.2.

For model A, the simplified SO_x chemistry from Figure 2.9 can be illustrated as

$$Aerosol \underset{Condensation}{\overset{Evaporation}{\rightleftharpoons}} H_2SO_4 \underset{H_2O}{\overset{h\upsilon}{\rightleftharpoons}} SO_3 \underset{O}{\overset{h\upsilon}{\rightleftharpoons}} SO_2 \underset{O}{\overset{h\upsilon}{\rightleftharpoons}} SO \underset{O_2}{\overset{h\upsilon}{\rightleftharpoons}} S \underset{O(weak)}{\rightleftharpoons} S_x .$$

Similar to model A, the chemistry in model B:

$$Aerosol \underset{Condensation}{\overset{Evaporation}{\rightleftharpoons}} S_x \underset{S \underset{h\upsilon}{\overset{O_2}{\rightleftharpoons}} SO}{\overset{O}{\rightleftharpoons}} SO \underset{h\upsilon}{\overset{O}{\rightleftharpoons}} SO_2 \underset{h\upsilon}{\overset{O}{\rightleftharpoons}} SO_3 \underset{h\upsilon(weak)}{\overset{H_2O}{\rightleftharpoons}} H_2SO_4 .$$

In fact OCS, S_2O and $(SO)_2$ are also in photochemical equilibrium with the species above but not shown here (see Figure 2.9). Therefore, the fast cycle allows us to derive the ratios of the sulfur species above 90 km analytically by equating the production and loss rates for each species (the subscripts refer to the reaction numbers in appendix A):

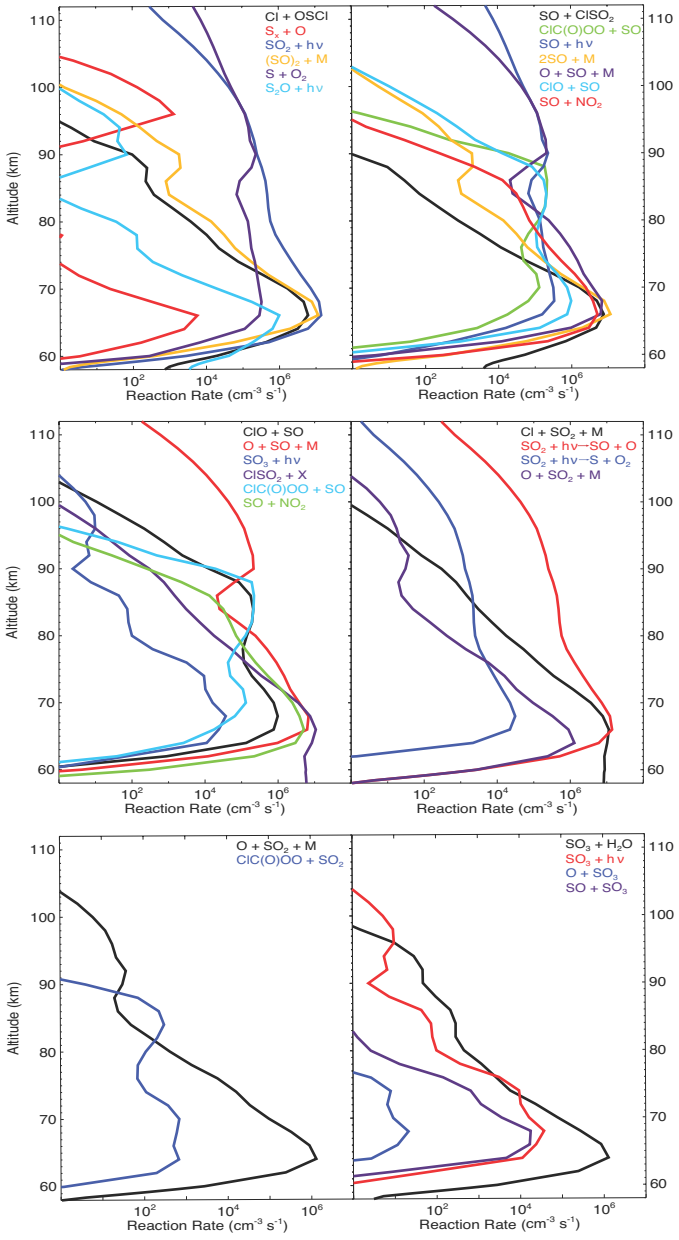

Figure 2.12. Important production and loss rates of SO (upper), SO_2 (middle) and SO_3 (lower) from model B.

Table 2.2. Summary of models A and B

Parameters	**Model A**	**Model B**
H_2SO_4 vapor profile above 90 km	Fixed Nightside profile (×0.25)	Fixed Dayside profile
S_x vapor profile above 90 km	Free	Fixed Nightside profile (×0.0003)
H_2SO_4 photolysis coefficient (s^{-1}) at 90 km	7.1×10^{-6}	7.4×10^{-8}
SO_3 column photolysis loss rate (cm^{-2} s^{-1}) above 90 km	5.8×10^{8}	8.7×10^{6}
O_2 column abundance (cm^{-2})	2.2×10^{18}	2.2×10^{18}
*S_x aerosol column production rate (cm^{-2} s^{-1})	3.3×10^{12} (total) 1.2×10^{7} (>90 km)	3.3×10^{12} (total) 1.1×10^{7} (>90 km)
H_2SO_4 column production rate (cm^{-2} s^{-1})	5.6×10^{11} (total) 5.5×10^{8} (>90 km)	5.6×10^{11} (total) 2.3×10^{7} (>90 km)
SO_2 column production rate (cm^{-2} s^{-1})	2.2×10^{13} (total) 6.6×10^{11} (>80 km)	2.2×10^{13} (total) 6.1×10^{11} (>80 km)
O column production rate (cm^{-2} s^{-1})	1.7×10^{13} (total) 4.3×10^{12} (>80 km)	1.7×10^{13} (total) 4.2×10^{12} (>80 km)

* Define the S_x aerosol production rate (converted to the sulfur content) as: $\sum_{i=1,8} i\times R(S_i)$, where $R(S_i)$ is the heterogeneous loss rates of the elemental sulfur S_i (i=1, 8).

$$\frac{[OCS]}{[S]} = \frac{k_{183}[ClCO] + k_{185}[CO][M]}{k_{302}[S] + J_{31}}, \tag{2.1}$$

$$\frac{[S]}{[SO]} = \frac{J_{27}}{k_{166}[O_2]}, \tag{2.2}$$

$$\frac{[SO]}{[SO_2]} = \frac{J_{29}}{k_{240}[O][M]}. \tag{2.3}$$

In model B:

$$\frac{[SO_2]}{[SO_3]} = \frac{J_{30} + k_{177}[H_2O]}{k_{258}[O][M]}. \tag{2.4}$$

But in model A, SO_3 is approximately independent of other SO_x because of the photolysis of sulfuric acid is the principal source:

$$[SO_3] = \frac{J_{32}[H_2SO_4]}{J_{30} + k_{177}[H_2O]}. \tag{2.5}$$

Again, SO_3 is the key species to distinguish the two pathways because other sulfur species are closely coupled to SO_2 no matter what causes the inversion layers.

The S_2O and $(SO)_2$ chemistry is less clear so it needs a more careful study in the future. In models A and B, the steady-state results are given by

$$\frac{[S_2O]}{[(SO)_2]} = \frac{k_{250}[O]}{J_{33} + k_{266}[O]}, \tag{2.6}$$

$$\frac{[(SO)_2]}{[SO]} = \frac{k_{249}[SO][M]}{k_{246}[O] + k_{254}[M]}. \tag{2.7}$$

The total column abundance of O_2 is about ~2.2×10^{18} cm^{-2} in models A and B. The atomic oxygen (O) column production rate above 80 km is ~4.3×10^{12} cm^{-2} s^{-1}. The O flux required to reproduce the mean O_2 emission of 0.52 MR in the nightside is ~2.9×10^{12} cm^{-2} s^{-1} (Krasnopolsky 2010c). Note that our calculation is at 70°N. If we use 45°N (midlatitude) instead, we obtain ~6×10^{12} cm^{-2} s^{-1}. This suggests that about 50% of the O atoms produced in the dayside are transported to the nightside and recombine to form O_2. Therefore, the transport process is at least as fast as the chemical loss processes. The loss timescale of O is 10^5~10^6 s above 80 km. The transport timescale is estimated to be ~10^4 s, based on the SSAS downward velocity ~ 43 cm/s around 100 km in the night side from Bertaux et al. (2007) and the scale height of 4 km in the lower thermosphere.

Both the SO and SO_2 profiles are derived from the observations above 90 km. They provide a test of the three-body reaction SO + O + M → SO_2 + M in the low temperature region, for which there are no laboratory measurements. The value adopted in our models is from Singleton and Cvetanovic (1988) at 298 K, $k_{240,0} = 4.2\times10^{-31}$ cm^6 $s^{-1}$and $k_{240,\infty} = 5.3\times10^{-11}$ cm^3 s^{-1}, and has been enhanced by a factor of 8.2 for the third-body CO_2. This reaction coefficient produces the $[SO_2]/[SO]$ ~2, which lies in the range of the Venus Express occultation observations for the terminator (Beyleav et al. 2010) and the dayside submillimeter observation range (Sandor et al. 2010). The nightside submillimeter observations find $[SO_2]/[SO]$ ~15~50 (Sandor et al. 2010). The reaction coefficient $k_{240,0}$ derived from Venus Express observations directly is about 3×10^{-30} at 100 km (168 K). It implies that this reaction may have no or very weak temperature dependence between 160~300 K. Grillo et al. (1979) and Lu et al. (2003) measured the temperature dependence in the high temperature region (~300~3000 K) and the two papers provided the dependence

as $T^{-1.84}$ and $T^{-2.17}$, respectively. However, this temperature dependence is too steep for the low temperature region.

One puzzle from the observed $[SO_2]/[SO]$ ratio is that the ratio seems to increase with temperature at 100 km (Belyaev et al. 2011), although this difference is within the uncertainty associated with fewer measurements in the high temperature region (the T2 (180~185 K) and T3 (190~192 K) regions). In addition, there is difficulty in separating the SO signal from the SO_2 signal in the spectrum.

2.4.2. Sensitivity Study

Due to the uncertainty in the adopted value of the accommodation coefficient, we test the sensitivity of model A by slowing down the heterogeneous nucleation processes (reducing α). As α decreases, the formation of S_x aerosols is slower so there are more sulfur species in the gas phase. Therefore, the model requires less SO_2 at the lower boundary to reproduce the SO_2 observations. The left panel of Figure 2.13 summarizes the cases with 1× (model A), 0.1× and 0.01× α. All three cases show that the major sink of sulfur species is the polysulfur aerosol. As the polysulfur nucleation process slows down, the H_2SO_4 production rate also decreases because of the lower SO_2 abundances around 62-64 km where the H_2SO_4 production peak is. One interesting phenomenon is that when the nucleation process is slower, the production rate of condensed S_x aerosol is less but the equivalent sulfur atom loss rate increases. This is because more high-order polysulfur molecules are produced and condense rapidly to form aerosols. Therefore, it is the result of the competition between the cycling of polysulfur and the nucleation processes. The region above 85 km is almost unaffected because the polysulfur sink at those levels is negligible. Preliminary work by Marcq et al. (2011b) suggests a correlation between cloud formation during brightening events, SO_2 depletion and enhancement in UV absorber. A possible interpretation is the conversion of SO_2 to polysulfur aerosols in the cloud region, provided that the unknown UV absorber contains polysulfur. Further work especially regarding H_2O variations is required to discriminate between this hypothesis and other possibilities.

The middle and right panels of Figure 2.13 show the sensitivity to different lower boundary values of SO_2 (2.5-5 ppm) and OCS (0.3-5 ppm). These cases all lie in the observational error bars. The change of SO_2 boundary conditions mainly impacts the region below 85 km. The OCS boundary conditions affect only the upper cloud region.

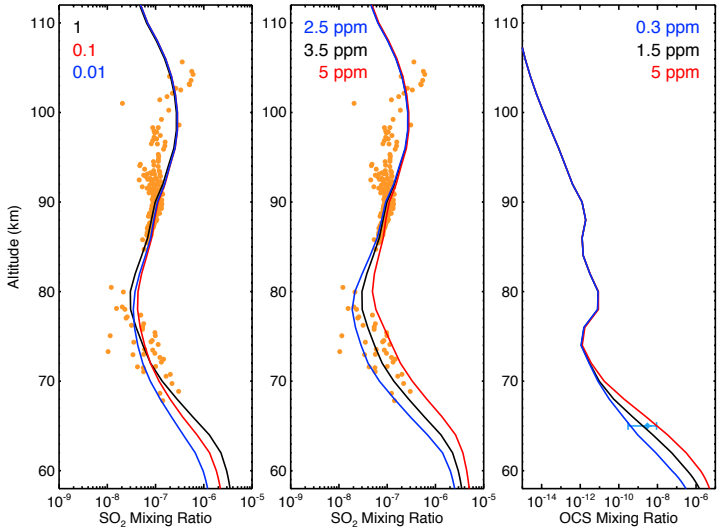

Figure 2.13. Sensitivity studies based on model A. Left panel: cases for different accommodation coefficients (see labels) of the heterogeneous nucleation rate. Middle panel: cases with different boundary conditions of SO_2 (see labels). Right panel: cases with different boundary conditions of OCS (see labels).

The major uncertainties of model A arise from the vapor abundances and the photolysis coefficient of H_2SO_4. Since half of the sulfur in H_2SO_4 goes into SO_x, we would expect a linear relationship between $[SO_2]$ and the product of J_{32} and $[H_2SO_4]$. In model A, the J_{32} and $[H_2SO_4]$ at 96 km are 6.7×10^{-6} s^{-1} and 5.0×10^{8} cm^{-3}, respectively, so $J_{32}[H_2SO_4]$ is $\sim3.3\times10^{3}$ cm^{-3} s^{-1}. For model B, although the relationship between the S_8 and SO_2 abundances is not derived explicitly, we also expect a linear relationship between the two species because all the major sulfur oxides in model B above 90 km are linearly dependent with each other. The reaction coefficients of $S_8 + O$ (k_{233}) and $[S_8]$ at 96 km are 7.0×10^{-12} cm^3 s^{-1} and 7.1×10^{2} cm^{-3} respectively, so $k_{233}[S_8]$ (the product of k_{233} and $[S_8]$) is $\sim5.0\times10^{-9}$

s^{-1}. Assuming that all eight sulfur atoms in S_8 eventually go into SO, the production rate is ~2×10^3 cm^{-3} s^{-1} given that the O abundance is ~4×10^{10} cm^{-3} at 96 km. This value is of the same order of magnitude as $J_{32}[H_2SO_4]$ from model A. Therefore, both models require a sulfur source at least this large to match the observations.

2.4.3. Sulfur Budget above 90 km

The recycling of aerosols from the region below 90 km is essential to maintain the inversion in steady state because sulfur will diffuse downward due to the inverted mixing ratio gradient. The production rates of H_2SO_4 and S_x aerosol for models A and B are shown in Figure 2.14. The H_2SO_4 production rate in model A has a secondary peak at 96 km where the SO_3 peak is located. But the S_x aerosol production rate above 90 km is small because the nucleation process is really slow when there are few aerosol particles to serve as condensation nuclei.

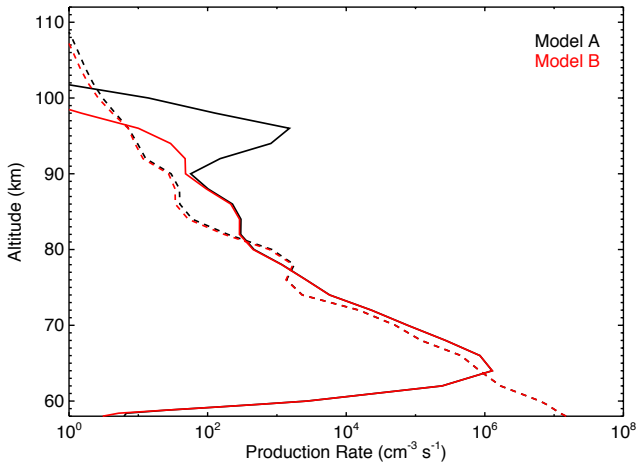

Figure 2.14. Production rate profiles of H_2SO_4 (solid) and S_x (dashed) for models A (black) and B (red).

In model A, the net column loss rate of H_2SO_4 vapor above 90 km is ~6×10^8 cm^{-2} s^{-1}, corresponding to ~50% of the column photolysis rate of H_2SO_4 in that region. Only ~2% sulfur is converted into polysulfur aerosol. So the total downward sulfur flux is ~6×10^8

cm^{-2} s^{-1} to maintain a steady state above 80 km. For reference, the 6×10^{8} cm^{-2} s^{-1} H_2SO_4 loss rate above the region below 90 km is roughly equal the H_2SO_4 column production rate in the region of 78-90 km through the hydration of SO_3. However, it is difficult to transport the H_2SO_4 vapor upward from below 90 km to compensate the loss above because the vapors will quickly condense into the aerosols. Instead, the aerosols must be transported upward on the dayside by the SSAS circulation. Assuming that all the aerosols above 90 km are the mode 1 aerosols with mean radius 0.2 μm and density 2 g cm^{-3}, the aerosol column loss rate is ~1 cm^{-2} s^{-1}. The column abundance of mode 1 aerosol above 90 km from Wilquet et al. (2009) is ~5.0×10^{6} cm^{-2}. Therefore the aerosol lifetime is ~100 Earth days in model A. The loss rate implies that the upward aerosol flux is also ~1 cm^{-2} s^{-1} across 90 km to supply the aerosol budget. Provided that the concentration of mode 1 aerosol at 90 km is ~10 cm^{-3} (Wilquet et al. 2010), the estimated flux is equivalent to an effective upward transport velocity ~0.1 cm s^{-1}.

In model B, the total equivalent sulfur column loss rate of the S_x vapor above 90 km is ~4×10^{8} cm^{-2} s^{-1}, which is roughly the same magnitude as the net sulfur flux from H_2SO_4 photolysis in model A, but the production rate of S_x aerosol is only ~1×10^{7} cm^{-2} s^{-1}. The H_2SO_4 aerosol production rate in model B is ~2×10^{7} cm^{-2} s^{-1}. Therefore, most of the sulfur from S_x aerosol diffuses downward as SO_2 and SO. For reference, the equivalent sulfur column production rate of the S_x aerosol in the region of 78-90 km is ~4.0×10^{8} cm^{-2} s^{-1}. Therefore, if those aerosols can be transported upward, it would be enough to compensate for the loss in the region above 90 km. Assuming that all the polysulfur aerosol above 90 km has a mean radius of ~0.1 μm (half of the H_2SO_4 aerosol) and the density is 2 g cm^{-3}, the aerosol column loss rate is ~3 cm^{-2} s^{-1}. If the polysulfur aerosol abundance is about 1% of that of H_2SO_4 aerosol, S_x aerosol above 90 km will be removed in ~1 Earth day. The estimated upward flux cross the 90 km level is equivalent to an effective upward transport velocity ~30 cm s^{-1}.

If the SSAS circulation dominates the upper atmosphere, it might be very efficient for transporting the aerosols upward. The downward velocity at 100 km near the anti-solar

point is estimated to be ~43 cm s^{-1} from the observed nighttime temperature profiles in Bertaux et al. (2007). Another derivation in Liang and Yung (2009) obtained a different value of ~1 cm s^{-1} at 100 km, which should be corrected to ~10 cm s^{-1}. So the two different calculations are consistent. However, one should always keep in mind that the SSAS circulation is a longitudinal pattern, therefore the vertical velocity should strongly depend on the solar zenith angle. The SSAS pattern from recent VTGCM model results by Bougher et al. (personal communication) show that the vertical velocity in the dayside is on the order of 10 cm s^{-1} above 100 km and on the order of 1 cm s^{-1} from 80~100 km. Therefore the velocity required in model A (~0.1 cm s^{-1}) is readily achieved. But the velocity implied by model B (~30 cm s^{-1}) appears to be larger than the dynamic model results.

2.4.4. Timescales

The dynamics in the 1-D photochemistry-diffsion model is only a simple parameterization for the complicated transition zone between 90~100 km. The aerosol microphysics is also simplified because we just assume the instantaneous condensations of H_2O and H_2SO_4 and ignore the aerosol growth and loss processes. Future 2-D models including SSAS, zonal wind transport, microphysical processes and photochemical processes for both the dayside and nightside hemisphere might be sufficient to represent all the dynamical and chemical processes in the upper regions. We estimate some typical timescales here.

(1) Transport: The timescale for the SSAS transport τ_{SSAS} is ~10^4 s (based on Bertaux et al. 2007) for vertical transport over the 4 km scale height near 100 km. Zonal transport timescale due to Rretrograde Zonal (RZ) flow τ_{RZ} is ~10^5 s for transport from the subsolar point to the antisolar point, provided that the thermal wind velocity is ~50 m s^{-1} by Piccialli et al. (2008) based on the cyclostrophic approximation. Eddy diffusion timescale τ_{eddy} is also ~10^5 s near 100 km (Figure 2.15).

(2) Aerosol condensation: We assume that the condensation is dominated by the

heterogeneous nucleation with timescale τ_{cond}~10^4-10^5 s (Figure 2.15) for the accommodation coefficient α=1. τ_{cond} is inversely proportional to α in the free molecular regime for the upper region. Therefore, the lower value of α might be more appropriate for the H_2SO_4 condensation in model A since the mechanism assumes that the nighttime H_2SO_4 vapor could be transported to the dayside and undergo photolysis. Homogeneous nucleation may be important in the dayside since both of H_2SO_4 and S_x are highly supersaturated. For example, the dayside saturation ratios at 100 km are about 10^6 and 10^4 for H_2SO_4 in model A and S_8 in model B, respectively. In model A, these dayside condensation processes will compete with the photodissociation of H_2SO_4. However, the homogeneous nucleation rate markedly depends on the SVP, which is a steep function of temperature but not well determined in the lower temperature range. Due to the condensation and photolysis of H_2SO_4 in the dayside, a zonal gradient of the H_2SO_4 vapor abundance from the nightside to the dayside would be expected.

(3) Chemistry: H_2SO_4 photolysis timescale τ_{photo} depends on the cross section. For model A, τ_{photo} is ~10^5 s. S_x + O timescale τ_{sx+o} depends on the reaction coefficient and the atomic oxygen abundance, τ_{Sx+O} is ~1-10 s in the model B. That is why ~0.1-1 ppt S_x could provide a sulfur source as large as the photolysis of ~0.1 ppm H_2SO_4 does. The reaction between polysulfur and atomic oxygen is so fast that it has to happen in the nightside. However, as shown above, whether the circulation could support the S_x aerosol upward flux across 90 km needs more future studies.

2.4.5. Basic Differences between Models A and B

Here, we present several basic differences between models A and B for future considerations.

First, the two mechanisms are probably applied to different horizontal regions. By roughly estimating the chemical timescales and dynamical timescales, we found that the S_x + O

reaction in model B is much faster than the transport. As the S_x aerosols are evaporated in the nightside, the S_x vapor will be oxidized in less than 10 s, therefore the SO_x is first produced in the nightside and then transported to the dayside by the zonal wind and photodissociated. On the other hand, H_2SO_4 photolysis has to happen in the dayside in model A. So the SO_x should be first produced in the dayside and then transported to the nightside. A big issue of model A is the H_2SO_4 condensation rate in the dayside since it is highly supersaturated. If the homogenous nucleation were very fast, the supersaturated vapor pressure could not be maintained, and the production of SO_2 from the photolysis of H_2SO_4 would be too small. Therefore, the nightside H_2SO_4 abundances would be also supersaturated in order to supply enough H_2SO_4 for the dayside.

Second, the two mechanisms might require different aerosol flux from below. Since the aerosols cannot be fully recycled above 90 km due to diffusion loss of sulfur, an upward aerosol flux is needed. The estimated aerosol flux is ~1 and ~3 cm^{-2} s^{-1}, corresponding to an effective upward transport velocity ~0.1 and ~30 cm s^{-1} for model A and model B, respectively. However, the estimation of S_x transport velocity here is based on the assumption of the S_x/H_2SO_4 ratio ~1% (Carlson 2010), which remains to be confirmed by future measurements.

Third, in terms of possible observational evidence, model A requires H_2SO_4 number density ~10^8 cm^{-3} around 96 km in the dayside, which might be observed. The estimated abundance of S_8 in the nightside is only ~10^2 cm^{-3} around 96 km, which would be hard to observe. SO_3 might provide another possibility to distinguish the two mechanisms because SO_3 is controlled mainly by the H_2SO_4 photolysis in model A but by the SO_2 oxidization in model B. The abundance of SO_3 at 96 km is ~3.3×10^7 and ~2.2×10^5 cm^{-3} for models A and B, respectively. Future observations might be able to detect this difference. On the other hand, if the SO radical is produced mainly by the polysulfur oxidization in the nightside, it might be possible to observe the nightglow of SO excited states, in analogous to the O_2 nightglow. The electronic transition of the SO ($a^1\Delta \rightarrow X^3\Sigma^{-1}$) at 1.7 μm has been detected in Io's atmosphere (de Pater et al. 2002).

2.4.6. OCS Above the Cloud Tops

The OCS mixing ratio in the upper cloud layer is puzzling. OCS originates from the lower atmosphere. Marcq et al. (2005; 2006) reported an OCS mixing ratio ~0.55 ± 0.15 ppm at ~36 km, decreasing with altitude with a gradient of -0.28 ppm/km based on the ground-based telescope IRTF observation. The VIRTIS measurement (Marcq et al. 2008) found the OCS mixing ratio ranging between 2.5 ± 1 and 4 ± 1 ppm at 33 km, agreeing with the previous value ~4.4 ppm from Pollack et al. (1993). Therefore, OCS would only be ~0.1 ppm or less in the lower cloud layer (~47 km). However, a sensitivity study of model A (Figure 2.13) shows that 0.3-5 ppm OCS at the upper cloud deck (~58 km) is required to reproduce the OCS mixing ratio at 65 km in the observed range 0.3-9 ppb reported by Krasnopolsky (2010b). Krasnopolsky (2008) reported even larger values, ~14 ppb around 65 km and ~2 ppb around 70 km. Venus Express results suggest that the upper limit of OCS is 1.6 ± 2 ppb in the region 70-90 km (Vandaele et al. 2008). But model A can produce only several tens of ppt OCS around 70 km. One tentative detection of OCS reported from ground-based observations near 12 μm (Sonnabend et al. 2005) found an abundance consistent with that calculated by Mills (1998), which specified 0.1 ppm OCS at 58 km. Besides, the scale height of OCS in model A is ~1 km at 65 km, which matches only the lower limit of the observations (1-4 km from Krasnopolsky 2010b). It seems that the eddy transport required in the upper cloud region needs to be more efficient to transport OCS upward. This is also consistent with the ~4 km scale height of SO_2 around 68 km in the Venus Express measurements. Although the eddy diffusivity at ~60 km has been estimated to be less than 4.0×10^4 $cm^2\ s^{-1}$ (Woo and Ishmaru 1981), it could have large variations in the cloud layer, leading to large variation in the detected OCS values and maybe related to the decadal variation of SO_2 at the upper cloud top (see Figure 7 of Belyaev et al. 2008).

The unexpected large amount of OCS will affect the polysulfur production. There are two pathways to produce atomic sulfur (see Figure 2.9). One is the photodissociation of SO and ClS (Mills and Allen 2007), The other way is from the photolysis of OCS. If the OCS

abundance is large (e.g. model A), the primary source of atomic sulfur below ~62 km is from the photolysis of OCS instead of that of SO and ClS. There are also two pathways to produce S_2. One is from the chlorosulfane chemistry (Mills and Allen 2007) and the other is from the reaction between S and OCS. It turns out that the reaction rate of S + OCS in model A is as large as the ClS_2 photolysis below 60 km. Therefore if there is an abundant OCS layer near the lower boundary, it may greatly enhance the production of S_x in the 58-60 km region.

2.4.7. Elemental Sulfur Supersaturation

Even using the highest nucleation rate ($\alpha = 1$), the model A results show that the S_2, S_3, S_4 and S_5 are highly supersaturated based on the SVP from Lyons (2008) (see Figure 2.6). The column abundances of gaseous S_2, S_3, S_4 and S_5 above 58 km are 1.4×10^{13}, 9.0×10^{10}, and 2.1×10^{11}, 4.3×10^{9} cm^{-2}, respectively. S_5 is supersaturated with the saturation ratio ~1000 peaking at 60 km but decreases rapidly. The saturation ratio of S_4 is about 10^7 at the lower boundary and becomes moderately supersaturated above 76 km. S_3 is oversaturated by a factor of 10^5-10^{10} from 58 to 100 km. S_2 is extremely supersaturated at all altitudes. The saturation ratio is 10^8 at the bottom and the top, with a peak of 10^{15} at 90 km, where the heterogeneous nucleation of S_2 is negligible compared with the production processes from atomic sulfur through the three-body reaction 2S + M, and the major loss processes of S_2 are oxidization to SO and the photo-dissociation to atomic sulfur. As illustrated in Figure 2.9, the main production processes of S_x can be summarized as $S + S_{x-1} \rightarrow S_x$ and $S_2 + S_{x-2} \rightarrow S_x$, but the reactions $ClS + S_2$ and $S_2O + S_2O$ are also important for S_3 production at the bottom and top of the model atmosphere, respectively. The loss mechanisms of S_x include the heterogeneous nucleation, conversion to other allotropes, and oxidization through $S_x + O \rightarrow S_{x-1} + SO$.

Figure 2.15 shows the comparison of the diurnally averaged photolysis timescales of S_2, S_3 and S_4 with the timescales of the nucleation and eddy transport. The S_2 loss process is dominated by the nucleation from 58 km to about 72 km where the photolysis is as fast as

the nucleation, but the conversion from S_2 to S_4 is also important around 60 km. The photolysis timescales of S_3 and S_4 are of the order of 1s, much smaller than the nucleation timescale (~10 s at 60 km and ~100 s at 70 km). Therefore, for S_3 and S_4, photolysis by visible light is the major loss pathway and the heterogeneous nucleation processes are negligible. Since the S_3 and S_4 aerosols are the possible candidates of the unknown UV absorbers although they are unstable (Carlson 2010), the condensed S_3 and S_4 are probably produced from the heterogeneous S_x chemistry over the H_2SO_4 droplet surfaces (Lyons 2008). Since the supersaturation ratios are very large for S_x vapors, the homogenous nucleation process will be important and thus should be considered in future work. A proper treatment of the microphysical processes coupled with atmosphere dynamical processes within the cloud layer is needed to elucidate the S_x chemistry.

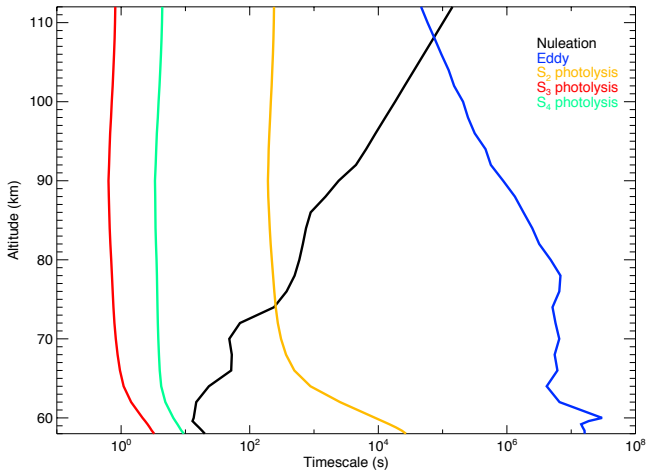

Figure 2.15. Timescales for the heterogeneous nucleation, eddy transport and photolysis for S_2, S_3 and S_4.

2.4.8. Alternative Hypotheses

Eddy diffusion is able to transport the species only from a region of high mixing ratio to that of a low mixing ratio, and so it cannot generate an inversion layer. A sudden large injection of SO_2 from either volcano (Smrekar et al. 2010) or the instability in the cloud region (e.g., VMC measurements from Markiewicz et al. 2007) may provide a sulfur

source at ~70 km, where the long-term natural variability of SO_2 has been documented but not understood. However, it is difficult for these mechanisms to explain the SO_2 inversion layer above 80 km because (1) volcano eruption could only reach 70 km but not higher based on a recent Venus convective plume model (Glaze et al. 2010); (2) even if the sudden injection reaches ~100 km high, it is also difficult to maintain the steady SO_2 inversion for an extended period in the Venus Express era because the gas-phase SO_2 lifetime is short (~a few earth days or less above 70 km). A continuous upwelling of SO_2 from the lower region to the upper region (advection) is possible although the dynamics maintaining the inversion profiles is not understood. The upward flux can be estimated by balancing the downward flux by diffusion:

$$\Phi = K_{zz}[M]\frac{df}{dz}, \tag{2.8}$$

where Φ is the vertical flux, K_{zz} eddy diffusivity, *[M]* number density, *f* mixing ratio, and *z* altitude. Assuming the K_{zz}~10^6 cm^2s^{-1}, df ~ 10^{-7}, *[M]*~ 10^{17} cm^{-3} (at 80 km), dz~10 km (80~90 km), we obtain Φ ~ 10^{10} $cm^{-2}s^{-1}$. To maintain the inversion requires an equal upward flux at 80 km.

Compared with the dynamical mechanism which transports SO_2 directly from 80 km, our mechanism of in situ chemical production from parents transported in aerosol is more plausible because (1) the inversion can be explained by the shape of the equilibrium vapor pressure profile above 90 km (models A and B); (2) it needs the upward transport of aerosols only around the 90 km region, where the SSAS circulation is strong and has been verified by the nighttime warm layer (Bertaux et al. 2007).

2.5. Summary and Conclusion

This study is motivated by the recent measurements from Venus Express, especially the SO_2 profile from 70 to 110 km and the SO profile above 80 km, and some ground-based observations (SO and SO_2 from Sandor et al. 2010; OCS from Krasnopolsky 2010b). The three primary chemical cycles: oxygen cycle, chlorine cycle and sulfur cycle are closely

coupled in the upper cloud region. We included the heterogeneous nucleation of elemental sulfur and found that the S_2, S_3, S_4 and S_5 near the lower boundary (58 km) are highly supersaturated, even using the fastest removal rates by nucleation. Mills and Allen (2007) pointed out that the chlorosulfanes chemistry may play an important role in producing the polysulfurs in the upper cloud layer. However, in order to reproduce the recent ground-based observations, the required OCS mixing ratio at the lower boundary (1.5 ppm) is found to be significantly larger than the previous estimations (e.g., Yung et al. 2009). This enhanced OCS layer near the lower boundary would greatly increase the polysulfur production rate through the photolysis to atomic sulfur. But it is also possible to reduce the required OCS abundance at the lower boundary if we increase the eddy diffusion transport in the upper cloud layer.

In the region above 80 km, we propose two possible solutions to explain the inversion layer of SO_2. The essence of our idea to solve this problem is to "reverse" the sulfur cycle in the region below 80 km. In 58-80 km, the SO_2 and OCS are the parent species transported from the lower atmosphere as the sulfur sources, while the H_2SO_4 and possible polysulfur aerosols are considered to be the ultimate sulfur sinks and their production rates are shown in Figure 2.14. However, in the upper region the aerosols might become the sulfur source rather than the sink to provide enough sulfur for the inversion layers but it requires large aerosol evaporation. We relate this possible evaporation to the warm layer above 90 km in the night side observed by Venus Express (Bertaux et al. 2007). Therefore the SO and SO_2 inversion layers above 90 km are the natural results of the temperature inversion induced by the adiabatic heating of the SSAS flow. While the inversion layers in the region between 80~90 km are due to the downward diffusion from the lower thermosphere.

If H_2SO_4 aerosol is the source, the cross section of H_2SO_4 photolysis and the SVP is needed to be determined accurately. However, the laboratory work has yet to be done. From the modeling results, the possible solutions are the following.

(1) Use the photolysis cross sections from Lane et al. (2008) for the UV region and

Mills et al. (2005) and Feierabend et al. (2006) data for the visible region, but the H_2SO_4 saturation ratio is about ~100 under nighttime temperature. That means the large supersaturation exists not only in the dayside but also in the nightside. The photolysis coefficient (J_{32}) at 90 km is ~7.3×10^{-8} s^{-1}.

(2) Use the UV cross sections from Lane et al. (2008) and $H_2SO_4{\cdot}H_2O$ cross sections in the visible region from Vaida et al. (2003). This case requires that the hydrate abundance be roughly the same order of magnitude of the pure H_2SO_4 saturated vapor abundance with the saturation ratio ~0.25 under nighttime temperature. The photolysis coefficient at 90 km is ~6.8×10^{-6} s^{-1}.

(3) Use the same cross sections as (1) but also use 1×10^{-21} cm^2 $molecule^{-1}$ in the UV region of 195-330 nm, as shown by the dashed line in Figure A.7. The required H_2SO_4 saturation ratio is ~0.25 under nighttime temperature. The photolysis coefficient at 90 km is ~7.0×10^{-6} s^{-1}.

The major difference between (3) and the other two possibilities (see Zhang et al. 2010) is that, in (3) the photolysis rate is contributed mainly by the UV flux, while in (1) and (2) the dominant sources are the visible and IR photons.

In model A we discussed possibility (3), and the model B considers the S_x aerosol as the source instead. The models A and B show some similar behaviors, which represent the general features of the upper region chemistry despite the different sulfur sources. Although there are uncertainties of the model parameters, the calculated SO_2 mixing ratio merely depends on the input sulfur flux: in terms of the H_2SO_4 photolysis production rate in model A and the S_8 oxidization rate in model B, respectively. Because of the existence of the fast sulfur cycle, we consider all the sulfur oxides in the upper region as a box. The sulfur flux flow in the upper atmosphere is summarized in Figure 2.16 to illustrate the vertical transport and gas-particle conversion processes. The required sulfur flux inputs in the box above 90 km is ~6×10^{8} cm^{-2} s^{-1}, roughly consistent in both models A and B. All the

sulfur oxides output from models A and B, except SO_3, are very similar. This is because that the gas phase sulfur chemistry in the upper region is simpler than that in the lower region (below 80 km) because it is driven by the photolysis reactions and backward recombination with O and O_2. However, the complexity comes from the coupling of the gaseous chemistry with the aerosol microphysics and the SSAS and zonal transport, both of which are poorly determined at this time. Thus, the calculations cannot be considered a proof of our hypothesis, but a demonstration of its plausibility. Future observations and more complete modeling work are needed to fully reveal the behavior of the coupled system.

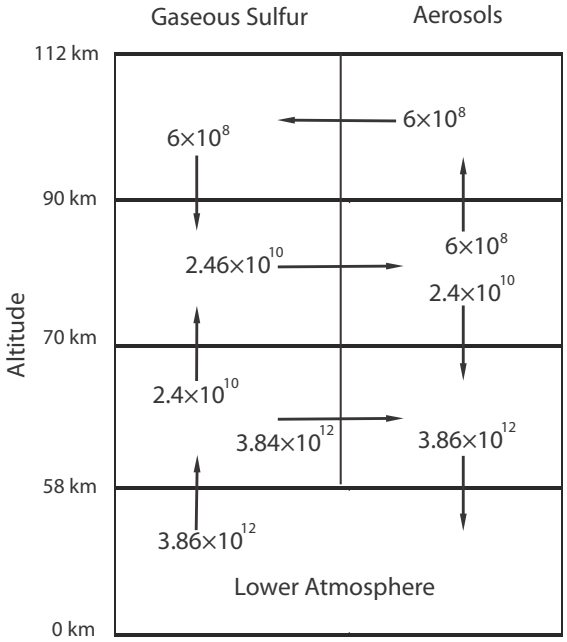

Figure 2.16. Sulfur flux flow (in units of $cm^{-2}\ s^{-1}$) in the upper atmosphere of Venus.

Finally, we briefly summarize the following important tasks for the future.

Observations:

(1) Abundances of SO_3 and H_2SO_4 in the lower thermosphere and SO nightglow in the nightside and better constraints of SO_2 and OCS abundances in the upper cloud region. During the review process of this current paper, Sandor et al. (2011) reported their

observations on the sulfuric acid in Venus' 85–100 km upper mesosphere. The upper limit of H_2SO_4 mixing ratio is found to be 3 ppb (~10^6 cm^{-3}), which is two orders of magnitude less than the H_2SO_4 abundance required by Zhang et al. (2010).

Laboraory measurements:

(2) Measurements of photodissociation cross section of H_2SO_4 in the UV region, especially in the lower energy range (~195-330 nm).

(3) Laboratory measurements of H_2SO_4 SVP in the lower temperature region (~150-240 K).

(4) Determination of polysulfur reaction coefficients.

Unsolved problems:

(5) An explanation of the longtime variation of SO_2 at the upper cloud top ~70 km and the possible variation of the OCS abundance in the upper cloud region.

(6) The microphysical properties of S_x and H_2SO_4 aerosols, their formation and loss processes, transport, vertical profiles and the cause of the multi-modal distributions.

(7) Coupled mesosphere-thermosphere (~58-135 km) chemistry including the neutral species and ions to reveal the role of SSAS transport in both dayside and nightside of Venus.

Chapter III

Radiative Forcing of the Stratosphere of Jupiter, Part I: Atmospheric Cooling Rates from Voyager to Cassini‡

That which always was,
and is, and will be everlasting fire,
the same for all, the cosmos,
made neither by god nor man,
replenishes in measure
as it burns away.

—*Heraclitus, 535~475 BC*

Summary

We developed a line-by-line heating and cooling rate model for the stratosphere of Jupiter, based on two complete sets of global maps of temperature, C_2H_2 and C_2H_6, retrieved from the Cassini and Voyager observations in the latitude and vertical plane, with a careful error analysis. The non-LTE effect is found unimportant on the thermal cooling rate below 0.01 mbar. The most important coolants are the molecular hydrogen between 10~100 mbar, and hydrocarbons, including ethane (C_2H_6), acetylene (C_2H_2) and methane (CH_4), in the region above. The two-dimensional cooling rate maps are influenced primarily by the temperature structure, and also by the meridional distributions of C_2H_2 and C_2H_6. The "quasi-quadrennial oscillation" (QQO)-type thermal structure at the 1 mbar level in the Cassini data and the strong C_2H_6 latitudinal contrast in the Voyager era are the two most prominent features influencing the cooling rate patterns. The globally averaged CH_4 heating and

‡ Submitted as: Zhang, X., Nixon, C.A., Shia, R.L., West, R.A., Irwin, P., Yelle, R.V., Allen, M.A., Yung Y.L., 2012. Radiative forcing of the stratosphere of Jupiter, part I: atmospheric cooling rates from Voyager to Cassini, Planetary and Space Sciences.

cooling rates are not balanced, clearly in the lower stratosphere under 10 mbar, and possibly in the upper stratosphere above 1 mbar. Possible heating sources from the gravity wave breaking and aerosols are discussed. The radiative relaxation timescale in the lower stratosphere implies that the temperature profile might not be purely radiatively controlled.

3.1. Introduction

The stratosphere of Jupiter is expected to be in radiative equilibrium due to the inhibition of strong vertical motion by the lower stratospheric temperature inversion above the tropopause (~100 mbar) and the approximate isotherm above ~5 mbar (Moses et al. 2004). Although the major constituents in the atmosphere are hydrogen and helium, the stratospheric radiative budget is mainly controlled by trace amounts of hydrocarbons, including ~0.2% methane (CH_4) and its photochemical products, acetylene (C_2H_2) and ethane (C_2H_6), and aerosols. Previous studies (e.g., Wallace et al. 1974; Appleby 1990) showed that the stratosphere is primarily heated by the absorption of solar flux via the near-infrared (NIR) bands of CH_4 between 1~5 μm. The heating effect of aerosols is less certain. West et al. (1992) found this process to be important around 10 mbar or below, especially in the polar regions. But other studies (Moreno and Sedano 1997; Yelle et al. 2001) claimed that aerosol heating is negligible. The heating from the gravity wave breaking could be also important in the upper stratosphere (Young et al. 2005). On the other hand, the detailed analysis by Yelle et al. (2001) revealed that the most important coolants in the stratosphere of Jupiter are the secondary hydrocarbons, C_2H_2 and C_2H_6, with less important but not negligible contributions from CH_4 and the H_2-H_2 and H_2-He collisional induced transitions, through their thermal emissions at the mid-infrared (MIR) wavelengths.

The thermal emission from those MIR bands, and the absorption from the NIR CH_4 bands, can be directly observed from ground-based and space-based instruments. Therefore, provided enough information can be obtained from the observations, the solar heating and thermal cooling rates can be determined precisely to test the radiative equilibrium hypothesis. However, previous radiative equilibrium models (Cess and Khetan 1973;

Wallace et al. 1974; Cess and Chen 1975; Appleby and Hogan 1984; Appleby 1990; Conrath et al. 1990; West et al. 1992; Moreno and Sedano 1997), as described in Yelle et al. (2001), are all subject to large uncertainties of the temperature and gas abundance profiles, and aerosol distributions. Yelle et al. (2001) estimated the globally averaged temperature profile based on the Galileo probe data in the hot spot ($5° N$) and hydrocarbon profiles based on the available ground-based and space-based observations at that time. They concluded that radiative equilibrium could be achieved from the gas heating and cooling rate balance, although their model tests showed a large uncertainty range for the secondary hydrocarbon profiles, especially for C_2H_2.

The observations and related analysis of the stratosphere of Jupiter prior to 2000 are summarized in Moses et al. (2004). Those results, although successfully revealing the main features for certain latitudes, did not provide the spatially resolved information for the full planet. Until the analysis of the Voyager and Cassini flyby data by Simon-Miller et al. (2006), the detailed two-dimensional temperature maps in the latitude-altitude plane have been lacking. Later, Nixon et al. (2007; 2010) retrieved the distributions of the temperature, C_2H_2 and C_2H_6 together based on the Voyager and Cassini infrared spectra. Those maps with detailed latitudinal and vertical information of the temperature and major coolants in the stratosphere of Jupiter provide us the opportunity to analyze the radiative heating and cooling budgets in detail. This is the first motivation of this study.

The second motivation might be more important. Although the stable stratification prohibits the stratosphere from strong vertical and lateral convection, the stratosphere is not stagnant. In fact, observations have shown that the temperature change is much larger than can be explained by the instantaneous radiative equilibrium model (Simon-Miller et al. 2006), possibly owing to the effect of the stratospheric dynamics. The distributions of C_2H_2 and C_2H_6 from Nixon et al. (2010) imply a possible meridional circulation in the stratosphere of Jupiter because the two species also serve as the ideal tracers for transport. The opposite latitudinal trends of the short-lived species (C_2H_2) and the long-lived species (C_2H_6) are a strong evidence of the horizontal advection. On the other hand, the SL-9

debris transport model by Friedson et al. (1999) and the two-dimensional chemical-transport model by Liang et al. (2005) suggested that the horizontal eddy mixing might be more important. Therefore, whether the stratospheric transport is governed by the horizontal diffusion or advection is unsolved. Furthermore, whether the stratospheric circulation is driven by the top-down radiative differential heating or by the bottom-up mechanical forcing from the troposphere is not well determined as well. Previous studies (e.g. Gierasch et al. 1986; Conrath et al. 1990; West et al. 1992) led to different conclusions based on different assumptions of the radiative forcing or wave drag parameterization. In order to answer both questions, i.e., mixing versus advection, and radiative forcing versus mechanical forcing, the spatially resolved stratospheric radiative forcing needs to be precisely calculated.

This study aims to understand the radiative budget and the related uncertainties based on the state-of-art global datasets in the stratosphere of Jupiter. We will investigate the details of the heating rate and cooling rate in both spectral and spatial domains. It will be divided in two parts, corresponding to two publications. In this chapter, we will analyze the Cassini and Voyager infrared spectra to quantify the information of the temperature, gas abundances and their uncertainties, and calculate the thermal cooling rate maps for the two eras using a high-resolution line-by-line radiative transfer model, and revisit the globally averaged solar heating and thermal cooling balance. In chapter IV, we will combine the ground-based NIR data and the high-resolution images from Cassini Imaging Sub System (ISS) to retrieve the global map of stratospheric aerosols and their optical properties, and from that we obtain the latitudinal aerosol heating rate map. Combining the aerosol heating rate with the gas heating and cooling rates, we complete the picture of radiative forcing in the stratosphere of Jupiter.

This chapter is structured as follows. Section 3.2 describes how to obtain the best-estimate distributions of the atmospheric temperature and gas abundances, and their associated uncertainties from the Cassini and Voyager spectra. Section 3.3 introduces our line-by-line cooling rate model and discusses the cooling rate results. Section 3.4 focuses on the

globally averaged heating and cooling balance, followed by a summary and implications for the stratospheric dynamics in section 3.5.

3.2. Jovian Stratospheric Maps

3.2.1 Retrieval and Error Analysis Method

In order to characterize the uncertainties of the retrieval results from Cassini Composite Infrared Spectrometer (CIRS) and Voyager Infrared Spectrometer (IRIS), we revisit the same data in Nixon et al. (2010). The CIRS data and IRIS data are both mid-IR spectra from 600 to 1400 cm^{-1}. The spectral features in this region are dominated by the mid-infrared emissions from the acetylene ν_5 band centered at 729 cm^{-1}, ethane ν_9 band at 822 cm^{-1}, and methane ν_4 band at 1304 cm^{-1}. All the emission features are sitting on top of the H_2-H_2 and H_2-He collisional induced absorption (CIA) continua. The two Michelson-type instruments, i.e., IRIS and CIRS, are similar to each other in the Mid-IR region, but the spectral resolution and spatial resolution from the interferometer of CIRS are much higher than the single bolometer of IRIS. For instance, the full-width-to-half-maximum (FWHM) of CIRS is 0.48 cm^{-1} versus 4.3 cm^{-1} of IRIS. The field of view (FOV) of CIRS is 0.29 mrad versus 4.36 mrad of IRIS (see Nixon et al. (2010) for more details). Due to the different data quality, we choose two different retrieval methods for CIRS and IRIS data respectively. But the methods share the same theoretical basis.

In principle, the retrieval problem as an inversion problem is ill-posed because multiple solutions exist, and the solutions do not depend continuously on the measurements and the associated uncertainties. Regularization approaches are needed. Rodgers (2000) introduces a method based on the Bayesian statistics, in which an additional *a priori* state and the uncertainty covariance are incorporated along with the information from the measurements. The optimal atmospheric states can be solved through a nonlinear minimization algorithm. In this study, we adopt NEMESIS, a retrieval algorithm based on the iterative Levenberg–Marquardt scheme (Levenberg 1944; Marquardt 1963), developed by Irwin et al. (2004;

2008) and first used for retrieving the Jovian hydrocarbon abundances from CIRS spectra by Nixon et al. (2007). The *correlated-k* approximation and *k*-coefficients tables computed from high-resolution spectral line databases make the radiative-transfer forward model in NEMESIS very efficient as well as accurate. In order to avoid large oscillations in the retrieved vertical profiles, we adopt the smoothing criteria suggested by Irwin et al. (2008). A good retrieval profile should be able to match the observations weighted by the measurement covariance matrix S_e (including both measurement errors and estimated forward model errors), and also has sufficient smoothing supplied by diagonal elements of the quantity $K_n S_x K_n^T$, where S_x is the error covariance matrix of the *a priori* state vector and K_n is the Jacobian matrix or the matrix of functional derivatives which measures the sensitivity of the forward model with respect to the change of state vector. We prefer the solutions that are constrained quasi equally by the measurements and by the *a priori* profile, i.e., when S_e and $K_n S_x K_n^T$ are of the same order of magnitude. See Irwin et al. (2008) for details.

Given an *a priori* profile and the assumption that *a priori* and *posteriori* follow the Gaussian statistics, Rodgers' method (2000) estimates the *posteriori* error matrix $\hat{S}$ as

$$\hat{S} = (S_x^{-1} + K_n^T S_e^{-1} K_n)^{-1}, \tag{3.1}$$

where S_x and K_n have been introduced above, and S_e is the error covariance matrix of the measurements. In principle, both S_x and K_n might rely on the choice of *a priori* information. Since the *a priori* profile and its uncertainty are not well understood for the Jovian stratosphere, the *posteriori* uncertainties will depend on the choice. In order to mimic this bias, in this study we adopt and estimate the "*ensemble uncertainty*" in the following way. First, we set up as many as possible retrievals based on different conditions, such as *a priori* profiles, *a priori* uncertainties, atmospheric correlation lengths, etc., to find all possible solutions in the full parameter space. Second, for each retrieval case, we estimate the *posteriori* using the Rodgers' method. Third, by taking into account all of the retrieval results with their estimated errors, we achieve the "ensemble uncertainty" for each state variable. This uncertainty is able to characterize the appropriate uncertainty ranges of

our retrieved parameters, provided the intrinsic variability of the atmospheric profiles and the detection noise level of the current data.

3.2.2 *A priori* Information

Besides being used for the regularization, the *a priori* state also has its physical meaning, i.e., the best knowledge of the atmospheric state before the measurements were made. Figure 3.1 summarizes the prior knowledge of temperature, CH_4, C_2H_2 and C_2H_6 profiles for Jupiter, from various sources of ground-based and space-based data. The data are mostly from Yelle et al. (2001) and the table 7.1 in Moses et al. (2004), with the recent New Horizons data from Greathouse et al. (2010). The only vertical temperature profiles were obtained from the in-situ measurement of Galileo probe (Seiff et al. 1998, data from Young et al. 2005). The probe descended in the hot spot region ($\sim 7° N$) and surprisingly showed very wavy structure of the temperature, suggesting a strong wave activity in the low latitude region. The temperature profiles above 0.01 mbar from New Horizons occultation data are colder than the Galileo probe data, showing a possible large latitudinal and temporal variation. But the shape of Jupiter is not exactly known, which might have affected the altitude calibration (private communication with T. Greathouse).

For the gas profiles, 1-D diffusive-photochemical model results (Moses et al. 2005, Model C, hereafter "Moses model") are plotted in Figure 3.1. The homopause, above which species with different mass would separate from each other by the molecular diffusion, seems variable, or at least not well constrained, as shown from the CH_4 data points in Figure 3.1, on top of which the CH_4 profiles are calculated with three different eddy diffusivities to represent the effect of the vertical transport. In fact the current CH_4 measurements in the upper stratosphere can be visually grouped in three clusters. The occultation measurements from the egress of New Horizons by Greathouse et al. (2010) are consistent with the Moses model, while the ingress data from New Horizons has a lower homopause. The values seem consistent with the Voyager data from Festou et al. (1981). Reducing the eddy diffusivity in the Moses model by a factor of 2 is able to explain the

lower homopause. Observations from the Infrared Space Observatory (ISO) in the CH_4 ν_3 band by Drossart et al. (1999) and Voyager UVS data by Yelle et al. (1996) suggest a higher homopause, corresponding to an eddy diffusivity 3 times larger than the Moses value. Since in the CIRS retrieval scheme we prescribe the CH_4 vertical profile, it would introduce uncertainty into the temperature retrieval around the homopause. However, as we will show below, the sensitivity of the CIRS spectra is not high enough to retrieve the temperature above 0.1 mbar, and therefore our retrieval results are similar based on different prescribed CH_4 profiles.

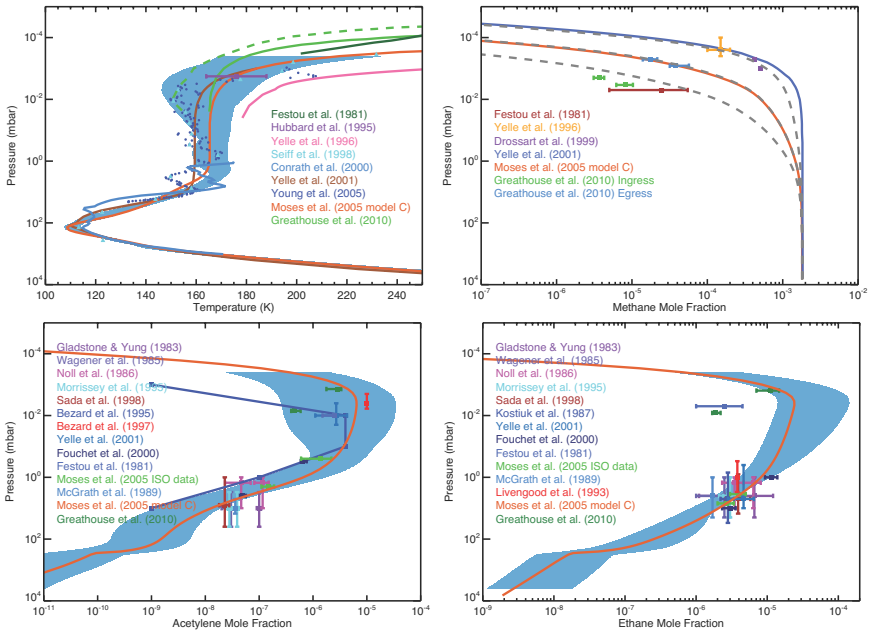

Figure 3.1. Summary of the previous measurements of temperature and gas volume mixing ratios of CH_4, C_2H_2 and C_2H_6 on Jupiter since the 1980s. The blue shaded regions are the globally averaged values with uncertainties from the CIRS retrieval in this study. The gray dashed line in the upper right panel shows 3 different CH_4 profiles from different eddy diffusivity profiles based on the photochemical model from Moses et al. (2005). For the New Horizons data points (Greathouse et al. 2010) of C_2H_2 and C_2H_6, the higher tangent height measurements are from the egress, and the others are from the ingress.

The previous C_2H_2 and C_2H_6 measurements are mainly located around the 1 mbar level. The C_2H_2 values at the ~10 mbar level are not consistent with each other, while the C_2H_6

measurements have better agreement (Nixon et al. 2010). The net chemical production regions (source regions) and the mixing ratio profiles of C_2H_2 and C_2H_6 as by-products of CH_4 photolysis are located around 0.01 mbar from the Moses model. However, for C_2H_2 in the upper stratosphere, measurements by the NASA Infrared Telescope Facility (IRTF) (Bézard, et al. 1997; Yelle et al. 2001), ISO (Fouchet et al. 2000) and the recent New Horizons occultation data (Greathouse et al. 2010) do not agree with each other. The same situation is for C_2H_6 in the upper stratosphere: the ISO measurement (Fouchet et al. 2000) and the New Horizon data are not fully consistent. Despite being limited by the data quality, those observations, combined with the temperature and CH_4 observations, might imply large temporal and spatial variability of C_2H_2 and C_2H_6 in the upper stratosphere. However, the CIRS/IRIS retrieval in this study cannot resolve this issue because from the nadir-view measurements we are not able to retrieve the gas abundances above the 0.1 mbar level.

3.2.3 CIRS Retrieval Results

The 0.48 cm^{-1} resolution CIRS spectra from December 1~14, 2000 are zonally averaged to enhance the signal to noise ratio for the meridional variation. The spectra are grouped in 29 latitudinal bins spanning from $70° S$ to $70° N$, with ~5° in width. For each latitude we perform the "level-by-level retrieval" method as used in Nixon et al. (2010), i.e., retrieving the vertical structures of temperature and composition for each pressure level from the nadir-view spectra from CIRS. The mixing ratios of hydrogen and helium are taken as 0.863 and 0134 from the Galileo probe measurements (Von Zahn et al. 1998; Niemann et al. 1998), respectively. The para hydrogen fraction is calculated in the forward model, with the equilibrium value of 0.25 in the deep atmosphere and varying with the local temperature of each level.

We wish to find all possible solutions in the full parameter space. For the temperature retrieval at each latitude, our parameter space includes 3 CH_4 profiles (Figure 3.1), 5 *a priori* temperature profiles based on the previous work described in section 3.2.2, 4 *a priori*

temperature uncertainties from 2.5 to 20 K, 3 vertical correlation lengths from 1 to 3 scale heights, resulting in 3×5×4×3 different cases. The global mean temperature profiles from the 180 retrievals are shown in Figure 3.2, with different *a priori* profiles on top of them. The retrieval solutions from 100~0.1 mbar are stable with small uncertainties, despite the variance of *a priori* conditions, giving confidence in our retrieval results. For a nadir view mid-IR spectrum, based on the temperature functional derivatives (Nixon et al. 2007), the temperature in the upper troposphere and lower stratosphere are well constrained by the H_2-H_2 continuum from 600-670 cm^{-1} in the CIRS data. Compared with previous measurements, the retrieved global mean temperature from 10-100 mbar is colder than the one in the Moses model but hotter than all the previous measurements: the Voyager radio occultation data (Conrath et al. 2000), the Galileo probe data (Seiff et al. 1998), as well as the fitted temperature profile (Yelle et al. 2001) based on the Galileo data, implying a possible temporal and spatial variation. The CH_4 ν_4 band is able to probe in the middle and upper stratosphere. Especially, the temperature above 0.1 mbar can be retrieved from the Q branch of the CH_4 ν_4 band. However, provided the measurement uncertainties, the resolution of the CIRS spectra is not high enough to be sensitive to the upper stratosphere, so all the retrieved temperatures follow the prescribed *a priori* profiles. Higher resolution observations from ground-based telescopes (i.e., recent TEXES observations by Greathouse et al. 2011) and future limb view observations would be able to provide the information in the low optical depth region. The CH_4 profiles with different homopause levels only affect the retrieval results above 0.01 mbar, so the different CH_4 profiles essentially result in similar retrieval profiles below 0.1 mbar.

Among the retrieved temperature results, we selected 5 typical profiles to retrieve gas mixing ratio distributions of C_2H_2 and C_2H_6 using the same method. 3 *a priori* gas VMR profiles are used. Combined with 4 *a priori* uncertainties (0.5, 1, 2, and 4 folds), and 3 correlation lengths from 2 to 4 scale heights, for each species, we have 180 retrieval cases. The global mean results for C_2H_2 that match the CIRS spectra are shown in Figure 3.2. The retrieval results are stable below 0.1 mbar, and consistent with the previous observations at ~1 ppm at 1 mbar (Figure 3.1), but seem smaller than the previous results at 10 mbar. Note

that the previous results are not self-consistent either. The Q branch of the C_2H_2 ν_5 band, which is supposed to probe the upper stratosphere, is not well resolved because of the resolution limit. Therefore there is little information retrieved in the upper region and the retrieved profiles are scattered due to the extremely loose constraints. The C_2H_6 retrieval results are shown in Figure 3.2. The results are consistent with most of the previous observations around 1-10 mbar but are larger than some previous values (Figure 3.1). The photochemical model results of C_2H_2 and C_2H_6 from Moses et al. (2005), which are one set of our *a priori* profiles, fall within the uncertainty range of the retrieved global mean profiles. From the current measurements we lack sensitivity to probe the source regions (~0.01 mbar) of the two major photolysis products as well as coolants in the Jovian stratosphere.

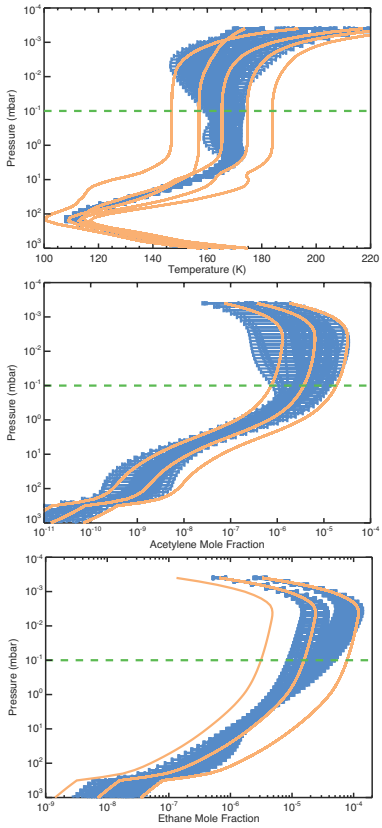

Figure 3.2. The ensemble retrieval results of globally averaged values of temperature, C_2H_2 and C_2H_6 from Cassini CIRS observations, starting from different *a-priori* profiles (orange lines). The error bars are estimated based on Bayesian statistics in Rodger's method. There is no information above ~0.1 mbar (green dashed lines) from CIRS spectra.

Overall we conclude that our CIRS retrieval results of temperature and gas species below 0.1 mbar are robust, with appropriate uncertainties. Roughly speaking, the global mean temperature and gas species are consistent with previous measurement. Although the spectral resolution of CIRS is not as high as the ground-based telescope observations that could probe higher in the stratosphere, the merit of CIRS measurements is that it is able to provide detailed spatial maps for those atmospheric profiles in the middle and lower stratospheres and upper troposphere of Jupiter. Figure 3.3 shows the global mean profile of temperature and the two-dimensional (latitude-altitude) maps of three major coolants, CH_4, C_2H_2 and C_2H_6 from a typical CIRS retrieval case. Our results are roughly consistent with the temperature maps in Simon-Miller et al. (2006) and later extended to higher regions by Nixon et al. (2007). Similar gas mixing ratio maps are also shown in Nixon et al. (2007; 2010). In principle, we have more than one map from different retrieval cases. However, in the region where we have information, the difference of latitudinal patterns between various cases is generally small. Therefore our result agrees well with the previous results, but the uncertainties in the previous maps seem underestimated. For a detailed discussion of those maps refer to Nixon et al. (2007; 2010). Here we emphasize three predominant features: (1) The Jovian "quasi-quadrennial oscillation" (QQO) type structures in the temperature map at ~1 mbar. This phenomenon is the stratospheric temperature oscillation in the low latitude region, with a period of about four earth years, analogous to the Earth's "quasi-biennial oscillation" (QBO, 26-28 month period). In the next section we will see that this feature plays important roles in shaping the instantaneous cooling rate map and global energy balances in the Jovian stratosphere; (2) the C_2H_2 latitudinal distribution below its source region shows a smoothly decreasing trend from equator to pole, implying a photochemistry-dominated processes (Nixon et al. 2007) because the photolysis of CH_4 is stronger in the lower latitudes than in the higher latitudes; (3) The C_2H_6 latitudinal distribution below 1 mbar reveals an opposite trend compared with C_2H_2. The C_2H_6 seems increasing from equator to pole, suggesting a transport-dominated processes (Nixon et al. 2007) with an upward transport in the lower latitude and a downward transport in the higher latitude. Nixon et al. (2007) estimated the transport timescale is between the two timescales of the two tracers, from 10^8 *s* (C_2H_2) to 10^{10} *s* (C_2H_6). Note that the two opposite

trends from C_2H_2 and C_2H_6 could compensate each other so as to flatten the latitudinal difference of cooling rate.

3.2.4 IRIS Retrieval Results

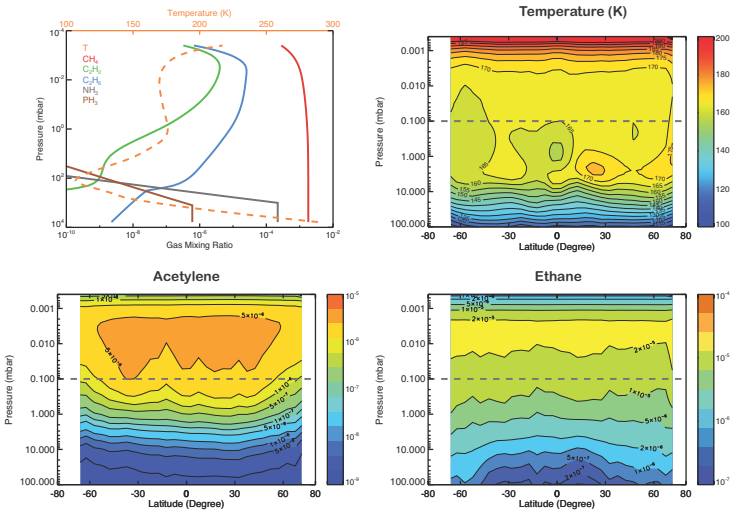

Figure 3.3. A typical set of retrieval results from Cassini CIRS data. Upper left: globally averaged values of temperatures and gas volume mixing ratios; Upper right: zonally averaged stratospheric temperature map; Lower left: zonally averaged stratospheric C_2H_2 map; Lower right: zonally averaged stratospheric C_2H_6 map. The values above ~0.1 mbar (gray dashed lines) should be considered as estimates since the CIRS spectra are not sensitive to the pressure level above.

The 3.9 cm^{-1} resolution IRIS spectra from Voyager 1 cover from 60° *S* to 60° *N* of Jupiter's disk during the 1979 flyby. The spectra are averaged in 10° width latitudinal bins, stepped every 5°. For each latitude we still choose the "level-by-level retrieval" method for temperature structure. However, a typical IRIS spectrum for one latitude only contains ~45 and ~25 spectral points in the C_2H_2 and C_2H_6 bands, respectively. This information is not enough to retrieve the vertical profiles of the gases. Instead, we choose to fix the shape of the mixing ratio profiles and scale them to fit the IRIS spectra. This method enhances the latitudinal contrast to retrieve meridional distributions of the gases. This "scaling retrieval" method for the C_2H_2 and C_2H_6 abundances can be simultaneously combined with the

"level-by-level retrieval" of temperature profiles in NEMESIS to maximize the use of information since we retrieval all variables together.

We started with the *a priori* profiles from a typical set of CIRS retrieval results. For temperature, we only uses one CH_4 profile (the highest homopause profile in Figure 3.1) for the IRIS retrieval because from CIRS retrieval tests we already know that different CH_4 profiles would not change the retrieval results. The *a priori* profile is shifted to -15 and +10 K, combined with 4 *a priori* uncertainties from 2.5 to 20 K and 3 correlation lengths from 1 to 3 scale heights to estimate the ensemble uncertainty for each level. For gas species, we also increase and decrease the *a priori* profile by a factor of 5, combined with 3 *a priori* uncertainties (1, 2, and 4 folds, respectively) for each gas. Together we have about 3000 retrieval cases, among which ~500 cases can fit the data reasonably well. The globally averaged profiles with their ensemble uncertainties are shown in Figure 3.4. Figure 3.5 shows a typical case with the global mean profile of temperature and the two-dimensional maps of CH_4, C_2H_2 and C_2H_6.

The globally averaged temperature structure from the Voyager data generally agrees with the Cassini results, except that the IRIS temperature is systematically colder than the CIRS result by 3~4 K in the upper troposphere between 300 and 400 mbar, and by 2~3 K in the lower stratosphere between 10 and 100 mbar, respectively. The latitudinal variation is also different in the two regions. In the lower stratosphere, the difference between IRIS temperatures and the CIRS result is more uniformly distributed with latitude. On the other hand, in the upper troposphere, the IRIS temperature at the equator ($\pm 5°$) is hotter than the CIRS data and colder at other latitudes. But the northern hemispheric difference is larger. These latitudinal differences are consistent with the Figure 3.8 in Nixon et al. (2010). The tropospheric temperature difference, according to the recent work by Li et al. (2012), causes the global-averaged emitted power to increase ~3.8% from the Voyager to the Cassini epoch, with greatest contribution from the northern hemispheric difference. In this study we find that the lower stratospheric temperature difference will also have a significant effect on the local energy balance in the two eras as well. Comparing Figure 3.3

and Figure 3.5 we find that the "QQO"-type structure does not appear in the IRIS temperature map. This shows a more dynamic environment in the Jovian stratosphere in the Cassini era. Additionally, the latitudinal variation of the CIRS tropospheric temperatures is more violent than the IRIS results, suggesting a possible relationship between the tropospheric dynamics (e.g., wave forcing) and the stratospheric temperature oscillations (Friedson et al. 1999; Simon-Miller et al. 2006), although the recent study by Simon-Miller et al. (2007) shows the interaction between the troposphere and stratosphere might be uncorrelated or at least more complicated than what we thought.

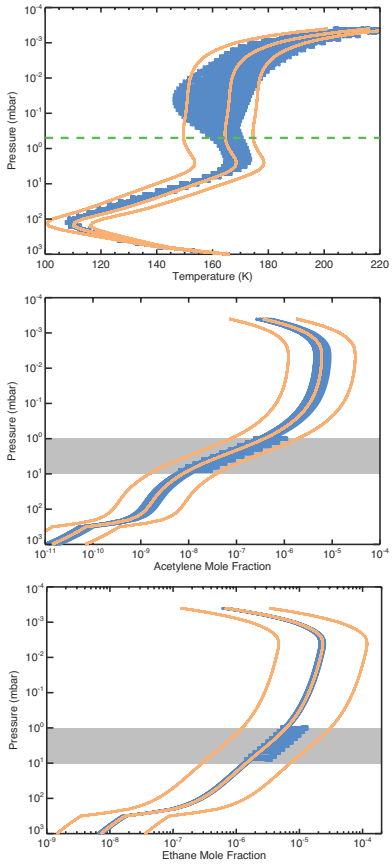

Figure 3.4. Retrieval results of the globally averaged values of temperature, C_2H_2 and C_2H_6 from Voyager IRIS observations, started from different *a-priori* profiles (orange lines). The middle orange curve in each panel is from the CIRS retrieval. The error bars are estimated based on Bayesian statistics in Rodger's method. There is no information above ~ 0.5 mbar (green dashed lines) for temperature. For the scaling retrieval results for C_2H_2 and C_2H_6, we only put the error bars in the region where the information exists between 1 to 10 mbar (gray shaded area).

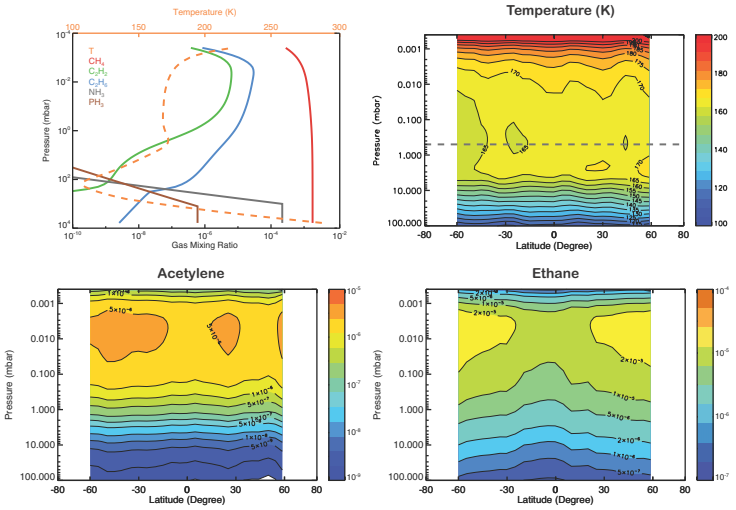

Figure 3.5. A typical set of retrieval results from Voyager IRIS data. Upper left: globally averaged values of temperatures and gas volume mixing ratios; upper right: zonally averaged stratospheric temperature map; lower left: zonally averaged stratospheric C_2H_2 map; lower right: zonally averaged stratospheric C_2H_6 map. The values above ~0.5 mbar (gray dashed lines) in the temperature map should be considered as estimates. There is no information outside the region of 1-10 mbar for C_2H_2 and C_2H_6.

The 2-D maps of the gas species also show differences between the Voyager and Cassini epochs, although there is no statistically significant difference between the global mean profiles. Since we only retrieve the total column density (or scale factor) for each gas, the uncertainty should only correspond to the pressure level where the spectra have sensitivity, from 10 to 100 mbar (gray shaded area in Figure 3.4). Although the error bars in the IRIS gases appear to be smaller than the CIRS results from the plots, it is not appropriate to conclude the IRIS gas retrievals in Figure 3.4 are "better" than the CIRS results, because the profile retrieval of CIRS data distribute the error probability distribution in a much larger parameter space. From Figure 3.3 and Figure 3.5, the IRIS C_2H_2 meridional distribution is flatter than the CIRS result, while the IRIS C_2H_6 has a more dramatic latitudinal contrast. If the stratospheric circulation is hypothesized to shape the latitudinal distribution of the tracers, we expect the circulation might be stronger in shaping the gases observed in the Voyager era than in the Cassini data because stronger circulation would

help reduce the latitudinal contrast of short-lived species such as C_2H_2, but increase that of long-lived species such as C_2H_6. In the following sections, our cooling rate calculation further supports this hypothesis.

3.3. Cooling Rates

3.3.1 Model Description

In the radiative equilibrium state, an atmosphere is balanced between the solar heating and IR cooling. The Jovian stratosphere is heated primarily by the near IR CH_4 bands in the short wavelength region (<5 μm, i.e., >2000 cm^{-1}). But the aerosol contribution may be potentially important (West et al. 1992). The atmosphere cools due to the longwave thermal infrared emission. The outgoing radiance is absorbed, reemitted and scattered by the hydrocarbon species, aerosols and clouds and eventually causes the atmosphere to cool to space. Given the profiles of temperature and gas abundances, upward and downward energy flux can be calculated via the radiative transfer model for each atmospheric layer, and the net flux of each layer contributes to the IR heating or cooling effect. In the Jovian stratosphere, the dominant coolants and their vibrational bands in the infrared region from 5 to 10 μm (100-2000 cm^{-1}) include CH_4 (ν_4), C_2H_2 (ν_5) and C_2H_6 (ν_9), and the molecular hydrogen and helium via their collision-induced absorptions (Yelle, et al. 2001). Those bands and continuum features are consistent with the major spectral features seen in the CIRS and IRIS spectra.

Based on Goody and Yung (1995), the monochromatic cooling rate can be derived from the flux divergence in an integral form

$$\overline{\overline{H_{cool}}}(\tau) = \frac{dF_\nu(\tau)}{d\tau}$$

$$= 2\pi\left[-B_\nu(\tau_i)E_2(\tau) + \left(B_\nu(\tau_s) - B_\nu(\tau)\right)E_2(\tau_s - \tau) + \int_0^{\tau_s}\left(B_\nu(t) - B_\nu(\tau)\right)E_1(|t-\tau|)dt\right], \quad (3.2)$$

where F is the thermal flux, ν is the wavenumber, B is the atmospheric source function, τ is the optical depth, and $E_n(x) = \int_1^\infty \frac{e^{-xt}}{t^n} dt = \int_x^\infty \frac{x^{n-1}e^{-t}}{t^n} dt$ is the exponential integral function. Scaled by the mass in the layer, the cooling rate (in the units of erg g^{-1} s^{-1}) as function of pressure p can be obtained from the hydrostatic law:

$$\overline{\overline{H_{cool}}}(p) = \frac{g d\tau}{dp} \overline{\overline{H_{cool}}}(\tau) \tag{3.3}$$

where g is gravity.

The cooling rate includes three terms: Newtonian cooling, surface exchange, and mutual exchange, corresponding to the three main terms in the large bracket of the right hand side, sequentially. The Newtonian cooling is simply the cooling to space effect by thermal emission from each layer, and the surface exchange term refers to the contribution of the surface emission flux from below to each layer. The third part shows the interaction effect by the upward and downward emission fluxes from all other layers.

Compared with the integration calculation of thermal radiance at the top of the atmosphere (TOA) in the last section, the cooling rate profile calculation requires much more high-resolution spectra data and more accurate treatment because it essentially calculates the difference of the fluxes between layers. The most accurate calculation for atmospheric cooling rate is the line-by-line (LBL) calculation, which is able to resolve the shape of every single spectral line. The spectrally resolved optical depth is calculated from the Reference Forward Model (RFM, http://www.atm.ox.ac.uk/RFM/#publications), which was originally developed for the Earth's atmosphere and modified in this work to include the H_2-H_2 and H_2-He collisional induced opacities. With the input from RFM, our LBL radiative transfer model calculates the cooling rate profile using a finite difference scheme described in appendix B. The model is able to give the most precise results by far since our spectral sampling rate (0.001 cm^{-1}) in the calculation is less than the mean half width of the lines. Moreover, we have achieved several simple but realistic analytical solutions of monochromatic cooling rate for some typical atmospheric temperature profiles (appendix B). Our radiative transfer calculation has been rigorously validated against those analytical

solutions (appendix B). None of the previous calculations has achieved the high resolution of our benchmark models.

The pressure broadening of hydrocarbons in the hydrogen atmosphere could be different from that in Earth's atmosphere where the experimental data are based on the recently updated C_2H_6 spectroscopic line parameters in the ν_9 band with hydrogen-broadening widths adopted (Vander Auwera et al. 2007; Orton et al. 2008). The H_2-broadening widths are held constant in this band, with a value of 0.115 cm^{-1}, compared with the air-broadening width 0.067 cm^{-1} from the 2008 HITRAN database. For the ν_5 band of C_2H_2, we use a parameterized fit to the results of Varanasi (1992) for the hydrogen-broadened line width. The H_2 -broadening widths vary with wavenumber, with values of ~0.08 cm^{-1}, compared to the air-broadening width of ~0.06 cm^{-1} from the 2008 HITRAN database. For the CH_4 broadening data, Bailey et al. (2011) evaluated the currently available data and suggested that line widths in the Jovian atmosphere (H_2-He mixture) is similar to those in the Earth's atmosphere (N_2-O_2 mixture). Therefore we took the 2008 HITRAN database as our spectroscopic source for CH_4 in the mid-IR region. The H_2-H_2 and H_2-He collisional-induced opacities are from Orton et al. (2007), in which the absorption coefficients are recalculated for the low temperature region, based on an *ab initio* quantum mechanical model.

3.3.2 One-Dimensional Cooling Rate

We use the Cassini CIRS data to describe the cooling rate calculation. Figure 3.3 shows the global mean profile of temperature and three major coolants, CH_4, C_2H_2 and C_2H_6 from a typical retrieval case. NH_3 is also one of our retrieval parameters since there are overlapping bands of NH_3 and C_2H_6. Therefore, NH_3 is also included, although it is not important for the stratospheric cooling.

The contributions of different spectral bands are clearly distinct in the spectrally resolved global-mean cooling rates on Jupiter (Figure 3.6). The H_2-H_2 and H_2-He continuum band

dominates the lower stratosphere (below 1 mbar) for wavenumbers less than 700 cm^{-1}. The C_2H_2 and C_2H_6 bands overlap each other, and dominate the higher stratosphere above 1 mbar in the 700-900 cm^{-1} region. The Q branch of the C_2H_2 ν_5 band forms a very strong but narrow feature from 1 mbar through the top of stratosphere, leading to very efficient cooling from that spectral region. The broad methane ν_4 band dominates the cooling in the top region of the stratosphere. The integrated cooling rates of the three distinct bands (H_2-H_2/H_2-He, C_2H_2-C_2H_6, and CH_4) are plotted in Figure 3.6. The major coolants of the Jovian stratosphere are C_2H_2 and C_2H_6 from 5 to 0.01 mbar, and hydrogen below 5 mbar. The cooling by CH_4 is relatively inefficient between 0.01 and 1 mbar, mainly because the ν_4 CH_4 band is relatively far away from the mid-IR energy peak (~18 μm, corresponding to the stratospheric temperature ~160 K). However, CH_4 has a significant contribution in the 1-10 mbar region and its profile shows a prominent local enhancement in Figure 3.6, with a magnitude as large as C_2H_6. It results from the pressure broadening effect of CH_4 lines below 1 mbar, where the wings become optically thick enough to cool more effectively (with personal communication with T. Greathouse). As the concentrations of C_2H_2 and C_2H_6 drop quickly due to molecular diffusion above the homopause (~0.01 mbar), their contribution becomes negligible and therefore the methane cooling dominates. The general shape of the cooling rate profile is smooth, except that there are two small "bumps" at ~5 and ~50 mbar. The former reflects the similar feature in the temperature profile (Figure 3.3) at the same level and the CH_4 line broadening effect. The second one reflects the transition between the H_2-H_2/H_2-He cooling dominant region below to the hydrocarbon cooling dominant region above. The cooling rate at 1 mbar is ~100 ergs/g/s, equivalent to ~0.03 K per Jovian Day, based on the specific heat capacity of 14.30 J/g/K for molecular hydrogen and 5.19 J/g/K for helium (Lide, 2005, p.812).

The Newtonian or cooling-to-space approximation, which neglects the flux exchange between the atmospheric layers, is not always good for the Jovian stratosphere. The Newtonian cooling rate is shown in dashed line in Figure 3.6. Since our radiative transfer model reaches ~6 bar, the contribution from the lower boundary of the stratosphere is negligible due to the large hydrogen opacity in the troposphere. Therefore the difference

between the Newtonian cooling rate and total cooling rate comes from the flux exchange between the layers (see equation (3.1)). Between 0.5 and 50 mbar the Newtonian cooling rate only contributes to half or even less of the total cooling rate, implying that the flux exchange from other layers is at least as important as the outgoing emission by the layer itself. This happens because of the large temperature gradient in the lower stratosphere. An extreme case will be the tropopause region where the temperature minimum leads to a thermal flux convergence from the layers above and below. Those fluxes from other layers are so large that they overcome their own emitted flux, leading to net heating effect (same as Yelle et al. 2001). The tropopause region is not shown in Figure 3.5, but we can see that the heating causes the cooling rate to rapidly approach zero in the lower stratosphere. In the upper stratosphere above 1 mbar where the temperature structure is roughly constant, Newtonian cooling behaves as a good approximation.

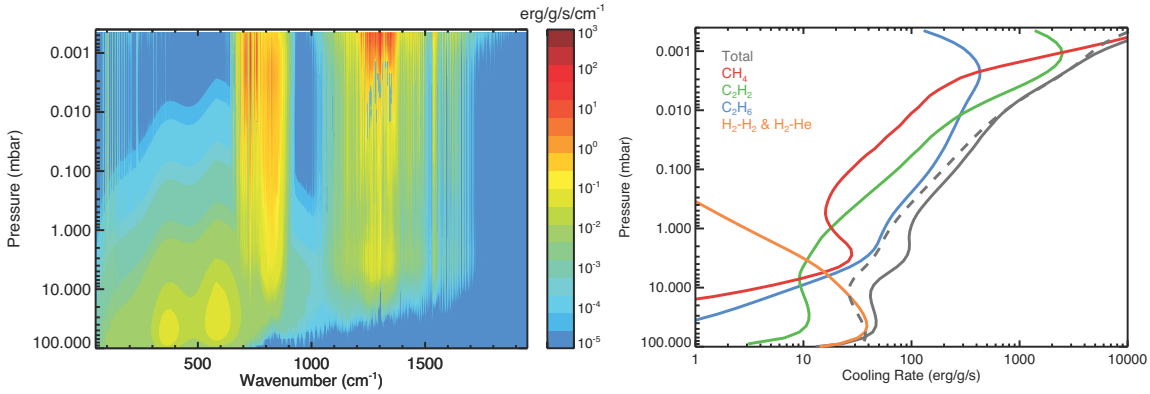

Figure 3.6. Infrared cooling rate in the stratosphere of Jupiter based on a typical set of retrieval results from Cassini CIRS data (Figure 3.3). Left: Spectrally resolved cooling rate from the line-by-line calculation; right: Contribution of the cooling rates from different vibrational-rotational bands and collisional induced continua. The dashed line is calculated based on the Newtonian cooling approximation.

3.3.3 Non-LTE Effect

In the top stratosphere where the collisions are not frequent enough, other processes, such as radiative absorption and emission, play the role of determining the distribution of

molecules between the different energy levels. Under these conditions, the conventional "local thermodynamic equilibrium (LTE)" situation, which assumes the molecules in different energy states obey the Boltzmann distribution, breaks down. These so-called "Non-Local Thermodynamic Equilibrium (Non-LTE)" processes may significantly affect the population of the ro-vibrational levels of radiatively active species in the infrared region and therefore the atmospheric heat balance in the upper stratosphere of Jupiter and other planets. Appleby (1990) investigated the non-LTE effect of CH_4 on giant planets and concluded that the LTE situation of CH_4 $\nu_4$band is only valid below 0.01 mbar for all the four giant planets. Yelle (1991) developed a multi-level non-LTE model for CH_4, C_2H_2, C_2H_6 and HCN and showed the significance of non-LTE effect on the cooling rate in the upper atmosphere of Titan. Other studies (e.g., Drossart et al. 1993; Halthore et al. 1994; Drossart et al. 1999) investigated non-LTE emission of CH_4 at 3.3 μm and the observational evidence in the upper atmosphere of Jupiter. In this section, we introduce a non-LTE radiative transfer model to investigate the importance of non-LTE effects on the cooling rates via the mid-IR bands of the hydrocarbon species on Jupiter.

A full non-LTE calculation includes the vibrational-translational processes (V-T processes) between the vibrational energy levels and the ground states, and the vibrational-vibrational (V-V) transitions between different vibrational energy levels. In this study, we only consider a simple two-level approach to catch the essence of this problem on Jupiter. Because the vibrational bands of CH_4 (ν_4), C_2H_2 (ν_5) and C_2H_6 (ν_9) are the lowest energy levels above their ground states, respectively, the two-level assumption may be sufficient for the non-LTE calculation in the mid-IR region. The exchange between the higher and lower vibrational energy levels through V-V processes usually replenish the population of the lower levels, such as the $\nu_3 \rightarrow \nu_4$ transfer for CH_4 (see the simulation in Halthore et al. 1994). Therefore our calculation in principle gives a higher limit for the non-LTE pressure levels.

In our two-level model, the non-LTE effect is dominated by the V-T processes, i.e., competition of collisional processes and radiative processes (spontaneous emission and

induced emission and absorption) between the mid-IR vibrational levels and the ground states. The rotational sub-levels within the ro-vibrational bands are still in LTE. Under those assumptions, the formalism of non-LTE becomes concise and clear. We modified the source function to include the continuum absorption from H_2-H_2 and H_2-He CIA that is assumed to be always in LTE. This modification is necessary since in the higher atmosphere where the hydrocarbon abundances drop rapidly with pressure, the CIA component is negligible. Because of the strong overlapping between C_2H_2 ν_5 and C_2H_6 ν_9 bands in the 700-850 cm^{-1}, we treat the two bands together to calculate the mean radiation field $\bar{I}$. The cooling rate is still a line-by-line calculation based on the non-LTE source function. The detail of our non-LTE model is described in appendix B. We introduced two numerical methods to solve the differential-integral equation and adopted the iteration method for Jupiter calculation in this study.

The radiative budget of the upper stratosphere of Jupiter depends crucially on the collisional de-activation (quenching) rates for the V-T processes. However, those rates of the excited states of the major hydrocarbon species, such as CH_4, C_2H_2, and C_2H_6, in a hydrogen-rich atmosphere are the major unknown parameters in the literature. Table 3.1 summarizes the current knowledge of de-activation rates of the hydrocarbons in the hydrogen and nitrogen atmospheres at 1 μbar and 296 K. The only source of C_2H_2 data in hydrogen gas is from Häger (1981). The rate for C_2H_6 in the hydrogen atmosphere is lacking, so we assume it is the same as that of C_2H_2, as their rates in the nitrogen atmosphere are approximately the same as well. For all three hydrocarbons, the collisional de-activations by molecular hydrogen at 1 μbar and 296 K are more than one order of magnitude more efficient than that by nitrogen. It implies that the non-LTE effect due to the V-T transitions on Jupiter can only occur at much lower pressure levels than on Titan.

The stratospheric temperature of Jupiter is approximately 170 K. But the extrapolation of collisional de-activation rate from room temperature to 170 K is tricky because the temperature dependence is highly uncertain. Classical theory states that the collisional de-activation rate is proportional to the bulk atmospheric number density, the collisional rate,

and the de-excitation probability P_{10} (e.g., Lellouch et al. 1990; Yelle 1991). The Landau-Teller theory (Laudau and Teller 1936) shows $P_{10} \propto \exp(-bT^{-\frac{1}{3}})$ and later the modified expression by Schwartz et al. (1952) gives $P_{10} \propto \exp\left(-bT^{-\frac{1}{3}}\right) \exp(h\nu/2kT)$. However, both theories could not agree with the experimental data satisfactorily (Yelle 1991). In the previous studies on Jupiter, Appleby (1990) incorporated the temperature dependence of number density and collisional rate with P_{10} in a Landau-Teller type formula for the CH_4 (ν_4)-H_2 relaxation rate: $C_{10} \propto \exp\left(-61T^{-\frac{1}{3}}\right) p$, where p is the pressure. Halthore et al. (1994) used a similar formula: $C_{10} \propto \exp\left(-40T^{-\frac{1}{3}}\right) p$. These formulas imply a factor of 6.4 (in Appleby 1990) and 3.4 (in Halthore et al. 1994) decrease from 296 to 170 K. On the other hand, if we assume P_{10} is a constant, the classical theory implies $C_{10} \propto T^{\frac{1}{2}} p$ and results in a factor of 1.3 decrease. For C_2H_2 and C_2H_6, we do not have any temperature dependence information from the literature.

Table 3.1. Collisional de-activation rates (s^{-1}) at 1 μbar and 296 K

	H_2 Atmosphere	**N_2 Atmosphere**
C_2H_2 (729 cm^{-1}) (A_{10} = 4.74)	C_{10} = 62.93 (Häger 1981)	C_{10} = 1.03 (Häger 1981) C_{10} = 0.797 (Yelle 1991)
C_2H_6 (821 cm^{-1}) (A_{10} = 0.37)	C_{10} = 62.93 (Estimated in this study, assumed the same as C_2H_2)	C_{10} = 0.963 (Estimated by Yelle 1991)
CH_4 (1310 cm^{-1}) (A_{10} = 2.12)	C_{10} = 4.4 (Appleby 1990) C_{10} = 8.33 (Yardley 1970) C_{10} = 10 (Baumgärtner and Hess 1974)	C_{10} = 0.0453 (Yelle 1991, based on Yardley 1970)

In this study, we first adopt the scaling of the collisional de-activation rate with pressure and temperature from the classical theory with a constant P_{10}, i.e.,

$$C_{10} = C_{10}(296\ K)\frac{p}{p_0}\left(\frac{T}{T_0}\right)^{\frac{1}{2}}, \tag{3.4}$$

where $p_0 = 1$ μbar and $T_0 = 296$ K. $C_{10}(296\text{ K})$ values are given in table 3.1. This estimation (in case I) is probably the upper limit of the C_{10}. In order to capture the uncertainty, we also have a low-limit case (case II) in which C_{10} is decreased by a factor of 10 for all three hydrocarbons.

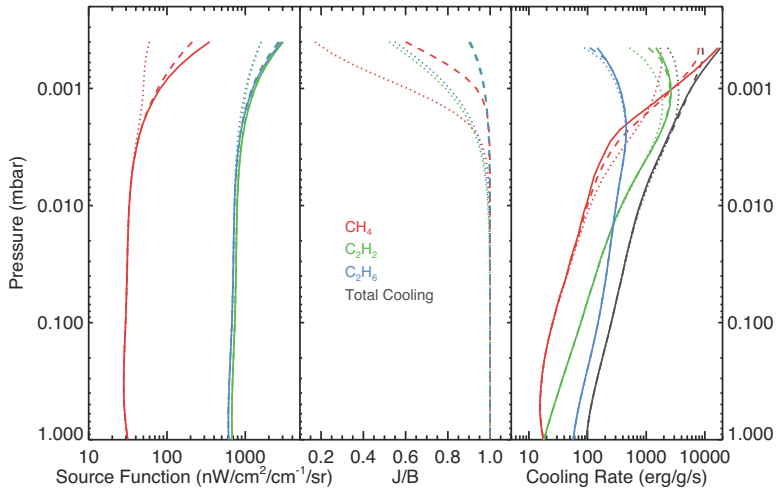

Figure 3.7. Non-LTE model results. Solid lines are from the LTE calculations. Dashed lines are Non-LTE case I, and dotted lines are non-LTE case II. Left: band-integrated source functions for CH_4, C_2H_2 and C_2H_6; Middle: the ratio of the non-LTE source functions (J) over the LTE source functions (B); Right: Comparison between the non-LTE and LTE cooling rates. This figure shows that non-LTE is prediected to be significant only at pressures less than 0.01 mbar.

The mean source functions versus Planck functions (LTE) for the CH_4 band and C_2H_2-C_2H_6 bands are plotted in Figure 3.7 for both cases, as well as the cooling rates from each band. The cooling rates from H_2-H_2 and H_2-He continua are not plotted here because (1) they are always in LTE; (2) they only contribute to the lower stratosphere cooling rate where the non-LTE is not important (see Figure 3.6). Generally speaking, the non-LTE source functions are smaller than the LTE source functions and result in less cooling. But the CH_4 case seems counterintuitive because the non-LTE cooling rate is larger than the LTE cooling rate. We attribute it to the energy exchange between the layers. In the LTE situation, the layers between 0.001 and 0.01 mbar are heated primarily by the upper layers due to the sharp thermal gradient in the transition zone between the top of the stratosphere

and hot thermosphere above. When the collisional de-activation rate is lower (non-LTE), the radiative heat sources in the above layers become weaker (see the left panel of Figure 3.7), leading to a larger cooling effect. The C_2H_2 and C_2H_6 do not show such pronounced behaviors because their collisional de-activation rates are not as low as CH_4.

Overall, we conclude that even in the upper limit case, the non-LTE effect does not have a significant impact on the cooling rate below 0.01 mbar in the Jovian stratosphere. It might be important in the stratosphere above that pressure level, but our current knowledge of hydrocarbon abundances at those pressure levels has large uncertainties, therefore we do not investigate more non-LTE effects in this study.

3.3.4 Two-Dimensional Cooling Rates

The most valuable results from the IRIS and CIRS measurements are the detailed spatial maps for temperature and gas species, from which we obtain the high-resolution stratospheric cooling rate maps in the meridional plane (Figure 3.8). Although the solar forcing could vary ~20% due to the eccentricity change, the latitudinal distribution pattern of solar heating would not change much. On the other hand, the pattern of the cooling rate seems change dramatically. Therefore, the change of the instantaneous cooling rate pattern accounts for most of the total radiative forcing change. The difference map (Figure 3.8, lower panel) shows that the amplitude of the temporal variation in the cooling rates could reach as large as half of the background value, implying that the instantaneous radiative forcing in the Jovian stratosphere has undergone a dramatic change from the Voyager to Cassini epochs.

There are several factors affecting the cooling rate map. First, the spatial variations are mostly due to the temperature field. Influenced by the QQO structure in the temperature map from Cassini observations, the cooling rate map shows a wavelike pattern around 1 mbar, especially in the low latitude region. On the other hand, without the temperature anomalies, the cooling rate map in the Voyager epoch exhibits much less variation.

Secondly, the secondary hydrocarbons, C_2H_2 and C_2H_6, dominate the cooling rate profile above 10 mbar (Figure 3.6). Since the latitudinal trends of C_2H_2 and C_2H_6 are opposite to each other in the Cassini results, they compensate each other to reduce the meridional variations of the cooling rate. Conversely, C_2H_2 and temperature from Voyager observations are nearly uniformly distributed with latitude, while C_2H_6 has large variations. The net effect is that the cooling rate map around 1-10 mbar in the Voyager epoch shows a similar latitudinal shape as its C_2H_6 distribution.

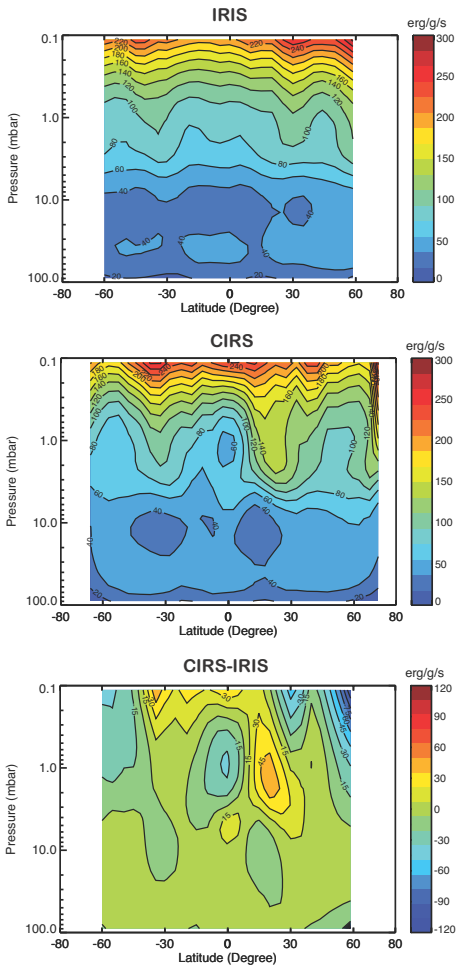

Figure 3.8. Zonally averaged stratospheric cooling rate map from 0.1 to 100 mbar. Upper panel: result based on a typical set of retrieval results from IRIS data (Figure 3.3); Middle panel: result based on a typical set of retrieval results from CIRS data (Figure 3.5); Lower panel: Difference between the two cooling rate maps (CIRS-IRIS).

If we assume the Voyager thermal map is the "normal" situation, the features in the Cassini map and the difference map could have a potentially large impact on the Jovian stratosphere. Analogous to Earth, if there exists a Brewer-Dobson-type circulation in the Jovian stratosphere, the cooling rate anomalies associated with the QQO structure would induce a modification to the normal meridional circulation, like the QBO-induced circulation in the Earth stratosphere. However Jupiter's modification could be much larger because the normal background temperature field (i.e., the Voyager thermal map) is more uniform on Jupiter than that on Earth, which has a strong seasonal cycle. Note that the QQO-induced radiative forcing anomaly is almost half of the mean field amplitude. Therefore its effect might significantly alter the tracer transport in the stratosphere of Jupiter.

3.4. Global Energy Balance

3.4.1 Solar Heating and Thermal Conduction

The globally averaged solar heating rate due to gas absorption can be expressed analytically (appendix B):

$$\overline{H_{heat}}(\tau_\nu) = \frac{1}{2} F_\nu E_2(\tau_\nu) \tag{3.5}$$

where F_ν is the TOA solar flux at wavenumber ν. The optical depth τ_ν is mainly attributed to the NIR absorption bands of the major heat agent CH_4. We also include the NIR H_2-H_2 absorption based on Borysow (2002) and H_2-He continuum based on Borysow et al. (1998; 1989a; 1989b; 1992). Baily et al. (2011) collected the latest CH_4 absorption coefficient data from various sources. Using this database, Kedziora-Chudczer and Bailey (2011) were able to obtain a fit to the high-resolution NIR spectra. Their study also suggested the CH_4 line width due to air broadening is close to that in the H_2-He mixture. Therefore we adopted the CH_4 opacities from their most updated database, including the important bands at 1.1, 1.3, 1.7, 2.3, 3.3 and 7.6 μm from the near-infrared to mid-infrared region, as identified by Yelle et al. (2001). The spectral resolution in our LBL calculation is 0.005 cm^{-1}. Figure 3.9

and Figure 3.9 show the spectrally resolved heating rate and the integrated heating rate from each band, respectively. The heating rate in each band is concentrated in an approximate 500 cm^{-1}-wide region in the spectral domain. The largest heating rates are from the 2.3 and 3.3 μm strong bands, the 7.6 μm band is also strong but it is too far away from the solar radiation peak (~0.5 μm). The weak bands exhibit steeper heating rate slopes that we will explain in section 3.4.3. The total heating rate profile from CH_4 absorption generally agrees with the results from Yelle et al. (2001). The small difference between our work and the previous study is attributed to the difference of the line-by-line list we use (Baily et al., 2011) and the old *correlated-k* coefficients (e.g., Baines et al., 1993; Irwin et al., 1996), which have been significantly improved in recent years (e.g., Irwin et al., 2006; Karkoschka and Tomasko, 2010; Baily et al., 2011).

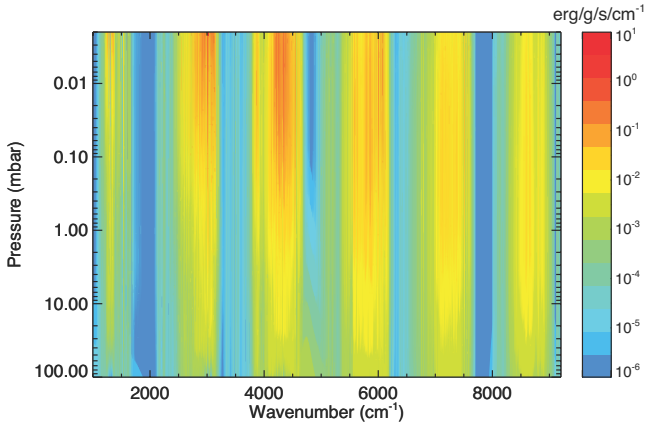

Figure 3.9. Spectrally resolved CH_4 heating rate from 1000 to 9000 cm^{-1}.

The heating/cooling rate from thermal conduction can be estimated from

$$\frac{dT}{dt} = \frac{K}{\rho C_p}\frac{d^2T}{dz^2}, \tag{3.6}$$

where K is the thermal conductivity, typically on the order of ~0.1 W m^{-1} K^{-1} for hydrogen molecules (Lide, 2005, p.1199). From the equation we can see the heating/cooling rate highly depends on the temperature profile. The curvature of the temperature profile, or the vertical gradient of the lapse rate, is nearly zero, or less than 10^{-7} K m^{-2} in most of the stratosphere, therefore its heating/cooling effect due to thermal conduction must be negligible. The only region where the thermal conduction could be important is at several

microbars, as shown by Yelle et al. (2001). The reason should be attributed to the existence of a sharp temperature gradient connecting the cold stratosphere with the hot thermosphere above as well as the low atmospheric density at those pressure levels. However, due to the poor knowledge of the precise shape of the temperature profile at those pressure levels, we do not attempt to discuss the possible significance of thermal conduction in this study.

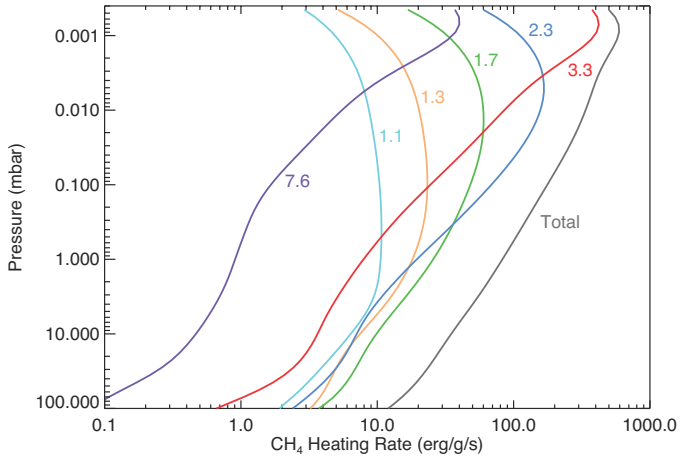

Figure 3.10. Globally averaged CH_4 heating rates. Contributions from different ro-vibrational CH_4 bands are plotted with colors. The CH_4 profile is shown in the upper left panel of Figure 3.1, with the highest homopause, consistent with Galileo data and ISO data.

3.4.2 Heating and Cooling Balance

The globally averaged solar heating rate and atmospheric cooling rates with uncertainties are shown in Figure 3.11. The uncertainties of the heating rate are mainly from the uncertainties of the CH_4 profiles (see Figure 3.1) and the change of the orbital distances provided the eccentricity ~0.05. We estimated the cooling rate uncertainties from a Monte Carlo method based on the retrieval uncertainties in the area-weighted global-mean temperature profiles (Figures 3.2 and 3.4), for CIRS and IRIS respectively. In principle, the globally averaged cooling rate should be calculated as a global mean of the latitudinal cooling rate map (e.g., Figure 3.8). However, we found since the temperature does not vary too much with latitude, the calculation based on the area-weighted global mean temperature profile agrees well with the latitudinal mean of the 2-D cooling map. The difference is only

around 1%. Therefore there is no systematic error in this approach but on the other hand it saves a lot of computational time. Note that in our plot the cooling rate uncertainties should be interpreted as non-independent error bars, which from different pressure levels are correlated with each other. For example, the full lower-limit profile (left edge) of the yellow region in Figure 3.11 cannot be a solution of the stratospheric cooling rate in the Voyager era because it will not agree with the IRIS spectra.

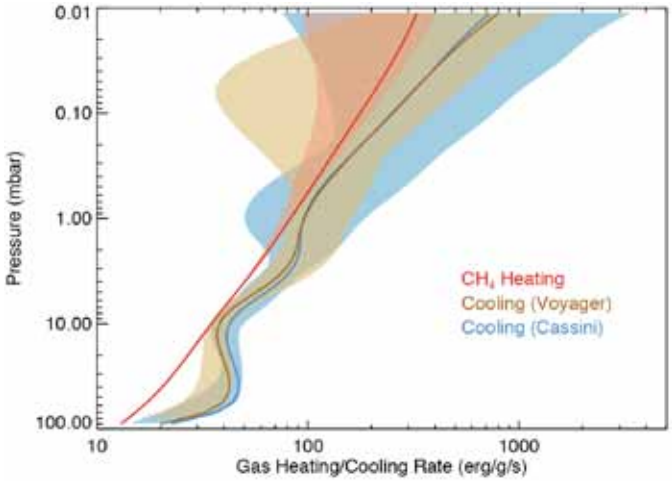

Figure 3.11. Instantaneous global energy balance plot of Jovian stratosphere in the Voyager and Cassini era. The blue and yellow shaded region shows the uncertainty range of the cooling rates, estimated from the error propagation method (Monte Carlo method) based on the CIRS and IRIS retrieval uncertainties in Figure 3.2 and 3.4, respectively. The red region shows the uncertainty of the global mean heating rate.

Below 10 mbar the globally averaged cooling rate in the Voyager era is generally smaller than the Cassini results, mainly arising from the temperature difference. The two cooling rates agree with each other in the region above 10 mbar. Between 1 and 10 mbar the heating rate appears to marginally touch the lower limits of the cooling rates. But in the lowest stratosphere region between 10 and 100 mbar, it is clear that the globally averaged heating rate does not match the either the CIRS or the IRIS cooling rate. The peak of the cooling rate is about 45 erg g^{-1} s^{-1}, larger than the heating rate by a factor of 2 at 50 mbar. In this region the cooling rate is simple because it is only dominated by the H_2-H_2 and H_2-He continua. In Yelle et al. (2001) it seems the difference between the heating and cooling

rates is smaller, mainly because they used a colder temperature from the Galileo temperature profile in the equatorial region. The temperature profile is only located at the coldest edge of the uncertainty range of our derived CIRS temperature profile in the lower stratosphere (Figure 3.1). The colder temperature could have two effects. First, it will locally decrease the Newtonian cooling effect, leading to a smaller cooling rate; Secondly, it will enhance the heating effect by hot troposphere below via the mutual flux exchange. Both effects would decrease the cooling rates. In fact in Yelle et al. (2001) the total cooling rate in the lower stratosphere is smaller than the CIA cooling rates, because after 20 mbar the hydrocarbon cooling rates drop rapidly with pressure and actually turn into the heating effect in the lower stratosphere and compensate the CIA cooling rates. There is no such phenomenon in our nominal case (Figure 3.6). In fact CH_4 also turns into heating below 30 mbar and does C_2H_6 below 70 mbar, but C_2H_2 has the cooling effect down to 100 mbar.

Could the globally averaged temperature derived from CIRS observations be too high? This is not likely because the H_2-H_2 CIA between 600 and 670 cm^{-1} is able to constrain the lower stratospheric temperature very well. We make a sanity check by making a sensitivity forward modeling test. Figure 3.12 shows that in order to match the heating rate in the lower region, the temperature from 10~100 mbar needs to be reduced by 10 K, which is not allowed by the CIRS spectra, otherwise the simulated TOA radiance will not even be close to the observations. This is illustrated using the equatorial region spectra as an example in Figure 3.12. Therefore our calculation suggests the lower stratosphere of Jupiter seems not in radiative equilibrium due to pure gas heating and cooling.

Above 1 mbar The CH_4 heating rate is contained within the cooling rate error bars mainly from the temperature uncertainties. However, since our nominal cooling rate profiles (solid lines in Figure 3.11) stand for the most probable solutions which produce the best fit of the CIRS and IRIS data, it suggests that there is also a possibility that the heating and cooling rates are not balanced in the lower pressure region either, not only the magnitude, but also the gradients (in the logarithmic coordinates). The heating rate approximately follows $\sim p^{-0.31}$, versus $\sim p^{-0.46}$ for the cooling rate. In the next section we make a theoretical

interpretation for the slopes, and explain why these are different under the nominal conditions.

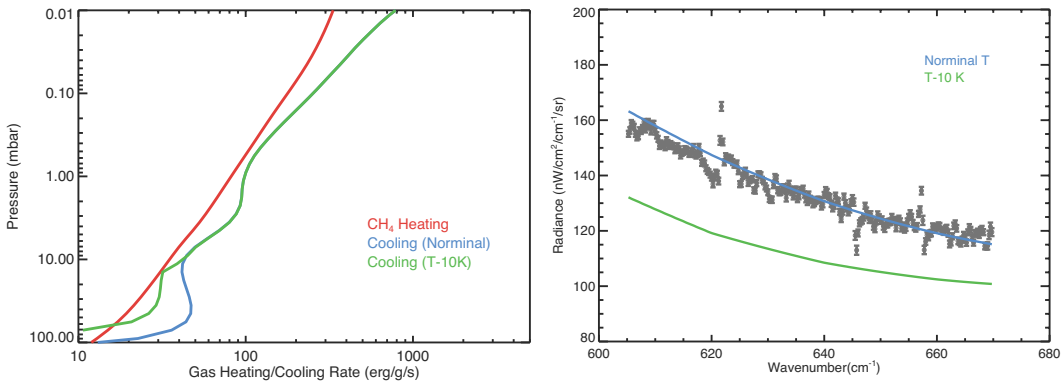

Figure 3.12. Sensitivity test of the CIRS cooling rate in the lower stratosphere. In order to match the gas heating rate, the lower stratospheric temperature needs to be decreased by ~10 K in the 10~100 mbar region (left panel). However, the colder temperature profile cannot explain the continuum data (in black) in the equatorial region (right panel).

3.4.3 Approximate Theory of Heating and Cooling Rates

The major heating and cooling agents are CH_4 and C_2H_6 in the stratosphere of Jupiter above 5 mbar, respectively. First we consider a simple 1-D diffusive-photochemical model of Jupiter below the homopause, where previous work suggested that CH_4 and C_2H_6 should be in the diffusive equilibrium since their loss timescales are much longer than the transport timescale (e.g., Moses et al. 2005). Without chemistry, the diffusion equation is

$$\frac{\partial \chi}{\partial t} - e^{\xi} \frac{\partial}{\partial \xi}\left(e^{-\xi} K(\xi) \frac{\partial \chi}{\partial \xi}\right) = 0. \tag{3.7}$$

Here we use a dimensionless coordinate $\xi = ln(p_s/p)$, where p is pressure and p_s is the reference pressure. χ is the mixing ratio of the tracer. $K(\xi) = K_0 e^{\gamma \xi}$ is the parameterized eddy diffusivity. For Jupiter, γ~0.5-0.6 (see Figure 3.7 in Moses et al. 2005), which is also close to the theoretical prediction based on the wave-breaking turbulent mixing process (Lindzen 1981). In steady state, $\partial \chi / \partial t = 0$. The solution is

$$\chi(\xi) = C_1 + C_2 \frac{e^{(1-\gamma)\xi}}{K_0(1-\gamma)}, \tag{3.8}$$

where C_1 is the lower boundary value (deep source term) and C_2 contains the diffusive flux (diffusion term). In fact CH_4 and C_2H_6 are two extremes of this solution. CH_4 originates from the deep atmosphere, so the deep source term is much larger than the diffusion term. Therefore it has a constant mixing ratio profile all the way up to the homopause. On the other hand, since the source of C_2H_6 is from the upper stratosphere due to CH_4 photolysis, the deep source term is nearly zero, so the diffusion term dominates and the mixing ratio profile of C_2H_6 behaves as $\chi \propto p^{(\gamma-1)}$. Integrated with pressure, the column densities from the top of the atmosphere to the pressure level p are proportional to p for CH_4 and p^γ for C_2H_6, respectively.

We also simplify the cooling rate calculation from the Newtonian cooling approximation, which is not bad above 1 mbar (Figure 3.6). The cooling rate is approximately

$$\overline{H_{cool}}(p) \sim -\frac{2\pi g d\bar{\tau}}{dp} B_\nu(\bar{\tau}) E_2(\bar{\tau}), \tag{3.9}$$

where $\bar{\tau}$ is the averaged opacity, which is related to the equivalent width. In the stratosphere, since this band is relatively weak (mean opacity $\bar{\tau}$~0.1 at 100 mbar), we can neglect the broadening effect, so the mean opacity of the C_2H_6 ν_9 band is proportional to its column density and behaves as $\bar{\tau} \propto p^\gamma$. The mean opacity is small in the stratosphere, so $E_2(\bar{\tau})$ is approximately constant, or within the same order of magnitude. Provided that the Jovian stratosphere is roughly isothermal, $B_\nu(\bar{\tau})$ is constant (Figure 3.7). Therefore,

$$\overline{H_{cool}}(p) \propto \frac{d\bar{\tau}}{dp} \propto p^{(\gamma-1)}. \tag{3.10}$$

Since C_2H_6 is the major coolant, the slope of cooling rate in the logarithmic coordinate should be close to $(\gamma - 1)$~0.4-0.5, consistent with -0.46 from our numerical model.

The same argument in fact also applies to the region (below 10 mbar) where the H_2-H_2 CIA dominates the cooling rate[§]. For the collisional induced absorption, $\bar{\tau} \propto p^2$, therefore,

[§] Only qualitatively since the Newtonian cooling approximation is not very good in the lower stratosphere, but the physical basis is similar.

$\overline{H_{cool}}(p) \propto p$. That is why the cooling rate by H_2-H_2 CIA in Figure 3.6 drops with altitude, and it affects the total cooling rate slope below 10 mbar (Figure 3.11). At the very bottom region at nearly 100 mbar, the cooling rate increases with altitude due to the strong temperature inversion above the tropopause.

On the other hand, the heating rate due to CH_4 is from its several NIR bands. The line strengths of those bands decrease as function of wavelength. The curve of growth theory (Goody and Yung 1995) predicts the equivalent width, or the related average opacity $\bar{\tau} \propto p$ for weak bands, but $\bar{\tau} \propto p^{1/2}$ for strong bands because the pressure broadening effect cannot be neglected. If we again neglect the $E_2(\tau_\nu)$ term in the heating rate expression:

$$\overline{H_{heat}}(p) = \frac{1}{2} F_\nu E_2(\tau_\nu) \frac{g d\bar{\tau}}{dp}. \tag{3.11}$$

We expect that the heating rate from the CH_4 weak bands, such as its 1.1 and 1.3 μm bands, should be roughly constant ($d\bar{\tau}/dp \sim constant$); while that from its strong bands, such as the 3.3 and 7.6 μm bands, should behave as $\overline{H_{cool}}(p) \propto p^{-1/2}$. If the $E_2(\tau_\nu)$ term is not neglected, the slope is slightly steeper for the strong bands. For the moderately strong bands, such as the 1.7 and 2.3 μm bands, the heating rate slopes fall within the two limits. This is consistent with the plot of band integrated heating rates (Figure 3.10). The slope of the total heating rate should lie between -0.5 and 0. This is also consistent with our numerical model results (-0.31).

Therefore, in an ideal case, the heating rate profile from the CH_4 absorption is not likely to balance the cooling rate profile in the stratosphere from 5 to 0.1 mbar, provided all of the above assumptions are valid. The critical assumptions here are (i) isothermal atmosphere and (ii) idealized C_2H_6 profile by certain eddy transport processes. If (1) the temperature profile is not isothermal, i.e., slightly decreasing with altitude; or (2) the eddy diffusivity profile increases faster than $p^{-(0.5-0.6)}$, balance between the gas heating and cooling rates is still possible. However, current observations are not able to reject those hypotheses.

3.4.4 Possible Heating Sources

Besides the CH_4 heating, there are two other possible heating sources in the stratosphere. The first one is due to gravity wave breaking. The temperature fluctuations observed by the Galileo probe were interpreted as breaking gravity waves in both the thermosphere (e.g., Young et al. 1997) and stratosphere (e.g., Young et al. 2005). The wavy structures are also observed in the low latitudes in the recent high-resolution TEXES data (Greathouse et al. 2011). Gravity wave breaking could directly convert the damped energy into heat as well as cause the transport of potential temperature that might heat or cool the local atmospheric layers (Strobel et al. 1985). Whether the net effect is heating or cooling is critically dependent on the eddy Prandtl number (*Pr*), which measures the relative magnitude of the momentum diffusion versus thermal diffusion. The heating rate is proportional to the eddy thermal diffusion coefficient, which should be equal to the eddy diffusion coefficient of long-lived chemical species (Strobel et al. 1985), for instance, the eddy diffusivity used in the 1-D photochemical model in Moses et al. (2005).

There is a possible relationship between the gas cooling rate and gravity wave heating rate. In an ideal situation, we assume the cooling rate in an atmosphere is dominated by a secondary photochemical product, which is chemically inert but radiatively active, such as C_2H_6 in the stratosphere of Jupiter. First, from the theory of Lindzen (1981), the eddy diffusivity produced by the damped gravity waves should behave as a function of pressure: $K_{zz} \propto p^{-0.5}$. Using this eddy profile, in section 3.4.3 we predicted the mixing ratio profile of the coolant to scale as $\chi \propto p^{0.5}$. From our approximate cooling rate theory (section 3.4.3), the cooling rate in the atmosphere would behave as $\overline{H_{cool}}(p) \propto p^{-0.5}$. On the other hand, if the eddy Prandtl number is large, the damped gravity waves would also heat the atmosphere, with the heating rate $Q \propto K_{zz} \propto p^{-0.5}$. Therefore, the slopes of the gravity wave heating rate and the gas cooling rate would be naturally the same, although the magnitude of the gravity wave heating would depend on the details of the thermal energy conversion rate, stability of the atmosphere, etc.

The above argument is actually very close to the real situation in the Jovian stratosphere. Young et al. (2005) estimated that if *Pr* is larger than 1.7, the wave breaking will heat the stratosphere of Jupiter for the pressure level above 1 mbar, and the heating rate dur to wave breaking could be comparable to the cooling rate in Yelle et al. (2001). Using the magnitude estimate from Young et al. (2005) and the natural correlation between the slopes of the gravity wave heating rate and the gas cooling rate, we conclude that the heating from the gravity wave breaking might be important, and may help solve the seemingly imbalance above 1 mbar, if there is any.

The second possible heat source is aerosol. The heating effect due to stratospheric aerosols is potentially important around 10 mbar or below, especially in the polar regions, as shown by previous study by West et al. (1992). However, other studies (Moreno and Sedano 1997; Yelle et al. 2001) found that the aerosol heating can be negligible, at least in the visible region. A strong heating by the polar haze layer not only affects the total global energy balance, it might also induce a radiation-driven circulation from the poles to the midlatitudes (West et al. 1992). Unlike the large uncertainty and the potential observational difficulty of the gravity wave properties, it is possible to quantify the aerosol heating rate from the currently available measurements. To do this requires a high-resolution spatial map of the stratospheric aerosols in both vertical and latitudinal coordinates, which is beyond the scope of this paper. In chapter IV, we retrieve the distributions of the aerosols and clouds based on the high-resolution images from Cassini Imaging Subsystem (ISS). We will provide a detailed discussion on the latitudinal distribution of the heating rate from the gas and aerosols and their effects on the radiative budget, and from that we complete the picture of radiative forcing in the stratosphere of Jupiter.

3.5. Summary and Discussion

In this study, we developed a line-by-line heating and cooling rate model for the stratosphere of Jupiter, based on two complete sets of global maps of temperature, C_2H_2 and C_2H_6 retrieved from the Cassini and Voyager observations in the latitude and vertical plane, with a careful error analysis. The data quality limits our information below 0.1 mbar,

above which we estimate the atmospheric profiles from previous measurements and photochemical model results. We found that the non-LTE effect is not important on the thermal cooling rate below 0.01 mbar. The cooling rate increases from ~20 erg g^{-1} s^{-1} at 100 mbar to ~45 erg g^{-1} s^{-1} at 50 mbar, primarily due to the stratospheric temperature inversion, and then decreases from 50 mbar to ~35 erg g^{-1} s^{-1} at 10 mbar due to the unique quadratic dependence of the H_2-H_2 CIA absorption coefficient on pressure. Above 10 mbar, the hydrocarbons, especially C_2H_6, are the primary cooling agents. The cooling rate slope increases as $\sim p^{-0.46}$, with a value of ~100 erg g^{-1} s^{-1} at 1 mbar to ~800 erg g^{-1} s^{-1} at 0.01 mbar. C_2H_2 cooling might dominate the 0.01-0.001mbar, and CH_4 dominates the region above due to the rapid falloff of C_2H_2 and C_2H_6 abundances. CH_4 also contributes to the local cooling effect at ~5 mbar due to its pressure broadened wings. The 2-D cooling rate maps are influenced primarily by the temperature structure, and also by the meridional distributions of C_2H_2 and C_2H_6. The QQO-type thermal structure at the 1 mbar level in the Cassini data and the strong C_2H_6 latitudinal contrast in the Voyager era are the two most prominent features influencing the cooling rate patterns.

The stratospheric cooling rate seems larger in the Cassini era than in the Voyager era, in the global average sense. This is mainly due to the temperature difference. The total emitted powers in our nominal models are ~14.2 W m^{-2} for the Cassini era and ~13.5 W m^{-2} for the Voyager era. Compared with the direct integral results from Li et al. (2012), 14.10$\pm$0.02 W/m^2 for Cassini and 13.59$\pm$0.14 W m^{-2} for Voyager, our Cassini values are slightly larger but the Voyager values are within the uncertainty range. The outgoing longwave radiation is mainly from the troposphere around 300-400 mbar (Li et al. 2012). Since our retrieval model only considers the spectra beyond 600 cm^{-1}, although the information is enough for the stratosphere, it may not be enough to accurately retrieve the temperature structure at 300~400 mbar. The spectra in the longer wavelengths might be needed. But it seems that the Jovian temperature is systematically warmer during the Cassini era than in the Voyager era, not only in the troposphere, but also in the stratosphere. This 2-3 K difference between 10~100 mbar causes ~5 erg g^{-1} s^{-1} difference in the local cooling rates.

The heating rate is primarily due to the solar flux absorption by the NIR CH_4 bands. The heating rate profile approximately follows ~$p^{-0.31}$, which is a mixing effect from the NIR strong bands ($\sim p^{-0.5}$) and weak bands (almost constant with pressure). Our calculation shows that the globally averaged gas heating and cooling rates are not balanced, clearly in the lower stratosphere under 10 mbar, and possibly in the upper stratosphere above 1 mbar. We think that different temperature profiles or different gas mixing ratio profiles within the current allowed uncertainty range above 1 mbar might lead to a better agreement between the gas heating rate and cooling rate. However, that is not an acceptable solution to the lower stratospheric heat imbalance because it will violate the observations. Therefore we suspect there might be a missing heating source in the lower stratosphere of Jupiter. We have discussed two possible solutions, either from the gravity wave breaking, or aerosol heating.

Here we propose a possible alternative explanation. Noting that the seasonal change of total solar flux can reach 20% due to the orbital eccentricity, and the observed temporal variation of the temperature is large, about 6 K in 3 years in midlatitudes and 8 K in 2 years in the lower latitude (Simon-Miller et al. 2006), it was thought the lower stratospheric temperature is not purely radiatively controlled (Conrath et al. 1990; Simon-Miller et al. 2006; Nixon et al. 2007). So it is also possible that this imbalance is a natural behavior of instantaneous radiative forcing since the energy storage may result a time lag. To further elaborate the details, we calculated the radiative relaxation timescale, or radiative time constant, τ_{rad}, in the Jovian stratosphere, defined as

$$\tau_{rad}(p) = \frac{C_p dT}{d\overline{H_{cool}}(p,T)}, \tag{3.12}$$

which is numerically calculated from the change of cooling rate when the local temperature is changed by 1 K in this study.

Here we crudely estimate τ_{rad} as function of pressure analytically. We use the approximate cooling rate expression, i.e., Equation (3.1). The only temperature dependence is from the Planck function, $B_\nu(T)$, in which we assume the stimulated emission term,

$1-\exp(-hc\nu/k_bT)\sim1$, where h is Planck constant, c is the speed of light, k_b is Boltzmann constant, and ν is wavernumber. This is a fairly good approximation, for example, for 850 cm^{-1} and $T\sim170$ K, $1-\exp(-hc\nu/k_bT)\sim0.9993$. Take the temperature derivative of $B_\nu(T)$

$$\frac{dB_\nu(T)}{dT}\sim\frac{hc\nu}{k_bT^2}B_\nu(T). \tag{3.13}$$

We obtain

$$\tau_{rad}(p)\sim\frac{C_pk_bT^2}{2\pi ghc\nu\frac{d\bar{\tau}}{dp}B_\nu(\bar{\tau})E_2(\bar{\tau})}\propto\left(\frac{d\bar{\tau}}{dp}\right)^{-1}. \tag{3.14}$$

Therefore, it appears that the radiative relaxation timescale is inversely proportional to the cooling rate when the optical depth does not strongly depend on the temperature, which is intuitively correct. Above 10 mbar, ethane is the major coolant, $d\bar{\tau}\propto p^{1/2}$, so $\tau_{rad}(p)\propto p^{1/2}$. Below 10 mbar, H_2-H_2 CIA dominates, $d\bar{\tau}\propto p^2$, so $\tau_{rad}(p)\propto p^{-1}$. Therefore, qualitatively, the radiative time constant should increase from 100 to 10 mbar and decrease with pressure above 10 mbar.

Following the convention by Conrath et al. (1990), we represent the radiative timescale in units of orbital phase timescale, or reciprocal of the orbital frequency, $2\pi/\tau_{orb}$, where τ_{orb} is the orbital period of Jupiter (~3.7×10^8 s). In Figure 3.13, we compared the timescales of radiative relaxation, vertical eddy transport, and the chemical loss of C_2H_2 and C_2H_6. The globally averaged radiative relaxation timescale is calculated based on the Cassini results. The other timescales are from the 1-D photochemical model by Moses et al. (2005).

With the updated temperature profile and gas abundances, the radiative relaxation timescale calculated in our work is significantly different from the results from Conrath et al. (1990). First, in the upper stratosphere above 3 mbar, τ_{rad} is less than 1, while in Conrath et al. (1990), τ_{rad} in the whole stratosphere is much longer than a season. Secondly, the relaxation timescale becomes shorter as the altitude gets higher, showing that the radiative control is more and more important in the upper stratosphere. This trend is just

the opposite to the result from Conrath et al. (1990), who found that the temperature response should be slower with altitude. As our simple derivation shows, a decreasing trend of τ_{rad} seems more natural in the upper stratosphere, and that the τ_{rad} peaks at ~10 mbar is from the transition between the hydrogen cooling region and the ethane cooling region**.

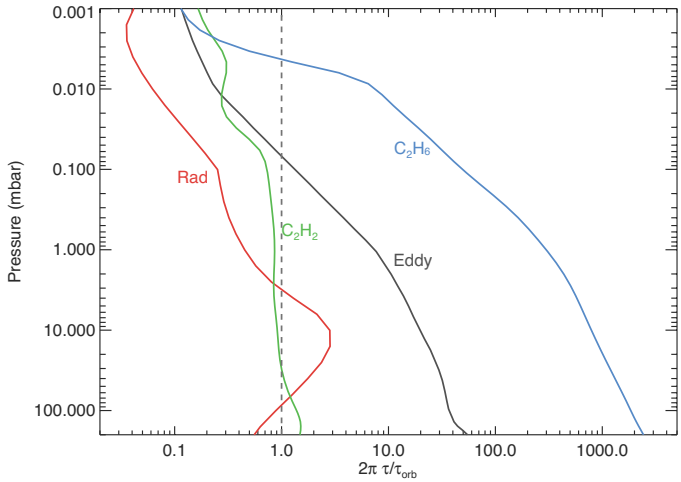

Figure 3.13. Timescales of the radiative relaxation, vertical eddy transport, and the chemical loss of C_2H_2 and C_2H_6, in unit of the orbital phase timescale of Jupiter.

It seems the large relaxation timescale in the lower stratosphere supports our hypothesis that there should be a seasonal lag. However, the reality might be more complicated. Simon-Miller et al. (2006) computed the cross correlation between the hemispheric contrast and sub-solar latitude for both the troposphere and stratosphere, and found that the temperature hemispheric asymmetry is nearly in phase or slightly lag behind the isolation change, as also pointed out by Nixon et al. (2007). In this work, a simple phase lag model

** It is not appropriate to interpret our results from a commonly used expression of radiative relaxation timescale: $\tau_{rad}(p) \sim \frac{pC_p}{4g\sigma T^3}$, which is suitable only at the optical depth unity level. In the equation (3.14), if $d\bar{\tau} = 1$, and let $dp = p_{\tau=1}$, we obtain $\tau_{rad}(p) \sim p_{\tau=1}$. It stands only for an averaged radiative timescale for the entire atmosphere, but not for the relaxation timescale for any pressure level. Therefore it should not be used to interpret the increasing/decreasing trend of radiative timescale as a function of pressure in our results.

(linear response, $\tan^{-1}(2\pi\,\tau_{rad}/\tau_{orb})$) predicts the phase lag would be 65° at ~20 mbar. Therefore, although in our work the isolation effect is larger than the previous work (e.g., Conrath et al. 1990), it seems still not enough to explain the puzzle of the temperature response in Jovian stratosphere. In any sense, mechanical forcing and horizontal energy advection seems play a significant role in the lower stratosphere. On the other hand, the phase lag is ~15° at 1 mbar, and even smaller above, showing that the isolation might dominate the seasonal variations in the upper stratosphere.

The chemical loss timescale of C_2H_2 is close or slight smaller than the orbital phase timescale, and greatly shorter than the eddy transport timescale. This implies the C_2H_2 latitudinal distribution might be influenced by the insolation pattern, which dominates the photolysis of C_2H_2. Although the effect might not be significant, because the photolysis products of C_2H_2, i.e., C_2 and C_2H, would be effectively recycled back to C_2H_2 via reacting with H_2 and CH_4, in a very short timescale (Moses et al. 2005). On the other hand, C_2H_6 is a long-lived species. Therefore its distribution is modulated by the long-timescale transport processes and may have a very large phase lag to the insolation pattern or even uncorrelated. Therefore, the larger latitudinal contrast in the Voyager C_2H_6 map should not be interpreted as the direct effect of the stronger latitudinal transport during the Voyager era, although this C_2H_6 pattern would further enhance the latitudinal contrast of the cooling rate in the stratosphere of Jupiter, and might lead to a more efficient advection. However, whether the stratospheric circulation on Jupiter is induced by the differential heating or the underlying mechanical forcing is still on debate (e.g., Conrath et al. 1990; West et al. 1992).

Chapter IV

Radiative Forcing of the Stratosphere of Jupiter, Part II: Effects of Aerosol and Cloud[††]

Darkness was there. All wrapped around by darkness, and all was Water indiscriminate. Then that which was hidden by Void, that One, emerging, stirring, through power of Ardor, came to be.

—*Nasadiya Sukta, Ancient India*

Summary

We retrieved the global distributions of stratospheric aerosols on Jupiter based ground-based NIR spectra and multiple-phase-angle images from Cassini Imaging Science Subsystem (ISS). The polar haze layer is located at ~10-20 mbar, higher than the middle and low latitudes (~50 mbar). The Mie sphere particles are mainly located in the low latitudes around between 40° S and 25° N with a radius between 0.2 and 0.5 μm. The rest of the stratosphere is covered by the fractal aggregated particles composed of ~0.01 μm monomers. The number of the monomers ranges from ~2000 in the middle latitudes to about 600-800 in the polar region. The derived imaginary part of the refractive index is about 0.02 in the UV filter and 0.001 in the near-infrared (NIR) filters. The column densities of the aerosols are ~10^7 cm^{-2} at the low latitudes and ~10^{10} cm^{-2} in the high latitudes. About 0.6-0.7 W/m^2 of the incoming solar flux is absorbed by stratospheric aerosols and CH_4 in the optical wavelength. The aerosol heating rate is roughly equivalent to the gas heating rate due to the CH_4 NIR bands in the lower stratosphere. Two-dimensional net heating rate map shows that the local heating at poles significantly changes the latitudinal distribution of the net radiative energy and possibly drives a stratospheric

[††] To be submitted as: Zhang X., West, R.A., Banfield, D., Yung, Y.L., 2012. Radiative forcing of the stratosphere of Jupiter, part II: effects of aerosol and cloud.

circulation in the high latitudes.

4.1. Introduction

In the previous chapter (chapter III), we obtained the cooling rate for the stratosphere of Jupiter based on the spatially resolved Voyager and Cassini observations, and found that the globally averaged CH_4 heating and gas cooling rates are not balanced, especially in the region from 10 to 100 mbar. Although the breaking of gravity waves might be an important heat source, it is likely to heat the stratosphere only above 1 mbar (Young et al. 2005), and its heating rate is hard to quantify because the properties of the gravity waves are largely unknown. The other possible heat source, stratospheric aerosols, is relatively easier to investigate. To evaluate the stratospheric aerosol heating rate and its effect on the local and global radiative budget, three crucial pieces of information are required: (1) the latitudinal and vertical distribution of aerosols; (2) the optical properties of the aerosols, such as the optical depth, single scattering albedo, phase function, etc., for the entire wavelength range from ultraviolet (UV) to the near-infrared (NIR) region; (3) the properties of the tropospheric hazes and clouds and their effects on the stratospheric heating rate.

Two previous attempts have been made to retrieve the global map of haze and clouds on Jupiter. Banfield et al. (1998) assumed the single scattering nature of aerosol layers in the *H* and *K* band spectra, and successfully retrieved the latitudinal and vertical distributions of stratospheric and tropospheric hazes covering the entire southern hemisphere and northern equatorial region below $25° N$. They discovered the low-latitude stratospheric haze layer is located at ~50 mbar and its altitude level increases sharply to ~20 mbar in the high latitudes (polar hood). The tropospheric haze top is around 0.2 bar and is non-uniform with latitude. The hazes are relatively clear in the tropopause region, which is unexpected from the previous model (Kaye and Strobel 1983). Recently, Kedziora-Chudczer and Bailey (2011) used a line-by-line multiple scattering radiative transfer model to simulate much higher resolution spectra. Their data cover the entire disk of Jupiter. Assuming a 1.3 μm particle layer in the troposphere and a 0.3 μm particle in the stratosphere, they are able to explain

the data, and their results are generally consistent with Banfield et al. (1998), except that another distinct haze layer is discovered around 5 mbar in the higher latitudes.

Many previous studies focused on the aerosol properties in the UV and visible range, from various data sources such as the intensity measurements from spacecraft (e.g., *Pioneer 10* in Tomasko et al. 1978 and *Voyager* in Hord et al. 1979), space-based telescopes (e.g., Tomasko et al. 1986), and ground-based telescopes (e.g., West 1979), and polarization measurements (e.g., Smith 1986). Please see the review in West et al. (2004) for details. Generally speaking, the low latitude aerosols are composed of small particles with radii between 0.2-0.5 μm (Tomasko et al. 1986), while the high latitude aerosols are more complicated. It was proposed that the high-latitude particles are fractal aggregates (West and Smith 1991) in order to explain both the positive polarization (Smith 1986) and the modest forward scattering (e.g., Tomasko et al. 1978). However, there is no study that further investigates the details of the aggregates, such as the monomers radius, the number of monomers, fractal dimension, and refractive index, etc. On the other hand, some studies on the polar aerosol and clouds (e.g., Moreno 1996; Barrado-Izagirre et al. 2008) still focus on the small particles (<0.1 μm) to explain the low phase angle images, although small particles in fact are not consistent with high phase angle data (Rages et al. 1999).

Previous studies on the aerosol heating rate are not consistent with each other. Based on the latitudinal distribution of aerosols from the observations by Voyager and International Ultraviolet Explorer (IUE), West et al. (1992) calculated the first aerosol heating rate map in the stratosphere of Jupiter and found that the aerosol heating effect is so large, especially at the polar region, that it might drive a circulation from the poles to the midlatitudes. However, Moreno and Sedano (1997) derived the aerosol properties based on a microphysical model and the Hubble Space Telescope (HST) images. They found the aerosol heating rate is significantly smaller than that in West et al. (1992), especially in the northern polar region. However, the vertical profile of Jovian stratospheric aerosol was not well determined until Banfiled et al. (1998). Now we know the derived aerosol vertical profile from the NIR spectra (Banfield et al. 1998) differs significantly from the

microphysical model results in Moreno and Sedano (1997). Since the nature of the fractal aggregates has not been revealed, both the sub-micron Mie particles in West et al. (1992) and the tiny particles (<0.1 μm) in Moreno and Sedano (1997) are not consistent with the observations as we discussed in the previous paragraph. In light of the observations by Banfield et al. (1998), more work on aerosol heating is justified.

In this study we will revisit the ground-based NIR spectra in Banfield et al. (1998). We updated the methane absorption coefficients in the original retrieval model and relax the previous assumptions, from which the updated stratospheric aerosol distributions are obtained. The aerosol and cloud properties will be retrieved based on the images from the Imaging Subsystem (ISS) onboard Cassini during its Jupiter flyby in the late 2000 and early 2001. We will combine the low, middle and high phase angle images together to accurately characterize the size, shape and phase functions of stratospheric hazes. This approach is similar to the *Pioneer* data analysis in the blue and red channels by Tomasko et al. (1978), except that we now consider the Mie particles in the low latitudes and fractal aggregates in the high latitudes. Based on those results, our aerosol heating rates are consistent with observations.

This chapter is structured as follows. In section 4.2 we will revisit the NIR ground-based measurement by Banfield et al. (1998) and retrieve the stratospheric aerosol distributions. In section 4.3 we develop a retrieval model for the aerosol properties from Cassini ISS images in the UV and NIR filters. The stratospheric aerosol heating rates are derived in section 4.4, with a discussion on the impact of aerosol heating on the global and local radiative budget, followed by conclusions in section 4.5.

4.2. Retrieval from NIR Spectra

The NIR spectra used in Banfiled et al. (1998) and revisited in this study were taken in August 14 1995, from the 200-inch Hale telescope at Palomar observatory. The spectra were obtained in broadband *H* (1.45-1.8 μm) and *K* (1.95-2.5 μm) telluric windows, with

the spectral resolution ~100, covering from 25° N to the south pole (~80° S) of Jupiter. Since the aerosol optical depth is small in the H and K bands, Banfield et al. (1996) developed a direct retrieval technique based on the single-scattering approximation for the NIR spectra, under which the radiative transfer inversion problem is linear. Therefore a simple and effective retrieval technique can be applied to minimize the difference between the simulated spectra and the observations in the least-square sense, with a Tikhonov-type regularization term in the cost function to smooth the inverted profiles. A two-point Gaussian correlation matrix is used as the smoothness constraint, mathematically similar to the covariance matrix in the retrieval method developed by Rodgers (2000) based on Bayesian theory (used in chapter III). But Banfield's method does not require any *a priori* information. The retrieval result is called f value, which is, in principle, proportional to the product of phase function, cross section, single scattering albedo and mixing ratio of the particles. In the entire spectral region, any pixel with reflectivity (I/F) greater than 0.075 was removed to make sure the single scattering approximation is robust. See Banfield et al. (1996; 1998) for details of the observations, calibrations and the inverse model.

Banfield et al. (1996) assumed the retrieved f value is constant with wavelength. Banfield et al. (1998) relaxed the assumption by incorporating the spectral shape of the aerosol extinction efficiency, but still assumed a constant particle size of 0.3 μm with latitude and altitude. In this study, we further improve this retrieval technique by (1) updating the CH_4 absorption coefficient, and (2) allowing the aerosol size to be varied with latitude.

We use the *correlated-k* method to calculate the atmospheric transmission. Although the line-by-line (LBL) CH_4 absorption coefficients have been greatly improved in recent years (chapter III), to date the CH_4 line database is still incomplete for the visible region and NIR bands shorter than ~1.6 μm (Karkoschka and Tomasko 2010). The optimization solvers for the aerosol retrieval are usually computationally expensive. Therefore LBL calculation is not appropriate. On the other hand, the *correlated-k* calculation is accurate enough for the NIR low-resolution spectra and broadband filters for Cassini ISS images. Irwin et al. (2006) improved the NIR CH_4 *correlated-k* table for variety of temperature and pressure

grids based on the laboratory measurements. Recently, Karkoschka and Tomasko (2010) constructed the updated *correlated-k* data for both visible and NIR CH_4 bands, based on the laboratory data and observed spectra from the Huygens probe on Titan and Hubble Space Telescope observations. Those CH_4 absorption data seem more reliable for the spectroscopic analysis on giant planets. In this study we adopt the *correlated-k* data from Karkoschka and Tomasko (2010). The upper panel of Figure 4.1 shows the total optical depth of CH_4 and H_2-H_2 collisional induced absorption (CIA) from the top of the atmosphere to 100 mbar. The old CH_4 coefficients in Banfield et al. (1998) generally overestimate the CH_4 opacity and the band shapes are also slightly different. The H_2-H_2 CIA data are obtained from Borysow (2002).

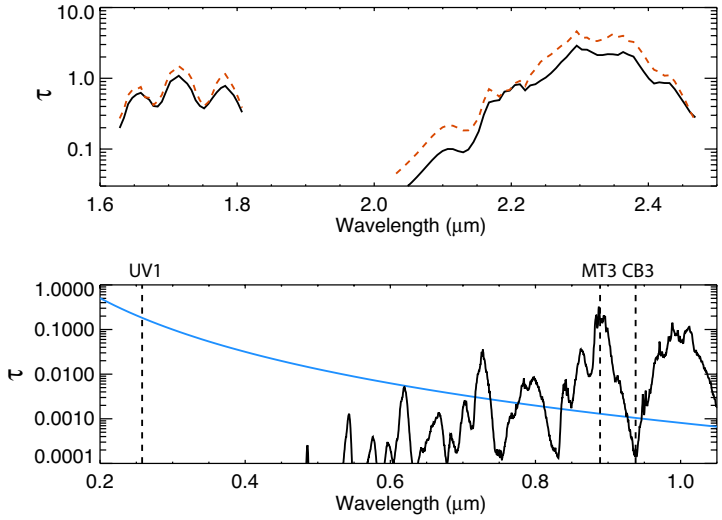

Figure 4.1. Total gas optical depth including CH_4 and H_2-H_2 CIA at 100 mbar. Upper panel shows the difference between the results based on the old *correlated-k* coefficients (red dashed curve) used in Banfield et al. (1998) and the new data (black solid curve) from Karkoschka and Tomasko (2010) for the *H* and *K* bands in the NIR region. Lower panel shows the comparison between the CH_4 optical depth (black) and Rayleigh scattering optical depth (blue) from 0.2 to 1.0 μm. Three dashed lines correspond to the ISS filters used in this study, CB3 (0.938 μm), MT3 (0.889 μm), and UV1 (0.258 μm), respectively.

Banfield et al. (1998) found the spectra are actually not very sensitive to the particle size. This is generally true except for the polar region. Figure 4.2 compares the two optimized

solutions based on the prescribed 0.3 and 0.7 μm aerosols for 70° S and the equator. The equatorial spectrum is relatively insensitive to the particle size. However the 0.3 μm particle fails to fit the polar region spectrum below 2.1 μm, while the 0.7 μm particle is able to reproduce the observations. Qualitatively the slope of the spectra relies on the size parameter change of the Mie particles, defined as $2\pi r/\lambda$, where r is the aerosol radius and λ is the wavelength. For the 0.3 μm particle, from 1.7 to 2.4 μm, the size parameter decreases from 1.1 to 0.78, while that of the 0.7 μm particle decreases from 2.6 to 1.8. Provided the refractive index in this region 1.4+0i (assumed constant with wavelength, Banfield et al. 1998), the scattering efficiency drops about a factor of 4 for the 0.3 μm particle and only a factor of 3 for the 0.7 μm particle from 1.7 to 2.4 μm. This steeper slope from the smaller particles leads to a brighter H band than the larger particles, if both can match the K band data.

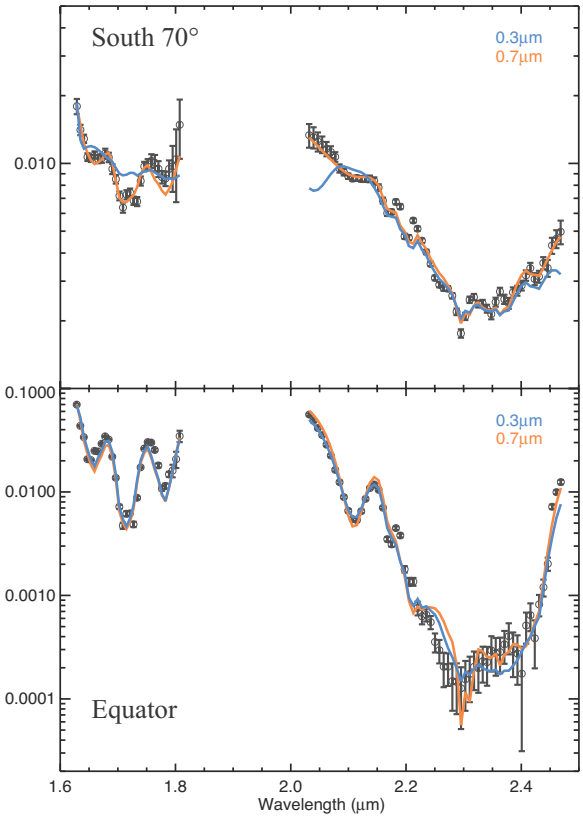

Figure 4.2. Comparison of the best solutions with the prescribed 0.3 and 0.7 μm particles, for 70° S (upper panel) and the equatorial region (lower panel), respectively. The observed spectra from Banfield et al. (1998) are shown in black with error bars.

Based on the above experiment, we improve the retrieval technique by varying the aerosol size with latitude. Through a grid search method, the optimal solution for each latitude can be obtained. The observations require larger particles (>0.6 μm) in the polar stratosphere (poleward beyond 60° S), but in the other regions the spectra are not able to distinguish between the larger and smaller particles. One of the solutions in Rages et al. (1999) from the analysis of the Galileo measurements in the north polar region (60° N) is 1.3 μm particle radius at 1 mbar level, which seems consistent with our solution for the south polar region, although one can ask a question that whether these large particles are sustainable in the 1 mbar region or higher (Rages et al. 1999). An alternative solution by Kedziora-Chudczer and Bailey (2011) is a two-mode haze model, in which they assume the lower layer (tropospheric haze or cloud) is composed of the 1.3 μm particles and the upper layers (stratospheric haze) is composed of the 0.3 μm particles. They have a much higher resolution spectra and their line-by-line forward model fitting procedure is able to match the data. Therefore the 0.7 μm particle size in the polar region may be an average of the mixture of the 1.3 μm tropospheric haze and 0.3 μm stratospheric particle size although our broadband data could not tell the difference.

The retrieved aerosol map (*f* value) is shown in Figure 4.3. This map generally agrees with the result from Banfield et al. (1998), except the aerosol layers are shifted slightly downward. This is because the new CH_4 absorption coefficients are slightly smaller than the old ones. The location of the haze layer increases from about 50 mbar at equator to above 20 mbar at the south pole. The haze layers are found concentrated within one or two scale heights. Note that this map shows a clear region around the tropopause (~100 mbar), consistent with Banfield et al. (1998). It is contrary to the hydrazine photochemical model results by Kaye and Strobel (1983). It might be attributed to a deep source in the troposphere without strong upward transport or the fast fallout of heavy particles around the tropopause region, but a satisfactory physical explanation is still lacking (Banfield et al. 1998). The clear region is also found by Kedziora-Chudczer and Bailey (2011). The locations of the haze layers in their selected band and zones are generally consistent with our results, although they do not provide detailed latitudinal and vertical aerosol profiles.

Kedziora-Chudczer and Bailey (2011) also found some very high stratospheric haze layer above 10 mbar that is beyond our sensitivity region.

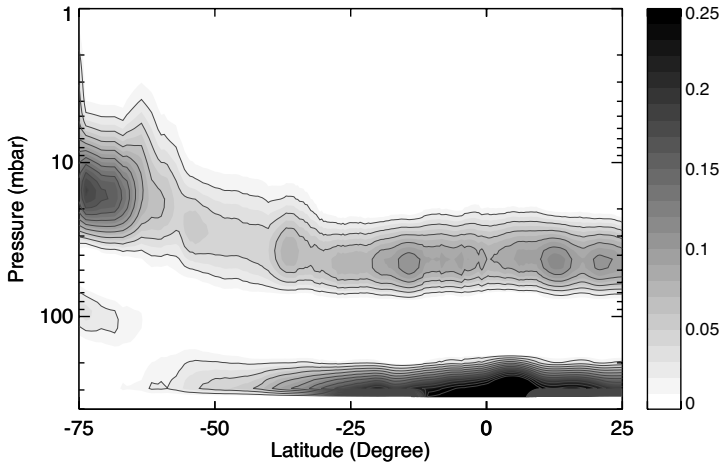

Figure 4.3. Retrieved aerosol map (*f* value) in the stratosphere and upper troposphere of Jupiter.

4.3. Retrieval from Cassini Images

4.3.1. ISS data Description

The ISS onboard Cassini acquired ~26000 high-quality time-lapse images of Jupiter during its six-months-long flyby from 1 October 2000 to 22 March 2001 (Proco et al. 2003). A proper combination of the images from different filters can be used for a specific purpose. For example, the methane channels and corresponding continuum filters (e.g., MT1/CB1, MT2/CB2, MT3/CB3) provide vertical structure information of the atmospheric aerosols and clouds. The UV1 filter samples the upper troposphere and stratospheric haze layer. Furthermore, Cassini ISS provides images from low to high phase angles, which contain valuable information of the phase functions of the stratospheric particles and from that we are able to characterize the particle shape and optical properties, as shown by previous studies, e.g., Tomasko et al. (1978) for the *Pioneer* data and Rages et al. (1999) for the *Galileo* data.

We are trying to simultaneously retrieve the aerosol and cloud information by combining the low phase angle, middle phase angle and high phase angle images for the three Cassini ISS filters CB3, MT3 and UV1 channels. They are located near the two ends of our wavelength range from NIR to UV for the heating rate calculation. The lower panel of Figure 4.1 shows the CH_4 and Rayleigh scattering optical depth at 100 mbar from UV to NIR region. The Rayleigh scattering optical depth is based on Chan and Dalgarno (1965): $\tau/p = 0.0083(1 + 0.014\lambda^{-2} + 0.00027\lambda^{-4})\lambda^{-4}$, for wavelength λ in μm and pressure p in bar. Three broadband ISS filters are indicated in the figure. The CB3 filter (0.938 μm) is the cloud continuum channel sampling the methane-free wavelength. The MT3 filter is located in a strong methane absorption band centered at 0.889 μm. This channel is designed to sample the upper atmosphere. The MT3/CB3 filters are sensitive to the location of the tropospheric haze layer and the aerosol properties at ~10 mbar in the high phase angle images. The UV1 filter is centered at 0.258 μm, the observed reflective spectra from which are not affected by CH_4 but by strong Rayleigh scattering. Figure 4.1 shows that the Rayleigh scattering optical depth at the UV1 channel is roughly the same as the methane optical depth in MT3 channel. Therefore the UV channel is also more sensitive to the higher atmospheric scatters like the stratospheric hazes.

We selected 38 Cassini ISS images, covering all the latitudes of Jupiter from 75° S to 75° N, and phase angles from 0.9° to 141°. All images are calibrated based on West et al. (2010). The detailed information of the image index numbers from the Planetary Data System (PDS) and mean phase angles are shown in Table 4.1. Figure 4.4 shows some selected ISS images from the three filters. A significant latitudinal contrast is shown in the MT3 images, revealing brighter bands near the equator and the polar region, and brighter northern hemisphere than the southern hemisphere. The brighter regions imply either the cloud top might be higher in the equatorial region and northern midlatitudes. The low and midlatitudes in the UV1 images are smeared out by the Rayleigh scattering above the cloud and haze layers. A darker band in the equatorial region also implies a higher cloud top or darker scatterers. The strong evidence for the higher stratospheric haze layer in the polar region comes from the bright polar caps in

the MT3 images and corresponding darker polar region in the UV1 images because only the higher stratospheric haze layer can overcome the CH_4 absorption and Rayleigh scattering. That the polar haze layers locate in the higher stratosphere is consistent with the results from the NIR retrieval results in section 4.2.

Table 4.1. Selected Cassin ISS images for aerosol retrieval

CB3 Filter		MT3 Filter		UV1 Filter	
Image Number	Mean Phase Angle	Image Number	Mean Phase Angle	Image Number	Mean Phase Angle
N1352917174	17.5481	N1352917145	17.5485	N1352917104	17.5477
N1355181340	3.50334	N1355181377	3.50287	N1355181442	3.50749
N1355181726	3.45836	N1355181763	3.45719	N1355182158	3.70272
N1355182081	3.69890	N1355182101	3.69926	N1355182519	3.73102
N1355182442	3.73089	N1355182462	3.73028	N1355720416	6.44159
N1356751773	52.9151	N1355366470	0.93606	N1355720779	6.59232
N1356754443	53.0653	N1355716697	6.47109	N1355723337	6.56814
N1358257928	119.584	N1355717439	6.47009	N1357558433	99.7739
N1358258182	119.580	N1359305173	131.917	N1358243072	119.323
N1360176531	136.444	N1359306172	131.921	N1358243326	119.318
N1360177530	136.445	N1363092096	140.987	N1358855316	128.024
N1363092160	140.988			N1358856323	128.021
				N1358860176	128.066
				N1358861183	128.062
				N1363187297	141.022

The spectral information from the three filters is not enough to retrieve a vertical profile of the haze layer with sufficient vertical resolution for circulation model. Therefore we incorporate the vertical profiles from the NIR retrieval results in section 4.2 and retrieved the total column abundances of aerosols for each latitude. For the region northward than 25° N where the NIR retrieval results are not available, we assume the shape of the vertical aerosol profile is the same as its conjugated latitude in the southern hemisphere. This is not

a bad assumption according to the haze layer locations retrieved by Kedziora-Chudczer and Bailey (2011).

We divided the whole globe into 31 latitude bins evenly from 75° S to 75° N, with a width of 5° in each bin. For each latitude, we randomly sampled 10 pixels (I/F values) to represent the limb darkening profile. We tested different samples to validate our results.

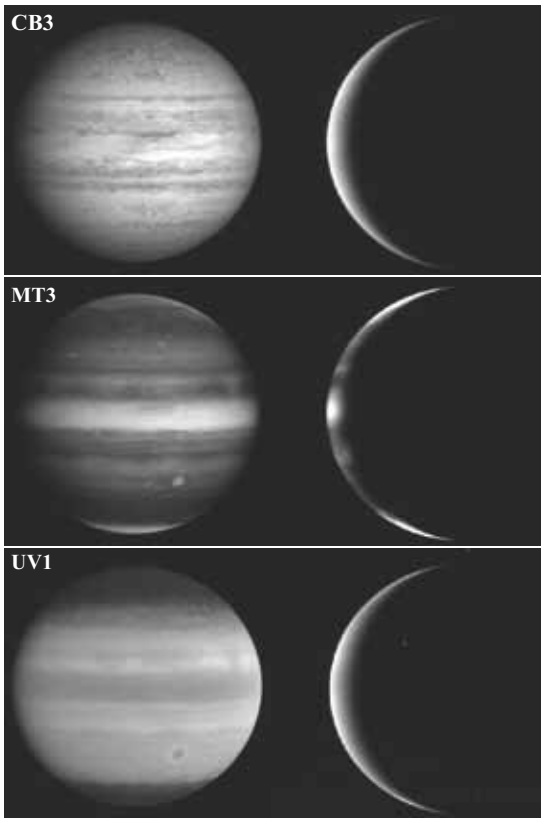

Figure 4.4. Sample images from three ISS filters. From top to bottom: CB3 (0.938 μm), MT3 (0.889 μm), UV1 (0.258 μm). For each filter, we show a low phase angle (~17.5°) image on the left and a high phase angle (~141°) image on the right.

4.3.2. Retrieval Model Description

We developed a retrieval model for the ISS data. Roughly speaking, our model is composed of two parts: the forward module and the optimization module. The forward

module consists of a radiative transfer module and an aerosol optical property module. For the radiative transfer module that simulates the reflectivity (I/F) for a specific incident angle, viewing angle and phase angle, we use the DISORT model (DIScrete Ordinates Radiative Transfer Program for a Multi-Layered Plane-Parallel Medium). The DISORT model was originally written in Fortran by Stammes et al. (1988) using the discrete ordinates method and has recently been updated and translated into the C by Timothy Dowling (2010, personal communication). Compared with the original single-precision Fortran code, the new version of the DISORT, called CDISORT, is using double precision and has removed possible spurious numerical spikes, and its speed is 3-4 times faster than the original version in our retrieval calculation. In order to be accurate, we use 32 streams to characterize the intensity angular distribution, which has been shown to display almost no difference from the 64-stream choice.

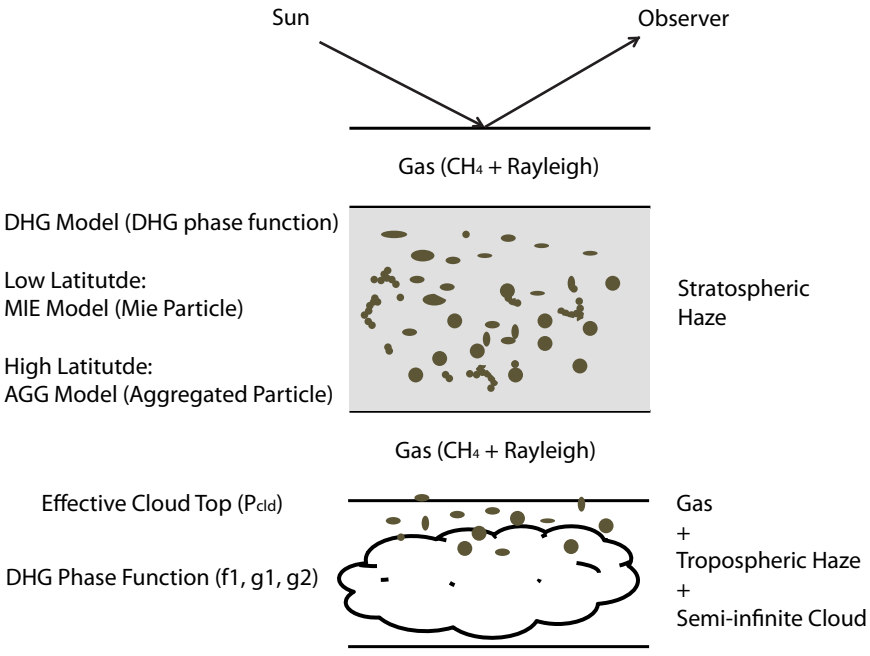

Figure 4.5. Cartoon of the retrieval model structure.

As illustrated by the cartoon in Figure 4.5, our forward module includes several atmospheric layers, including the haze layer, the cloud layer and the gas layers, from 1

mbar to the tropospheric cloud top. Typically above the cloud top our model has 12 vertical grid, which is enough to approximate the vertical profile of the stratospheric haze layer from the NIR retrieval. We are not trying to use a Mie sphere particle to approximate the optical properties of the tropospheric cloud layer because the cloud in fact is likely to be composed of ice crystals such as ammonia ice (West et al. 2004) whose shape is irregular. Instead, since we are more interested in the stratospheric haze layer, for simplicity, we parameterized the CH_4 absorption, Rayleigh scattering, aerosols and clouds in the troposphere all together as a semi-infinite "effective cloud layer" (or a bottom scattering layer), which can be characterized by its single scattering albedo and a double Henyey-Greenstein (DHG) phase function (Tomasko et al. 1978):

$$P(\theta) = \frac{f_1}{4\pi}\frac{1-{g_1}^2}{(1+{g_1}^2-2g_1\cos\theta)^{3/2}} + \frac{1-f_1}{4\pi}\frac{1-{g_2}^2}{(1+{g_2}^2-2g_2\cos\theta)^{3/2}}$$

where P is the phase function and θ is the scattering angle. The three parameters in the DHG phase function are: the partition factor f_1, the forward asymmetry factor g_1, and the backward asymmetry factor g_2. We retrieved two DHG phase functions for clouds: one for the NIR filters (CB3/MT3) and the other for the UV1 filter, and with three single scattering albedo for each filter, because the averaged single scattering albedo might be affected the tropospheric CH_4 absorption in the MT3 filter but not in the CB3 filter. Besides the optical properties, the effective cloud top is also a free parameter in the model.

For the haze optical property simulator, we also tried several choices. The simplest choice would be two single scattering albedos and two DHG phase functions one each for the NIR and UV filters, respectively. We called this the DHG model. This simple model is relatively linear compared with our other more realistic choices, and therefore it can fit the spectra faster. Although the physical meaning in the DHG model results is not very clear, it can help to reveal the nature of the aerosol properties for each individual filter. We found that the DHG model first and we found DHG model helps to distinguish the two possible aerosol types: Mie particle and fractal aggregated particle (section 4.3.2). Based on these preliminary results, we choose two more realistic models as our final choices: the Mie particle model (hereafter "MIE model"), in which we assume the aerosols are Mie spheres;

and the Fractal aggregates model (hereafter "AGG model"), in which we assume the aerosols are fractal particles aggregated from a number of tiny monomers. Another practical benefit from the DHG model is that it provided the approximate phase function for the NIR and UV filters, which provided a good initial guess for the phase function in the AGG model.

The phase function and cross sections of Mie particles are simple based on the Mie theory, but that of the fractal aggregates are relatively tricky. In principle they can be strictly calculated from the electromagnetic scattering computation using the multi-sphere methods, for example, by the MSTM code from Mackowski and Mishchenko (2011). However, it is still computationally too expensive to meet our retrieval needs even with the help of parallel computing. Instead, we use a very useful parameterization method for the aggregates with a fractal dimension of 2 (Tomasko et al. 2008).[‡‡] Their empirical code has been validated with the strict multi-sphere calculation in a large parameter space, spanning the size parameter of the monomer from 10^{-4} to 1.5 and number of monomers from 2 to 1024. For the monomer size parameter smaller than 0.5, the model is robust for even larger number of monomers (~4028). Based on this empirical code, Tomasko et al. (2008) were able to fit the descent imager/spectral radiometer (DISR) instrument aboard the Huygens probe for Titan and found the fractal aggregates in the Titan lower atmosphere are composed of thousands of 0.05 μm monomers. Therefore, we adopt the empirical code as our AGG model. Since our data are not very sensitive to the real part of the refractive index, we fix it as the values in Khare et al. (1984) in both MIE and AGG models.

Our optimization module is based on a widely used nonlinear least square optimization package, MPFIT, in Interactive Data Language (IDL) language (Markwardt 2008). The algorithms were translated from the original Fortran code, MINPACK-1, a minimization routine developed by Jorge Moré in the 1970s (Moré 1978). The algorithm is based on the

[‡‡]A typo has been found in their equation (A. 12b). The correct expression should be (personal communication with Mark Lemmon): depol_11 = C_p11_m_3*M0*taus_out^{E_p11_t_1}.

Levenberg–Marquardt iteration scheme (Levenberg 1944; Marquardt 1963), and the errors are calculated from the posterior covariance matrix. This algorithm does not require any *a priori* knowledge, which is typically suitable for our purpose due to the poor knowledge about Jovian aerosols. The IDL package supports the upper and lower constraints for the retrieved parameters. That is also very useful because many parameters in our retrieval are bounded within their physically allowed region. For example, the single scattering albedo cannot be larger than unity. From our synthetic data tests, the minimization package approaches to the true values quickly and shows a robust behavior. The initial guess is sometimes crucial, so we always test different initial guess and choose the best fitting results. Multiple solutions also exist, however, which is inevitable because of the nature of ill-posed retrieved problem when the information and constraints are not enough. See Moré (1978) and Markwardt (2008) for more detailed information of the code and its numerical scheme. The retrieval for one latitude generally converges within 20 iterations. The detailed computational time depends on the choice of the optical property module, the initial guess, and the number of observations, but it usually finishes within several hours.

4.3.3. DHG Model Results

In the DHG model retrieval, we use DHG phase functions for both haze and clouds, and for UV and NIR filters separately. Therefore the aerosol properties between the UV and NIR regions are almost separated, except that they still share the same tropospheric cloud top. Due to the homogenous nature seen from the CB3 channel, we can actually use the same NIR phase function for clouds in all the latitudes. Since we only use the DHG model results for a hint of the aerosol properties, we are not going to discuss many details on the retrieval itself and the related uncertainties. Multiple solutions exist, but the retrieved optical depth and the general shapes of the aerosol phase functions look similar, especially in the middle and high latitude regions. The typical fitting results for the equator, northern midlatitude and the northern polar region are summarized in Table 4.2. The low latitude stratospheric particles are optically thin (on the order of 0.01) in both NIR and UV wavelengths, while the middle and high latitude particles are optically thicker, with the NIR optical depth on

the order of 0.1 and UV optical depth larger than 1. Both the NIR and UV phase functions show a modest forward scattering peak ($g_1>g_2$) for all the latitudes. The single scattering albedos (SSA) of the aerosols are higher in the NIR wavelengths (>0.95) and lower in the UV wavelengths (0.6-0.8).

The most important DHG model retrieval results are the ratio of the extinction efficiency between the UV and NIR channels, which we call the UV/NIR extinction ratio, and the phase functions in the NIR filters (Figure 4.6). In order to explain the reflective spectra, the UV/NIR extinction ratio for the equator is required to be on the order of unity or less, but 10 or more for the midlatitudes and polar region. Provided that the particle size parameter drops by a factor of ~3.5 from the UV to the NIR wavelengths, only a particle with size between the UV and NIR wavelengths could possibly achieve the UV/NIR extinction ratio on the order of unity, and only a particle smaller than the UV wavelength could generate the ratio larger than 10. In Figure 4.6 we show the UV/NIR ratio as a function of radius (or the monomer radius for aggregates) based on the refractive index from Khare et al. (1984). For the Mie particles, only those smaller than 0.1 μm would be able to match the middle and high latitudes data while only those larger than 0.3 μm would be able to match the equatorial data. However, the fractal aggregates are different. The UV/NIR ratio of the aggregates relies more on the monomer size than the total cross section of the aggregates. For the 0.05 μm monomer, although the aggregates with 500 monomers have a volume equivalent to the 0.4 μm Mie particle, the UV/NIR ratio is still about 10 (Figure 4.6). Therefore, the UV/NIR extinction ratios from the DHG model results imply that the particle is larger at the equator, and smaller, or at least the monomer is smaller, in the mid and high latitudes.

The other hint of the particle shape is from the NIR phase functions, which show the forward scattering peaks for all the latitudes (Figure 4.6). This is a strong indication of a larger particle, whose size should not be too small compared with the NIR wavelengths (~0.9 μm). Figure 4.6 shows that a 0.3 μm Mie particle could roughly explain the phase functions but a 0.08 μm Mie particle could not. Therefore we conclude that the middle and

high latitude particles cannot be the Mie particles because they should be small from large UV/NIR extinction ratio, but on the other hand they should be large from the forward scattering phase function.

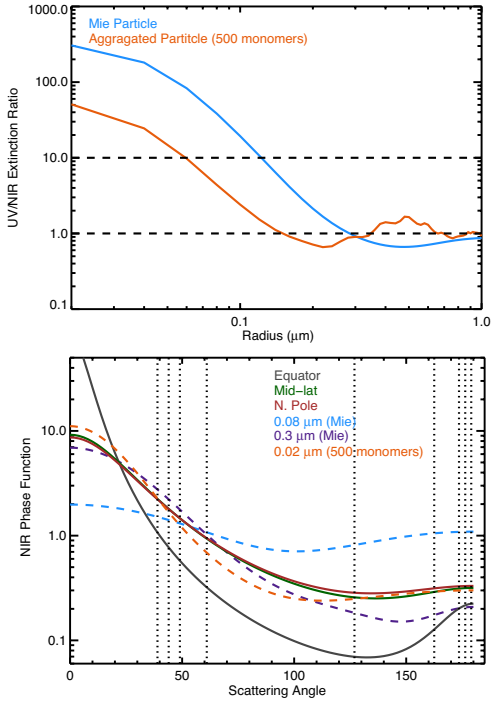

Figure 4.6. UV/NIR extinction ratios (upper panel) and aerosol NIR phase functions (lower panel) from the DHG model. For the aggregates, the horizontal axis corresponds to the monomer radius. The dotted lines indicate the scattering angles for with the ISS image data.

The fractal aggregates can solve this dilemma. As shown in Figure 4.6, the aggregates composed of 500 monomers (with monomer radius ~0.02 μm) could match both the UV/NIR extinction ratio and the NIR phase function. For the low latitude region, such as the equator, both the Mie particle and fractal aggregates can be the solution. Some previous studies (e.g., Moreno 1996; Barrado-Izagirre et al. 2008) show the polar haze size is below 0.1 μm, which is consistent with our UV/NIR ratio data. However, the other crucial information to characterize the shape of the particle, i.e., high phase angle images, was not used in those studies. Therefore, their low phase angle image data are only able to constrain

the total extinction/scattering optical depth and the monomer size instead of the total particle size.

Table 4.2. Typical DHG model results for latitude 0°, 45° N, and 65° N

Retrieved Parameters	0°	45° N	65° N
Cloud Top Pressure (mbar)	150.0	245.0	500.0
NIR Optical Depth (at 100 mbar)	0.0713	0.0924	0.2703
UV Optical Depth (at 100 mbar)	0.0308	1.0767	9.8221
Cloud NIR Phase Function (f_1)	0.9900	0.9704	0.9546
Aerosol NIR Phase Function (g_1)	0.8514	0.5901	0.5824
Aerosol NIR Phase Function (g_2)	-0.6945	-0.4766	-0.3935
Aerosol UV Phase Function (f_1)	0.3898	0.8162	0.8421
Aerosol UV Phase Function (g_1)	0.9500	0.6475	0.8637
Aerosol UV Phase Function (g_2)	-0.2498	-0.1000	-0.1143
Aerosol SSA at NIR	0.9882	0.9511	0.9579
Aerosol SSA at UV	0.7615	0.6455	0.8039
Cloud NIR Phase Function (f_1)	0.9675	0.9675	0.9675
Cloud NIR Phase Function (g_1)	0.6650	0.6650	0.6650
Cloud NIR Phase Function (g_2)	-0.5954	-0.5954	-0.5954
Cloud UV Phase Function (f_1)	0.8303	0.2558	0.5235
Cloud UV Phase Function (g_1)	0.8311	0.9500	0.9500
Cloud UV Phase Function (g_2)	-0.3657	-0.1000	-0.9500
Cloud SSA at CB3	0.9933	0.9878	0.9781
Cloud SSA at MT3	0.8670	0.7889	0.7500
Cloud SSA at UV1	0.9209	0.9260	0.9000

West and Smith (1991) proposed the idea of aggregates to reconcile the Pioneer polarimetric observations, which indicated the existence of small particles (Smith 1986), and the intensity observations from high phase angle images, which indicated the existence of large particles (e.g., Tomasko et al. 1978). Without the polarization data in this study, the enhanced UV extinction and forward scattering NIR phase function in the middle and high latitude regions can also give the hint of the possible existence of fractal aggregates. But we

are not able to tell the difference between the Mie particle and fractal aggregates in the low latitude region, especially when the particles are optically thin (Table 4.2). If the low latitude particles are fractal aggregates, from Figure 4.6 the monomer radius is likely to be larger than 0.1 μm in order to match the unity UV/NIR extinction ratio. Whether those large monomers can form the aggregates is uncertain. Furthermore, Tomasko et al. (1986) shows the Mie particle size of the equatorial region is from 0.2 to 0.5 μm. Therefore, even if the equatorial particles are fractal aggregates, the number of monomers is not expected to be large (on the order of ~10). Under this situation the difference between the Mie particle and fractal aggregates is actually marginal in terms of the optical properties. Our heating rate would not be altered much based on either of the two assumptions. Future determination of the exact shape of the low latitudinal particles needs to incorporate the polarization data. For simplicity, we will just use the MIE particle for the stratospheric haze at low latitudes.

Based on the preliminary results from the DHG model, we will conduct the retrieval using the MIE model and the AGG model in the following two sections. We will group the latitudes into four regions: the low latitudes (40° S -25° N), midlatitudes (50° S-45° S and 30° N- 45° N), south polar region (65° S-55° S), and north polar region (50° N-65° N). The low latitude boundaries are determined empirically based on fitting results, with the MIE model suitable inside but the AGG model is required outside. In fact the low latitude boundaries can be seen from the MT3 and UV1 images in Figure 4.4. The optical depth increases across the boundaries. The polar region (polar caps) boundaries are distinct in the circumpolar wave structures in the MT3 and UV1 images, as shown by Barrado-Izagirre et al. (2008). Within each region, the aerosols are the same except with column density varying with latitude. The cloud phase functions in the NIR and UV wavelengths are homogenous in each region, respectively. All the latitudes can share the same NIR cloud phase function but with different single scattering albedo. The cloud top changes with latitude as well. In other words, we found the ISS images can be explained using approximately four types of stratospheric hazes with four types of UV clouds and only one type of NIR cloud at the bottom. In the very high latitude regions poleward than 70° S and

70° N, the fitting of the UV data is not very satisfactory. Therefore we need to treat the aerosol properties for each latitude individually.

4.3.4. Low Latitudes: MIE Model Results

Table 4.3. Best-fitted MIE model results for the low latitude regions (40° S-25° N)*

Retrieved Parameters	Solution A	Solution B
Mean Particle Radius r_{eff} (μm) (fixed)	0.3	0.5
Size Distribution Parameter v_{eff} (μm) (fixed)	0.1	0.1
NIR Imaginary Refractive Index (fixed)	1×10^{-3}	1.6×10^{-3}
UV Imaginary Refractive Index (fixed)	2×10^{-2}	1.86×10^{-1}
Total Column above 100 mbar (cm^{-2}) (equator)	$(2.0\pm0.2)\times10^{7}$	$(2.4\pm0.2)\times10^{7}$
Cloud NIR Phase Function (f_1)	0.9675	0.9207
Cloud NIR Phase Function (g_1)	0.6650	0.8507
Cloud NIR Phase Function (g_2)	-0.5954	-0.1000
Cloud UV Phase Function (f_1)	0.8303	0.7230
Cloud UV Phase Function (g_1)	0.8311	0.8574
Cloud UV Phase Function (g_2)	-0.3657	-0.2767
Troposheric SSA at CB3 (Equator)	0.9933	0.9974
Troposheric SSA at MT3 (Equator)	0.8706	0.9195
Troposheric SSA at UV1 (Equator)	0.9135	0.9109

* We use the two-parameter gamma function for the aerosol size distribution, characterized by $\mathbf{r}_{eff}$ and $\mathbf{v}_{eff}$. The errors of cloud parameters estimated from covariance matrix are usually on the order of 0.1% of the retrieved values, which are likely to be underestimated because of the existence of multiple solutions. Empirically we estimated the uncertainty range of the cloud phase function could be on the order of 10% of the retrieved values, while that of the cloud single scattering albedo might be on the order of 1% level.

Similar to Tomasko et al. (1986), we are not able to determine the stratospheric particle size accurately in the low latitude region because they are optically thin and most of the photons are scattered by the tropospheric clouds. The approximate size range found in this study is between 0.2 and 0.5 μm. Therefore we fixed the Mie particle properties in the MIE

model, in which we use the two-parameter gamma function for the aerosol size distribution. A different choice of size distribution does not strongly influence the retrieval results. The same DHG cloud phase functions are applied to all the low latitudes but the cloud SSA needs to be changed with latitude in order to get the best fit. Multiple solutions exist according to the choice of the stratospheric particle size and refractive index, as shown in Table 4.3. Solution A uses the imaginary refractive index from our AGG model fitting (see section 4.3.5) and a 0.3 μm particle mean radius. Solution B corresponds to the refractive index from Khare et al. (1984) and a 0.5 μm particle. Both solutions can fit the limb-darkening profiles well. A typical fit of the solution A is shown in Figure 4.7 in low and high phase angles. For the other intermediate phase angles (not shown in the plot) the fitting is also good. Although the two cases have different aerosol properties, the total aerosol optical depths above 100 mbar are more or less the same, about ~0.026 (NIR) and ~0.025 (UV) for solution A and ~0.034 (NIR) and ~0.022 (UV) in solution B. The total column density above 100 mbar is ~2×10^7 cm^{-2} for solution A and ~2.4×10^7 cm^{-2} for solution B. The detailed latitudinal information will be discussed in section 4.3.6.

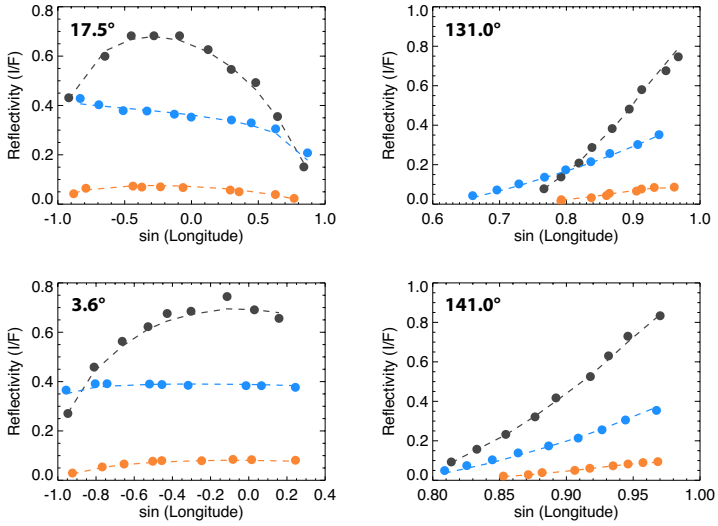

Figure 4.7. Atmospheric reflectivity (I/F) as function of longitude in the equatorial region for multiple phase angles indicated in the upper left of each panel. Circles are the observations and dashed lines are the results from the stratospheric MIE model (solution A). Black, orange and blue colors correspond to the CB3, MT3, and UV1 filters, respectively.

Table 4.4. Best-fitted AGG model results

Retrieved Parameters	Midlatitude	South Pole	North Pole
Monomer Radius (μm)	$(0.97\pm0.06)\times10^{-2}$	$(1.05\pm0.12)\times10^{-2}$	$(1.03\pm0.08)\times10^{-2}$
Number of Monomers	2044 ± 298	646 ± 139	812 ± 130
NIR Imaginary Refractive Index	$(1.15\pm0.13)\times10^{-3}$	$(0.83\pm0.12)\times10^{-3}$	$(1.15\pm0.10)\times10^{-3}$
UV Imaginary Refractive Index	$(2.54\pm0.18)\times10^{-2}$	$(1.96\pm0.26)\times10^{-2}$	$(2.75\pm0.26)\times10^{-2}$
Total Column above 100 mbar (cm^{-2})*	$(6.5\pm0.6)\times10^{9}$	$(4.1\pm0.8)\times10^{10}$	$(4.9\pm0.6)\times10^{10}$
Cloud NIR Phase Function (f_1)	0.9675	0.9675	0.9675
Cloud NIR Phase Function (g_1)	0.6650	0.6650	0.6650
Cloud NIR Phase Function (g_2)	-0.5954	-0.5954	-0.5954
Cloud UV Phase Function (f_1)	0.2558	0.9642	0.9900
Cloud UV Phase Function (g_1)	0.9500	0.9500	0.9500
Cloud UV Phase Function (g_2)	-0.1000	-0.9500	-0.1000
Cloud SSA at CB3	0.9884	0.9886	0.9760
Cloud SSA at MT3	0.7500	0.7500	0.7500
Cloud SSA at UV1	0.9000	0.9000	0.9000

*For the total column density, we use the 45° N, 65° N and 65° S values to represent the middle latitudes, south polar and north polar regions, respectively.

4.3.5. Middle and High Latitudes: AGG Model Results

Outside the low latitude region, MIE model fails. The midlatitudes (50° S-45° S and 30° N-45° N) show different types of aerosols and UV clouds from the polar region. AGG model results show that the midlatitude particles can be fitted by ~2000 monomers but the polar aggregates are only composed of 600-800 monomers, although the monomer size is roughly the same, ~0.01 μm (Table 4.4). The typical fitting results are in Figure 4.8 for midlatitudes and Figure 4.9 for high-latitudes. The fitting is generally good including the intermediate phase angles not shown in the figures, except that the UV intensity is slightly overestimated in the high phase angles but underestimated in the lower phase angles. We tested different initial conditions for each region, but all the solutions are not significantly

different. Therefore the values quoted in Table 4.4 are the most likely solutions for the fractal aggregates in the stratosphere of Jupiter. Although the midlatitude aggregates are larger than the polar aggregates, the total column density (6.5×10^9 cm^{-2}) is almost one order of magnitude smaller (~6×10^9 cm^{-2} in the midlatitude versus 4×10^{10} cm^{-2} in the polar latitudes, Table 4.4). Therefore the aerosol optical depth in the midlatitudes is actually smaller. At 100 mbar, the NIR optical depth is ~0.07 in the midlatitudes and ~0.2 in the polar region, and the UV optical depth is ~2.4 in the midlatitudes and ~8 in the polar region. The detailed latitudinal information will be discussed in section 4.3.6.

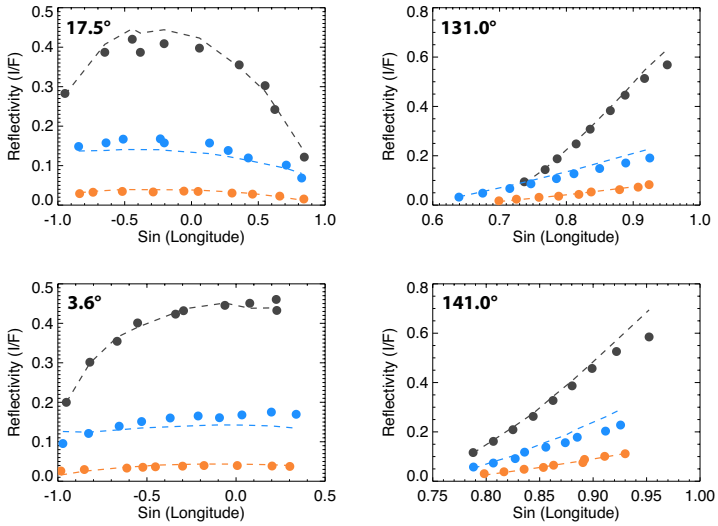

Figure 4.8. Atmospheric reflectivity (I/F) as function of longitude in the midlatitude (45° N) for multiple phase angles indicated in the upper left of each panel. Circles are the observations and dashed lines are the results from the AGG model. Black, orange and blue colors correspond to the CB3, MT3, and UV1 filters, respectively.

The similarity between the monomers in the midlatitudes and high latitudes implies the source of the midlatitude particles might be in the polar region, possibly due to the complex hydrocarbon synthesis driven by the energetic particle precipitation in the aurora region (e.g., Hord et al. 1979; Pryor and Hord 1991; Wong et al. 2003). This hypothesis seems also consistent with the NIR retrieval results (Figure 4.3), showing a continuous downward

slope as if the aerosols are transported from the polar region to the midlatitudes in the southern hemisphere. During the transport, the high-altitude high-latitude polar fractal aggregates might slowly settle downward and grow, and lead to the larger particle size in the midlatitudes. We do not find any correlation between the midlatitude particles and low latitude particles from the ISS data, although they reside on the same pressure levels revealed by the NIR data. This might suggest that the low latitude particles are generated via a different chemical pathway, e.g., by the neutral photochemical processes driven by the UV photons instead of high energetic particles.

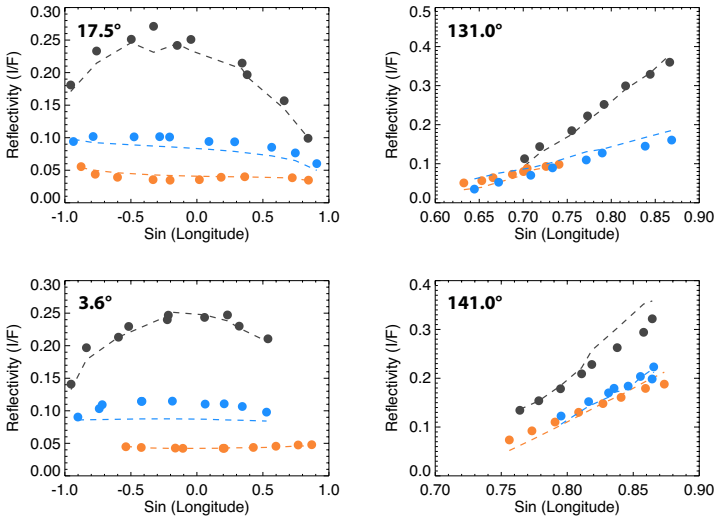

Figure 4.9. Atmospheric reflectivity (I/F) as function of longitude in the north polar region (65° N) for multiple phase angles indicated in the upper left of each panel. Circles are the observations and dashed lines are the results from the AGG model. Black, orange and blue colors correspond to the CB3, MT3, and UV1 filters, respectively.

The derived imaginary part of the refractive index of the fractal aggregates is about 0.02-0.03 in the UV wavelength and ~0.001 in the NIR wavelength, consistent in both the middle and high latitude regions. The value in the UV wavelength is roughly consistent with the polar region values from Moreno (1996), Very few previous laboratory measurements focused on the refractive index for the aerosols in the hydrogen dominant environment. Khare et al. (1987) measured the imaginary part of the refractive index of thin

hydrocarbon films produced in the mixture of 7% CH_4 and 93 percent H_2 from the charge particle irrradiation at 0.13 mbar pressure from 0.4 to 2.5 μm. Their results in the NIR region seem one order of magnitude smaller than our retrieval results (Figure 4.10). Our results imply that the particle produced in the H_2 environment has weaker absorptivity than that from the N_2 environment, as shown by the comparison of our results with the widely used tholin refractive index measured in Khare et al. (1984) for the Titan environment (Figure 4. 10). The change of the absorptivity might be related to the unpaired electrons of nitrogen interacting with the delocalized π electrons from aromatics (Imanaka et al. 2004). Since our data are not very sensitive to the real part of the refractive index, we just fix it as the values from Khare et al. (1984). The retrieved imaginary part might be good candidates for the future laboratory experiments.

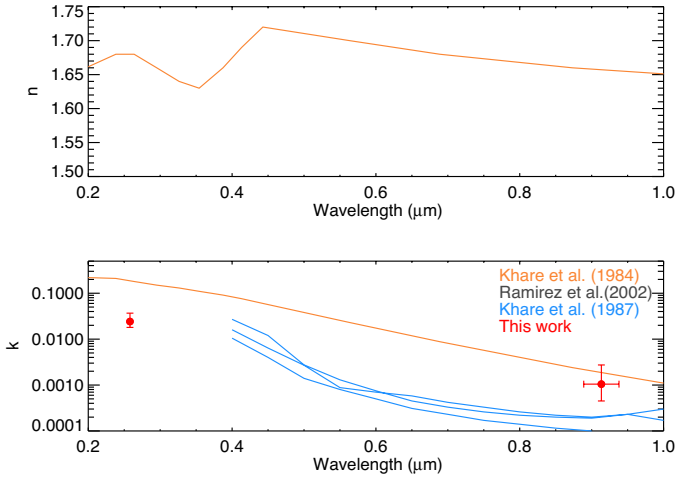

Figure 4.10: Real (upper panel) and imaginary (lower panel) part of the refractive index of aerosols from laboratory measurements. Retrieved imaginary refractive index for the Cassini ISS NIR and UV filters are plotted for comparison.

For the four highest polar latitudes, 70° S, 75° S, 70° N, and 75° N, the fitting of the UV images is less satisfactory if we assume the same aerosol properties in Table 4.5. Therefore we have to treat each latitude individually. Generally speaking the fitting is not as good as for lower polar latitudes, possibly because of the heterogeneous nature of the high-latitude aerosols in the aurora region, as discovered by West (1988) and Rages et al. (1999).

Specifically, we almost cannot fit the UV spectra for 75° N, even using the DHG model which has the most free parameters. But the CB3 and MT3 channels can be still fitted well by the same NIR cloud as other latitudes. The results are summarized in Table 4.5. The retrieved monomer size is also roughly 0.01 μm but with fewer number of monomers than at lower polar latitudes. Again, this decreasing trend of the number of monomers from midlatitudes towards the poles indicates that the particles are possibly produced in the polar region. The derived imaginary part of the refractive index in the NIR and UV filters generally agree with the other latitudes, yet with larger uncertainties.

Table 4.5. Best-fitted AGG model results for north and south polar regions

Retrieved Parameters	75° N	70° N	70° S	75° S
Monomer Radius (μm)	$(1.00\pm0.70)\times10^{-2}$	$(0.94\pm0.26)\times10^{-2}$	$(1.95\pm0.06)\times10^{-2}$	$(2.16\pm0.08)\times10^{-2}$
Number of monomers	398±528	560±241	276±26	136±12
NIR imaginary refractive index	$(1.58\pm1.13)\times10^{-3}$	$(1.05\pm0.31)\times10^{-3}$	$(0.64\pm0.19)\times10^{-3}$	$(2.61\pm0.13)\times10^{-3}$
UV imaginary refractive index	$(4.0\pm3.24)\times10^{-2}$	$(2.74\pm0.94)\times10^{-2}$	$(2.55\pm0.07)\times10^{-2}$	$(2.43\pm0.08)\times10^{-2}$
Total column density above 100 mbar (cm^{-2})	$(1.3\pm1.4)\times10^{11}$	$(1.2\pm0.4)\times10^{11}$	$(1.8\pm0.1)\times10^{10}$	$(3.1\pm0.1)\times10^{10}$
Cloud NIR Phase Function (f_1)	0.9675	0.9675	0.9675	0.9675
Cloud NIR Phase Function (g_1)	0.6650	0.6650	0.6650	0.6650
Cloud NIR Phase Function (g_2)	-0.5954	-0.5954	-0.5954	-0.5954
Cloud UV Phase Function (f_1)	0.9900	0.9900	0.9642	0.9642
Cloud UV Phase Function (g_1)	0.9500	0.9500	0.9500	0.9500
Cloud UV Phase Function (g_2)	-0.1000	-0.1000	-0.9500	-0.9500
Cloud SSA at CB3	0.9837	0.9837	0.9879	0.9990
Cloud SSA at MT3	0.7500	0.7500	0.7500	0.7500
Cloud SSA at UV1	0.9000	0.9000	0.9000	0.9000

4.3.6. Summary of the ISS Retrieval Results

We summarize all the results in Figs. 4.11-4.13. Figure 4.11 shows the latitudinal distributions of the effective cloud top, aerosol optical depths, haze SSA and cloud SSA.

The effective cloud top is around 0.2-0.3 bar, roughly consistent with the NIR results. The cloud top does not change dramatically from latitude to latitude, but the equatorial zone and the northern midlatitudes shows a higher effective cloud top. Although the cloud is barely seen in the higher latitudes from the high phase angle images, our low phase angle images seem to imply the northern polar region tends to have lower effective cloud top than the southern polar region, but there might be big uncertainty associated with it due to the degeneracy of the multiple solutions. This conclusion is qualitatively consistent with the tropospheric haze tops retrieved from the low phase angle images from other ISS filters and Hubble Telescope observations (Barrado-Izagirre et al. 2008).

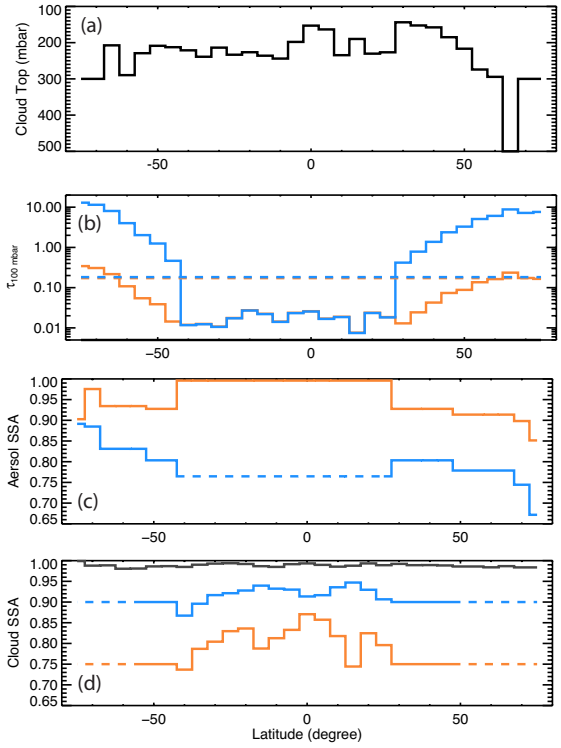

Figure 4.11. Summary of important retrieved parameters as function of latitude with a 5° bin width. From top to bottom: (a) effective cloud top in the troposphere; (b) total aerosol optical depth at 100 mbar in the NIR filter (orange solid line) and UV filter (blue solid line), with the CH_4 optical depth (orange dashed line) and Rayleigh scattering optical depth mbar (blue dashed line) at 100 mbar; (c) aerosol SSA in the NIR filter (orange) and UV filter (blue); (d) cloud SSA in the CB3 (black), MT3 (orange), and UV1 (blue) filters. The dashed lines in (c) and (d) indicate the fixed values in the retrieved model because they are less well constrained.

The belts and zones in the low latitudes can be seen from the cloud SSA in all three filters because the scattering of clouds contributes to the most reflectivity. The zones tend to be brighter and the belts tend to be darker in the NIR filters and the opposite behavior exhibits in the UV1 filter. This is expected because cloud scattering in the UV1 channel is mixed with conservative Rayleigh scattering. For the higher latitudes, we have less sensitivity of the clouds.

The aerosol optical depths in the UV and NIR wavelengths in the low latitude regions are roughly the same but the UV/NIR extinction ratio crucially depends on the assumed particle size. It seems that they overlap each other in Figure 4.11 due to our choice of the 0.3 μm particle. The NIR optical depth increases continuously towards the high latitudes until it is comparable to the CH_4 optical depth (~0.2) in MT3 wavelengths near the poles. The UV optical depth shows discontinuities at the boundaries between the low latitudes and middle latitudes where it exceeds the Rayleigh scattering optical depth (~0.2 at 100 mbar). The discontinuities are required in order to match the UV intensities. The UV/NIR extinction ratio in the middle and high latitudes is roughly constant (~35), mainly because they share similar monomer size (~0.01 μm). The optical depth increases with latitude faster in the south polar region than in the north polar region.

The difference between the south pole and north pole is also shown in the aerosol SSA in the UV filters. The south polar aggregates are brighter than the north polar particles, because the imaginary part of the refractive index is larger (~0.027 for the north versus ~0.019 for the south). The difference of the SSA is robust because we also see this difference from the DHG model retrieval (Table 4.2). The difference implies a possible compositional difference between the two types of aggregates. The single scattering albedo in the low latitudes cannot be determined because it depends entirely on the choice of the imaginary refractive index, which could be very different (Table 4.3). But if we assume the refractive index of the lower latitude particles are the same as the higher latitude aggregates, their SSA is approximately 0.75 (Figure 4.11).

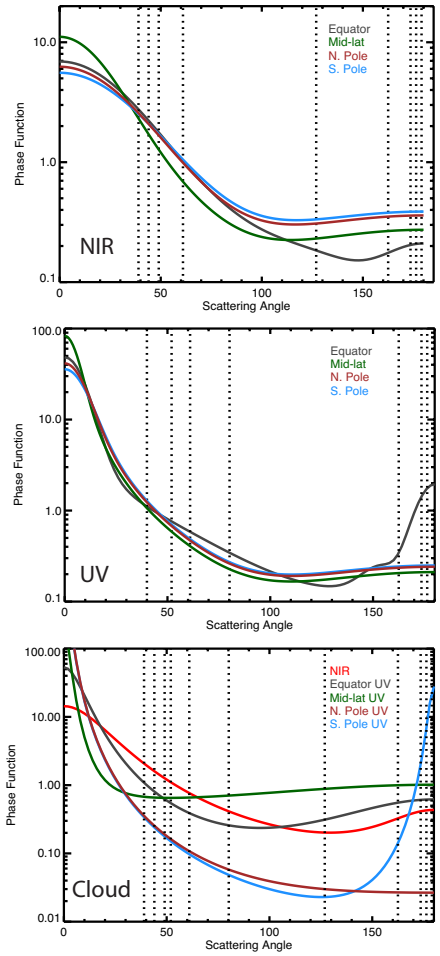

Figure 4.12. Retrieved phase functions for aerosol in the NIR filter (upper panel and in the UV filter (middle panel), and the cloud phase functions (lower panel), for different regions. We assume the cloud in the NIR channel is uniform with latitude. The dotted lines indicate the scattering angles associated with the ISS images.

The aerosol and cloud phase functions are plotted in Figure 4.12. The aerosol phase functions in the four regions all look similar in both the NIR and UV regions. Again note that the phase function of the low latitudes depends on the particle size. The similarity of the phase function implies that the middle and high latitude aerosols may have the same origin. Although there might be very large uncertainties associated with the clouds, they do look different in the four regions in our retrieval results. Detailed analysis of the clouds may require more cloud channel data to separate the tropospheric haze from the bottom layer clouds, which is beyond the scope of this work because we focus on the stratospheric

haze. The effect of the clouds on the stratospheric heating rate will be discussed in section 4.4.

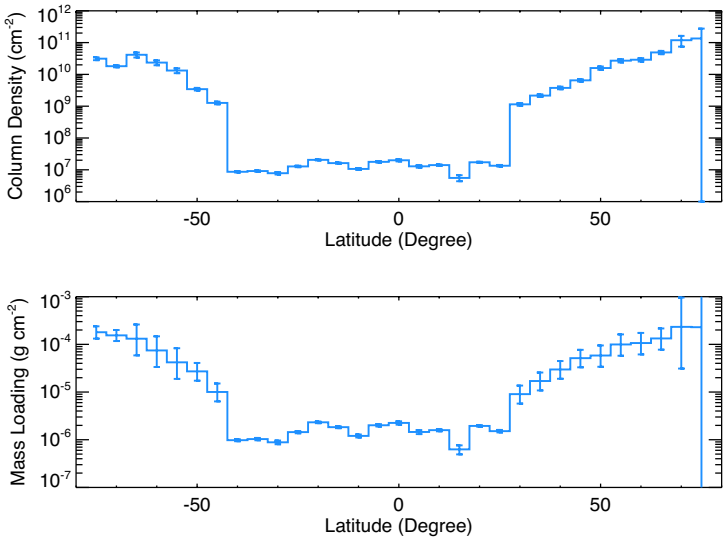

Figure 4.13. Total aerosol column density and mass loading (assume the density is 1 $g\ cm^{-3}$) above 100 mbar as function of latitude. The error bars in 75° N are large because the UV spectra are not well fitted. The error bars in the low latitudes are based on the solution A in Table 4.3, which might be underestimated because of the existence of multiple solutions.

Last, we show the latitudinal profiles of the total aerosol column density and mass loading above 100 mbar in Figure 4.13. The column density is ~10^7 cm^{-2} in the low latitudes and ranges from ~10^9 cm^{-2} in the midlatitudes to ~10^{10}-10^{11} cm^{-2} in the polar region. The maximum aerosol number density also changes dramatically from low latitudes to high latitudes. At equator, the aerosol number density peaks at about 50 mbar, with the value of ~10 cm^{-3}. In the polar region, for instance, at 65° N, the aerosol number density peaks at about 20 mbar, with the value of ~10^4 cm^{-3} (see Figure 4.14). Assuming that the mass density is about 1 g cm^{-3}, the mass loading of the particles is ~10^{-6} g cm^{-2} in the low latitudes and ~10^{-4} g cm^{-2} in the high latitudes. The derived column density and mass loading at midlatitudes are roughly consistent with Tomasko et al. (1986), who estimated aerosol mass loading on the order of 10^{-6} g cm^{-2} in the low latitudes and on the order of 10^{-5} g cm^{-2} in the high latitudes, and the total column density at 45° N is about 5×10^8 cm^{-2}. Our

results also generally agree with the global map of aerosol volume density per unit gas abundances in West et al. (1992).

However, our values are different from the Galileo high phase angle results (Rages et al. 1999), which show the number density ~0.15 cm^{-3} at 100 mbar, and ~0.1 cm^{-3} and 0.7 cm^{-3} at 20 mbar for the equatorial region and 60° N, respectively. The difference is mainly due to the different vertical aerosol profile we are using. Our aerosol distribution shows a clear region at 100 mbar so the particle number density near the 100 mbar is low. At ~20 mbar, in fact the number density in our equatorial model is also roughly ~0.1 cm^{-3}. But the peak is actually located around 50 mbar. For the polar region, the required UV optical depth is ~10, provided the extinction cross section of the aggregates on the order of 10^{-10} cm^2 at the UV wavelength, the total column density is required to be larger than 10^{10} cm^{-2}. Since we have a very concentrated particle haze layer from the NIR retrieval and layer thickness is usually within one or two atmospheric scale heights (~25-50 km), the number density is ~ 10^4 cm^{-3}. The particle density profiles can be used to constrain the future chemical and microphysical models.

4.4. Heating Rate and Global Energy Balance

4.4.1 Heating Rate

Aerosol and clouds absorbs the solar flux and heats the stratosphere of Jupiter. Provided detailed information of particles including their size, shape, refractive index, and latitudinal and vertical distributions, the heating rate calculation is straightforward. The same forward module in our retrieval model is used. Since the aerosol distribution is heterogeneous with latitude, we could not directly apply an analytical formula for the global-mean heating rate, as we did for CH_4 (chapter III). In order to accurately calculate the upward and downward zonally averaged fluxes for each pressure level, we consider all the wavelengths from 0.2 to 1 μm with the resolution of 0.001 μm, all emission angles in 32 streams, and the diurnal average using the Gaussian quadrature method with 10 Gaussian points along the longitude

for each latitude band. From the calculated upward and downward fluxes from CDISORT, the net energy flux deposited in each atmospheric layer can directly converted to the heating rate (Goody and Yung 1995).

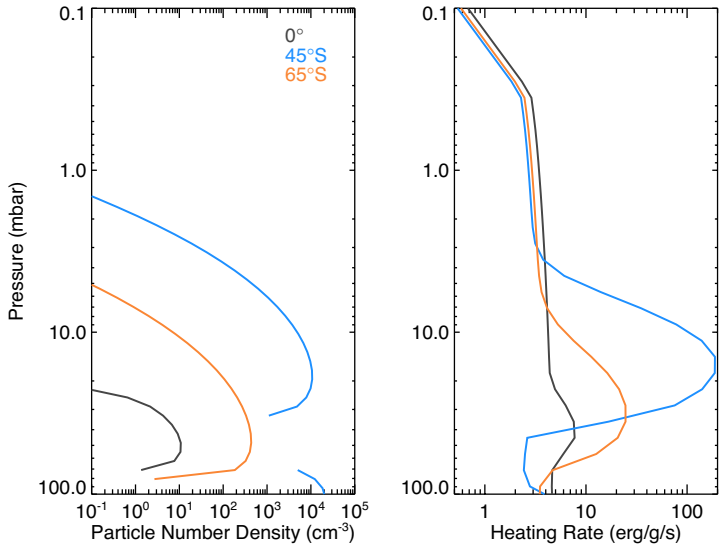

Figure 4.14. Particle number density as function of pressure for low, middle and high latitude regions (left panel) and the corresponding aerosol heating rates (right panel).

The vertical profile of heating rate is similar to the aerosol density profile (Figure 4.14). Above the aerosol layer, the heating rate is dominated by CH_4 absorption. The almost constant CH_4 heating rate is due to its optically thin nature, as shown analytically in chapter III. The decrease of heating rate on the top is due to the CH_4 mixing ratio profile from Moses et al. (2005), which starts decreasing above ~1 mbar (see Figure 4.3.1). Note that the CH_4 heating rates for the lower and higher latitudes are roughly the same, which seems counterintuitive but in fact is understandable. Although the perpendicular solar flux in the high latitudes is smaller than that in the low latitudes, the slant path for the absorption in each atmospheric layer is longer. Under the optically thin approximation, the two effects cancel out. The aerosol heating rate in the high latitude region reaches ~200 erg g^{-1} s^{-1}, which is more than one order of magnitude larger than the gas heating rate, while that in the low latitudes peaks at ~8 erg g^{-1} s^{-1}, only about a factor of 2 stronger than the CH_4 heating. The maximum heating rate is found at roughly the same pressure levels as the aerosol

density peaks, at ~20 mbar in the high latitudes, decreasing towards ~50 mbar in the middle and low latitudes.

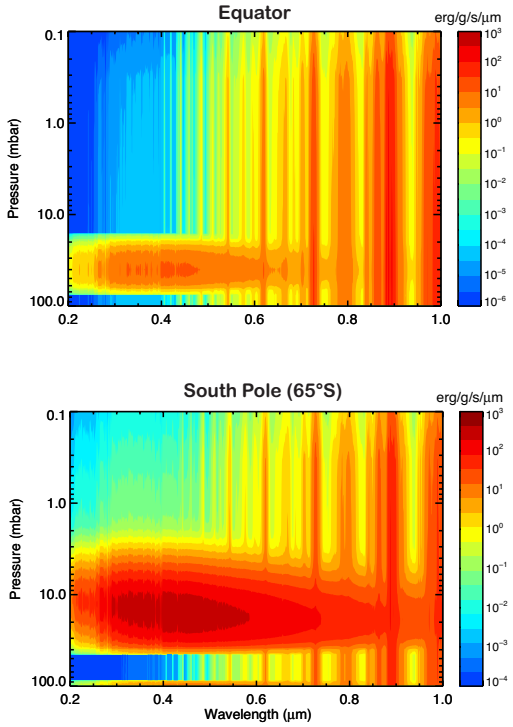

Figure 4.15. Spectrally resolved aerosol and CH_4 heating rate as function of wavelength and pressure for the equator region (upper panel) and south polar region (lower panel).

Figure 4.15 shows the spectrally resolved aerosol and CH_4 heating rate as function of wavelength and pressure for the equator region and the south pole. Compared with the spectrally resolved CH_4 heating rate in the NIR wavelengths from 1 to 10 μm (Figure 3.9) where the strong CH_4 bands completely dominate the heating (with a minor contribution from the hydrogen collisional absorption), the visible wavelengths heating rate looks entirely different. In the low latitudes, the heating rate is contributed by the aerosol layer around 50 mbar in the shorter wavelength region below 0.5 μm, and beyond that the absorption from the CH_4 bands dominates. In the high latitudes, the heating by the aerosol layer at 20 mbar is much strong, almost dominating all the wavelength range, with the CH_4 contribution in the NIR region. The maximum aerosol heating is located around the

wavelength of the solar spectrum peak (~0.5 μm) but slightly shorter than that because of the increasing absorption of aerosols towards the UV wavelength.

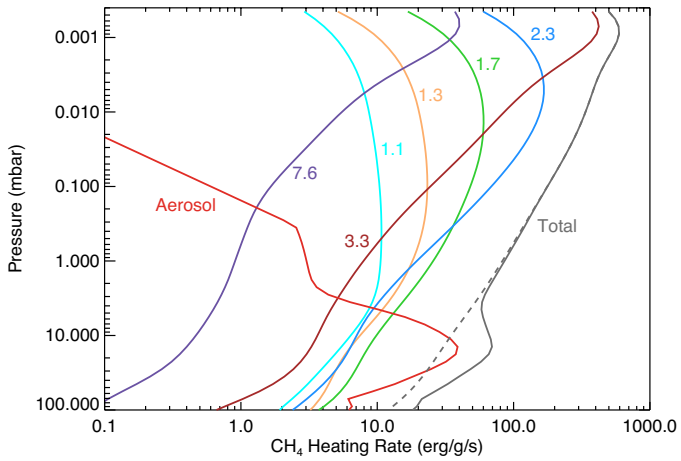

Figure 4.16. Globally averaged radiative heating rates. The CH_4 heating rates in the NIR and Mid-IR region are obtained from chapter III. Contributions from different ro-vibrational CH_4 bands are plotted with colors. The dashed line is the total gas heating rate and the solid black line is the total heating rate including aerosols.

Roughly speaking, the aerosol heating enhances the total global heating rate by a factor of 2 in the stratosphere below ~10 mbar (Figure 4.16). Therefore, compared with the NIR CH_4 bands, aerosols actually dominate the lower stratospheric heating rate below 10 mbar. The maximum of the aerosol heating rate is almost ~40 erg g^{-1} s^{-1} at 20 mbar, even larger than the total NIR CH_4 heating rate at the same pressure level. The aerosol heating rate drops very fast above 5 mbar and is not important to the total heating rate in the upper stratosphere. But this conclusion is not definite, since our NIR retrieval is only sensitive to ~10 mbar, above which is beyond the sensitivity. Using higher-resolution spectra, Kedziora-Chudczer and Bailey (2011) found one more layer above 10 mbar. Therefore, different aerosol vertical structure might have different heating rate profile. However, qualitatively, with or without aerosols, the two-dimensional stratospheric heating rate map looks very different (Figure 4.17). The pure CH_4 heating rate has the maximum at the equator region and increases with altitude, but the largest heating sources move to the two polar region around 10-20 mbar once the aerosol heating is included, while the low

latitudes are less influenced. The heating in the north pole is stronger than in the south pole mainly because the aerosols are darker in the north (Table 4.4). Therefore, we conclude that the stratospheric aerosols not only affect the total global heating budget but also the dark and thick aerosol layers in the high latitudes completely change the pattern of the solar energy deposition.

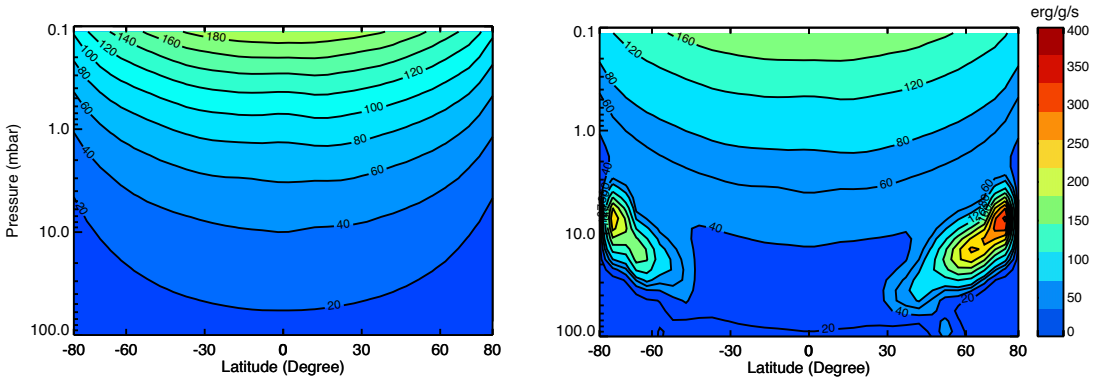

Figure 4.17. Zonal averaged solar heating rate map in the stratosphere of Jupiter from 100 to 0.1 mbar. Left panel: heating rates by CH_4 absorption only. Right panel: heating rates by CH_4 and stratospheric aerosols.

Qualitatively, our heating rate agrees with West et al. (1992), who found the polar aerosol heating to be very important. We confirm their conclusion and also agree with the location of their polar heating sources, i.e., ~10 mbar. Quantitatively, below 10 mbar, our total heating rate is about 50% larger than their values (see their Figure 4.3), which means their aerosols does not contribute too much to the global heating budget because the CH_4 NIR heating rate is almost 40 erg g^{-1} s^{-1} at 10 mbar. Above 10 mbar their heating rate decreases slightly and keeps almost constant to above 1 mbar (~40 erg g^{-1} s^{-1}), while our heating rate keeps increasing with altitude to ~100 erg g^{-1} s^{-1} at 1 mbar. The primary reason is due to the difference of the CH_4 absorption coefficients in the NIR bands, which has been greatly improved since the 1990s. The global averaged total heating rate from Moreno and Sedano (1997) shows an increasing trend with altitude and only reaches ~50 erg g^{-1} s^{-1} at 10 mbar, smaller than our value, and ~100 erg g^{-1} s^{-1} at 1 mbar, roughly consistent with our results. Their work suggested a much weaker aerosol heating than our results in the north pole, and the peak of their heating rate profile locates at about 2 mbar in the south pole, much higher

than our aerosol layer. This difference is caused by different vertical aerosol distributions. Their aerosol density profile was based on a microphysical model instead of the NIR retrieval results as we adopt in this work. Lastly, our aerosol heating rates are much larger than the results in Yelle et al. (2001) but their calculation was mainly based on the Moreno and Sedano (1997) that we have discussed above.

4.4.2 Global Energy Balance

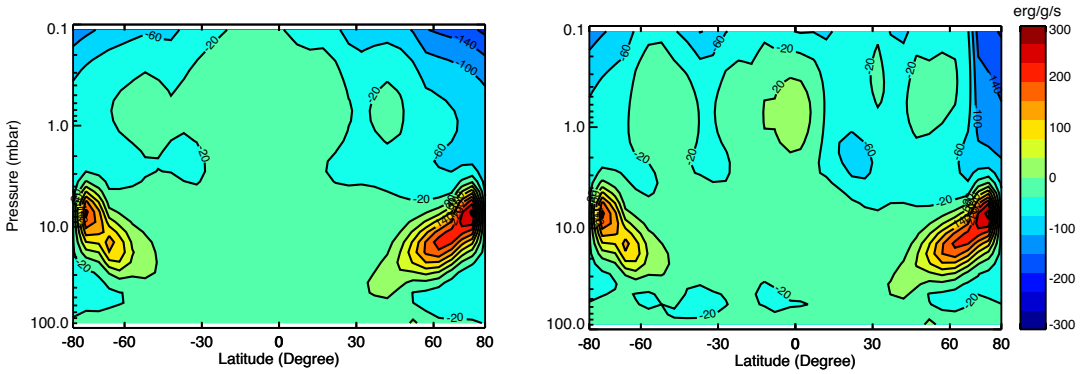

Figure 4.18. Zonal averaged net radiative forcing map in the stratosphere of Jupiter from 100 to 0.1 mbar for Voyager era (left) and Cassini era (right), based on the same aerosol heating rate.

Incorporating thermal infrared cooling rate maps we derived from Cassini CIRS and Voyager IRIS observations (chapter III), we derived the instantaneous net heating rate map during the Cassini flyby (Figure 4.18). If we assume the aerosol forcing is the same for the Voyager flyby, which may not be a bad assumption because we have seen the permanent polar caps for many years (West et al. 1992), we could also derive the same map for the Voyager era. The most prominent features are the strong polar heating sources at ~10-20 mbar. The "quasi-quadrennial oscillation"(QQO) type structure above 5 mbar dominates the low latitude region in the Cassini map but is missing in the Voyager map, showing a temporal variability of the radiative forcing. Without aerosol, we expect the net radiative heating rate would be positive in the low latitudes and negative in the high latitudes, leading to a radiation-driven circulation with the air rising from the equator and sinking at the poles. However, the existence of the dark and thick polar aerosol layer will inevitably

alter this situation, leading to the polar reverse subcells with the air rising from pole and sinking in the middle latitudes or low latitudes in the lower stratosphere, as predicted by the previous work in West et al. (1992). This polar subcell may help transport the fresh aggregates away from their polar source region to the middle latitudes, as we see from the Cassini retrieval results.

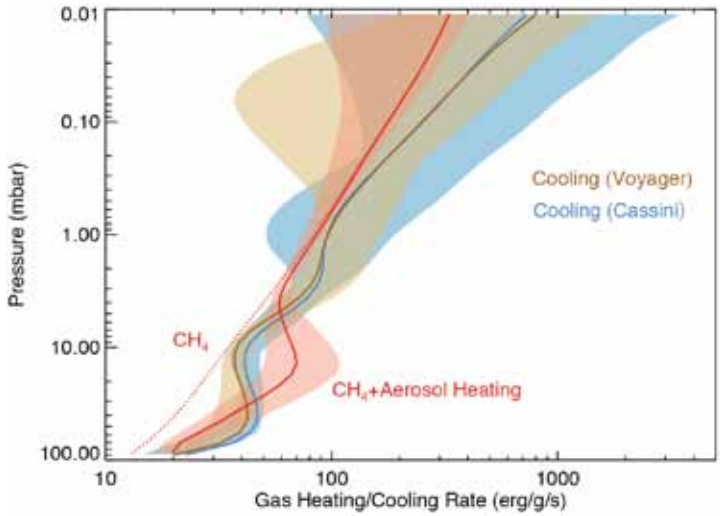

Figure 4.19. Instantaneous global energy balance of Jovian stratosphere in the Voyager and Cassini era. The CH_4 heating rate (dotted red line) and gas cooling rates are from chapter III.

In principle, we would expect the globally averaged annual-mean heating and cooling rates are balanced with each other. Since the obliquity of Jupiter is small, the seasonal radiative effect may not be large. In chapter III we found the globally averaged CH_4 heating rate is systematically smaller than the gas cooling rate, especially below 10 mbar, which led us suspect that there might be a missing heating source. In this study we found in fact the aerosols could enhance the total heating rate by a factor of 2 below 10 mbar. Therefore, the aerosols, primarily the polar aerosols, might a plausible candidate for the missing heating source. Figure 4.19 is the updated version of Figure 4.10 in chapter III. With aerosols, the balance between the heating and cooling rates are much better, especially in the lowest stratosphere below 50 mbar. However, the heating rate peaks at 10-20 mbar, where by coincidence the cooling rate profile has a local minimum, which is a transition region between the molecular hydrogen dominant cooling region and the hydrocarbon dominant

cooling region (chapter III). Therefore our aerosol heating is larger than the cooling rate around the heating peak. Again, this might be due to the vertical structure of aerosol profile retrieved from the NIR spectra. The recent retrieval from Kedziora-Chudczer and Bailey (2011) shows there might be no haze near 10 mbar. Instead, they have a upper haze layer around 5 mbar, which might solve the 10 mbar heating excess and at the same time compensate the cooling rate at around 5 mbar. Another possibility is that the instantaneous heating and cooling rates are not expected to exactly balance for each atmospheric level, especially around ~10 mbar where the radiative timescale is longer than the season (Figure 3.13). The temporal record of the temperature needs to be taken into account and a dynamical model may be required to explain this phenomena. The other possibility is the uncertainty of our vertical aerosol profile and retrieved parameters. The red shaded region is estimated by varying the aerosol heating rate by a factor of 2 from the sensitivity tests (section 4.4.3) but generally the error bars are hard to quantify. The aerosol may also have a cooling effect in the thermal infrared region although by far there is no evidence of the strong thermal emission by aerosols in the polar region. Aerosols do not help solve any possible imbalance above 5 mbar, where the dissipation of the gravity wave may serve as the candidate (chapter III).

4.4.3 Sensitivity Test

We perform a sensitivity test for the retrieved parameters (Figure 4.20). For the tropospheric hazes and clouds, we test two extreme cases: a completely dark cloud (or no cloud) and a completely white cloud for all the wavelengths. The results show that the cloud effect on the equatorial heating rate is large. If the bottom cloud does not reflect any light, the whole profile of the equatorial heating rate would reduce by 50% in the lower stratosphere and 30% in the upper region, which implies the cloud almost double the heating rate in the optically thin haze layer in the stratosphere. On the other hand, a white cloud only enhances the heating rate by 10%, because the bottom cloud from our retrieval results are already bright enough, with a mean single scattering albedo of ~0.9. In the south polar region, the cloud effect is smaller because the haze layer is optical thick compared

with the low latitudes. The cloud reflection also enhances the heating rate but only by 30% below 30 mbar and 10% in the region above. A completely white cloud would enhance the heating rate locally within the haze layer by ~20%.

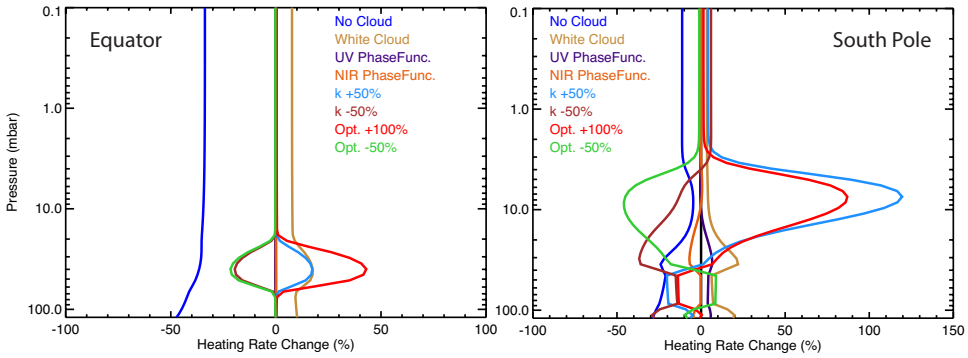

Figure 4.20. Sensitivity test for the aerosol heating rates at the equator region (left) and the south polar region (right). The cases are: with completely dark cloud (blue), with completely bright cloud (yellow), using the phase function of the UV filter for all wavelengths (purple), using the phase function of the NIR filter for all wavelengths (orange), increasing the imaginary part of the refractive index by 50% (light blue), reducing the imaginary part of the refractive index by 50% (brown), increasing the optical depth by 50% (red), and reducing the optical depth by 50% (green).

Aerosol heating seems not very sensitive to the phase functions. We test a case with the NIR phase function for all the wavelengths and another case with the UV phase function for all the wavelengths. The equatorial heating rate almost does not change and the change of the polar heating rate is also small (<10%). This might be understandable since the heating rate is an integrated effect, and the distribution of energy streams may not be very important. Therefore it implies that the heating rate probably does not require an accurate determination of the aerosol shape based on the realistic model such as our MIE and AGG models. We found the retrieved phase functions from the DHG model may be actually acceptable. That would be a practical method for the future aerosol heating rate calculation.

But the heating rate is sensitive to the total optical depth and single scattering albedo of the aerosols. Those may be the two most important parameters for the aerosol heating rate

calculation. The retrieved optical depth uncertainty is usually less than 20%. In the extreme testing cases, changing the aerosol optical depth by a factor of 2 will change the heating rate by less than 50% in the low latitudes and less than factor of 2 in the high latitudes. The retrieved uncertainty of the imaginary part of the refractive index is less than 20%, except for the very high latitudes, where it could reach 30%-40%. Another uncertainty is from the interpolation of the imaginary part as function of wavelength. In the heating rate calculation, we assume the logarithmic value of the imaginary part is linear with wavelength. This is not unrealistic but the uncertainty is hard to quantify. In the near blue wavelengths (~410 nm), Moreno and Sedano (1997) reported the values in the polar region less than 0.005, while our interpolation gives the value about 0.009. But reducing the imaginary part by a factor of 2 for all the wavelengths only decreases the heating rate by less than 20% in the low latitudes and less than 40% in the high latitudes, while increasing the k value by 50% will enhance the heating rate by a factor of 2 in the high latitudes and ~20% in the low latitudes. Taking all the considerations into account, we estimated our global mean heating rate may be good within a factor of 2 (Figure 4.19).

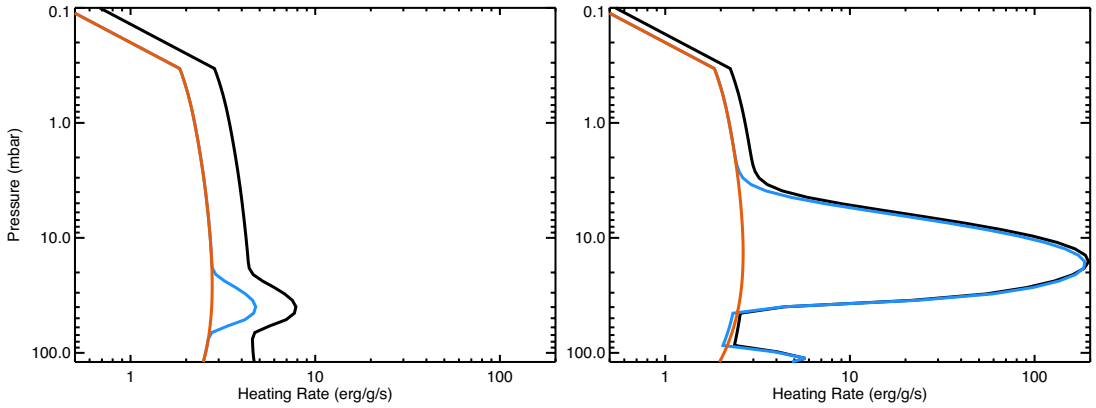

Figure 4.21: Heating rates (black) at equator (left) and south polar region (right, 65° S), in comparison with the heating from the CH_4 absorption (orange, from 0.2 to 1 μm) and that based on the single scattering approximation (blue).

We are also trying to find an approximate method for the aerosol heating rate calculation. Since the rigorous way, i.e., 32 streams in discrete ordinate method, is computational

expensive. For the practical reason, e.g., heating rate calculation in climate models and general circulation models, etc., the aerosol heating rate calculation cannot rely on the complicated radiative transfer solvers. Two-stream approximation is a good choice. Even simpler, we found in fact the single scattering approximation might be acceptable. Assuming the aerosol is a pure absorber with the effective absorption optical depth, $\tau_{abs} = \tau(1-\omega)$, where τ is the total extinction and ω is the single scattering albedo, the heating rate can be calculated very fast without CDISORT. The results are shown in Figure 4.21. The lower latitude result is smaller by a factor of ~1.5 compared with the accurate results. From Figure 4.20 we know this is the cloud reflection effect since we only consider the haze absorption. But in practice we can estimate the effect of the cloud by multiplying the heating rate by a factor of $(1+\omega_{cloud}g_2)$, where the ω_{cloud} is the single scattering albedo of the clouds and g_2 backscattering asymmetry factor in the DHG phase function. For the high latitudes, the approximation is pretty good (Figure 4.21) because the cloud reflection effect is less and haze optical depth is large. Therefore, for approximate calculations, single scattering estimation may be adequate.

4.4.4 Bond Albedo

Based on the retrieved hazes and clouds, the total reflected solar flux in the optical wavelengths is about 4.87 W/m^2. As a sanity check, we compute the planetary bond albedo as ~0.361, within the uncertainty range of the observations: 0.343 ± 0.032, by Hanel et al. (1981) based on the Voyager data. Furthermore, we can actually calculate the latitudinal contribution of the bond albedo (Figure 4.22). The latitudinal bond albedo is defined as the total reflected solar flux divided by the zonally averaged incoming solar flux for each latitudinal band. The latter is $F\cos\theta\,/\pi$, where F is the globally averaged incoming solar flux, θ is the latitude. The belts and zones are distinctly shown in the latitudinal bond albedo profile. The latitudinal albedo values are typically between 0.3 and 0.4, except for the north region where the albedo is between 0.26 and 0.28. This is primarily due to the darker haze absorption in the north pole. Direct integral over all filters and all phase angles of the Cassini ISS is possible. The integrated reflecting power, or latitudinal albedo profile

can be used to compare with our predicted values.

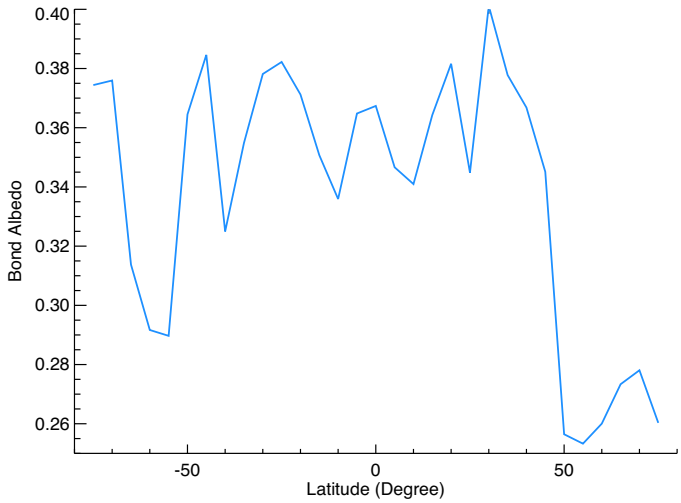

Figure 4.22: Bond albedo of Jupiter for each latitude based on the retrieved aerosol and cloud structures. The area-weighted mean planetary bond albedo value is ~0.361.

4.5. Concluding Remarks

In this study, we analyzed two types of observations to retrieve the Jovian aerosols. The spectral shape of the ground-based NIR data in the CH_4 bands are used to derive the latitudinal and vertical profiles of the aerosols, from which we can further determine the aerosol size, shape and optical properties in the optical wavelengths based on the UV and visible-IR limb-darkening profiles in multiple phase angles from Cassini ISS. Combining the two pieces of information, an aerosol heating rate map is obtained. Due to the limitation of the data quality, our retrieval assumes the aerosol properties are uniform with longitude and altitude, which can be relaxed with higher-quality data. The main results in our work are summarized as follows:

1. We distinguished two types of aerosols in the stratosphere of Jupiter. The Mie sphere particles are mainly located in the low latitudes between 40° S and 25° N, with a radius between 0.2 and 0.5 μm. The low latitude boundaries imply the hemispheric asymmetry of the haze properties. The rest of the stratosphere is

covered by the fractal aggregated particles composed of ~0.01 μm monomers. The number of the monomers is different for different regions, ranging from ~2000 in the middle latitudes to about 600-800 in the polar region below $\pm 65°$. In the even poleward regions, the number of monomers is even less. The derived imaginary part of the refractive index is about 0.02 in the UV filter and 0.001 in the NIR filters. The polar haze is darker and optically thicker than the lower latitude haze. The north polar haze is even darker than the south polar haze. The column density of the aerosols ranges from ~10^7 cm^{-2} at the low latitudes to ~10^{10} cm^{-2} in the polar region.

2. The tropospheric haze layer top (effective cloud top) is about 200-300 mbar, consistent in both NIR and Cassini ISS retrievals. The north polar cloud layer appears to be deeper than the south pole. The NIR retrieval shows the polar haze layer is at ~10-20 mbar, higher than the middle and low latitudes (~50 mbar), implying the possible particle source in the high latitudes and an efficient transport from the polar region to the middle latitudes. This hypothesis is consistent with the other two facts: (1) the monomer number in the fractal aggregates increases towards the lower latitudes; and (2) the aerosol heating in the polar region is large, which might induce a circulation from the poles to the midlatitudes.

3. The heating effect of the haze layer is prominent, especially in the polar region. The heating would have two effects: (1) it almost doubles the globally averaged heating rate in the lower stratosphere, therefore it helps solve the missing heat source problem. But the heating rate peaks at 10-20 mbar, which causes a new energy imbalance problem, which we attribute to the uncertainty of the vertical profile of aerosols retrieved from the NIR spectra. Future work might consider using the vertical structure from Kedziora-Chudczer and Bailey (2011); (2) the local heating at poles significantly changes the pattern of the solar energy depositions in the stratosphere of Jupiter, which will drive a stratospheric circulation in the high latitudes unless there is any strong cooling process. We predict the bond albedo

values as a function of latitude, with the area-weighted mean planetary albedo ~0.361.

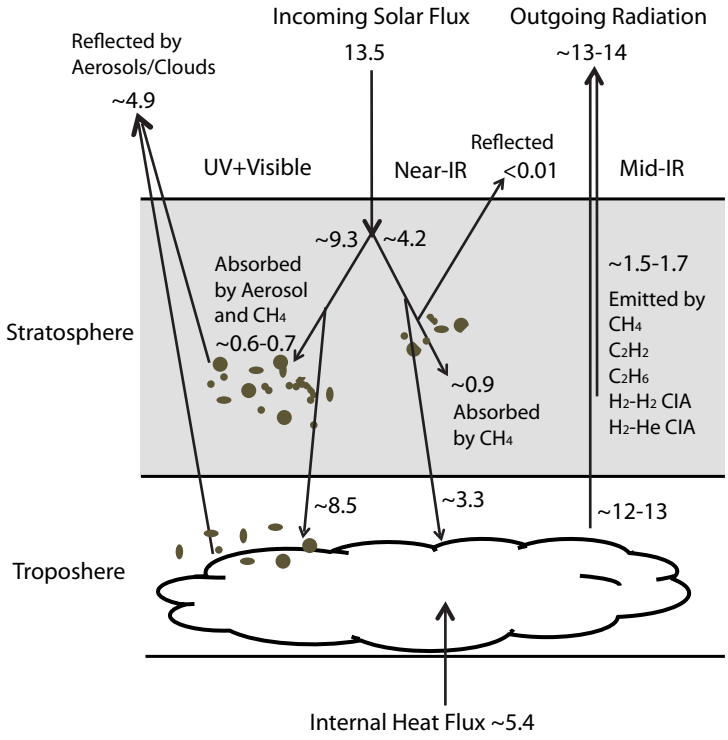

Figure 4.23: Estimate of the annual and global mean energy balance of Jovian atmosphere. The energy flux is in units of W/m^2.

Finally, we conclude this paper with a big picture of energy flows in the atmosphere of Jupiter, as shown in Figure 4.23. The globally averaged incoming solar flux at the top of atmosphere is about 13.5 W/m^2, with 9.3 W/m^2 in the optical region below 1 μm. About 0.6-0.7 W/m^2 is absorbed in the stratosphere, mainly by the polar aerosols and the rest by CH_4. The other ~8.5 W/m^2 penetrates into the troposphere. In total about 4.9 W/m^2 is reflected back, mainly by the tropospheric hazes and clouds. The total NIR solar flux is ~4.2 W/m^2. Since the reflection is negligible, about 0.9 W/m^2 of the solar flux is absorbed by the strong NIR CH_4 bands in the stratosphere and the rest in the troposphere. The total thermal emitting power by the atmosphere is about 13-14 W/m^2, based on the recent

detailed analysis by Li et al. (2012), and also the line-by-line thermal cooling model in our chapter III. The uncertainty range is mainly related to the temporal variability. Our previous work (chapter III) shows the stratospheric emitting power by the molecular hydrogen and hydrocarbons is about 1.5-1.7 W/m^2. Therefore the net thermal emitting power by the troposphere is 12-13 W/m^2. In summary, the troposphere is primarily heated by the internal heat flux (~5.4 W/m^2, Hanel et al. 1981) and incoming solar flux (~11.8 W/m^2) and cooled through the reflected sunlight (~4.9 W/m^2) and the outgoing longwave radiation (~12-13 W/m^2). The stratosphere is primarily heated by the NIR CH_4 bands (~0.9 W/m^2), with an important local (below 10 mbar) heating source mainly from the stratospheric hazes (~0.6-0.7 W/m^2), and cooled through the stratospheric emission (1.5-1.7 W/m^2). Again, stratospheric aerosols play an important role in the total energy balance in the stratosphere of Jupiter. Since the aerosol heating is mainly concentrated in the polar region, the efficient heat transport must occur to redistribute the energy in the lower stratosphere, possibly through the advection by stratospheric circulation driven by the differential heating or the underlying mechanical forcing (Conrath et al. 1990; West et al. 1992).

Chapter V

Jovian Stratosphere as a Chemical Transport System: Analytical Solutions and Numerical Simulations[§§]

They ascend and descend, ever inconstant. The strong and the weak change places, so that an invariable and compendious rule cannot be derived from them. It must vary as their changes indicate.

—*The chapters of I Ching, Ancient China*

Summary

We systematically investigated the possible analytical benchmark cases in both one- and two-dimensional (hereafter 1-D and 2-D) photochemical-advective-diffusive systems. We use the stratosphere of Jupiter as an example but the results can be applied to other planetary atmospheres. In the 1-D system, we show that CH_4 and C_2H_6 are mainly in diffusive equilibrium, and C_2H_2 profile can be approximated by the modified Bessel functions. In the 2-D system in the meridional plane, analytical solutions for two typical circulation patterns are derived. Simple tracer transport cases demonstrate that a short-lived species (such as C_2H_2) is dominated by the local chemical sources and sinks, while a long-lived species (such as C_2H_6) is significantly influenced by the circulation pattern. We find an equator-to-pole circulation could qualitatively explain the Cassini observations, but a pure diffusive transport process could not. For slowly rotating planets like the close-in extra-solar planets, the interaction between the advection by the zonal wind and chemistry might cause a phase lag in the final tracer distribution compared with the original source

[§§] To be submitted as: Zhang, X., Shia, R.L., Yung, Y.L., 2012. Jovian stratosphere as a chemical transport system: analytical solutions and numerical simulations.

distribution. The numerical simulation results from the 2-D Caltech/JPL chemical-transport model agree well with the analytical solutions for various cases.

5.1. Introduction

Jovian stratosphere is an ideal laboratory to study atmospheric tracer transport. The stratosphere is dominated by the hydrocarbon photochemistry, driven by the photolysis of the parent species, methane (CH_4), which is transported from the deep atmosphere. Two most abundant photochemical products, acetylene (C_2H_2) and ethane (C_2H_6), have properties to make them ideal tracers. First, besides CH_4, they show the most prominent features in the middle infrared emission spectra of Jupiter. Therefore their latitudinal and vertical distributions can be accurately determined. Second, their chemical lifetimes are different by about two orders of magnitude, ranging from several Earth years (C_2H_2) to several hundreds of Earth years (C_2H_6). That means they have different sensitivity to the transport. In fact, their latitudinal profiles (Nixon et al. 2007) show opposite trends, implying that the transport timescale is probably located within the two lifetimes. Third, their chemistry is relatively simple and most of the chemical reaction coefficients have been measured in the laboratory with small uncertainties. Unlike the other possible tracers, such as hydrogen cyanide (HCN) and carbon dioxide (CO_2), whose vertical distribution is not known (Lellouch et al. 2006), or aerosol, which might be affected by complicated microphysics, the simple combination of C_2H_2 and C_2H_6 contains a wealth of information of the stratospheric circulation on Jupiter.

Most of the previous studies focused on 1-D photochemical-diffusive models (e.g., Strobel 1974; Gladstone et al. 1996; Moses et al. 2005), which essentially ignore the latitudinal transport. The advantages of 1-D model are (1) it is numerically stable due to the nature of diffusive processes; (2) the computation is usually fast therefore it could include a very complicated network of chemical reactions (Moses et al. 2005). Once the horizontal and vertical advection terms are added, the model is subject to the numerical instability and

limited by the Courant-Friedrichs-Lewy (CFL) criterion, although the 2-D calculation is more realistic.

There is no definitive 2-D chemical-transport model for the stratosphere of Jupiter, taking into account the photochemistry, eddy and molecular diffusion, as well as the vertical and horizontal advection, although the existence of large-scale stratospheric circulation has been hypothesized since the 1990s (e.g., Conrath et al. 1990; West et al. 1992; Friedson et al. 1999) proposed that the horizontal eddy mixing processes dominate the transport of the SL9 debris in the stratosphere of Jupiter. Liang et al. (2005) used a 2-D chemical-diffusive model and found that the horizontal mixing might be enough to explain the latitudinal profiles of C_2H_2 and C_2H_6. A simple 1-D model in the latitudinal coordinate by Lellouch et al. (2006) shows that the dynamical pictures derived from HCN and CO_2 are not consistent with each other, and also not with the C_2H_2 and C_2H_6 profiles. Both Liang et al. (2005) and Lellouch et al. (2006) suggested that the *horizontal* eddy diffusivity is required to vary with latitude and altitude, leading to a more complicated picture. Note that the C_2H_6 distribution cited in their studies is decreasing from low latitudes to high latitudes. The recent analysis of Cassini and Voyager spectra has revealed more accurate latitudinal profiles of C_2H_6 (Nixon et al. 2010; chapter III), which are clearly enhanced in the high latitudes, especially in the Voyager era. One might also use a latitudinally varying *vertical* eddy diffusivity profile to explain the C_2H_6 *horizontal* distribution via changing its *vertical* slope for each latitude (Lellouch et al. 2006). However, this approach might be no different to a parameterization of a realistic horizontal and vertical advection process. Instead, a full photochemical-advective-diffusive model is needed to understand the tracer transport in the stratosphere of Jupiter.

As mentioned above, a very careful treatment in the numerical scheme is necessary in the model since the advection terms might lead to less accurate results. Shia et al. (1990) compared different numerical schemes and adopted the modified Prather scheme (Prather 1986) in the Caltech/JPL Kinetics chemical-transport model. In that paper, the authors derived several analytical solutions to validate the numerical results, in both 1-D and 2-D.

But the authors only used the analytic solutions to test the numerical scheme and did not pay much attention to the underlying physical implications of those analytical results. Therefore, some of their analytical results were only mathematically correct but physically counterintuitive (such as the negative chemical production rate, etc.).

On the other hand, the nonlinear feedbacks in the complicated photochemical-advective-diffusive system may blur the physical insights. A simple but realistic analytical solution can be considered as a benchmark case in understanding the basic behavior of the system, although only to some extent. Previous studies did not focus much on the analytical benchmark cases in the atmospheric tracer transport. In civil engineering, the regional Gaussian-plume dispersion models have been studies for many years, and the analytical solutions for the three-dimensional (3-D) diffusion equation could be obtained, although they may not be in the explicit forms (e.g., Lin and Hildemann, 1997). But those solutions are not useful for this study because (1) they are too complicated to show any physical insight; (2) they are restricted to a nonreactive contaminant; and (3) they are not in the planetary scale in which the sphericity of the planet should be taken into account. For the simple planetary-scale analytical solutions, besides Shia et al. (1990), previous attempts mainly focused on the 1-D solutions. Neglecting the chemistry, Chamberlain and Hunten (1987) derived the 1-D analytical solution with an exponential form of eddy and molecular diffusivities. Yelle et al. (2001) reported a 1-D diffusive equilibrium CH_4 profile, which is essentially a special case of that by Chamberlain and Hunten (1987). A systematic study of the available analytical cases in the planetary chemical-transport system has been lacking.

In this study we systematically investigate the behavior of the photochemical-advective-diffusive system through various representative analytical benchmark cases, such as for the long-lived species versus the short-lived species. Those analytical formulae will be used to validate the numerical simulations in which the numerical schemes are usually not trivial. We will focus on the hydrocarbons in the stratosphere of Jupiter because the observations of C_2H_2 and C_2H_6 show a beautiful example of the tracer transport systems. In order to derive the analytical formulae, we need to make some crucial assumptions, therefore we

will leave the detailed numerical modeling with realistic hydrocarbon chemistry and circulation pattern inferred from the radiative modeling (chapters III and IV) to the next step. Finally, our results could be applied to other planetary atmospheres as well.

This paper is structured as follows. In section 5.2, we will introduce the photochemical-advective-diffusive equation. In section 5.3, we will solve the equation in the 1-D system. In sections 5.4 and 5.5 we will focus on the 2-D systems in the meridional plane and zonal plane, respectively, followed by a short summary in section 5.6.

5.2. The Nature of the Problem

Let us first consider a chemical system in a fast rotating atmosphere. Therefore every quantity can be zonally averaged. We adopt the Transformed Eulerian Mean (TEM) formulation (Andrews et al. 1987, hereafter AHL1987) here. Chemical species are transported vertically and meridionally by the *residue mean circulation* driven by the diabatic circulation, with a vertical effective transport velocity w and a meridional effective transport velocity v. We also parameterize the eddy transport in a "diffusion" tensor that governs the tracer mixing processes both vertically and meridionally (See AHL1987, p. 354). Molecular diffusion dominates in the region above the homopause.

We adopt a vertical coordinate $z = H\ ln(p_s/p)$, where p is pressure and p_s is the reference pressure, which is usually taken to be 1 bar for giant planets. H is the pressure scale height of the background atmosphere. The meridonal coordinate is $y = a\theta$, where a is planetary radius, and θ is the latitude. We further define a dimensionless coordinate $\xi = z/H$. The volume mixing ratio of gas (or tracer) i is $\chi = N_i/N$, where N_i and N are the concentrations of gas and background atmosphere, respectively. The full form of zonal-averaged Eulerian mean transport equation for 2-D chemical system is (Shia et al. 1990):

$$\frac{\partial \chi}{\partial t} + v\frac{\partial \chi}{\partial y} + w\frac{\partial \chi}{\partial z}$$
$$-\frac{1}{cos\theta}\frac{\partial}{\partial y}[cos\theta(K_{yy}\frac{\partial \chi}{\partial y} + K_{yz}\frac{\partial \chi}{\partial z})] - e^{\xi}\frac{\partial}{\partial z}\left[e^{-\xi}\left(K_{zy}\frac{\partial \chi}{\partial y} + K_{zz}\frac{\partial \chi}{\partial z}\right)\right] = \frac{P-L}{N}, \quad (5.1)$$

where P and L are the chemical source and loss terms, respectively. Here we simplify this problem by using only the diagonal term of the diffusion tensor. This is particularly an advantage of the TEM formulism since the diabatic circulation has already taken into account the y-z direction transport so that we can neglect the K_{yz} and K_{zy} terms (AHL 1987, p. 380). Now the equation becomes

$$\frac{\partial \chi}{\partial t} + v\frac{\partial \chi}{\partial y} + w\frac{\partial \chi}{\partial z} - \frac{1}{cos\theta}\frac{\partial}{\partial y}(cos\theta\, K_{yy}\frac{\partial \chi}{\partial y}) - e^{\xi}\frac{\partial}{\partial z}\left(e^{-\xi}K_{zz}\frac{\partial \chi}{\partial z}\right) = \frac{P-L}{N}. \quad (5.2)$$

Strictly speaking, we should also consider the molecular diffusion above the homopause. However, since the residue circulation usually does not extend to such low pressure region, we just simply neglect it in the 2-D systems, especially for the horizontal diffusive cases. We will still consider molecular diffusion in the 1-D system.

For the numerical simulation, we use the Caltech/JPL kinetics model. The 1-D model is taken from the state-of-art chemical model for Jovian stratosphere from Moses et al. (2005). But we simplify it by assuming an isothermal atmosphere and using a simplified molecular and eddy diffusivity profiles (see section 5.2 for details), with the chemistry only including the C_2 hydrocarbons. This idealized model is indeed very close to the full chemistry model. Figure 5.1 shows the numerical results compare with the full chemistry model from Moses (2005), a reduced C_2 chemistry model with realistic chemistry and diffusivity, and our idealized model. The idealized model we introduced above agrees well with the full chemistry model. The simplified eddy diffusivity and molecular diffusivity are shown in Figure 5.2. For the 2-D model, we adopt the one from Shia et al. (1990) and assume there is only one tracer in the system. The details will be in section 5.4. The model with the zonal circulation is still under developed therefore we are not going to show the numerical results in this study.

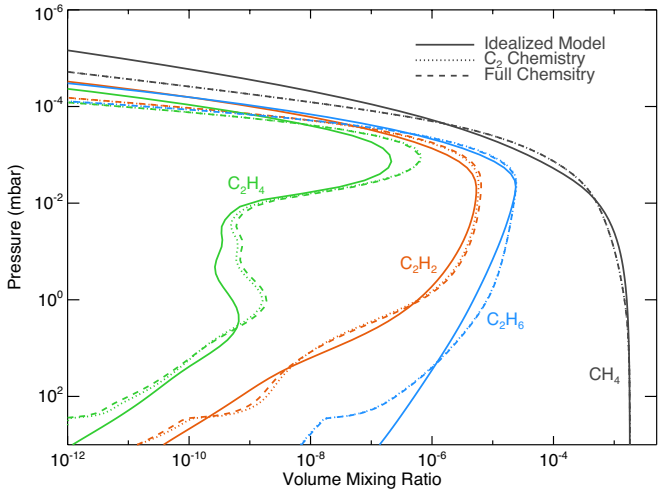

Figure 5.1. Simulated hydrocarbon profiles from the idealized model, the C_2 chemistry model (with realistic eddy and molecular diffusivities as the full chemistry model) and the full chemistry model.

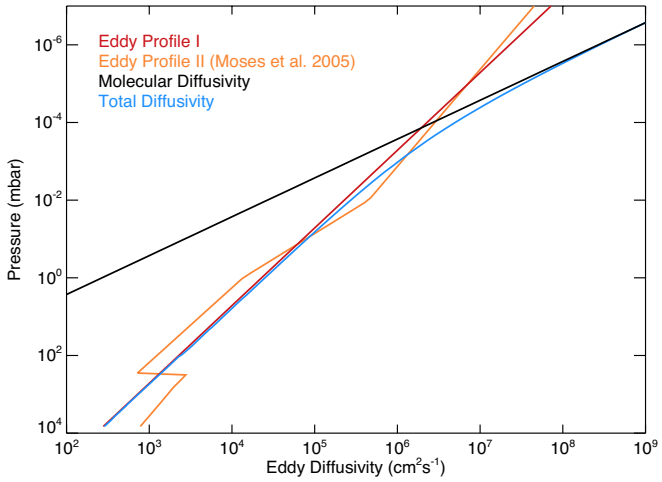

Figure 5.2. Profiles of eddy diffusivity and molecular diffusivity (for CH_4) in the idealized model (eddy profile I) compared with the full chemistry models (eddy profile II). The blue curve is the total diffusivity for the idealized model.

5.3. 1-D System

Let us first consider the 1-D problem as a globally averaged example. equation (5.1) can be reduced to:

$$\frac{\partial \chi}{\partial t} + w\frac{\partial \chi}{\partial z} - e^{\xi}\frac{\partial}{\partial z}\left(e^{-\xi}K_{zz}\frac{\partial \chi}{\partial z}\right) = \frac{P-L}{N}. \quad (5.3)$$

Above the homopause, the vertical diffusive flux $\phi_z = NK_{zz}\partial\chi/\partial z$ needs to be modified to include the molecular separation:

$$\phi_z = NK_{zz}\frac{\partial \chi}{\partial z} + ND_i\frac{\partial(N_i/N_{eq,i})}{\partial z}, \quad (5.4)$$

where D_i is the molecular diffusivity for gas component i in the background atmosphere, $N_{eq,i}$ is the equilibrium density profile with the scale height of species i.

After some manipulation, the molecular diffusive flux can be expressed as:

$$ND_i\frac{\partial(N_i/N_{eq,i})}{\partial z} = ND_i\frac{\partial \chi}{\partial z} + ND_i\left(\frac{1}{N}\frac{\partial N}{\partial z} - \frac{1}{N_{eq,i}}\frac{\partial N_{eq,i}}{\partial z}\right)\chi = ND_i\frac{\partial \chi}{\partial z} + \frac{f}{H}ND_i\chi, \quad (5.5)$$

where $f = m_i/m - 1$, m_i and m are the molecular mass of the species i and the background atmosphere, respectively. Therefore the total diffusive flux is

$$\phi_z = N(K_{zz} + D_i)\frac{\partial \chi}{\partial z} + fND_i\chi. \quad (5.6)$$

And the continuity equation becomes

$$\frac{\partial \chi}{\partial t} + w\frac{\partial \chi}{\partial z} - e^{\xi}\frac{\partial}{\partial z}\left\{e^{-\xi}\left[(K_{zz} + D_i)\frac{\partial \chi}{\partial z} + \frac{fD_i}{H}\chi\right]\right\} = \frac{P-L}{N}. \quad (5.7)$$

In order to derive analytical solutions, we assume some forms for eddy diffusivity and molecular diffusivity. Lindzen (1981) derived a wave-breaking turbulent mixing diffusivity, which satisfies $K_{zz} \propto N^{-1/2}$. The binary molecular diffusion theory implies $D_i \propto N^{-1}$. So in this paper we assume $K_{zz} = K_0 e^{\gamma\xi}$ and $D_i = D_0 e^{\xi}$, where γ~0.5. Therefore the homopause level is given by

$$\xi = \frac{1}{1-\gamma}\ln\left(\frac{K_0}{D_0}\right). \quad (5.8)$$

For an isothermal atmosphere which approximate Jovian stratosphere, we have $N = N_0 e^{-\xi}$. For the chemical production and loss terms, we assume $P = P_0 N_0 e^{\alpha\xi}$, and $L = L_0 N e^{\beta\xi}\chi = L_0 N_0 e^{(\beta-1)\xi}\chi$. For a non-divergent flow we take $w = w_0 e^{\xi} \propto N^{-1}$. For steady state with $\partial\chi/\partial t = 0$ in the vertical coordinate ξ

$$\left[D_0+K_0e^{(\gamma-1)\xi}\right]\frac{d^2\chi}{d\xi^2}+\left[fD_0-w_0H+K_0(\gamma-1)e^{(\gamma-1)\xi}\right]\frac{d\chi}{d\xi}-L_0H^2e^{(\beta-1)\xi}\chi$$
$$+P_0H^2e^{\alpha\xi}=0. \quad (5.9)$$

There is no general solution for this equation except for some specific conditions. If $\gamma=\beta=1$, we could obtain an analytical solution by following the derivation of Shia et al. (1990). If $\beta=1$ and $P_0=0$, there could be a solution expressed by the complicated hypergeometric functions. Alternatively, in our idealized model, we consider the cases with $\gamma\sim0.5$, which approximates the situation in Jovian stratosphere (Moses et al. 2005). For Jupiter, we take $T_0=150K$, $H=24.1\ km$, $K_0\sim280\ cm^2s^{-1}$, and $D_0\sim0.04\ cm^2s^{-1}$ for CH_4 and $0.03\ cm^2s^{-1}$ for C_2H_2 and C_2H_6 (scaled by the square root of molecular mass). Again, the results from this idealized model are very close to those from the state-of-art Jupiter model (Moses et al. 2005), as shown in Figure 5.1.

5.3.1 Cases without Wind

In principle, it is not proper to include vertical wind in the 1-D model because it will go to infinity when the atmospheric density drops to zero at the top boundary. So we set $w_0=0$. In Jovian stratosphere, we think the following conditions are useful.

5.3.1.1 Diffusive Equilibrium with no Chemistry $P_0=L_0=w_0=0$

If we neglect the chemistry, the equation is

$$\left[D_0+K_0e^{(\gamma-1)\xi}\right]\frac{d^2\chi}{d\xi^2}+\left[fD_0+K_0(\gamma-1)e^{(\gamma-1)\xi}\right]\frac{d\chi}{d\xi}=0. \quad (5.10)$$

Integrate and obtain the equation with a constant flux F:

$$\left[D_0+K_0e^{(\gamma-1)\xi}\right]\frac{d\chi}{d\xi}+fD_0\chi=\frac{FH}{N_0}. \quad (5.11)$$

The general solution is

$$\chi(\xi) = \frac{FH}{fN_0D_0} + C_1\left[D_0e^{(1-\gamma)\xi} + K_0\right]^{\frac{f}{\gamma-1}}. \quad (5.12)$$

If we set the bottom boundary condition $\chi(0) = \chi_0$, the solution would be

$$\chi(\xi) = \frac{FH}{fN_0D_0} + \left(\chi_0 - \frac{FH}{fN_0D_0}\right)\left(\frac{D_0e^{(1-\gamma)\xi} + K_0}{D_0 + K_0}\right)^{\frac{f}{\gamma-1}}. \quad (5.13)$$

The form is similar to the solution derived in an alternative way by Chamberlain and Hunten (1989). Now let us consider two interesting cases.

(1) Jupiter's CH_4 is transported upward from the interior. If we neglect photolysis, CH_4 will be governed by the diffusion equilibrium. This is generally true because the strong self-shielding effect will limit its photolysis efficiency below some pressure level. The upward flux is on the order of $10^9\ cm^2s^{-1}$, so FH/fN_0D_0 is ~10^{-5}. Compared with the CH_4 mixing ratio in the deep interior, determined by the thermochemistry (χ_0~1.8×10^{-3}), the flux term can be ignored. Rewrite the solution as

$$\chi(\xi) = \chi_0\left(\frac{D_0e^{(1-\gamma)\xi} + K_0}{D_0 + K_0}\right)^{\frac{f}{\gamma-1}}. \quad (5.14)$$

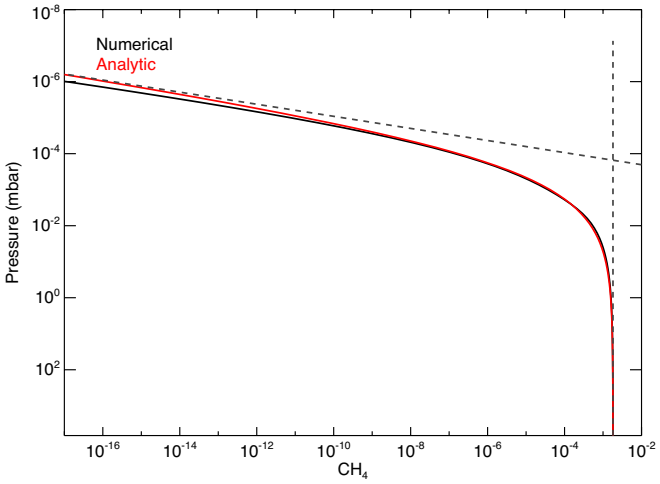

Figure 5.3. CH_4 from numerical simulations compared with analytical solutions. The dashed lines are asymptotic profiles.

Figure 5.3 shows the profile for CH_4 ($f \sim 6$). We can see the analytical solution matches the model result very well. In the lower atmosphere, where $D_0 \ll K_0$, it behaves as a constant mixing ratio profile; and in the upper atmosphere, where $D_0 \gg K_0$, note that the pressure $p \propto e^{-\xi}$, so it behaves as $\chi \propto p^f$.

(2) On the other hand, Jupiter's C_2H_6 is formed around the homopause region and transported downward. Therefore the flux term cannot be ignored. Interestingly, the flux is also on the order of $10^9 cm^2 s^{-1}$, so FH/fN_0D_0 is $\sim 10^{-5}$. For C_2H_6, $f \sim 12$. Since the source of C_2H_6 is in the upper atmosphere, we can set the lower boundary condition as $\chi_0 = 0$, so the solution becomes

$$\chi(\xi) = \frac{FH}{fN_0D_0}\left[1 - \left(\frac{D_0 e^{(1-\gamma)\xi} + K_0}{D_0 + K_0}\right)^{\frac{f}{\gamma-1}}\right]. \tag{5.15}$$

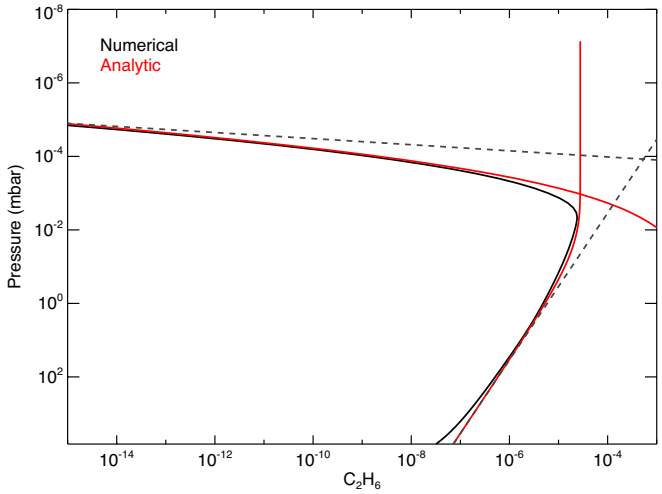

Figure 5.4. C_2H_6 from numerical simulations compared with analytical solutions. The dashed lines are asymptotic profiles.

Figure 5.4 shows that the analytical solution matches the model result very well below the homopause. In the lower atmosphere, where $D_0 \ll K_0$, we take the Taylor expansion of the solution and obtain

$$\chi(\xi, D_0 \ll K_0) = \frac{FH(e^{(1-\gamma)\xi} - 1)}{K_0 N_0 (1-\gamma)}, \tag{5.16}$$

which is consistent with the solution of the differential equation with $D_0 = 0$:

$$\chi(\xi, D_0 = 0) = C_2 + \frac{e^{(1-\gamma)\xi}}{K_0(1-\gamma)} \frac{FH}{N_0}. \tag{5.17}$$

The solution implies that the C_2H_6 mixing ratio profile should asymptotically behave as $\chi \propto p^{(\gamma-1)}$ (Figure 5.4).

Above the source region the flux changes sign (upward), but since the flux drops fast, we can still ignore it, and the following analytical solution still matches the model result well, similar to the condition of CH_4. Note that at the homopause $D_0 e^{(1-\gamma)\xi} = K_0$. So

$$\chi(\xi) = \chi_h \left[\frac{D_0 e^{(1-\gamma)\xi} + K_0}{2K_0} \right]^{\frac{f}{\gamma-1}}, \tag{5.18}$$

where χ_h is the volume mixing ratio at the homopause.

Therefore we conclude in Jovian stratosphere, CH_4 and C_2H_6 are mostly in the diffusive equilibrium, especially in the region where transport is much faster than the chemical processes.

5.3.1.2 Eddy/Molecular Diffusion with Chemical Loss and $P_0 = w_0 = 0$

If we add the source or loss term, we have to eliminate either eddy diffusion or molecular diffusion term in order to derive an analytical solution.

(1) If $K_0 = 0$ (well above the homopause), the equation is

$$\frac{d^2\chi}{d\xi^2} + f\frac{d\chi}{d\xi} - \frac{L_0 H^2}{D_0} e^{(\beta-1)\xi} \chi = 0. \tag{5.19}$$

(2) If $D_0 = 0$ (well below the homopause), the equation is

$$\frac{d^2\chi}{d\xi^2} + (\gamma - 1)\frac{d\chi}{d\xi} - \frac{L_0 H^2}{K_0} e^{(\beta-\gamma)\xi}\chi = 0. \quad (5.20)$$

They have similar form and note that the coefficients in the third terms, i.e., $\frac{L_0 H^2}{K_0} e^{(\beta-\gamma)\xi}$ and $\frac{L_0 H^2}{D_0} e^{(\beta-1)\xi}$, are the ratios of eddy or molecular transport timescale to the chemical loss timescale. The solutions can be expressed in terms of Bessel functions. For (1),

$$\chi = (\xi) = e^{\frac{-f\xi}{2}}\left[C_1 I_\nu\left(\frac{2H\sqrt{\frac{L_0}{D_0}}}{|\beta-1|}e^{\frac{(\beta-1)\xi}{2}}\right) + C_2 K_\nu\left(\frac{2H\sqrt{\frac{L_0}{D_0}}}{|\beta-1|}e^{\frac{(\beta-1)\xi}{2}}\right)\right], \quad (5.21)$$

where $\nu = |\frac{f}{\beta-1}|$, I_ν and K_ν are Modified Bessel functions of the first kind and second kind, respectively.

For (2),

$$\chi(\xi) = e^{\frac{(1-\gamma)\xi}{2}}\left[C_1 I_\nu\left(\frac{2H\sqrt{\frac{L_0}{K_0}}}{|\beta-\gamma|}e^{\frac{(\beta-\gamma)\xi}{2}}\right) + C_2 K_\nu\left(\frac{2H\sqrt{\frac{L_0}{K_0}}}{|\beta-\gamma|}e^{\frac{(\beta-\gamma)\xi}{2}}\right)\right], \quad (5.22)$$

where $\nu = |\frac{1-\gamma}{\beta-\gamma}|$.

A nice asymptotic property of Bessel function is that, for small x, $I_\nu(x) \propto x^\nu$ and $K_\nu(x) \propto x^{-\nu}$, therefore, in the limit of $L_0 \to 0$, the two solutions will be reduced back to the simple power law profile as function of p, consistent with what we showed in the no-chemistry cases in section 5.3.1.1.

Let us explain the C_2H_2 profile in the Jovian stratosphere. Above the homopause, the profile can be approximated by the diffusive equilibrium, as we showed for the C_2H_6 profile. It agrees very well with the numerical simulations (Figure 5.5). In the eddy diffusion dominated region, C_2H_2 is transported downward, with a major chemical loss by combining with a hydrogen atom to form C_2H_3. This is a three-body reaction so the rate is given by $L = k[C_2H_2][H]N$, where $[H]$ is the number density of hydrogen atom. In fact

the product $k[H]N$ is approximately constant through the lower region ($\sim 10^8\ cm^{-3}s^{-1}$). Therefore β is roughly 0 for C_2H_2. This is not surprising because the major sources of hydrogen atoms are from (1) C_2H_2 photolysis directly; (2) C_2H+H_2; (3) C_2+H_2. Note that the latter two reactions are actually driven by C_2H_2 photolysis as well. So the production rate of hydrogen atom is proportional to the C_2H_2 abundance. On the other hand, the loss of hydrogen atom is also through combining with C_2H_2 and C_2H_3, these reaction rates are also roughly proportional to C_2H_2 and background atmospheric abundance. Therefore by equating the sources and sinks of the hydrogen atom, the product $k[H]N$ can be expressed by several reaction constants and therefore is roughly a constant.

Assume $\beta \sim 0$ and $L_0 \sim k[H]N \sim 10^8\ cm^{-3}s^{-1}$, and we obtain $2H\sqrt{L_0/K_0} \sim 30$. We need to ignore the I_ν term because the $\chi(\xi)$ is expected to increase with altitude provided the source region above. The analytical C_2H_2 profile is

$$\chi(\xi) = C_1 e^{\frac{(1-\gamma)\xi}{2}} K_\nu\left(\frac{2H\sqrt{L_0/K_0}}{|\beta-\gamma|} e^{\frac{(\beta-\gamma)\xi}{2}}\right) = C_1 e^{\frac{\xi}{4}} K_\nu\left(15e^{\frac{\xi}{4}}\right), \qquad (5.23)$$

where $\nu = \left|\frac{1-\gamma}{\beta-\gamma}\right| = 1$.

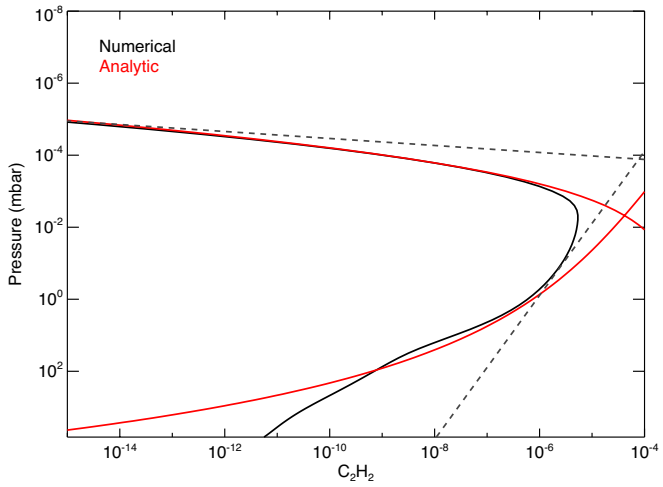

Figure 5.5. C_2H_2 from numerical simulations compared with analytical solutions. The dashed lines are asymptotic profiles.

It is shown in Figure 5.5. The profile qualitatively agrees with the model result, although not good as the CH_4 and C_2H_6 cases in section 5.3.1.1 because we simplified the chemistry. But we conclude that the C_2H_2 profile on Jupiter can be approximated by the modified Bessel function K_ν.

5.3.1.3 Eddy/Molecular Diffusion with Chemical production and $L_0 = w_0 = 0$

One can also do the same for the net production case (without chemical loss):

$$\left[D_0+K_0e^{(\gamma-1)\xi}\right]\frac{d^2\chi}{d\xi^2}+\left[fD_0+K_0(\gamma-1)e^{(\gamma-1)\xi}\right]\frac{d\chi}{d\xi}+P_0H^2e^{\alpha\xi}=0. \quad (5.24)$$

This equation could have an analytical solution with hypergeometric function. For special cases:

(1) If $K_0 = 0$ (well above the homopause), the equation is

$$\frac{d^2\chi}{d\xi^2}+f\frac{d\chi}{d\xi}+\frac{P_0H^2}{D_0}e^{\alpha\xi}=0. \quad (5.25)$$

(2) If $D_0 = 0$ (well below the homopause), the equation is

$$\frac{d^2\chi}{d\xi^2}+(\gamma-1)\frac{d\chi}{d\xi}+\frac{P_0H^2}{K_0}e^{(\alpha+1-\gamma)\xi}=0. \quad (5.26)$$

The solutions are similar:

For (1),

$$\chi(\xi)=\frac{P_0H^2}{D_0(f\alpha+\alpha^2)}e^{\alpha\xi}+C_1e^{-f\xi}+C_2. \quad (5.27)$$

For (2),

$$\chi(\xi)=\frac{P_0H^2}{K_0\alpha(\alpha+1-\gamma)}e^{(\alpha+1-\gamma)\xi}+C_1e^{(1-\gamma)\xi}+C_2. \quad (5.28)$$

The two solutions will approach the "no-chemistry" solutions we derived in section 5.3.1.1, at the limit of $P_0 \to 0$. It looks like an additional profile determined by the production rate and "superimposed" on the diffusive equilibrium profile.

5.3.2 Cases with Wind

If we artificially add wind in the 1-D case, it is also useful since we can roughly simulate the effect of vertical transport in the 2-D case.

(a) From equation (5.9) we can make a simple parameterization. If we define a new "mass factor" $f^* = f - \frac{w_0 H}{D_0}$, the equation will be reduced to the "wind-free case" that we discussed in section 5.3.1. The physical meaning of the correct factor $w_0 H/D_0$ is the ratio of molecular diffusive timescale to the vertical advection timescale. Naively we can imagine an upward wind tends to make the gas molecule "lighter," while a downward wind will make the species "heavier." This result can be directly applied to CH_4, as shown in Figure 5.6, with $w_0 = \pm 5\times10^{-8}\ cm\ s^{-1}$. Since it is not proper to put the wind into numerical simulations, otherwise it will cause numerical problems. We only show the analytical solutions for qualitative illustration. The results show the upward wind will lift up the homopause and downward wind will push it down. It actually transports the more/less-abundant species from below/above and thus increases/decreases the mixing ratio of CH_4.

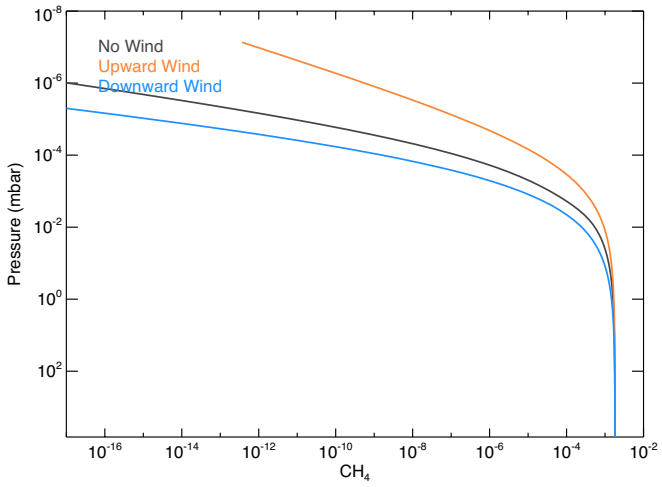

Figure 5.6. Analytical CH_4 profiles from the cases with and without wind. $w_0 = \pm 5\times10^{-8}\ cm\ s^{-1}$.

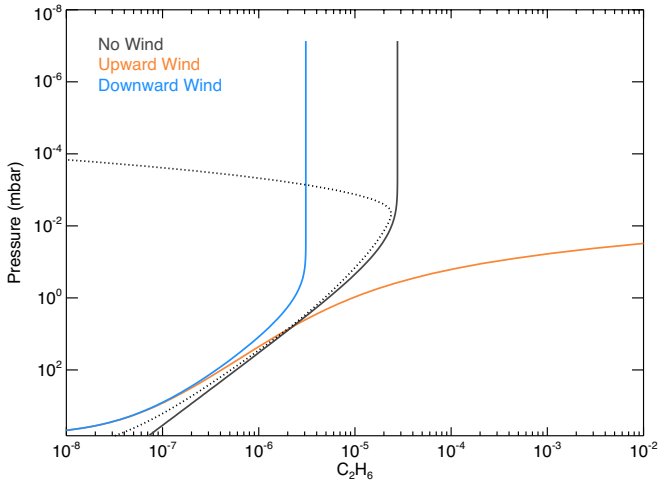

Figure 5.7. Analytical C_2H_6 profiles from the cases with and without wind. $w_0 = \pm 1\times10^{-6}\ cm\ s^{-1}$. The dotted line is with the molecular diffusion in the upper atmosphere.

Since in the 2-D simulation we generally care about is the region below the homopause and also most of the latitudinal observations are located around 1 mbar or below for Jupiter, we present solutions with only eddy diffusivity and wind transport. These solutions would be different from the solutions before. Consider a long-lived species such as C_2H_6 with a source flux from above:

$$\left[K_0 e^{(\gamma-1)\xi}\right]\frac{d^2\chi}{d\xi^2} + \left[-w_0 H + K_0(\gamma-1)e^{(\gamma-1)\xi}\right]\frac{d\chi}{d\xi} = 0. \tag{5.29}$$

The solution is

$$\chi(\xi) = -\frac{F}{w_0 N_0} + C_2 e^{\frac{w_0 H e^{(1-\gamma)\xi}}{K_0(1-\gamma)}}. \tag{5.30}$$

If we assume $\chi(\xi) = 0$ as the bottom boundary condition, the solution is

$$\chi(\xi) = \frac{F}{w_0 N_0}\left(e^{\frac{w_0 H(e^{(1-\gamma)\xi}-1)}{K_0(1-\gamma)}} - 1\right). \tag{5.31}$$

Compared with the solution without wind, this solution could have a different slope, depends on the ratio of diffusion timescale to the advection timescale, $w_0 H/K_0$. Figure 5.7 shows two typical vertical profiles of C_2H_6, with an upward wind and downward wind ($\sim w_0 = \pm 1\times10^{-6}\ cm\ s^{-1}$) respectively, compared with the wind-free theoretical curve. It

shows an upward wind will increase the mixing ratio in the higher altitude by preventing it from being transported downward but a downward wind tends to lower down the mixing ratio of C_2H_6. Therefore, if we neglect the horizontal transport, the rising air at the equator and sinking air at the poles will result in more C_2H_6 at equator and less C_2H_6 at poles, which is opposite to the CIRS measurements (chapter III). That suggests the horizontal transport is actually important and a "pseudo-2D" photochemical model is not sufficient to explain the observations.

(b) When we add the chemical source/loss, the equation cannot be solved analytically in general, unless we neglect the eddy diffusion term

$$\frac{d\chi}{d\xi} - \frac{P_0 H}{w_0} e^{\alpha\xi} + \frac{L_0 H}{w_0} e^{(\beta-1)\xi}\chi = 0. \tag{5.32}$$

To simplify the calculation, we further assume $\alpha = \beta - 1$ and $\beta \neq 0$, the solution is

$$\chi(\xi) = \frac{P_0}{L_0} + C_1 \mathrm{e}^{-\frac{L_0 H}{w_0 \beta} e^{\beta\xi}}. \tag{5.33}$$

Instead, if we consider a zonal-direction 1-D model to simulate the abundance distribution with a periodic boundary condition, the solution could be applied to the dayside-nightside transport on Venus or tidally locked extra-solar planets. See discussion in section 5.5, where we actually consider a 2-D problem in the zonal plane.

5.4. 2-D System in the Meridional Plane

Now let us consider the 2-D problem below the homopause. We still assume the atmosphere to be isothermal and barotropic. From previous experience, we note that the equation with eddy diffusion ($\gamma \sim 0.5$), advection and chemistry all together cannot be solved analytically, even in the 1-D case. Therefore we are trying to decouple the processes. We need to introduce the streamfunction ψ so that

$$v = -\frac{1}{\cos\theta} e^{\xi} \frac{\partial}{\partial z}\left(e^{-\xi}\psi\right), \tag{5.34}$$

$$w = \frac{1}{\cos\theta}\frac{\partial\psi}{\partial y}. \tag{5.35}$$

5.4.1 Without Chemistry $P_0 = L_0 = 0$

Let us first ignore the chemistry. The steady state of equation (5.2) becomes

$$v\frac{\partial \chi}{\partial y} + w\frac{\partial \chi}{\partial z} - \frac{1}{\cos\theta}\frac{\partial}{\partial y}\left(\cos\theta\ K_{yy}\frac{\partial \chi}{\partial y}\right) - e^{\xi}\frac{\partial}{\partial z}(e^{-\xi}K_{zz}\frac{\partial \chi}{\partial z}) = 0. \qquad (5.36)$$

(1) If we also neglect the eddy diffusion term, the solution would be trivial: for any given streamfunction ψ, the solution of equation

$$v\frac{\partial \chi}{\partial y} + w\frac{\partial \chi}{\partial z} = 0 \qquad (5.37)$$

is $\chi(\theta,\xi) = G(e^{-\xi}\psi(\theta,\xi))$, where G is any functional form determined by the boundary conditions. $e^{-\xi}\psi$ is the mass-weighted stream function.

(2) If ignoring the advection term, we now have a 2-D diffusion equation:

$$\frac{1}{a^2\cos\theta}\frac{\partial}{\partial\theta}\left(\cos\theta\ K_{yy}\frac{\partial \chi}{\partial\theta}\right) + \frac{e^{\xi}}{H^2}\frac{\partial}{\partial\xi}\left(K_0 e^{(\gamma-1)\xi}\frac{\partial \chi}{\partial\xi}\right) = 0, \qquad (5.38)$$

where we assume K_{yy} is a constant. But this solution will be trivial too because there is no horizontal diffusion flux without chemical source. Therefore it will be reduced to the 1-D case.

5.4.2 With Chemistry

Let us introduce the chemistry. The source and sink terms are parameterized as: $P(\theta,\xi) = P_0 N_0 e^{\alpha\xi} f(\theta)$, and $L(\theta,\xi) = L_0 N e^{\beta\xi} g(\theta)\chi = L_0 N_0 e^{(\beta-1)\xi} g(\theta)\chi$. If representing the photochemical source and sink, $f(\theta)$ is more like to be symmetric with latitude for Jupiter (obliquity is almost zero), for example, $f(\theta) \sim (\cos\theta)^n$.

5.4.2.1 Pure Advection Cases

First we neglect the eddy diffusion terms. Consider a more general case:

$$v\frac{\partial \chi}{\partial y} + w\frac{\partial \chi}{\partial z} - p + l\chi = 0, \tag{5.39}$$

where $p = P(\theta, \xi)/N$, and $l\chi = L(\theta, \xi)/N$.

So the equation becomes

$$\frac{e^{\xi}}{aH\cos\theta}\left(\frac{\partial\left(e^{-\xi}\psi\right)}{\partial\theta}\frac{\partial\chi(\theta,\xi,G)}{\partial\xi} - \frac{\partial\left(e^{-\xi}\psi\right)}{\partial\xi}\frac{\partial\chi(\theta,\xi,G)}{\partial\theta}\right) - p + l\chi(\theta,\xi,G) = 0. \tag{5.40}$$

Note that for any functional form G, the following relationship holds true:

$$\frac{\partial\left(e^{-\xi}\psi\right)}{\partial\theta}\frac{\partial G(e^{-\xi}\psi)}{\partial\xi} - \frac{\partial\left(e^{-\xi}\psi\right)}{\partial\xi}\frac{\partial G\left(e^{-\xi}\psi\right)}{\partial\theta} = 0. \tag{5.41}$$

Therefore, given $p(\theta,\xi) = P_0 e^{(\alpha+1)\xi} f(\theta)$, and $l(\theta,\xi) = L_0 e^{\beta\xi} g(\theta)$, and $\psi(\theta,\xi) = \psi_1(\theta)\psi_2(\xi)$, we wish to find a solution with separate variables in the form of $\chi(\theta,\xi,G) = A_1(\theta)A_2(\xi) + K_1(\theta)K_2(\xi)G(e^{-\xi}\psi)$. Substituting into the equation (5.40), we obtain the following two ODEs:

$$\frac{d\ln(\psi_1)}{d\theta}\frac{d\ln(K_2)}{d\xi} - \frac{d\ln\left(e^{-\xi}\psi_2\right)}{d\xi}\frac{d\ln(K_1)}{d\theta} + \frac{L_0 aHg(\theta)\cos\theta\, e^{\beta\xi}}{\psi_1\psi_2} = 0, \tag{5.42}$$

and

$$\frac{d\ln(\psi_1)}{d\theta}\frac{d\ln(A_2)}{d\xi} - \frac{d\ln\left(e^{-\xi}\psi_2\right)}{d\xi}\frac{d\ln(A_1)}{d\theta} + \frac{L_0 aHg(\theta)\cos\theta\, e^{\beta\xi}}{\psi_1\psi_2} - \frac{P_0 aHf(\theta)\cos\theta\, e^{(\alpha+1)\xi}}{A_1\psi_1 A_2\psi_2} = 0. \tag{5.43}$$

The first equation is a special case of the second one. In order to get the analytical solution, we have to choose $f(\theta)$ and $g(\theta)$ carefully. We discuss the following two conditions:

(i) Let $\frac{d\ln(\psi_1)}{d\theta} = r\frac{d\ln(A_1)}{d\theta}$, in order to solve A_2, we need to diminish the θ terms in the production and loss terms, i.e., both $\frac{g(\theta)\cos\theta}{d\psi_1/d\theta}$ and $\frac{f(\theta)\cos\theta}{A_1 d\psi_1/d\theta}$ should be constants. Note that

$w(\theta,\xi)=\frac{1}{\cos\theta}\frac{\partial\psi}{\partial y}$, therefore $g(\theta)/w(\theta,\xi)$ is a constant in latitude. However, the vertical velocity $w(\theta,\xi)$ could be positive or negative for different latitudes, therefore $g(\theta)$ has to be positive or negative for the corresponding latitude, so does $f(\theta)$. That means the production and loss rates could change sign from latitude to latitude, which is less realistic. Mathematically we can still solve $\chi(\theta,\xi)$. In principle, for each given r (and thus A_1 and $f(\theta)$), there might exist an analytical solution for $A(\theta,\xi)$. On the other hand, the only r term in the solution of $K(\theta,\xi)$ will be in the form of $\left(e^{-\xi}\psi\right)^r$ and therefore can be absorbed in the $G(e^{-\xi}\psi)$ in $\chi(\theta,\xi,G)$. The analytical solution from Shia et al. (1990) corresponds to the situation that $r=0$ and $g(\theta)=f(\theta)$. For $r\neq 0$, it might end up with a solution with exponential integral functions.

(ii) Now we focus on the other possibility that the production and loss rate do not change sign for all latitudes. We assume $\frac{d\ln(A_2)}{d\xi}=r\frac{d\ln(e^{-\xi}\psi_2)}{d\xi}$, so we have $A_2=k\left(e^{-\xi}\psi_2\right)^r$. In order to solve A_1, we need to diminish the ξ terms in the production and loss terms, i.e., both $\frac{e^{(\beta-1)\xi}}{d(e^{-\xi}\psi_2)/d\xi}$ and $\frac{e^{\alpha\xi}}{k(e^{-\xi}\psi_2)^r d(e^{-\xi}\psi_2)/d\xi}$ are constants. Note that $d(e^{-\xi}\psi_2)/d\xi$ is the altitudinal dependence of the horizontal velocity. For a fully closed streamfunction, for example, the air rises from the equator, flows to the polar regions in the upper stratosphere, sinks at poles and comes back in the lower stratosphere, the horizontal velocity has to change sign with altitude. Therefore the production and loss terms would change sign with altitude accordingly. This is also less realistic. However, if we choose to study part of stratosphere, this is still useful for analyzing the behavior of the system. For simplicity, we let $\psi_2(\xi)=e^{\lambda\xi}$, $\beta=\lambda$, and $\alpha=(r+1)(\lambda-1)$. Therefore, for each given r (and thus α), there might exist an analytical solution for $A(\theta,\xi)$. The ODE is

$$\frac{dA_1}{d\theta}-\left(\frac{rd\ln(\psi_1)}{d\theta}+\frac{L_0aHg(\theta)\cos\theta}{(\lambda-1)\psi_1}\right)A_1+\frac{P_0aHf(\theta)\cos\theta}{k(\lambda-1)\psi_1}=0. \qquad (5.44)$$

If we define:

$$X(\theta) = \frac{P_0 aHf(\theta)\cos\theta}{k(\lambda-1)\psi_1}, \tag{5.45}$$

$$Y(\theta) = \frac{rd\ln(\psi_1)}{d\theta} + \frac{L_0 aHg(\theta)\cos\theta}{(\lambda-1)\psi_1}. \tag{5.46}$$

The solution is

$$A_1(\theta) = \mathrm{e}^{\int Y d\theta}\left[C_1 - \int X\mathrm{e}^{-\int Y d\theta} d\theta\right], \tag{5.47}$$

and also similarly,

$$K_1(\theta) = C_2\mathrm{e}^{\int Y d\theta}. \tag{5.48}$$

The integratable $\int X\mathrm{e}^{-\int Y d\theta} d\theta$ has a very strict requirement. We now discuss two typical streamfunctions:

(a) Imagine an axis-symmetric equator-to-pole circulation pattern in each hemisphere. We introduced a simple streamfunction $\psi(\theta,\xi) = aw_0 e^{\lambda\xi}\sin\theta\cos^2\theta$, so $w(\theta,\xi) = w_0 e^{\lambda\xi}(\cos^2\theta - 2\sin^2\theta)$, and $v(\theta,\xi) = \frac{(1-\lambda)aw_0 e^{\lambda\xi}}{H}\sin\theta\cos\theta$. The air rises from the equator and sinks at poles in the upper part of the circulation ($\lambda < 1$) and reversed in the lower part ($\lambda > 1$). Although we cannot find a way to unify the whole circulation pattern, the two branches could share the same form of solution. We assume $g(\theta) = \sin^2\theta$, so that

$$Y(\theta) = \frac{rd\ln(\psi_1)}{d\theta} + \frac{L_0 H\sin\theta}{(\lambda-1)w_0\cos\theta}, \tag{5.49}$$

and therefore we have

$$\mathrm{e}^{\int Y d\theta} = (\cos\theta)^{\frac{-L_0 H}{(\lambda-1)w_0}}\psi_1^r. \tag{5.50}$$

For simplicity we take $r = -1$ (so that $\alpha = 0$) and $f(\theta) = (\cos\theta)^{\frac{-L_0 H}{(\lambda-1)w_0}}$:

$$\int X\mathrm{e}^{-\int Y d\theta} d\theta = \int \frac{P_0 aH\cos\theta}{k(\lambda-1)} d\theta = \frac{P_0 aH\sin\theta}{k(\lambda-1)}, \tag{5.51}$$

and

$$A_1(\theta) = \frac{(\cos\theta)^{\frac{-L_0 H}{(\lambda-1)w_0}}}{aw_0 \sin\theta \cos^2\theta}\left[C_1 - \frac{P_0 aH \sin\theta}{k(\lambda-1)}\right], \tag{5.52}$$

$$A_2(\xi) = ke^{(1-\lambda)\xi}. \tag{5.53}$$

Similarly, we obtain $K(\theta,\xi)$ for any given r:

$$K(\theta,\xi) = C_2\,(\cos\theta)^{\frac{-L_0 H}{(\lambda-1)w_0}}\left(e^{-\xi}\psi\right)^r. \tag{5.54}$$

The only r term in the solution of $K(\theta,\xi)$ is in the form of $\left(e^{-\xi}\psi\right)^r$ and therefore can be absorbed into $G(e^{-\xi}\psi)$ in $\chi(\theta,\xi,G)$.

Therefore, for the streamfunction given by $\psi(\theta,\xi) = aw_0 e^{\lambda\xi}\sin\theta\cos^2\theta$, with a production rate $P(\theta,\xi) = P_0 N_0\,(\cos\theta)^{\frac{-L_0 H}{(\lambda-1)w_0}}$, and a loss rate $L(\theta,\xi) = L_0 N_0 e^{(\lambda-1)\xi}\sin^2\theta\,\chi$, the final solution for $\chi(\theta,\xi)$ is

$$\chi(\theta,\xi) = (\cos\theta)^{\frac{-L_0 H}{(\lambda-1)w_0}}\left[G\left(e^{-\xi}\psi\right) - \frac{P_0 aH\sin\theta}{(\lambda-1)e^{-\xi}\psi}\right]. \tag{5.55}$$

(b) Imagine the air rises from the south pole and sinks at the north pole in the upper atmosphere and comes back to the south pole in the lower atmosphere. The streamfunction may look like $\psi(\theta,\xi) = aw_0 e^{\lambda\xi}\cos^2\theta$, so $w(\theta,\xi) = -2w_0 e^{\lambda\xi}\sin\theta$, and $v(\theta,\xi) = \frac{(\lambda-1)aw_0 e^{\lambda\xi}}{H}\cos\theta$. As shown in (a), the same form of solution applies to the upper part of the circulation ($\lambda < 1$) as well as the lower part ($\lambda > 1$). We assume $g(\theta) = 1$, so that

$$Y(\theta) = \frac{rd\ln(\psi_1)}{d\theta} + \frac{L_0 H}{(\lambda-1)w_0\cos\theta}. \tag{5.56}$$

and we obtain

$$\mathrm{e}^{\int Y d\theta} = \left(\frac{1+\sin\theta}{1-\sin\theta}\right)^{\frac{L_0 H}{2(\lambda-1)w_0}}\psi_1^r. \tag{5.57}$$

Again, we take $r = -1$ (so that $\alpha = 0$) and $f(\theta) = \left(\frac{1+\sin\theta}{1-\sin\theta}\right)^{\frac{L_0 H}{2(\lambda-1)w_0}}$:

$$\int X\mathrm{e}^{-\int Y d\theta} d\theta = \int \frac{P_0 aH\cos\theta}{k(\lambda-1)} d\theta = \frac{P_0 aH\sin\theta}{k(\lambda-1)}, \tag{5.58}$$

and

$$A_1(\theta) = \frac{\left(\frac{1+\sin\theta}{1-\sin\theta}\right)^{\frac{L_0 H}{2(\lambda-1)w_0}}}{aw_0\cos^2\theta}\left[C_1 - \frac{P_0 aH\sin\theta}{k(\lambda-1)}\right], \tag{5.59}$$

$$A_2(\xi) = ke^{(1-\lambda)\xi}. \tag{5.60}$$

Similarly, we obtain $K(\theta,\xi)$ for any given r:

$$K(\theta,\xi) = C_2\left(\frac{1+\sin\theta}{1-\sin\theta}\right)^{\frac{L_0 H}{2(\lambda-1)w_0}}\left(e^{-\xi}\psi\right)^r. \tag{5.61}$$

The only r term in the solution of $K(\theta,\xi)$ is in the form of $\left(e^{-\xi}\psi\right)^r$ and therefore can be absorbed into $G(e^{-\xi}\psi)$ in $\chi(\theta,\xi,G)$.

Therefore, for the streamfunction given by $\psi(\theta,\xi) = aw_0 e^{\lambda\xi}\cos^2\theta$, with a production rate $P(\theta,\xi) = P_0 N_0\left(\frac{1+\sin\theta}{1-\sin\theta}\right)^{\frac{L_0 H}{2(\lambda-1)w_0}}$, and a loss rate $L(\theta,\xi) = L_0 N_0 e^{(\lambda-1)\xi}\chi$, the final solution for $\chi(\theta,\xi)$ is

$$\chi(\theta,\xi) = \left(\frac{1+\sin\theta}{1-\sin\theta}\right)^{\frac{L_0 H}{2(\lambda-1)w_0}}\left[G\left(e^{-\xi}\psi\right) - \frac{P_0 aH\sin\theta}{(\lambda-1)e^{-\xi}\psi}\right]. \tag{5.62}$$

5.4.2.2 Cases with Long-lived and Short-lived Species

We now test our numerical model against analytical solutions. The numerical model has a resolution 80×33, with 80 pressure grids from 100 mbar to 5 mbar, and 33 latitudes from 85° S to 85° N with increments of 5°. Two numerical schemes are tested. In the first scheme, called the "normal 2-D" mode, the photochemistry, diffusion, and advection are

solved together using a time-marching method (Shia et al. 1990). In the second scheme, called the "quasi 2-D" mode (Liang et al. 2005), first we perform a series of 1-D photochemical-diffusional calculations at different latitudes using the matrix inversion method (see section 5.3), and then the meridional advection and horizontal diffusion are applied to connect different latitudes. Our calculations show that, when reaching the steady state, the two modes converge into the same solution. But the "quasi 2-D" mode takes shorter time to reach the steady state than the "normal 2-D" mode, because the former allows very large time step in the 1-D diffusion calculation but the latter is limited by the CFL criterion for every time step.

We assume the Jupiter value $N_0 = 4.83\times10^{18}\ g\ cm^{-3}$ at 100 mbar, planetary radius $a = 7.1824\times10^{9}\ cm$, $w_0 = 10^{-3}\ cm\ s^{-1}$, $\lambda = 0.3$. So the transport timescale is about $3\times10^{9}\ s$. We test two cases, case I and case II, corresponding to the streamfucntions in (a) and (b), respectively. For each case, we tested two fictitious chemical tracers, the short-lived tracer with loss rate faster than transport ($L_0^{-1} = 10^{9}\ s$) and the long-lived tracer with loss rate slower than transport ($L_0^{-1} = 10^{11}\ s$). We assume $P_0 = 10^{-16} cm^{-3} s^{-1}$ for both cases. For the case I, in which air rises at the equator and sinks at the poles, our analytical solution is given by equation (5.55), with $G\left(e^{-\xi}\psi\right) = 5\times10^{-19}\left(e^{-\xi}\psi\right)^2$. For the case II, in which air rises at the south pole and sinks at the north pole, our analytical solution is given by equation (5.62), with $G\left(e^{-\xi}\psi\right) = \frac{P_0 aH}{(\lambda-1)e^{-\xi}\psi}$. We use the boundary values from the analytical solutions for the numerical model. The mass stream functions (scaled by the air density for each layer) are shown in Figure 5.8.

The results from case I are plotted in Figure 5.9, with the numerical simulation results (dots) on top of each curve. For the short-lived tracer, chemical production and loss dominates its local abundances. Because the production is higher at equator and loss is higher at the poles, the steady-state mixing ratio of the short-lived tracer is higher in the low latitudes and lower in the high latitudes in the upper pressure levels (~5-10 mbar), while in the lower pressure levels (~50-100 mbar), its latitudinal distribution is also effect by the lower boundary conditions. On the other hand, although with the production and loss

rate, the latitudinal distribution of the long-lived species has almost the opposite trend as the short-lived species, with higher mixing ratio in the higher latitudes and lower mixing ratio in the lower latitudes in the upper pressure levels, showing the transport dominant results. In the lower pressure levels, the solutions are also affected by the lower boundary conditions. The numerical results are based on our 2-D chemical-transport model (Caltech/JPL Kinetics Model), which is able to reproduce the analytical results perfectly. The largest differences between the analytical and numerical simulations are found in two poles, but still less than 4%.

Similar behavior is shown by the results from case II (Figure 5.9). Although both tracers have the higher production rate in the southern hemisphere and linear loss rate independent with latitude, their steady-state latitudinal distributions are significantly different. Again, the short-lived tracer is more dominated by the chemistry, while the long-lived tracer shows more transport-dominant behavior.

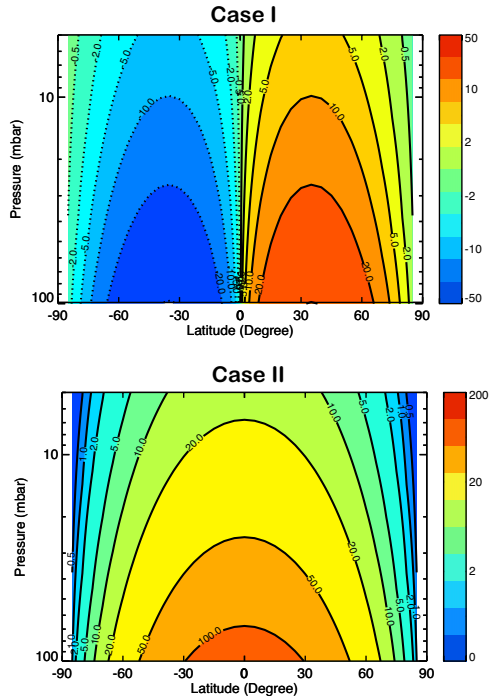

Figure 5.8. Analytic mass stream functions in units of $g\ cm^{-1}\ s^{-1}$. The top panel is for the case I with rising motion at the equator and sinking motion at the poles. The bottom panel is for the case II with rising motion at the south pole and sinking motion at the north pole.

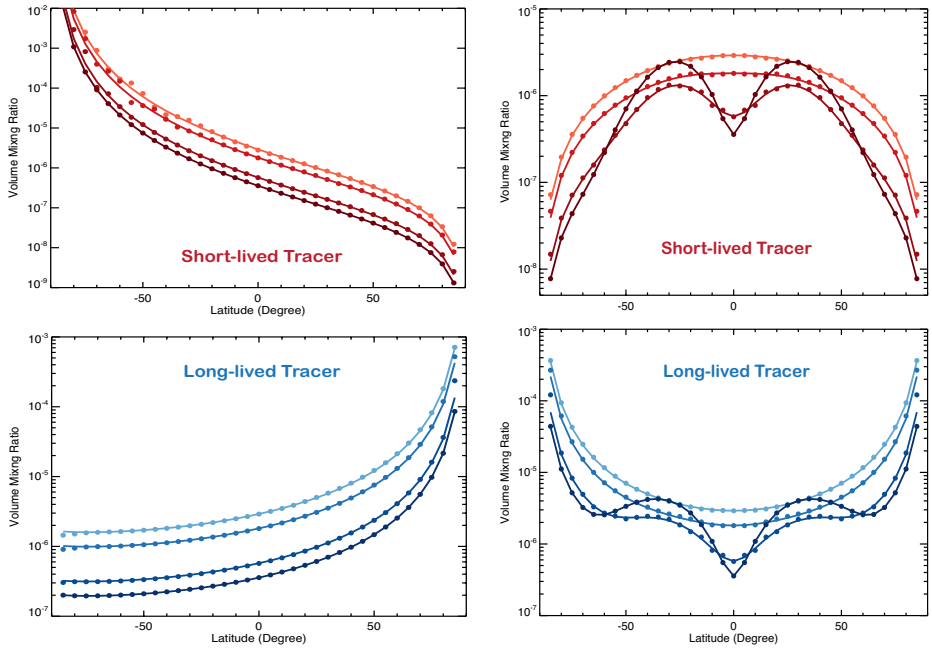

Figure 5.9. Comparison of analytical (lines) and numerical (dots) solutions in case I (left) and case II (right) for two fictitious chemical tracers, the short-lived tracer (upper panel) with loss rate faster than transport and the long-lived tracer (bottom panel) with loss rate slower than transport. The four curves in each panel correspond to 5, 10, 50, and 100 mbar, from the lightest color (lowest pressure) to the darkest color (highest pressure), respectively.

5.4.2.3 Pure Diffusive Cases

Ignoring the advection terms, we now have a 2-D diffusion equation:

$$\frac{1}{a^2\cos\theta}\frac{\partial}{\partial\theta}\left(\cos\theta\, K_{yy}\frac{\partial\chi}{\partial\theta}\right)+\frac{e^{\xi}}{H^2}\frac{\partial}{\partial\xi}\left(K_0 e^{(\gamma-1)\xi}\frac{\partial\chi}{\partial\xi}\right)+P_0 e^{(\alpha+1)\xi}f(\theta)-L_0 e^{\beta\xi}g(\theta)\chi = 0. \quad (5.63)$$

Here we consider a simple special solution. Since from the 1-D model we know the equation $\frac{\partial}{\partial\xi}\left(K_0 e^{(\gamma-1)\xi}\frac{d\chi}{d\xi}\right)=0$ has a solution like $\chi(\xi)=C_1+C_2 e^{(1-\gamma)\xi}$ (see section 5.3.1), if we further assume the solution of the 2-D diffusion equation can be expressed as $\chi(\theta,\xi)=A(\theta)G(\xi)$, so let $G(\xi)=C_1 e^{(1-\gamma)\xi}$, the equation will be reduced as

$$\frac{G(\xi)}{a^2\cos\theta}\frac{d}{d\theta}\left(\cos\theta\, K_{yy}\frac{dA(\theta)}{d\theta}\right)+P_0e^{(\alpha+1)\xi}f(\theta)-L_0e^{\beta\xi}g(\theta)A(\theta)G(\xi)=0. \quad (5.64)$$

Here we have assumed that the horizontal transport and vertical transport can be decoupled. This is valid based on the fact that the two transport timescales are significantly different. Figure 2 of Liang et al. (2005) shows that the vertical transport is much faster than the horizontal transport.

We artificially set $\alpha=-\gamma$, and $\beta=0$, and change the variable $x=\sin\theta$, so that

$$(1-x^2)\frac{d^2A}{dx^2}-2x\,\frac{dA}{dx}+\frac{a^2P_0}{K_{yy}C_1}f(1-x^2)-\frac{a^2L_0}{K_{yy}}g(1-x^2)A=0. \quad (5.65)$$

Now let us consider two cases:

(a) With a constant production and a linear loss rate, i.e., $f(1-x^2)=1$ and $g(1-x^2)=1$. The equation reduces to the Legendre equation, and the solution is

$$\chi(\theta,\xi)=e^{(1-\gamma)\xi}(C_1P_\nu(\sin\theta)+C_2Q_\nu(\sin\theta)+\frac{P_0}{L_0}), \quad (5.66)$$

where $P_\nu(\sin\theta)$ and $Q_\nu(\sin\theta)$ are Generalized Legendre functions with a negative non-integer $\nu=\frac{\sqrt{1-4a^2L_0/K_{yy}}-1}{2}$, in order to get the real solutions, it requires $K_{yy}/a^2>4L_0$, i.e., the horizontal transport is relatively faster than the loss processes.

In principle, we should have a symmetric solution in this symmetric system, i.e., $C_1P_\nu(\sin\theta)+C_2Q_\nu(\sin\theta)=C_1P_\nu(-\sin\theta)+C_2Q_\nu(-\sin\theta)$. Using the equality: $P_\nu(-x)=P_\nu(x)\cos\pi\nu-2\pi^{-1}\,Q_\nu(x)\sin\pi\nu$ (Polyanin and Zaitsev 2002), we obtain $C_2/C_1=-2\pi^{-1}\tan(\pi\nu/2)$, so that

$$\chi(\theta,\xi)=C_1e^{(1-\gamma)\xi}\left[P_\nu(\sin\theta)-\frac{2}{\pi}\tan\left(\frac{\pi\nu}{2}\right)Q_\nu(\sin\theta)+\frac{P_0}{C_1L_0}\right], \quad (5.67)$$

$C_1=0$ leads to a trivial case with a constant mixing ratio with latitude. If $C_1\neq0$, equation (5.67) will end up with a horizontal diffusional equilibrium solution. We called it the case

III. In the numerical simulations, we assume $P_0 = 10^{-16} cm^{-3} s^{-1}$, $L_0^{-1} = 10^{11}\ s$, $\gamma = 0.1$, and $K_{yy} = 2.1{\times}10^9\ cm^2\ s^{-1}$. The solution (Figure 5.10) shows an open-up bowl-shaped distribution with the minimum value at the equator and maximum value at the poles. So the horizontal flux is from pole to equator. At any latitude there should be a flux convergence to balance the chemical loss. And the area weighted loss rate has a maximum at equator, therefore a maximum flux convergence as well. However, in reality, the source flux is not uniform at the top. We solve the following case with a latitudinal-dependent production rate in (b).

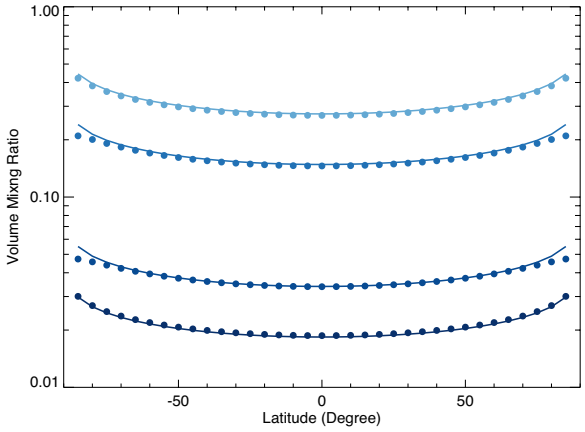

Figure 5.10. Comparison of analytical (lines) and numerical (dots) solutions in case III. The four curves correspond to 5, 10, 50, and 100 mbar, from the lightest color (lowest pressure) to the darkest color (highest pressure), respectively.

(b) Without loss, but with a production rate as $f(1-x^2) = (1-x^2)^n$, where $n = 0,1,2,3$ ...

The equation is

$$(1-x^2)\frac{d^2A}{dx^2} - 2x\,\frac{dA}{dx} + \frac{a^2P_0}{K_{yy}C_1}(1-x^2)^n = 0. \tag{5.68}$$

If $n = 0$, i.e., with a constant production rate, the solution is

$$\chi(\theta,\xi) = C_1 e^{(1-\gamma)\xi}\left[C_2 + \frac{a^2P_0}{2K_{yy}C_1}\ln(\cos^2\theta) + \frac{C_3}{2}\ln\left(\frac{1-\sin\theta}{1+\sin\theta}\right)\right]. \tag{5.69}$$

If $n = 1$, i.e., $f(1 - x^2) = \cos^2\theta$, the solution is

$$\chi(\theta, \xi) = C_1 e^{(1-\gamma)\xi} \left\{ C_2 + \frac{a^2 P_0}{6K_{yy}C_1} [-\sin^2\theta + 2\ln(\cos^2\theta)] + \frac{C_3}{2} \ln\left(\frac{1-\sin\theta}{1+\sin\theta}\right) \right\}. \tag{5.70}$$

Since the solutions should be symmetric to the equator, we should ignore the C_3 terms on the right hand side. The solutions are

$$\chi(\theta, \xi) = [C_1 + \frac{a^2 P_0}{2K_{yy}} \ln(\cos^2\theta)] e^{(1-\gamma)\xi} \quad (n = 0), \tag{5.71}$$

$$\chi(\theta, \xi) = \{C_1 + \frac{a^2 P_0}{6K_{yy}} [-\sin^2\theta + 2\ln(\cos^2\theta)]\} e^{(1-\gamma)\xi} \quad (n = 1). \tag{5.72}$$

The results of case IV ($n = 0$) and case V ($n = 1$) are shown in Figure 5.11 and 5.12, respectively. All the parameters are the same as case III, except $K_{yy} = 1\times10^9\ cm^2\ s^{-1}$. The solutions show an open-down bowl-shaped distribution with the maximum value at the equator and a sharp fall-off in the polar regions. So the horizontal flux is from equator to pole. Since there is no chemical loss in these cases, at any latitude there should be a flux divergence to balance the chemical production. The solutions demonstrate that, if the chemical loss can be ignored, any diffusive transport process with a chemical production rate that is either flat ($n = 0$) or peak ($n = 1$) in the low latitudes will result in a high mixing ratio in the low latitudes. Therefore, the horizontal mixing solution of C_2H_6, whose chemical loss can be ignored, will have an open-down bowl-shape. Our simple analytical cases are consistent with the model results in Liang et al. (2005) and Lellouch et al. (2006), but contrary to the Voyager and Cassini data (chapter III). We note that the ratio of production rate with the horizontal mixing determines the "flatness" of the bowl-shape distribution. A more efficient horizontal mixing leads to a flatter distribution. The horizontal efficient timescale should be much shorter than the chemical production timescale in the Liang et al. (2005) case, which is correct because in the lower atmosphere chemical production of C_2H_6 is not efficient. The observed latitudinal distribution from CIRS implies either the mean residue circulation plays an important role, or there could be a chemical source of C_2H_6 in the polar regions, although there is no evidence for any

possible ion chemistry initiated by precipitating particles in the aurora region that could enhance the ethane abundances. But this possible chemical mechanism should not significantly enhance the abundances of C_2H_2, which, in principle, is much more sensitive to the local chemical source but the observations do not show any enhancement of C_2H_2 in the polar regions.

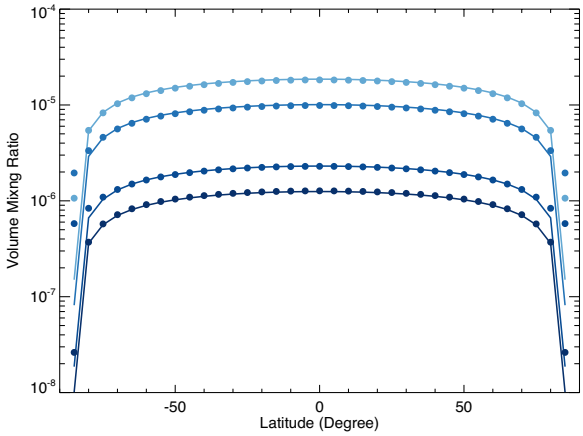

Figure 5.11. Comparison of analytical (lines) and numerical (dots) solutions in case IV. The four curves correspond to 5, 10, 50, and 100 mbar, from the lightest color (lowest pressure) to the darkest color (highest pressure), respectively.

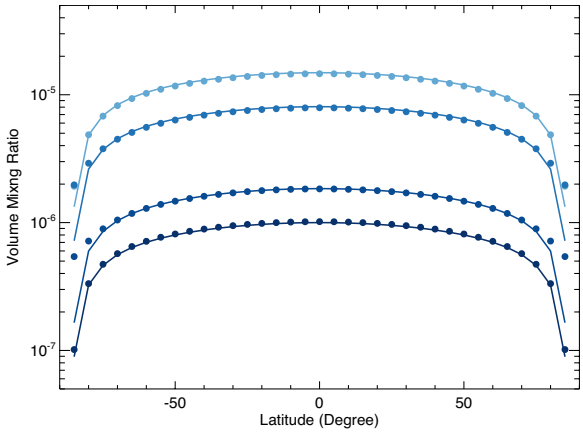

Figure 5.12. Comparison of analytical (lines) and numerical (dots) solutions in case V. The four curves correspond to 5, 10, 50, and 100 mbar, from the lightest color (lowest pressure) to the darkest color (highest pressure), respectively.

Therefore we have the following case with the production rate $f(1-x^2) = x^{2n} = \sin^{2n}\theta$, which has the peak production rate at poles. For $n = 1$, the solution is

$$\chi(\theta, \xi) = \{C_1 + \frac{a^2 P_0}{6K_{yy}}[\sin^2\theta + \ln(\cos^2\theta)]\}e^{(1-\gamma)\xi}. \quad (5.73)$$

However, the solution (case VI) also shows an open-down bowl-shaped distribution with the maximum value at the equator and minimum value at the poles (Figure 5.13). So if we ignore the advection terms, the required latitudinal slope of the production rate of C_2H_6 should be much steeper than the $\sin^2\theta$ in order to explain the CIRS observations. Numerical simulations with more realistic chemistry and eddy mixing are needed to confirm this hypothesis.

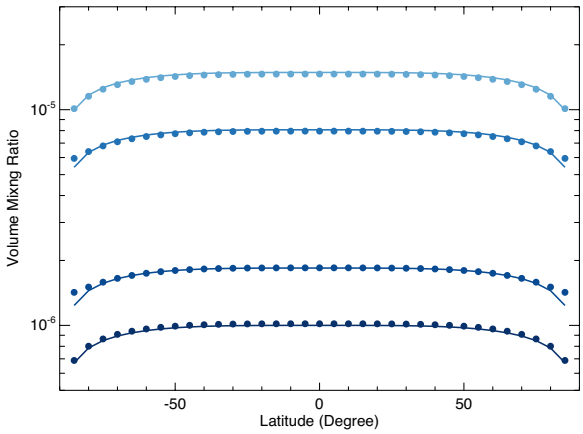

Figure 5.13. Comparison of analytical (lines) and numerical (dots) solutions in case VI. The four curves correspond to 5, 10, 50, and 100 mbar, from the lightest color (lowest pressure) to the darkest color (highest pressure), respectively.

5.5. 2-D System in the Zonal Plane

If we consider the system in an altitude-longitude plane, which can be applied to the slowly rotating planets such as Venus and Hot Jupiters, a strong subsolar-anti-solar circulation coupled with the zonal jets, and with the inhomogeneous production rate, will lead to a

different scenario. In the zonal plane, the horizontal eddy diffusion can be neglected. In the steady state, the governing equation is

$$\frac{u}{a}\frac{\partial \chi}{\partial \lambda} + w\frac{\partial \chi}{\partial z} - e^{\xi}\frac{\partial}{\partial z}\left(e^{-\xi}K_{zz}\frac{\partial \chi}{\partial z}\right) = \frac{P-L}{N}, \tag{5.74}$$

where λ is longitude, a is radius of the latitude circle.

We can formulate the streamfunction ψ as well:

$$u = -e^{\xi}\frac{\partial}{\partial z}\left(e^{-\xi}\psi\right), \tag{5.75}$$

$$w = \frac{1}{a}\frac{\partial \psi}{\partial \lambda}. \tag{5.76}$$

If we neglect the diffusion term, this is basically back to the similar argument in the 2-D problem in the meridional plane. The solution is related to the subsolar-anti-solar circulation, which is similar to that in the equator-pole circulation problem.

However, instead, if we neglect the vertical advection term, the problem is still well posed. Suppose a fast jets rapidly flows along the latitude circle with a constant velocity u, the air mass is conserved in that altitude. If the eddies are vertically pumped into the jets to supply the momentum, the vertical eddy mixing term could be more important than the vertical advection term.

$$\frac{u}{a}\frac{\partial \chi}{\partial z} - e^{\xi}\frac{\partial}{\partial z}\left(e^{-\xi}K_{zz}\frac{\partial \chi}{\partial z}\right) = \frac{P-L}{N}. \tag{5.77}$$

As usual, we assume $P(\lambda,\xi) = P_0N_0e^{\alpha\xi}f(\lambda)$, $L(\lambda,\xi) = L_0N_0e^{(\beta-1)\xi}g(\lambda)\chi$, and $K_{zz} = K_0e^{\gamma\xi}$. So the equation becomes

$$\frac{u}{a}\frac{\partial \chi}{\partial \lambda} - e^{\xi}\frac{\partial}{\partial z}\left(K_0e^{(\gamma-1)\xi}\frac{\partial \chi}{\partial z}\right) - P_0e^{(\alpha+1)\xi}f(\lambda) + L_0e^{\beta\xi}g(\lambda)\chi = 0. \tag{5.78}$$

Let us check a simple case with a special solution. Similar to the argument of the 2D diffusive system, we let $\alpha = -\gamma$ and $\beta = 0$, we assume the solution can be expressed as:

$\chi(\lambda,\xi) = A(\lambda)G(\xi)$, where $G(\xi) = C_1 e^{(1-\gamma)\xi}$, the equation can be reduced to a first order linear ODE:

$$\frac{u}{a}\frac{dA(\lambda)}{d\lambda} - \frac{P_0 f(\lambda)}{C_1} + L_0 g(\lambda)A(\lambda) = 0. \tag{5.79}$$

The solution is

$$A(\lambda) = \mathrm{e}^{-\frac{aL_0}{u}\int g(\lambda)d\lambda}\left[C_2 + \frac{aP_0}{uC_1}\int f(\lambda)\mathrm{e}^{\frac{aL_0}{u}\int g(\lambda)d\lambda}d\lambda\right]. \tag{5.80}$$

Finally we obtain the general form of $\chi(\lambda,\xi)$:

$$\chi(\lambda,\xi) = \mathrm{e}^{-\frac{aL_0}{u}\int g(\lambda)d\lambda}\left[C_1 + \frac{aP_0}{u}\int f(\lambda)\mathrm{e}^{\frac{aL_0}{u}\int g(\lambda)d\lambda}d\lambda\right]e^{(1-\gamma)\xi} \tag{5.81}$$

The periodic boundary condition, i.e., $\chi(0,\xi) = \chi(2\pi,\xi)$, requires C_1 to be 0. A simple case would be $f(\lambda) = 1 + \cos k\lambda$, where $k = 1$ stands for the two-modal production rate (day-night contrast). The solution would be

$$\chi(\lambda,\xi) = \frac{P_0}{L_0}\left[1 + \frac{1}{1+q^2}(\cos k\lambda + q\sin k\lambda)\right]e^{(1-\gamma)\xi}, \tag{5.82}$$

where the dimensionless variable $q = ku/aL_0$ measures chemical loss timescale versus the advection timescale (across an envelope of the production rate distribution).

The solution can be rewritten as:

$$\chi(\lambda,\xi) = \frac{P_0}{L_0}[1 + \frac{1}{\sqrt{1+q^2}}\cos(k\lambda - \phi)]e^{(1-\gamma)\xi} \tag{5.83}$$

where $\phi = \tan^{-1} q$ can be regarded as the phase lag of the mixing ratio distribution compared with the production rate distribution and the amplitude of the mixing ratio variation is smaller than the production rate variation by a factor of $\sqrt{1+q^2}$. When the advection timescale and the chemical loss timescale are comparable, i.e., $q = 1$, the phase shift is $45°$. If q is large, i.e., when the chemical loss is slower than the advection timescale, the zonal wind will quickly redistribute the chemicals and lead to a large phase

lag and smooth mixing ratio profile in the longitude. On the other hand, if q is small, the chemistry will dominate the distribution. Therefore the phase lag due to advection would be smaller since the local chemical equilibrium will be established more quickly, leading to a large mixing ratio contrast along the latitude circle. Figure 5.14 illustrates some typical cases with different values of q.

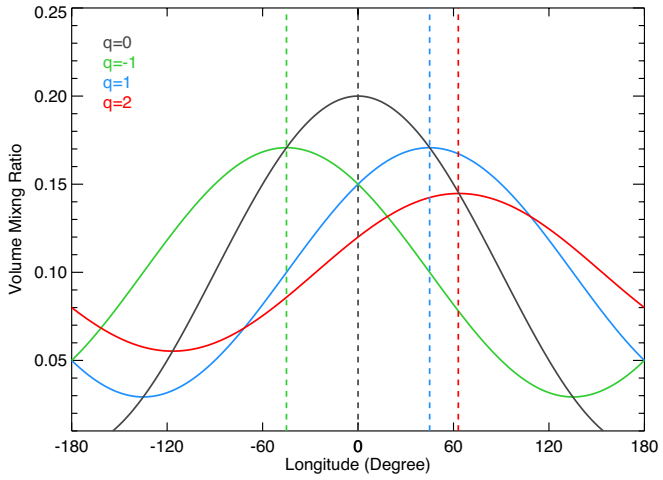

Figure 5.14. Analytical solutions for the zonal transport cases. Different ratios (q values) of the transport versus chemical timescales result in different phase lags and different amplitudes of the longitudinal mixing ratio profiles. The dashed lines indicate the longitudes corresponding to the peaks of the mixing ratio profiles. The chemical source distribution follows a cosine function with its peak at longitude 0°.

5.6. Concluding Remarks

In this study we systematically investigated the possible analytical benchmark cases in the photochemical-advective-diffusive system. Although our solutions are highly idealized, we can still gain physical insights on what control the vertical and latitudinal profiles of the short-lived and long-lived species in the stratosphere of Jupiter. In the 1-D system, we show that CH_4 and C_2H_6 are mainly in diffusive equilibrium, and C_2H_2 profile can be approximated by the modified Bessel functions. Those analytical solutions could be used for the simple treatment of photochemistry in climate models or general circulation models.

In the 2-D system in the meridional plane, analytical solutions for two typical circulation patterns are derived. Simple tracer transport cases demonstrate that the short-lived species is dominated by the local chemical sources and sinks, while the long-lived species is significantly influenced by the circulation pattern. This may help solve the opposite latitudinal distributions between C_2H_2 and C_2H_6, as revealed by the Cassini and Voyager spectra. On the other hand, it seems difficult for a pure diffusive transport process to produce a similar latitudinal profile of C_2H_6 whose chemical loss can be neglected. Intuitively it also makes sense because the horizontal eddy mixing is not able to reverse the latitudinal slope set by the photochemistry. Therefore, unless there is any missing chemical source for C_2H_6 (but not for C_2H_2) in the polar regions, the most probable solution is a meridional circulation pattern from equator to pole. The detailed structure of the residue circulation in the stratosphere of Jupiter requires a realistic numerical simulation. For the slowly rotating planet, which might have longitudinal heterogeneous chemical sources, the interaction between the advection by the zonal wind and chemistry might cause a phase lag in the final tracer distribution compared with the original source distribution. The magnitude of the phase lag and longitudinal contrast of the tracer profile depends on the relative strength between the advection timescale and the lifetime of the tracer. This is similar to the mechanism that causes the phase shift between the locations of the atmospheric temperature maximum and subsolar point on close-in giant planets, as first discovered by Knutson et al. (2007).

The analytical solutions can also be used to validate the numerical simulations from our 2-D Caltech/JPL chemical-transport model and generally show good agreements for various cases. The largest discrepancy usually happens in the polar regions, especially when the analytical solutions have singular values at the poles, such as equation (5.72). Increasing the horizontal and vertical resolution would lead to better agreement. This study prepares the theoretical basis and numerical tools for future realistic chemical transport modeling in planetary atmospheres.

Appendix A
Supplementary Materials for chapter II

A.1 Radiative Transfer Scheme

The diurnally averaged radiation calculation here is modified on the basis of Mills (1998). The direct attenuated flux and Rayleigh scattering calculations remain the same (see details in the appendices H and I of Mills 1998). In this study we adopt 550 log-linear optical depth grids, 112 wavelengths from 960 to 8000 Å, 14 zenith angles for the incoming photons, 8 Gaussian angles for the diffused photons. The wavelength-independent middle cloud albedo at the lower boundary is assumed to be 0.6. The depolarization factor of CO_2 Rayleigh scattering equals 0.443.

The absorption of the unknown UV absorber and scattering processes of haze and cloud particles are crucial for the radiation field, especially in the upper cloud layer. We follow the procedure described in Crisp (1986). First, we calculated the optical depths from the bimodal aerosol profiles (see appendix B) and scaled to match the optical depth values in Table 2.2 (equatorial cloud model) of Crisp (1986). Aerosol optical properties are calculated using Mie-code based on the parameters of equator hazes in Table 2.1 of Crisp (1986). For mode 1, the refractive index is 1.45, radius 0.49±0.22 μm. For mode 2, the refractive index is 1.44, radius 1.18±0.07 μm. Figure A.1 shows the scattering efficiencies (upper panel) and asymmetry factors (middle panel) of the two modes. Since the asymmetry factors do not vary with wavelength significantly, we choose 0.74 as the mean value for all wavelengths. The UV absorber is introduced by decreasing the single scattering albedo of the mode 1 aerosol between 3100 and 7800 Å. We take the empirical absorption efficiency values from Table 2.4 of Crisp (1986). Figure A.1 (lower panel) shows the single scattering albedo of the mode 1 aerosol mixed with the UV absorber. Because the single scattering albedo is not constant (from 0.85 to 1) with wavelength, we use the wavelength-dependent values in the calculation.

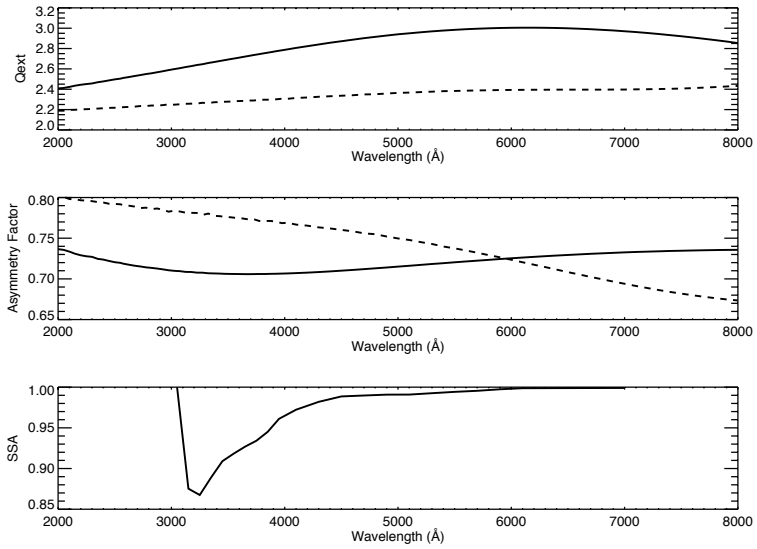

Figure A.1. Optical Properties of mode 1 (solid) and mode 2 (dashed) aerosols above the middle cloud top (~58 km) based on the parameters from Crisp (1986). Upper panel: extinction efficiency; middle panel: Asymmetry Factor; lower panel: single scattering albedo mixed with the empirical albedo of the unknown UV absorber from Crisp (1986).

The spectral actinic fluxes (in units of photons cm^{-2} s^{-1} $Å^{-1}$) for 58, 70 and 112 km at 45°N are plotted as functions of wavelength in Figure A.2, although in this study our calculation is at 70° N only. Due to absorptions by CO_2, SO_2 and SO, the UV flux decreases rapidly as it penetrates deeper into the atmosphere. Rayleigh scattering and aerosol scattering result in the larger actinic flux in the cloud and haze layers than that at the top of the atmosphere. In the wavelength range large than 2000 Å, the actinic flux peaks around ~65 km. The UV actinic flux at the lower boundary (~58 km) between 2000~3000 Å is roughly anti-correlated with the SO_2 cross sections and the minimum in its the cross section profile near 2400 Å may open a window for the UV flux to penetrate to the lower atmosphere of Venus. There is an analogous spectral window in the terrestrial atmosphere between 200 and 220 nm (Froidevaux and Yung 1982).

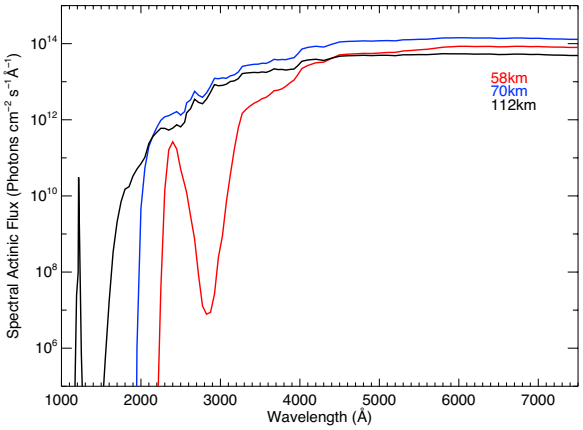

Figure A.2. Spectral actinic flux in the middle atmosphere of Venus at 45° N.

A.2. Photolysis Reactions on Venus

The reactions are summarized in Table A.1.

The photolysis coefficient (*J*) in the units of s^{-1} refers to 112 km and 68 km at midlatitude (45° N) with diurnal average (divided by 2). Total SO_2 absorption cross sections between 227 and 420 nm are updated based on recent measurements by Hermans et al. (2009) and Vandaele et al. (2009).

References: (a) Mills (1998) and references therein; (b) Moses et al. (2002) and references therein; (c) Sander et al. (2006) and references therein; (d) Moses et al. (2000) and references therein; (e) Bahou et al. (2001); (f) Burkholder et al. (2000); (g) Vaida et al. (2003); (h) Mills et al. (2005); (i) Burkholder and McKeen (1997); (j) Hintze et al. (2003); (k) Lane and Kjaergaard (2008); (l) Pernice et al. (2004); (m) DeMore et al. (1994) and references therein; (n) DeMore et al. (1997) and references therein.

A.3. Neutral Chemical Reactions on Venus

The reactions are summarized in Table A.2.

M represents the third body such as N_2 or CO_2 for three-body reactions. Two-body rate constants and high-pressure limiting rate constants for three-body reactions (k_∞) are in units of $cm^3\ s^{-1}$. Low-pressure limiting rate constants for three-body reactions (k_0) are in units of $cm^6\ s^{-1}$. k_{eq} is the equilibrium constant such that the cofficient for the reverse reaction is calculated as $k_{eq}/k_{forward}$. The entropies and enthalpies used for the k_{eq} calculations are taken from reference (f).

References: (a) Mills (1998) and references therein; (b) Moses et al. (2002) and references therein; (c) Sander et al. (2002) and references therein; (d) Baulch et al. (1992) and references therein; (e) Yung and DeMore (1982) and references therein; (f) Chase et al. (1985) (JANAF thermochemical tables) and references therein; (g) Moses et al. (2000) and references therein; (h) Baulch et al. (1981) and references therein; (i) Sander et al. (2006) and references therein; (j) Lovejoy et al. (1996); (k) Atkinson et al. (2004) and references therein; (l) Mills et al. (2007a) and references therein; (m) Lu et al. (2006); (n) Bryukov et al. (1993); (o) Atkinson et al. (1989) and references therein; (p) Brune et al. (1983); (q) Campbell and Thrush (1967); (r) Riley et al. (2003); (s) He et al. (1993); (t) Dodonov et al. (1981); (u) Sun et al. (2001).

*Reaction rate coefficients corrected by factors of 3.3 and 8.2 for the higher efficiency of the third body CO_2 than N_2 (R247, R258, R259) and Ar (R240), respectively (Singleton and Cvetanovic 1988).

Table A.1. Photolysis Reactions on Venus

	Reaction	Photolysis coefficient J (s^{-1}) at 112 km	Photolysis coefficient J (s^{-1}) at 68 km	Wavelength (nm)	Reference
R1	$O_2 + h\upsilon \rightarrow 2O$	8.8×10^{-8}	7.4×10^{-10}	$3 \le \lambda \le 242$	b
R2	$\rightarrow O + O(^1D)$	2.1×10^{-7}	0.0	$117 \le \lambda \le 178$	b
R3	$O_3 + h\upsilon \rightarrow O_2 + O$	1.2×10^{-3}	2.3×10^{-3}	$158 \le \lambda \le 800$	a
R4	$\rightarrow O_2(^1\Delta) + O(^1D)$	7.6×10^{-3}	1.1×10^{-2}	$53 \le \lambda \le 325$	a
R5	$\rightarrow O_2 + O(^1D)$	2.3×10^{-6}	3.2×10^{-6}	$320 \le \lambda \le 325$	a
R6	$\rightarrow O_2(^1\Delta) + O$	2.6×10^{-6}	3.2×10^{-6}	$120 \le \lambda \le 325$	a
R7	$\rightarrow 3O$	9.2×10^{-7}	1.0×10^{-11}	$53 \le \lambda \le 203$	a
R8	$OH + h\upsilon \rightarrow O + H$	4.8×10^{-6}	0.0	$91 \le \lambda \le 193$	d
R9	$HO_2 + h\upsilon \rightarrow OH + O$	5.4×10^{-4}	7.0×10^{-4}	$190 \le \lambda \le 260$	c
R10	$H_2O + h\upsilon \rightarrow H + OH$	3.1×10^{-6}	0.0	$61 \le \lambda \le 198$	a
R11	$\rightarrow H_2 + O(^1D)$	5.2×10^{-8}	0.0	$80 \le \lambda \le 143$	a
R12	$\rightarrow 2H + O$	6.2×10^{-8}	0.0	$80 \le \lambda \le 143$	a
R13	$H_2O_2 + h\upsilon \rightarrow 2OH$	9.7×10^{-5}	1.3×10^{-4}	$120 \le \lambda \le 350$	a
R14	$Cl_2 + h\upsilon \rightarrow 2Cl$	2.6×10^{-3}	3.9×10^{-3}	$240 \le \lambda \le 475$	a
R15	$ClO + h\upsilon \rightarrow Cl + O$	6.2×10^{-3}	8.4×10^{-3}	$230 \le \lambda \le 325$	a
R16	$HCl + h\upsilon \rightarrow H + Cl$	1.9×10^{-6}	5.5×10^{-8}	$135 \le \lambda \le 232$	e
R17	$HOCl + h\upsilon \rightarrow OH + Cl$	4.6×10^{-4}	6.4×10^{-4}	$200 \le \lambda \le 380$	a
R18	$COCl_2 + h\upsilon \rightarrow 2Cl + CO$	5.1×10^{-5}	7.4×10^{-5}	$182 \le \lambda \le 285$	a
R19	$CO_2 + h\upsilon \rightarrow CO + O$	1.1×10^{-8}	4.3×10^{-13}	$120 \le \lambda \le 204$	a
R20	$\rightarrow CO + O(^1D)$	3.5×10^{-9}	0.0	$63 \le \lambda \le 160$	a
R21	$S_2 + h\upsilon \rightarrow 2S$	4.0×10^{-3}	5.8×10^{-3}	$238 \le \lambda \le 278$	b
R22	$S_3 + h\upsilon \rightarrow S_2 + S$	1.2	2.4	$350 \le \lambda \le 455$	b
R23	$S_4 + h\upsilon \rightarrow 2S_2$	2.2×10^{-1}	5.5×10^{-1}	$425 \le \lambda \le 575$	b
R24	$ClS + h\upsilon \rightarrow S + Cl$	2.6×10^{-2}	5.9×10^{-2}	$337 \le \lambda \le 500$	a
R25	$Cl_2S + h\upsilon \rightarrow ClS + Cl$	2.2×10^{-3}	3.9×10^{-3}	$190 \le \lambda \le 460$	a
R26	$ClS_2 + h\upsilon \rightarrow S_2 + Cl$	6.8×10^{-2}	1.4×10^{-1}	$327 \le \lambda \le 485$	a
R27	$SO + h\upsilon \rightarrow S + O$	3.7×10^{-4}	1.8×10^{-4}	$113 \le \lambda \le 232$	a
R28	$SO_2 + h\upsilon \rightarrow S + O_2$	1.5×10^{-6}	1.9×10^{-7}	$63 \le \lambda \le 210$	a
R29	$\rightarrow SO + O$	2.0×10^{-4}	7.2×10^{-5}	$63 \le \lambda \le 220$	a
R30	$SO_3 + h\upsilon \rightarrow SO_2 + O$	3.6×10^{-5}	3.7×10^{-5}	$195 \le \lambda \le 300$	f
R31	$OCS + h\upsilon \rightarrow CO + S$	2.8×10^{-5}	4.2×10^{-5}	$185 \le \lambda \le 300$	a
R32	$H_2SO_4 + h\upsilon \rightarrow SO_3 + H_2O$	1.4×10^{-6}	1.4×10^{-7}	$121 \le \lambda \le 746$	g, h, i, j, k
R33	$S_2O + h\upsilon \rightarrow SO + S$	5.0×10^{-2}	6.2×10^{-2}	$260 \le \lambda \le 335$	a
R34	$ClC(O)OO + h\upsilon \rightarrow CO_2 + ClO$	5.3×10^{-3}	7.4×10^{-3}	$205 \le \lambda \le 305$	l
R35	$NO + h\upsilon \rightarrow N + O$	4.3×10^{-6}	0.0	$175 \le \lambda \le 195$	m
R36	$NO_2 + h\upsilon \rightarrow NO + O$	8.6×10^{-3}	1.5×10^{-2}	$120 \le \lambda \le 422$	m
R37	$NO_3 + h\upsilon \rightarrow NO_2 + O$	1.6×10^{-1}	4.4×10^{-1}	$410 \le \lambda \le 645$	n
R38	$\rightarrow NO + O_2$	2.4×10^{-2}	6.3×10^{-2}	$590 \le \lambda \le 645$	n
R39	$N_2O + h\upsilon \rightarrow N_2 + O(^1D)$	8.9×10^{-7}	3.0×10^{-3}	$100 \le \lambda \le 240$	m
R40	$HNO_2 + h\upsilon \rightarrow OH + NO$	1.9×10^{-3}	8.7×10^{-3}	$310 \le \lambda \le 390$	m
R41	$HNO_3 + h\upsilon \rightarrow NO_2 + OH$	1.2×10^{-4}	5.2×10^{-5}	$190 \le \lambda \le 350$	m

Table A.2. Neutral Chemical Reactions on Venus

	Reaction	Rate constant	Reference
R50	$O(^1D) + O_2 \rightarrow O + O_2$	$3.20\times10^{-11}\, e^{70./T}$	c
R51	$O(^1D) + N_2 \rightarrow O + N_2$	$1.80\times10^{-11}\, e^{110./T}$	c
R52	$O(^1D) + CO_2 \rightarrow O + CO_2$	$7.40\times10^{-11}\, e^{120./T}$	c
R53	$O_2(^1\Delta) + O \rightarrow O_2 + O$	2.00×10^{-16}	c
R54	$O_2(^1\Delta) + O_2 \rightarrow 2O_2$	$3.60\times10^{-18}\, e^{-220./T}$	c
R55	$O_2(^1\Delta) + H_2O \rightarrow O_2 + H_2O$	4.80×10^{-18}	c
R56	$O_2(^1\Delta) + N_2 \rightarrow O_2 + N_2$	1.00×10^{-20}	c
R57	$O_2(^1\Delta) + CO \rightarrow O_2 + CO$	1.00×10^{-20}	a
R58	$O_2(^1\Delta) + CO_2 \rightarrow O_2 + CO_2$	2.00×10^{-21}	Estimated
R59	$2O + CO_2 \rightarrow O_2 + CO_2$	$k_0 = 3.22\times10^{-28}\, T^{-2.0}$	Estimated
R60	$2O + CO_2 \rightarrow O_2(^1\Delta) + CO_2$	$k_0 = 9.68\times10^{-28}\, T^{-2.0}$	Estimated
R61	$2O + O_2 \rightarrow O_3 + O$	$k_0 = 5.90\times10^{-34}\,(T/300.)^{-2.4}$	a
		$k_\infty = 2.80\times10^{-12}$	
R62	$O + 2O_2 \rightarrow O_3 + O_2$	$k_0 = 5.90\times10^{-34}\,(T/300.)^{-2.4}$	a
		$k_\infty = 2.80\times10^{-12}$	
R63	$O + O_2 + N_2 \rightarrow O_3 + N_2$	$k_0 = 5.95\times10^{-34}\,(T/300.)^{-2.3}$	a
		$k_\infty = 2.80\times10^{-12}$	
R64	$O + O_2 + CO \rightarrow O_3 + CO$	$k_0 = 6.70\times10^{-34}\,(T/300.)^{-2.5}$	a
		$k_\infty = 2.80\times10^{-12}$	
R65	$O + O_2 + CO_2 \rightarrow O_3 + CO_2$	$k_0 = 1.40\times10^{-33}\,(T/300.)^{-2.5}$	a
		$k_\infty = 2.80\times10^{-12}$	
R66	$H + O_2 + N_2 \rightarrow HO_2 + N_2$	$k_0 = 5.70\times10^{-32}\,(T/300.)^{-1.6}$	c
		$k_\infty = 7.50\times10^{-11}$	
R67	$O + O_3 \rightarrow 2O_2$	$8.00\times10^{-12}\, e^{-2060./T}$	c
R68	$O(^1D) + O_3 \rightarrow 2O_2$	1.20×10^{-10}	c
R69	$O(^1D) + O_3 \rightarrow 2O + O_2$	1.20×10^{-10}	c
R70	$O_2(^1\Delta) + O_3 \rightarrow 2O_2 + O$	$5.20\times10^{-11}\, e^{-2840./T}$	c
R71	$H + O_3 \rightarrow OH + O_2$	$1.40\times10^{-10}\, e^{-470./T}$	c
R72	$OH + O_3 \rightarrow HO_2 + O_2$	$1.70\times10^{-12}\, e^{-940./T}$	c
R73	$OH + O_3 \rightarrow HO_2 + O_2(^1\Delta)$	$3.20\times10^{-14}\, e^{-940./T}$	a
R74	$HO_2 + O_3 \rightarrow OH + 2O_2$	$1.00\times10^{-14}\, e^{-490./T}$	c
R75	$O + H + M \rightarrow OH + M$	$k_0 = 1.30\times10^{-29}\, T^{-1.0}$	g
R76	$2H + M \rightarrow H_2 + M$	$k_0 = 2.70\times10^{-31}\, T^{-0.6}$	d
R77	$O + H_2 \rightarrow OH + H$	$8.50\times10^{-20}\, T^{2.7}\, e^{-3160./T}$	d
R78	$O(^1D) + H_2 \rightarrow H + OH$	1.10×10^{-10}	c
R79	$OH + H_2 \rightarrow H_2O + H$	$5.50\times10^{-12}\, e^{-2000./T}$	c
R80	$O + OH \rightarrow O_2 + H$	$2.20\times10^{-11}\, e^{120./T}$	c
R81	$H + OH + N_2 \rightarrow H_2O + N_2$	$k_0 = 6.10\times10^{-26}\, T^{-2.0}$	d
R82	$H + OH + CO_2 \rightarrow H_2O + CO_2$	$k_0 = 7.70\times10^{-26}\, T^{-2.0}$	d
R83	$2OH \rightarrow H_2O + O$	$4.20\times10^{-12}\, e^{-240./T}$	c
R84	$2OH + M \rightarrow H_2O_2 + M$	$k_0 = 6.90\times10^{-31}\,(T/300.)^{-1.0}$	c
		$k_\infty = 2.60\times10^{-11}$	
R85	$O + HO_2 \rightarrow OH + O_2$	$3.00\times10^{-11}\, e^{200./T}$	c

R86	$O + HO_2 \rightarrow OH + O_2(^1\Delta)$	$6.00\times10^{-13}\, e^{200./T}$	a
R87	$H + HO_2 \rightarrow 2OH$	7.21×10^{-11}	c
R88	$H + HO_2 \rightarrow H_2 + O_2$	7.29×10^{-12}	c
R89	$H + HO_2 \rightarrow H_2 + O_2(^1\Delta)$	1.30×10^{-13}	a
R90	$H + HO_2 \rightarrow H_2O + O$	1.62×10^{-12}	c
R91	$OH + HO_2 \rightarrow H_2O + O_2$	$4.80\times10^{-11}\, e^{250./T}$	c
R92	$OH + HO_2 \rightarrow H_2O + O_2(^1\Delta)$	$9.60\times10^{-13}\, e^{250./T}$	c
R93	$2HO_2 \rightarrow H_2O_2 + O_2$	$2.30\times10^{-13}\, e^{600./T}$	c
R94	$2HO_2 \rightarrow H_2O_2 + O_2(^1\Delta)$	$4.60\times10^{-15}\, e^{600./T}$	Estimated
R95	$2HO_2 + M \rightarrow H_2O_2 + O_2 + M$	$k_0 = 1.70\times10^{-33}\, e^{1000./T}$	c
R96	$O(^1D) + H_2O \rightarrow 2OH$	2.20×10^{-10}	c
R97	$O + H_2O_2 \rightarrow OH + HO_2$	$1.40\times10^{-12}\, e^{-2000./T}$	c
R98	$OH + H_2O_2 \rightarrow H_2O + HO_2$	$2.90\times10^{-12}\, e^{-160./T}$	c
R99	$Cl + O + M \rightarrow ClO + M$	$k_0 = 5.00\times10^{-32}$	e
R100	$Cl + O_3 \rightarrow ClO + O_2$	$2.30\times10^{-11}\, e^{-200./T}$	c
R101	$Cl + O_3 \rightarrow ClO + O_2(^1\Delta)$	$5.80\times10^{-13}\, e^{-260./T}$	c
R102	$Cl + H + M \rightarrow HCl + M$	$k_0 = 1.00\times10^{-32}$	e
R103	$Cl + H_2 \rightarrow HCl + H$	$3.70\times10^{-11}\, e^{-2300./T}$	c
R104	$Cl + OH \rightarrow HCl + O$	$8.33\times10^{-12}\, e^{-2790./T}$	h
R105	$Cl + HO_2 \rightarrow HCl + O_2$	$1.80\times10^{-11}\, e^{170./T}$	c
R106	$Cl + HO_2 \rightarrow OH + ClO$	$4.10\times10^{-11}\, e^{-450./T}$	c
R107	$Cl + H_2O_2 \rightarrow HCl + HO_2$	$1.10\times10^{-11}\, e^{-980./T}$	c
R108	$Cl + HOCl \rightarrow OH + Cl_2$	$6.00\times10^{-13}\, e^{-130./T}$	c
R109	$Cl + HOCl \rightarrow HCl + ClO$	$1.90\times10^{-12}\, e^{-130./T}$	c
R110	$Cl + ClCO \rightarrow Cl_2 + CO$	$2.16\times10^{-9}\, e^{-1670./T}$	h
R111	$Cl + CO + N_2 \rightarrow ClCO + N_2$	$k_0 = 1.30\times10^{-33}\, (T/300.)^{-3.8}$	a
R112	$Cl + OCS \rightarrow ClS + CO$	1.00×10^{-16}	c
R113	$Cl + ClS_2 \rightarrow S_2 + Cl_2$	1.00×10^{-12}	b
R114	$Cl + SO_2 + M \rightarrow ClSO_2 + M$	$k_0 = 1.30\times10^{-34}\, e^{940./T}$	a
R115	$2Cl + N_2 \rightarrow Cl_2 + N_2$	$k_0 = 6.10\times10^{-34}\, e^{900./T}$	a
R116	$2Cl + CO_2 \rightarrow Cl_2 + CO_2$	$k_0 = 2.60\times10^{-33}\, e^{900./T}$	a
R117	$O + Cl_2 \rightarrow ClO + Cl$	$7.40\times10^{-12}\, e^{-1650./T}$	a
R118	$O(^1D) + Cl_2 \rightarrow Cl + ClO$	1.55×10^{-10}	c
R119	$O(^1D) + Cl_2 \rightarrow Cl_2 + O$	5.25×10^{-11}	c
R120	$H + Cl_2 \rightarrow HCl + Cl$	$1.43\times10^{-10}\, e^{-590./T}$	a
R121	$OH + Cl_2 \rightarrow Cl + HOCl$	$1.40\times10^{-12}\, e^{-900./T}$	c
R122	$ClCO + Cl_2 \rightarrow COCl_2 + Cl$	$6.45\times10^{-2}\, k_{145}\, (107\alpha+[M])$	a
R123	$ClO + O \rightarrow Cl + O_2$	$3.00\times10^{-11}\, e^{70./T}$	c
R124	$ClO + O \rightarrow Cl + O_2(^1\Delta)$	$6.00\times10^{-13}\, e^{70./T}$	c
R125	$ClO + H_2 \rightarrow HCl + OH$	$1.00\times10^{-12}\, e^{-4800./T}$	c
R126	$ClO + OH \rightarrow HO_2 + Cl$	$7.40\times10^{-12}\, e^{270./T}$	c
R127	$ClO + OH \rightarrow HCl + O_2$	$6.00\times10^{-13}\, e^{230./T}$	c
R128	$ClO + HO_2 \rightarrow HOCl + O_2$	$2.70\times10^{-12}\, e^{220./T}$	c
R129	$ClO + CO \rightarrow CO_2 + Cl$	$1.00\times10^{-12}\, e^{-3700./T}$	c

R130	$2ClO \rightarrow Cl_2 + O_2$	$1.00\times10^{-12}\, e^{-1590./T}$	c
R131	$2ClO \rightarrow Cl_2 + O_2(^1\Delta)$	$2.00\times10^{-14}\, e^{-1590./T}$	c
R132	$ClO + OCS \rightarrow OSCl + CO$	2.00×10^{-16}	c
R133	$ClO + SO \rightarrow Cl + SO_2$	2.80×10^{-11}	c
R134	$ClO + SO_2 \rightarrow Cl + SO_3$	4.00×10^{-18}	c
R135	$ClO + SO_2 + M \rightarrow Cl + SO_3 + M$	$k_0 = 1.00\times10^{-35}$	a
		$k_\infty = 4.00\times10^{-19}$	
R136	$O + HCl \rightarrow OH + Cl$	$1.00\times10^{-11}\, e^{-3300./T}$	c
R137	$O(^1D) + HCl \rightarrow Cl + OH$	1.00×10^{-10}	c
R138	$O(^1D) + HCl \rightarrow ClO + H$	3.60×10^{-11}	c
R139	$O(^1D) + HCl \rightarrow O + HCl$	1.35×10^{-11}	c
R140	$OH + HCl \rightarrow Cl + H_2O$	$2.60\times10^{-12}\, e^{-350./T}$	c
R141	$O + HOCl \rightarrow OH + ClO$	1.70×10^{-13}	c
R142	$OH + HOCl \rightarrow H_2O + ClO$	$3.00\times10^{-12}\, e^{-500./T}$	c
R143	$O + ClCO \rightarrow Cl + CO_2$	3.00×10^{-11}	e
R144	$O + ClCO \rightarrow CO + ClO$	3.00×10^{-12}	e
R145	$ClCO + O_2 + M \rightarrow ClC(O)OO + M$	$k_0 = 5.70\times10^{-15}\, e^{500./T}/(10^{17}+0.05\times[M])$	e
R146	$H + ClCO \rightarrow HCl + CO$	1.00×10^{-11}	e
R147	$OH + ClCO \rightarrow HOCl + CO$	1.50×10^{-10}	a
R148	$2ClCO \rightarrow COCl_2 + CO$	5.00×10^{-11}	a
R149	$ClCO + ClC(O)OO \rightarrow 2CO_2 + 2Cl$	1.00×10^{-11}	a
R150	$ClCO + N_2 \rightarrow CO + Cl + N_2$	$k_{eq} = 1.60\times10^{-25}\, e^{4000./T}$	a
R151	$O(^1D) + COCl_2 \rightarrow Cl_2 + CO_2$	3.60×10^{-10}	c
R152	$O(^1D) + COCl_2 \rightarrow ClCO + ClO$	3.60×10^{-10}	a
R153	$O + ClC(O)OO \rightarrow Cl + O_2 + CO_2$	1.00×10^{-11}	e
R154	$H + ClC(O)OO \rightarrow Cl + OH + CO_2$	1.00×10^{-11}	e
R155	$Cl + ClC(O)OO \rightarrow Cl + ClO + CO_2$	1.00×10^{-11}	e
R156	$2ClC(O)OO \rightarrow 2Cl + 2CO_2 + O_2$	5.00×10^{-12}	a
R157	$H + O_2 + CO_2 \rightarrow HO_2 + CO_2$	$k_0 = 2.00\times10^{-31}\,(T/300.)^{-1.6}$	a
		$k_\infty = 7.50\times10^{-11}$	
R158	$H + HCl \rightarrow H_2 + Cl$	$1.50\times10^{-11}\, e^{-1750./T}$	a
R159	$Cl + CO + CO_2 \rightarrow ClCO + CO_2$	$k_0 = 4.20\times10^{-33}\,(T/300.)^{-3.8}$	a
R160	$ClCO + CO_2 \rightarrow CO + Cl + CO_2$	$k_{eq} = 1.60\times10^{-25}\, e^{4000./T}$	a
R161	$O + CO + M \rightarrow CO_2 + M$	$k_0 = 1.70\times10^{-33}\, e^{-1510./T}$	g
		$k_\infty = 2.66\times10^{-14}\, e^{-1459./T}$	
R162	$O + 2CO \rightarrow CO_2 + CO$	$k_0 = 6.50\times10^{-33}\, e^{-2180./T}$	a
R163	$2O + CO \rightarrow CO_2 + O$	$k_0 = 3.40\times10^{-33}\, e^{-2180./T}$	a
R164	$OH + CO \rightarrow CO_2 + H$	1.50×10^{-13}	c
R165	$S + O + M \rightarrow SO + M$	$k_0 = 1.50\times10^{-34}\, e^{900./T}$	b
R166	$S + O_2 \rightarrow SO + O$	2.30×10^{-12}	i
R167	$SO + O_2 \rightarrow SO_2 + O$	$1.60\times10^{-13}\, e^{-2280./T}$	k
R168	$HSO_3 + O_2 \rightarrow HO_2 + SO_3$	$1.30\times10^{-12}\, e^{-330./T}$	c
R169	$ClS + O_2 \rightarrow SO + ClO$	2.00×10^{-15}	l
R170	$S + O_3 \rightarrow SO + O_2$	1.20×10^{-11}	c

R171	$SO + O_3 \rightarrow SO_2 + O_2$	$4.50\times10^{-12}\, e^{-1170./T}$	k
R172	$SO + O_3 \rightarrow SO_2 + O_2(^1\Delta)$	$3.60\times10^{-13}\, e^{-1100./T}$	c
R173	$SO_2 + O_3 \rightarrow SO_3 + O_2$	$3.00\times10^{-12}\, e^{-7000./T}$	c
R174	$SO_2 + O_3 \rightarrow SO_3 + O_2(^1\Delta)$	$6.00\times10^{-14}\, e^{-7000./T}$	Estimated
R175	$S + OH \rightarrow SO + H$	6.60×10^{-11}	c
R176	$S + HO_2 \rightarrow SO + OH$	$3.00\times10^{-11}\, e^{200./T}$	e
R177	$SO_3 + H_2O \rightarrow H_2SO_4$	$2.26\times10^{-43}\, T\, e^{-6544/T}\, [H_2O]$	j
R178	$ClS + Cl_2 \rightarrow Cl_2S + Cl$	7.00×10^{-14}	l
R179	$S + Cl + M \rightarrow ClS + M$	$k_0 = 1.00\times10^{-29}\, T^{-1.0}$	b
R180	$S + Cl_2 \rightarrow ClS + Cl$	$2.80\times10^{-11}\, e^{-290./T}$	l
R181	$S + ClO \rightarrow SO + Cl$	4.00×10^{-11}	b
R182	$S + ClCO \rightarrow CO + ClS$	3.00×10^{-12}	Estimated
R183	$S + ClCO \rightarrow OCS + Cl$	3.00×10^{-12}	Estimated
R184	$S + ClC(O)OO \rightarrow Cl + SO + CO_2$	3.00×10^{-11}	a
R185	$S + CO + M \rightarrow OCS + M$	$k_0 = 4.00\times10^{-33}\, e^{-1940./T}$	Estimated
R186	$2S + M \rightarrow S_2 + M$	$k_0 = 1.18\times10^{-29}$	a
		$k_\infty = 1.00\times10^{-10}$	
R187	$O + S_2 \rightarrow SO + S$	$2.20\times10^{-11}\, e^{-84./T}$	b
R188	$S + S_2 + M \rightarrow S_3 + M$	$k_0 = 1.00\times10^{-25}\, T^{-2.0}$	a, b
		$k_\infty = 3.00\times10^{-11}$	
R189	$ClO + S_2 \rightarrow S_2O + Cl$	2.80×10^{-11}	b
R190	$2S_2 + M \rightarrow S_4 + M$	$k_0 = 2.20\times10^{-29}$	a
		$k_\infty = 1.00\times10^{-10}$	
R191	$O + S_3 \rightarrow SO + S_2$	8.00×10^{-11}	b
R192	$S + S_3 \rightarrow 2S_2$	8.00×10^{-11}	b
R193	$S + S_3 + M \rightarrow S_4 + M$	$k_0 = 1.00\times10^{-25}\, T^{-2.0}$	a, b
		$k_\infty = 3.00\times10^{-11}$	
R194	$S_2 + S_3 + M \rightarrow S_5 + M$	$k_0 = 1.00\times10^{-25}\, T^{-2.0}$	a, b
		$k_\infty = 3.00\times10^{-11}$	
R195	$2S_3 + M \rightarrow S_6 + M$	$k_0 = 1.00\times10^{-30}$	a
		$k_\infty = 3.00\times10^{-11}$	
R196	$O + S_4 \rightarrow SO + S_3$	8.00×10^{-11}	b
R197	$Cl + S_4 \rightarrow ClS_2 + S_2$	2.00×10^{-12}	l
R198	$S + S_4 \rightarrow S_2 + S_3$	8.00×10^{-11}	b
R199	$S_3 + S_4 \rightarrow S_2 + S_5$	$4.00\times10^{-11}\, e^{-200./T}$	b
R200	$S + S_4 + M \rightarrow S_5 + M$	$k_0 = 1.00\times10^{-25}\, T^{-2.0}$	a, b
		$k_\infty = 3.00\times10^{-11}$	
R201	$S_2 + S_4 + M \rightarrow S_6 + M$	$k_0 = 1.00\times10^{-25}\, T^{-2.0}$	a, b
		$k_\infty = 3.00\times10^{-11}$	
R202	$S_3 + S_4 + M \rightarrow S_7 + M$	$k_0 = 1.00\times10^{-25}\, T^{-2.0}$	a, b
		$k_\infty = 3.00\times10^{-11}$	
R203	$S_4 + M \rightarrow 2S_2 + M$	$k_{eq} = 2.71\times10^{-27}\, e^{13100./T}$	f
R204	$2S_4 + M \rightarrow S_8 + M$	$k_0 = 1.00\times10^{-30}$	a
		$k_\infty = 3.00\times10^{-11}$	

R205	$O + S_5 \rightarrow S_4 + SO$	$8.00\times10^{-11}\, e^{-200./T}$	b
R206	$S + S_5 \rightarrow 2S_3$	$3.00\times10^{-11}\, e^{-200./T}$	b
R207	$S + S_5 \rightarrow S_2 + S_4$	$5.00\times10^{-11}\, e^{-200./T}$	b
R208	$S_3 + S_5 \rightarrow S_2 + S_6$	$4.00\times10^{-11}\, e^{-200./T}$	b
R209	$S_4 + S_5 \rightarrow S_2 + S_7$	$2.00\times10^{-12}\, e^{-200./T}$	b
R210	$S_4 + S_5 \rightarrow S_3 + S_6$	$2.00\times10^{-12}\, e^{-200./T}$	b
R211	$S + S_5 + M \rightarrow S_6 + M$	$k_0 = 1.00\times10^{-25}\, T^{-2.0}$	a, b
		$k_\infty = 3.00\times10^{-11}$	
R212	$S_2 + S_5 + M \rightarrow S_7 + M$	$k_0 = 1.00\times10^{-25}\, T^{-2.0}$	a, b
		$k_\infty = 3.00\times10^{-11}$	
R213	$S_3 + S_5 + M \rightarrow S_8 + M$	$k_0 = 1.00\times10^{-25}\, T^{-2.0}$	a, b
		$k_\infty = 3.00\times10^{-11}$	
R214	$O + S_6 \rightarrow S_5 + SO$	$8.00\times10^{-11}\, e^{-300./T}$	b
R215	$S + S_6 \rightarrow S_3 + S_4$	$3.00\times10^{-11}\, e^{-300./T}$	b
R216	$S + S_6 \rightarrow S_2 + S_5$	$5.00\times10^{-11}\, e^{-300./T}$	b
R217	$S_3 + S_6 \rightarrow S_2 + S_7$	$4.00\times10^{-12}\, e^{-300./T}$	b
R218	$S_4 + S_6 \rightarrow S_2 + S_8$	$2.00\times10^{-12}\, e^{-300./T}$	b
R219	$S_4 + S_6 \rightarrow 2S_5$	$2.00\times10^{-12}\, e^{-300./T}$	b
R220	$S + S_6 + M \rightarrow S_7 + M$	$k_0 = 1.00\times10^{-25}\, T^{-2.0}$	a, b
		$k_\infty = 3.00\times10^{-11}$	
R221	$S_2 + S_6 + M \rightarrow S_8 + M$	$k_0 = 1.00\times10^{-25}\, T^{-2.0}$	a, b
		$k_\infty = 3.00\times10^{-11}$	
R222	$S_6 + M \rightarrow 2S_3 + M$	$k_{eq} = 2.41\times10^{-29}\, e^{21483./T}$	f
R223	$O + S_7 \rightarrow S_6 + SO$	$8.00\times10^{-11}\, e^{-200./T}$	b
R224	$S + S_7 \rightarrow S_2 + S_6$	$4.00\times10^{-11}\, e^{-200./T}$	b
R225	$S + S_7 \rightarrow S_3 + S_5$	$2.00\times10^{-11}\, e^{-200./T}$	b
R226	$S + S_7 \rightarrow 2S_4$	$2.00\times10^{-11}\, e^{-200./T}$	b
R227	$S_3 + S_7 \rightarrow S_2 + S_8$	$3.00\times10^{-11}\, e^{-200./T}$	b
R228	$S_3 + S_7 \rightarrow S_4 + S_6$	$1.00\times10^{-11}\, e^{-200./T}$	b
R229	$S_3 + S_7 \rightarrow 2S_5$	$1.00\times10^{-11}\, e^{-200./T}$	b
R230	$S_4 + S_7 \rightarrow S_3 + S_8$	$5.00\times10^{-12}\, e^{-200./T}$	b
R231	$S_4 + S_7 \rightarrow S_5 + S_6$	$5.00\times10^{-12}\, e^{-200./T}$	b
R232	$S + S_7 + M \rightarrow S_8 + M$	$k_0 = 1.00\times10^{-25}\, T^{-2.0}$	a, b
		$k_\infty = 3.00\times10^{-11}$	
R233	$O + S_8 \rightarrow S_7 + SO$	$8.00\times10^{-11}\, e^{-400./T}$	b
R234	$S + S_8 \rightarrow S_2 + S_7$	$4.00\times10^{-11}\, e^{-400./T}$	b
R235	$S + S_8 \rightarrow S_3 + S_6$	$2.00\times10^{-11}\, e^{-400./T}$	b
R236	$S + S_8 \rightarrow S_4 + S_5$	$2.00\times10^{-11}\, e^{-400./T}$	b
R237	$S_2 + S_8 \rightarrow 2S_5$	$1.00\times10^{-11}\, e^{-1400./T}$	b
R238	$S_8 + M \rightarrow 2S_4 + M$	$k_{eq} = 1.17\times10^{-29}\, e^{22695./T}$	f
R239	$O + SO \rightarrow S + O_2$	$6.60\times10^{-13}\, e^{-2760./T}$	a
R240	$O + SO + M \rightarrow SO_2 + M$	$k_0 = 5.10\times10^{-31}$	a*
		$k_\infty = 5.30\times10^{-11}$	
R241	$OH + SO \rightarrow SO_2 + H$	8.60×10^{-11}	c

R242	$HO_2 + SO \rightarrow SO_2 + OH$	2.80×10^{-11}	Estimated
R243	$Cl + SO + M \rightarrow OSCl + M$	$k_0 = 7.30\times10^{-21}\ T^{-5.0}$	l
R244	$ClC(O)OO + SO \rightarrow Cl + SO_2 + CO_2$	1.00×10^{-11}	a
R245	$ClS + SO \rightarrow S_2O + Cl$	1.00×10^{-11}	b
R246	$S_3 + SO \rightarrow S_2O + S_2$	1.00×10^{-12}	b
R247	$S + SO + M \rightarrow S_2O + M$	$k_0 = 3.30\times10^{-26}\ T^{-2.0}$	b*
R248	$2SO \rightarrow SO_2 + S$	$1.00\times10^{-12}\ e^{-1700./T}$	b
R249	$2SO + M \rightarrow (SO)_2 + M$	$k_0 = 4.40\times10^{-31}$	a
		$k_\infty = 1.00\times10^{-11}$	
R250	$O + (SO)_2 \rightarrow S_2O + O_2$	3.00×10^{-14}	a
R251	$O + (SO)_2 \rightarrow SO + SO_2$	3.00×10^{-15}	a
R252	$S_2 + (SO)_2 \rightarrow 2S_2O$	3.30×10^{-14}	a
R253	$SO + (SO)_2 \rightarrow S_2O + SO_2$	3.30×10^{-14}	b
R254	$(SO)_2 + M \rightarrow 2SO + M$	$k_{eq} = 1.00\times10^{-28}\ e^{6000./T}$	a
R255	$O + SO_2 \rightarrow SO + O_2$	$8.00\times10^{-12}\ e^{-9800./T}$	a
R256	$O(^1D) + SO_2 \rightarrow SO_2 + O$	7.00×10^{-11}	b
R257	$O(^1D) + SO_2 \rightarrow SO + O_2$	1.30×10^{-10}	b
R258	$O + SO_2 + M \rightarrow SO_3 + M$	$k_0 = 1.32\times10^{-31}\ e^{-1000./T}$	k*
R259	$OH + SO_2 + M \rightarrow HSO_3 + M$	$k_0 = 1.10\times10^{-30}\ (T/300.)^{-4.3}$	i*
		$k_\infty = 1.60\times10^{-12}$	
R260	$HO_2 + SO_2 \rightarrow OH + SO_3$	1.00×10^{-18}	c
R261	$ClC(O)OO + SO_2 \rightarrow Cl + SO_3 + CO_2$	1.00×10^{-15}	a
R262	$O + SO_3 \rightarrow SO_2 + O_2$	$2.32\times10^{-16}\ e^{-487./T}$	b
R263	$S + SO_3 \rightarrow SO_2 + SO$	1.00×10^{-16}	b
R264	$S_2 + SO_3 \rightarrow S_2O + SO_2$	2.00×10^{-16}	b
R265	$SO + SO_3 \rightarrow 2SO_2$	2.00×10^{-15}	b
R266	$O + S_2O \rightarrow 2SO$	1.70×10^{-12}	a
R267	$S + S_2O \rightarrow S_2 + SO$	$1.00\times10^{-12}\ e^{-1200./T}$	b
R268	$2S_2O \rightarrow S_3 + SO_2$	1.00×10^{-14}	a
R269	$O + ClS \rightarrow SO + Cl$	1.20×10^{-10}	l
R270	$Cl + ClS \rightarrow S + Cl_2$	1.00×10^{-14}	a
R271	$Cl + ClS + M \rightarrow Cl_2S + M$	$k_0 = 1.00\times10^{-30}$	l
		$k_\infty = 5.00\times10^{-11}$	
R272	$S + ClS \rightarrow S_2 + Cl$	1.00×10^{-11}	l
R273	$S_2 + ClS \rightarrow S_3 + Cl$	2.00×10^{-11}	b
R274	$2ClS \rightarrow S_2 + Cl_2$	6.00×10^{-12}	l
R275	$2ClS \rightarrow Cl_2S + S$	7.50×10^{-12}	a
R276	$2ClS \rightarrow ClS_2 + Cl$	5.40×10^{-11}	l
R277	$2ClS + M \rightarrow Cl_2S_2 + M$	$k_0 = 4.00\times10^{-31}$	a
		$k_\infty = 4.00\times10^{-12}$	
R278	$OCS + ClS \rightarrow ClS_2 + CO$	3.00×10^{-16}	a
R279	$O + ClS_2 \rightarrow SO + ClS$	1.00×10^{-13}	b
R280	$Cl + ClS_2 \rightarrow Cl_2 + S_2$	1.00×10^{-11}	l
R281	$ClS + ClS_2 \rightarrow Cl_2S + S_2$	1.00×10^{-12}	a

R282	$H + Cl_2S \rightarrow HCl + ClS$	2.00×10^{-11}	a
R283	$Cl + Cl_2S \rightarrow Cl_2 + ClS$	1.00×10^{-19}	a
R284	$2Cl_2S \rightarrow Cl_2S_2 + Cl_2$	1.00×10^{-20}	a
R285	$Cl + Cl_2S_2 \rightarrow Cl_2 + ClS_2$	4.30×10^{-12}	a
R286	$O + OSCl \rightarrow SO_2 + Cl$	$5.00\times10^{-11} e^{-600./T}$	b
R287	$O + OSCl \rightarrow SO + ClO$	$2.00\times10^{-11} e^{-600./T}$	b
R288	$Cl + OSCl \rightarrow Cl_2 + SO$	2.30×10^{-11}	l
R289	$S + OSCl \rightarrow S_2O + Cl$	$5.00\times10^{-11} e^{-600./T}$	b
R290	$S + OSCl \rightarrow SO + ClS$	$2.00\times10^{-11} e^{-600./T}$	b
R291	$SO + OSCl \rightarrow SO_2 + ClS$	6.00×10^{-13}	l
R292	$OSCl + M \rightarrow SO + Cl + M$	$7.29\times10^{-21} T^{-5.0}$	a
R293	$O + ClSO_2 \rightarrow SO_2 + ClO$	1.00×10^{-11}	a
R294	$H + ClSO_2 \rightarrow SO_2 + HCl$	1.00×10^{-11}	a
R295	$Cl + ClSO_2 \rightarrow SO_2 + Cl_2$	1.00×10^{-20}	b
R296	$ClS + ClSO_2 \rightarrow SO_2 + Cl_2S$	5.00×10^{-12}	l
R297	$S + ClSO_2 \rightarrow SO_2 + ClS$	1.00×10^{-11}	b
R298	$S_2 + ClSO_2 \rightarrow SO_2 + ClS_2$	$5.00\times10^{-11} e^{-800./T}$	b
R299	$SO + ClSO_2 \rightarrow OSCl + SO_2$	$5.00\times10^{-11} e^{-800./T}$	b
R300	$2ClSO_2 \rightarrow Cl_2 + 2SO_2$	5.00×10^{-13}	b
R301	$O + OCS \rightarrow SO + CO$	$1.60\times10^{-11} e^{-2150./T}$	k
R302	$S + OCS \rightarrow S_2 + CO$	$6.63\times10^{-20} T^{2.57} e^{-1180./T}$	m
R303	$S_2 + M \rightarrow 2S + M$	$k_{eq} = 2.68\times10^{-25} e^{50860./T}$	f
R304	$N + O_2 \rightarrow NO + O$	$1.50\times10^{-11} e^{-3600./T}$	c
R305	$HNO + O_2 \rightarrow NO + HO_2$	$3.65\times10^{-14} e^{-4600./T}$	n
R306	$N + O_3 \rightarrow NO + O_2$	2.00×10^{-16}	c
R307	$N + OH \rightarrow NO + H$	$3.80\times10^{-11} e^{85./T}$	o
R308	$O_2(^1\Delta) + N \rightarrow NO + O$	9.00×10^{-17}	c
R309	$N + HO_2 \rightarrow NO + OH$	2.20×10^{-11}	p
R310	$2N + M \rightarrow N_2 + M$	$k_0 = 8.27\times10^{-34} e^{490./T}$	q
R311	$O(^1D) + N_2 + M \rightarrow N_2O + M$	$k_0 = 3.50\times10^{-37} (T/300.)^{-0.6}$	c
R312	$O + NO + M \rightarrow NO_2 + M$	$k_0 = 9.00\times10^{-31} (T/300.)^{-1.5}$	c
		$k_\infty = 3.00\times10^{-11}$	
R313	$O_3 + NO \rightarrow NO_2 + O_2$	$3.00\times10^{-12} e^{-1500./T}$	c
R314	$H + NO + M \rightarrow HNO + M$	$k_0 = 3.23\times10^{-32}$	r
R315	$OH + NO + M \rightarrow HNO_2 + M$	$k_0 = 7.00\times10^{-31} (T/300.)^{-2.6}$	c
		$k_\infty = 3.60\times10^{-11} (T/300.)^{-0.1}$	
R316	$HO_2 + NO \rightarrow NO_2 + OH$	$3.50\times10^{-12} e^{250./T}$	c
R317	$N + NO \rightarrow N_2 + O$	$2.10\times10^{-11} e^{100./T}$	c
R318	$O + NO_2 \rightarrow NO + O_2$	$5.60\times10^{-12} e^{180./T}$	c
R319	$O + NO_2 + M \rightarrow NO_3 + M$	$k_0 = 2.50\times10^{-31} (T/300.)^{-1.8}$	c
		$k_\infty = 2.20\times10^{-11} (T/300.)^{-0.7}$	
R320	$O_3 + NO_2 \rightarrow NO_3 + O_2$	$1.20\times10^{-13} e^{-2450./T}$	c
R321	$H + NO_2 \rightarrow OH + NO$	$4.00\times10^{-10} e^{340./T}$	c
R322	$OH + NO_2 + M \rightarrow HNO_3 + M$	$k_0 = 2.00\times10^{-30} (T/300.)^{-3.0}$	c

		$k_\infty = 2.50\times10^{-11}\ e^{300./T}$	
R323	$HO_2 + NO_2 \rightarrow HNO_2 + O_2$	5.00×10^{-16}	c
R324	$N + NO_2 \rightarrow N_2O + O$	$5.80\times10^{-12}\ e^{220./T}$	c
R325	$NO_3 + NO_2 \rightarrow NO + NO_2 + O_2$	$4.50\times10^{-14}\ e^{-1260./T}$	c
R326	$O + NO_3 \rightarrow O_2 + NO_2$	1.00×10^{-11}	c
R327	$H + NO_3 \rightarrow OH + NO_2$	1.10×10^{-10}	s
R328	$OH + NO_3 \rightarrow HO_2 + NO_2$	2.20×10^{-11}	c
R329	$HO_2 + NO_3 \rightarrow HNO_3 + O_2$	3.50×10^{-12}	c
R330	$NO + NO_3 \rightarrow 2NO_2$	$1.50\times10^{-11}\ e^{170./T}$	c
R331	$2NO_3 \rightarrow 2NO_2 + O_2$	$8.50\times10^{-13}\ e^{2450./T}$	c
R332	$HCl + NO_3 \rightarrow HNO_3 + Cl$	5.00×10^{-17}	c
R333	$CO + NO_3 \rightarrow NO_2 + CO_2$	4.00×10^{-19}	c
R334	$O(^1D) + N_2O \rightarrow 2NO$	6.70×10^{-11}	c
R335	$O(^1D) + N_2O \rightarrow N_2 + O_2$	4.90×10^{-11}	c
R336	$H + HNO \rightarrow H_2 + NO$	1.30×10^{-10}	t
R337	$OH + HNO \rightarrow H_2O + NO$	5.00×10^{-11}	u
R338	$O_3 + HNO_2 \rightarrow O_2 + HNO_3$	5.00×10^{-19}	c
R339	$OH + HNO_2 \rightarrow H_2O + NO_2$	$1.80\times10^{-11}\ e^{-390./T}$	c
R340	$O + HNO_3 \rightarrow OH + NO_3$	3.00×10^{-17}	c
R341	$OH + HNO_3 \rightarrow NO_3 + H_2O$	$7.20\times10^{-15}\ e^{785./T}$	c
R342	$Cl + NO_3 \rightarrow ClO + NO_2$	2.40×10^{-11}	c
R343	$Cl + HNO_3 \rightarrow HCl + NO_3$	2.00×10^{-16}	c
R344	$ClO + NO \rightarrow Cl + NO_2$	$6.40\times10^{-12}\ e^{290./T}$	c
R345	$ClO + N_2O \rightarrow 2NO + Cl$	$1.00\times10^{-12}\ e^{-4300./T}$	c
R346	$SO + NO_2 \rightarrow SO_2 + NO$	1.40×10^{-11}	c
R347	$SO_2 + NO_2 \rightarrow SO_3 + NO$	2.00×10^{-26}	c
R348	$SO_2 + NO_3 \rightarrow SO_3 + NO_2$	7.00×10^{-21}	c
R349	$OCS + NO_3 \rightarrow CO + SO + NO_2$	1.00×10^{-16}	k
R350	S_x + Aerosol $\rightarrow$ Aerosol	See Appendix B	

A.4. Nucleation Rate of Elemental Sulfur

A.4.1. Aerosol profile

Above the middle cloud top (~58 km), the aerosols are found to exhibit a bimodal distribution in the upper cloud layer (58~70 km) and upper haze layer (70~90 km). In this study we combine the upper haze profiles from Wilquet et al. (2010) above 72 km and upper cloud particle profiles from Knollenberg and Hunten (1980) from 58 to 65 km. Due

to the lack of data for the intermediate altitudes (65~72 km) at present, interpolation is applied. Figure A.3 shows the bimodal aerosol profiles (left panel).

From the aerosol abundances, we can estimate the sulfur content. Mode 1 aerosols are ~0.2 μm in radius constantly for all altitudes. For mode 2 aerosols, we use 0.7 μm above 72 km (Wilquet et al. 2009) for the haze particles and 1.1 μm below for the cloud particles (Knollenberg and Hunten 1980). The right panel in Figure A.3 shows the equivalent sulfur mixing ratio (ESMR) by volume computed from the H_2SO_4 aerosol (solid line) abundances by assuming that the H_2SO_4 aerosol density is 2 g cm^{-3} and weight percent are 85% and 75% below and above 72 km, respectively. The ESMR in the H_2SO_4 droplet is close to 1 ppm at all altitudes, which is enough for the enhancement of sulfur oxides above 80 km. By assuming that the radius of elemental sulfur is about half of the H_2SO_4 aerosol radius and the density is also 2 g cm^{-3}, we found the ESMR in elemental sulfurs in excess of 1 ppb level at most altitude (Figure A.3, right panel, dashed line).

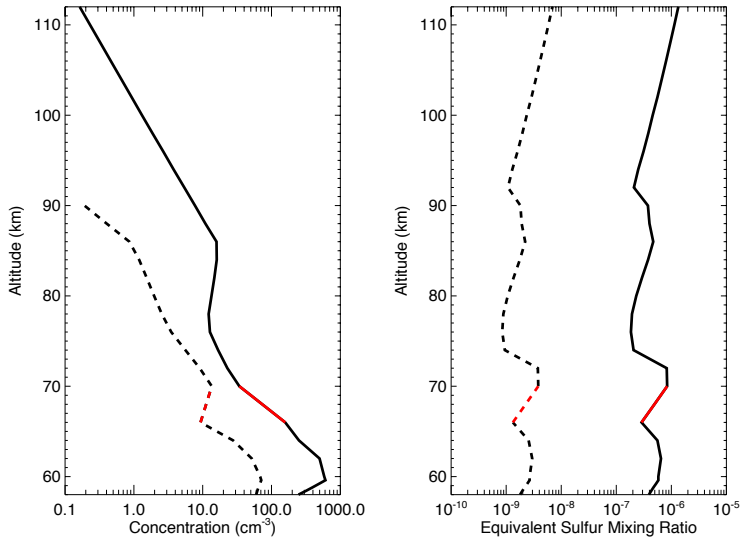

Figure A.3. Left panel: Concentration profiles of mode 1 (solid) and mode 2 (dashed) aerosols based on the upper haze profiles from Wilquet et al. (2009) above 72 km and upper cloud particle profiles from Knollenberg and Hunten (1980) from 58 to 65 km. Data are not available in the red region (~66-70 km). Right panel: The equivalent sulfur mixing ratio (ESMR) by volume computed from the H_2SO_4 aerosol (solid line) and the polysulfur aerosol (dashed line). See the text for details.

A.4.2 Heterogeneous Nucleation

The nucleation rate of elemental sulfurs onto H_2SO_4 droplets is estimated as follows. The nucleation rate constant in the continuum regime (where the particle size is much larger than the vapor mean free path λ) is expressed as (Seinfeld and Pandis 2006): $J_c = 4\pi R_p D_s$, where R_p is the H_2SO_4 aerosol radius and D_s the molecular diffusivity of elemental sulfur vapor.

However, in the Venus cloud layer, the Knudsen Number K_n (= λ/R_p) of S_x vapor is not far from 1, so the nucleation process lies in the transition regime where the mean free path λ of the diffusing vapor molecule (e.g., S_x vapor) is comparable to the pre-existing aerosol size. Therefore, we adopt the Dahneke approach (Dehneke 1983), which matches the fluxes of continuum regime ($K_n \ll 1$) and free molecular regime ($K_n \gg 1$) by introducing a function $f(K_n)$

$$f(K_n) = \frac{1 + K_n}{1 + 2K_n(1 + K_n)/\alpha}, \tag{A.1}$$

where α is the molecular accommodation coefficient, which is the probability of sticking when the vapor molecule encounters a particle. Here the mean free path λ in K_n is defined as $2D_s/v$, where v is the mean thermal velocity of the vapor molecule.

Finally we obtain the nucleation rate constant:

$$J = f(K_n)J_c = \frac{4\pi R_p D_s(1 + K_n)}{1 + 2K_n(1 + K_n)/\alpha}. \tag{A.2}$$

The molecular diffusivity D_s of sulfur vapor can be estimated using hard sphere approximation: D_s=b/N, where N is the total CO_2 gas density in the environment and b is the binary collision parameter:

$$b = \frac{3}{4\pi(d_s + d_g)^2}\left(\frac{2\pi kT(m_s + m_g)}{m_s m_g}\right)^{1/2}, \tag{A.3}$$

where d_s and d_g are the diameters of S_x and CO_2 molecule, respectively (assuming $d_s = d_g =$ 3 Å), k = Boltzmann constant, T = temperature, m_s and m_g are the mass of S_x and CO_2 molecule, respectively. Figure 2.15 shows the total nucleation timescale of S_2 calculated from two modes of aerosols (roughly the same for other allotropes), together with the eddy transport timescale and photolysis timescales of S_2, S_3 and S_4. See the discussion in section 2.4.

A.5. H_2SO_4 and S_x Vapor Abundances

A.5.1. H_2SO_4

If sulfuric acid is in thermodynamic equilibrium with the surrounding atmosphere, the saturation vapor pressure (SVP) over H_2SO_4 aerosol should mainly depend on the temperature and aerosol composition. However, non-thermodynamic equilibrium in the real atmosphere is common because the chemical and dynamic processes, such as the chemical production, loss, condensation, evaporation and transport, are often involved and play important roles. The condensation efficiency, which depends on many microphysical properties of the system like the temperature, diffusivity, aerosol size, surface tension, and interaction between molecules and aerosols, will greatly affect the H_2SO_4 vapor pressure over the liquid droplets. The very low condensation rate could cause large supersaturation of the H_2SO_4 vapor. For example, the saturation ratio of H_2SO_4 in the lower stratospheric sulfate layer (Junge layer) on Earth has been observed to be as large as 10^2-10^3 (Arnold 2006). A similar situation may exist in the Venus upper haze layer on the dayside when the H_2SO_4 vapor on the night side is transported to the dayside, because the SVP of H_2SO_4 in the night side is several orders of magnitude larger than that in the dayside (Zhang et al. 2010) due to the large temperature difference above 90 km. Zhang et al. (2010) proposed that this might be the key mechanism to explain the SO_2 inversion layer because the nighttime H_2SO_4 abundance could be enough to produce the observed SO_2 under photochemical processes if the H_2SO_4 photolysis cross section is 100 time larger than the current data from Vaida et al. (2003).

In the condensation processes, we assume that the sulfate aerosol will quickly establish equilibrium with respect to water because there are more collisions of aerosol particles with H_2O molecules than with H_2SO_4 molecules. Therefore, we could derive the H_2SO_4 aerosol composition (weight percent) from the water activity (or equilibrium relative humidity) defined as the partial pressure of water vapor divided by the SVP over pure water under the same temperature. The water activity is shown in Figure A.4 (left panel) for day and night temperature profile, respectively. We used the H_2O SVP as function of temperature from Tabazadeh et al. (1997), which is valid between 185 and 260K:

$$P_{H_2O} = \exp(18.4524 - \frac{3.5052\times10^3}{T} - \frac{3.3092\times10^5}{T^2} - \frac{1.2725\times10^7}{T^3}), \qquad (A.4)$$

where P_{H_2O} is the SVP of H_2O in mbar and T is temperature. We extrapolated the formula to the entire temperature range (156-274 K) of Venus mesosphere so there would be some uncertainties above 84 km for the dayside temperature and 84-90 km for the nightside.

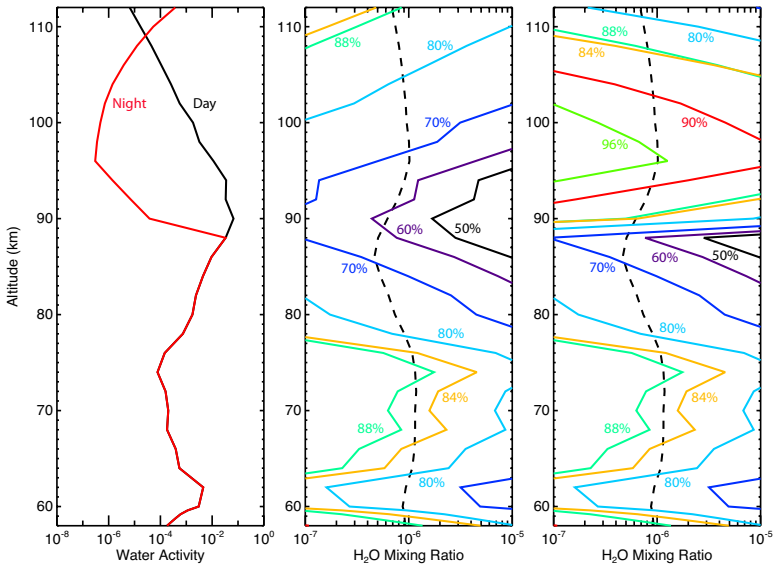

Figure A.4. Left panel: water activity profiles based on the daytime and nighttime temperature profiles. Middle and right panels: equilibrium H_2O mixing ratio contours from which H_2SO_4 weight percent for each altitude could be inferred by comparing the observed H_2O profile (dashed line). The middle and right panels are for the day and night temperature situations, respectively.

The H_2SO_4 weight percent is roughly estimated by comparing the observed H_2O mixing ratio profile with the theoretical profiles under different H_2SO_4 compositions, as shown in Figure A.4 (the middle and right panels). For the 50-80 wt% H_2SO_4, we computed the H_2O mixing ratio profiles based on Clegg and Brimblecombe (1995) and Tabazadeh et al. (1997). For the more concentrated acids, our calculation is based on Gmitro and Vermeulen (1964) although it may not be very accurate for the low temperature (Mills 1998). There are also some uncertainties in applying the Tabazadeh (1997) formula to Venus because the Clegg and Brimblecombe (1995) is only valid if the water activity larger than 0.01. The atmosphere of Venus is very dry (Figure A.4), and so actually only the results in the region from 85 to 100 km in the dayside and 85 to 90 km in the nightside seem robust. However, as we showed before, the H_2O SVP may have some uncertainties in those regions. Therefore, the H_2SO_4 weight percent derived here is only a rough estimate based on the current knowledge.

The H_2SO_4 weight percent falls with altitude, associated with the increase of relative humidity due to the temperature decrease. The values are about 90%-84% in 58-70 km and 84%-60% in 70-90 km, which are roughly consistent with the H_2SO_4 compositions obtained from aerosol refractive indexes based on the photometry measurements (85% and 75%, respectively). But in the region above 90 km, the large contrast of dayside and nightside temperatures results in large difference of the local H_2SO_4 weight percent. For example, H_2SO_4 at 100 km is ~75% in the dayside but can be larger than 96% in the nightside if the H_2O vapor profiles are the same for both hemispheres. Actually the temperature profile above 90 km has been found to be a function of longitude (Bertaux et al. 2007). Therefore, if the transport is efficient, the H_2SO_4 aerosols could have a broad range distribution of various concentrations above 90 km but the H_2SO_4 vapor abundances might be mainly determined by the warmest nightside temperature since the vapor abundances is extremely sensitive to the temperature.

The H_2SO_4 SVP is another uncertainty and maybe the major one. In the supplementary material of Zhang et al. (2010), three H_2SO_4 SVP formulas as function of temperature

and H_2SO_4 concentration have been discussed in details. These formulas could differ by several orders of magnitude but none of them has been verified in the temperature range of upper atmosphere of Venus. Instead of using the H_2SO_4 weight percent profile derived in Figure A.4, we simply assumed 85% H_2SO_4 below 70 km and 75% from 70 to 90 km and used the vapor pressure formulas from Ayers et al. (1980) corrected by Kulmala and Laaksonen (1990):

$$\ln P^0_{H_2SO_4} = 16.259 + \frac{\mu - \mu_0}{8.3143T} + 10156 \times \left(-\frac{1}{T} + \frac{0.38}{T_c - T_0}\left(1 + \ln(\frac{T_0}{T}) - \frac{T_0}{T}\right)\right), \quad \text{(A.5)}$$

where T_c = 905 K, T_0 = 360.15 K, $P^0_{H_2SO_4}$ is SVP of H_2SO_4 in atm, T is the temperature, μ and μ_0 are the chemical potentials of H_2SO_4 solutions of certain composition and pure acid, respectively. The values of $\mu_0 - \mu^{***}$ for the 85% and 75% H_2SO_4 are, respectively, 1555 cal^{-1} mole and 3681 cal^{-1} mole based on Giauque et al. (1960).

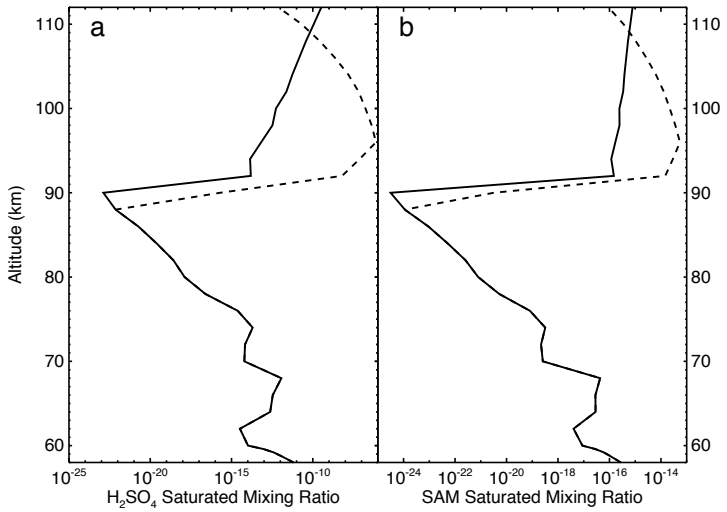

Figure A.5. Left panel: H_2SO_4 vapor volume mixing ratio profiles in equilibrium with the daytime (solid) and nighttime temperatures (dashed). Right panel: monohydrate ($H_2SO_4 \cdot H_2O$) vapor volume mixing ratio profiles.

*** The sign was flipped in Zhang, X., Liang, M. C., Mills, F. P., Belyaev, D., and Yung, Y. L., 2012. Sulfur chemistry in the middle atmosphere of Venus. Icarus 217, 2, 714-739.

In fact the H_2SO_4 abundances in the region below 80 km are not important because the H_2SO_4 photolysis is negligible for the lower region chemistry. But in the upper region the H_2SO_4 might behave like a sulfur source rather than a sink, and large abundance of H_2SO_4 is required in the upper region in order to reproduce the SO_2 inversion layer (Zhang et al. 2010). So we adopted the formula by Stull (1947) just for reference, simply because it gives the largest SVP in the Venus temperature range:

$$P_{H_2SO_4} = 10^{-3954.90/T+9.4570}, \quad \text{(A.6)}$$

where $P_{H_2SO_4}$ is the SVP of H_2SO_4 in mmHg and T is temperature. The H_2SO_4 SVP profiles in Figure A.5 (left panel) show large difference between the dayside and nightside caused by the difference in temperatures. Since H_2SO_4 is very hygroscopic, the right panel shows the abundance of monohydrate ($H_2SO_4 \cdot H_2O$), estimated based on the extrapolation of the equilibrium constants from the Vaida et al. (2003) for the earth atmosphere (223-271 K in the literature). The abundances of $H_2SO_4 \cdot H_2O$ above 90 km are less than 5% and much less ($<10^{-5}$) than that of pure H_2SO_4 for the dayside and nightside, respectively, although the equilibrium constants have not been verified in the Venus temperature region (~160-240 K).

A.5.2. S_x

Lyons (2008) summarized the previous laboratory measurements and computed vapor pressure over the liquid sulfur allotropes and the total solid sulfur vapor pressures over the orthorhombic sulfur and the monoclinic sulfur below the melting points. Based on the data, the author estimated the equilibrium vapor pressure over solid sulfur allotropes. In this study, we follow the same method and calculated the monoclinic S_x saturated volume mixing ratio profiles under the daytime and nighttime temperature situations. The results are shown in Figure A.6.

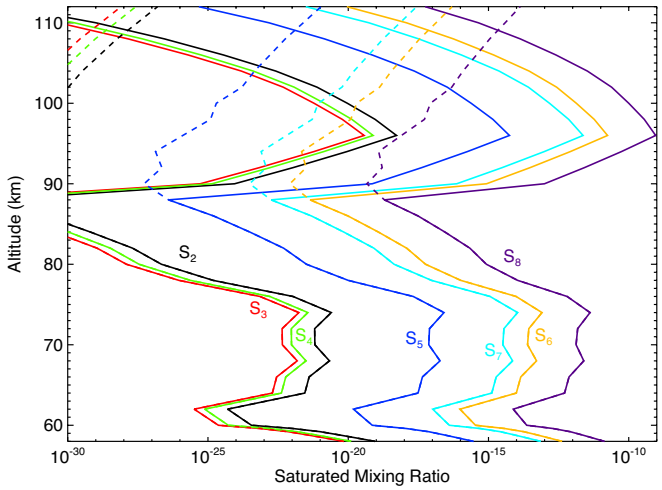

Figure A.6. Saturated vapor volume mixing ratio profiles of S_x allotropes based on the monoclinic S_x saturated vapor pressure over solid S_x based on Lyons (2008), in equilibrium with the daytime (dashed) and nighttime (solid) temperatures.

A.6. H_2SO_4 Photolysis Cross Section

H_2SO_4 was thought to be photodissociated by the UV photons only. Burkholder et al. (2000) and Hintze et al. (2003) estimated the upper limits for the UV cross section of H_2SO_4 based on the failure to detect any absorption beyond 140 nm. The upper limits are assumed to be 1×10^{-21} cm^2 molecule^{-1} in the interval 195-330 nm, 1×10^{-19} cm^2 molecule^{-1} in 160-195 nm, and 1×10^{-18} cm^2 molecule^{-1} in 140-160 nm. Lane et al. (2008) revisited the UV cross sections by calculating the electronic transitions based on the theoretical twin hierarchial approach and they found that the cross section in the Lyman-α region (~121.6 nm) is about $\sim6\times10^{-17}$ cm^2 molecule^{-1}, much larger than the previously assumed value. And it also seems that the cross section in the interval 195-330 nm is much smaller than the upper limits from Burkholder et al. (2000).

Vaida et al. (2003) proposed that in the visible region the excitation of the OH-stretching overtone transitions with $\nu \geq 4$ (~38.6 kcal mole^{-1}, or ~742 nm) is also enough to photolyze H_2SO_4 because the energy required for $H_2SO_4 + h\upsilon \rightarrow SO_3 + H_2O$ is only 32-40 kcal mole^{-1}. This mechanism has been verified by the laboratory experiments in $4\nu_9$ and $5\nu_9$ bands from

the cavity ring-down spectroscopy by Feierabend et al. (2006). Vaida et al. (2003) also proposed that, in the IR and visible regions the OH-stretching overtone transitions with $\nu \geq 3$ (~26.3 kcal/mole, or ~1.09 μm) are able to generate the photodissociation of $H_2SO_4 \cdot H_2O$ as well (required energy ~25 kcal $mole^{-1}$) and the total photolysis coefficient is about ~100 times larger than that of pure H_2SO_4, although a recent simulation by Miller and Gerber (2006) suggested that the $H_2SO_4 \cdot H_2O$ is more likely to thermally decompose to H_2SO_4 and H_2O before photodissociation.

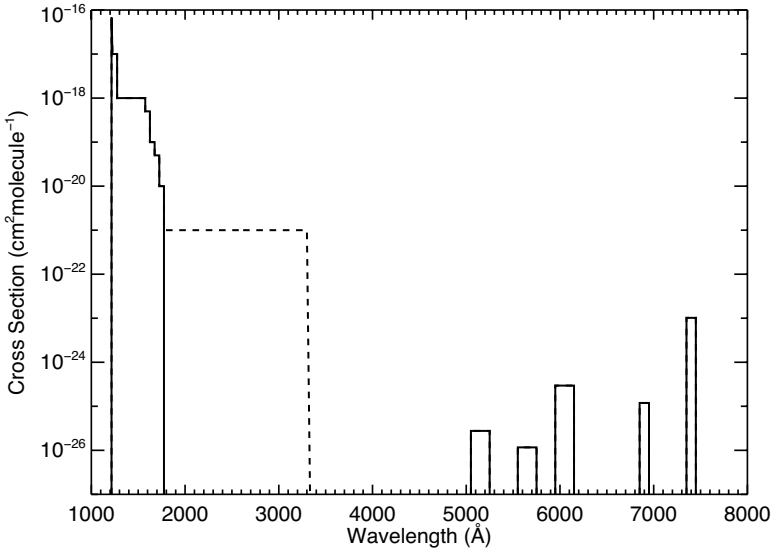

Figure A.7. H_2SO_4 cross sections binned in the model grids. Solid: data from Lane and Kjaergaard (2008) for the UV region, and Mills et al. (2005) and Feierabend et al. (2006) for the visible region. Dashed: same as the solid line but also with 1×10^{-21} cm^2 $molecule^{-1}$ in the UV region of 195-330 nm.

The solid line in Figure A.7 shows the cross sections from Lane et al. (2008) for the UV region and Mills et al. (2005) and Feierabend et al. (2006) data for the visible region and binned in our model spectral grid. As shown in Table 2.1, the H_2SO_4 photolysis coefficient is generally ~10^{-7} s^{-1} in the upper atmosphere. It is ~10^{-6} s^{-1} near the upper boundary (112 km) due to the photolysis by the Lyman-α line but only in a very thin layer (<1 km) because the Layman alpha intensity decreases very rapidly due to the CO_2 absorption. The major contribution to the photolysis is the solar pumping of the vibrational overtones by the 740

nm red light ($4\nu_9$ band, Vaida et al. 2003). The collisional deactivation mainly depends on the atmospheric pressure. In Miller et al. (2007) the quantum yield is nearly unity above 60 km where the pressure is 0.2 mbar in the Earth atmosphere. In Venus, this pressure level (0.2 mbar) is at ~90 km which is the lower boundary of the H_2SO_4 photolysis region we are interested here. Therefore the quantum yield is assumed to be unity above 90 km.

However, Zhang et al. (2010) showed that the photolysis coefficient ~10^{-7} s^{-1} is not enough to produce the observed SO_2, otherwise a very large supersaturation of H_2SO_4 (~100) under nighttime temperature is needed. Although this supersaturation is possible (as seen in Earth), empirically they also found the required cross section is about ~100 times larger than that of pure H_2SO_4 if keeping the H_2SO_4 vapor abundances roughly the same as the nighttime saturated abundances. This extreme situation may suggest the existence of large amount of $H_2SO_4 \cdot H_2O$ and maybe other hydrates (like $H_2SO_4 \cdot 2H_2O$), although it seems not very likely not only because the equilibrium abundance of the monohydrate is small (see Figure A.5) but also because the sulfuric acid hydrates might readily condense into the crystal phase even under the nighttime temperature (McGouldrick et al. 2010). Alternatively, the required large cross section actually could be achieved by assuming the UV cross section as the upper limit of 1×10^{-21} cm^2 $molecule^{-1}$ between 195 and 330 nm, as shown in dashed line in Figure A.7. We consider this possibility in the model A. Note that this change of H_2SO_4 photolysis may not affect much for the earth stratosphere below 35 km because of the absorption of O_3 Hartley band dominates the actinic flux in that region. However, this is very important for the Venus mesosphere above the cloud top since the SO_2 absorption is not as strong as O_3. The H_2SO_4 photolysis coefficient in this case is ~8.3×10^{-6} s^{-1} at 90 km, roughly the same as that of ~8.2×10^{-6} s^{-1} if we use the $H_2SO_4 \cdot H_2O$ photolysis cross section instead (model B in Zhang et al. 2010).

Appendix B

Supplementary Materials for chapter III

B.1. Analytical Solutions For Atmospheric Radiative Equilibrium State

B.1.1 Infrared (IR) Source Function in Radiative Equilibrium

The general equation of radiative transfer is

$$\mu \frac{dI}{d\tau} = I - B, \qquad (B.1)$$

where I is the IR radiation field (intensity), B is the atmospheric source function, τ is the optical depth and μ is the cosine of the view angle. Under Eddington approximation: $I(\mu) = I_0 + I_1\mu$, the moments are

$$\bar{I} = \int I(\mu) d\mu \, d\omega = I_0 \,, \qquad (B.2a)$$

$$F = \int \mu I \, d\mu \, d\omega = \frac{4\pi}{3} I_1, \qquad (B.2b)$$

$$K = \int \mu^2 I \, d\mu \, d\omega = \frac{4\pi}{3} I_0, \qquad (B.2c)$$

Substituting into equation (B.1) and we obtain

$$4\pi \frac{dB}{d\tau} = 3F - \frac{d^2F}{d\tau^2}. \qquad (B.3)$$

The upper boundary condition of thermal source function $B(\tau)$ can be estimated from the two-stream approximation. Suppose we only have one upward stream I^+, and one downward stream I^-:

$$F = \pi(I^+ - I^-), \qquad (B.4a)$$

$$\bar{I} = \frac{I^+ + I^-}{2}. \qquad (B.4b)$$

So equation (B.3) becomes

$$\frac{dF(\tau)}{d\tau} = 2F(\tau) + 4\pi I^-(\tau) - 4\pi B(\tau). \qquad (B.5)$$

If we assume no downward IR flux (I^-) at the upper boundary, we obtain

$$B(0) = \frac{F(0)}{2\pi} - \frac{1}{4\pi}\left(\frac{dF}{d\tau}\right)_{\tau=0}. \quad (B.6)$$

The radiative equilibrium state requires

$$\frac{dF}{d\tau} = -\frac{dF_{heat}}{d\tau} = -S(\tau), \quad (B.7)$$

where $F(\tau)$ is the thermal IR flux emitted by the atmosphere and F_{heat} is the heat flux from outside heat source. $S(\tau) = dF_{heat}/d\tau$ is called the heating rate. The primary heat flux is from the downward solar flux F_s, which is absorbed in the visible or near IR wavelengths so that it does not exchange the photons with the thermal IR wavelengths. On the other hand, there could be an upward heat flux $F_\oplus$, either from (1) the surface that is heated by absorbing the sunlight directly; or (2) the radioactive decay of the heavy elements in the crust of terrestrial plants; or (3) the upward convective heat flux from the deep interior of giant planets. $F_\oplus$ is mainly in the thermal IR region and usually treated as the lower boundary condition of the upward flux.

Here we discuss two cases:

(a) For a certain incident angle, solar Flux at τ_v is

$$F_s^-(\mu, \tau_v) = -\mu F_s\, e^{-\frac{\tau_v}{\mu}}, \quad (B.8)$$

where τ_v is the optical depth at visible (or near IR) wavelength v where the solar flux can be absorbed. $\mu = cos\theta$ is the cosine of the solar incident angle, F_s is the solar flux at the top of the atmosphere (TOA). Negative sign means downward flux. The radiative equilibrium thermal flux $F_{IR} = -F_{heat} = F_\oplus + \mu F_s\, e^{-\frac{\alpha\tau}{\mu}}$, where τ is the averaged optical depth in the thermal emission wavelengths and $\alpha = \tau_v/\tau$. From equation (B.3), we solve the $B(\tau)$:

$$B(\tau) = \frac{3F_\oplus}{4\pi}\left(\frac{2}{3} + \tau\right) + \frac{3\mu F_s}{4\pi}\left[\frac{2}{3} + \frac{\mu}{\alpha} + \left(\frac{\alpha}{3\mu} - \frac{\mu}{\alpha}\right)e^{-\frac{\alpha\tau}{\mu}}\right]. \quad (B.9)$$

This is basically the same as the result in Goody and Yung (1995).

(b) For a global averaged solar flux (including the diurnally average):

$$\overline{F^-}(\tau_v) = \frac{\int_0^{\frac{\pi}{2}} F_v^-(\mu, \tau_v)\, 2\pi R^2 sin\theta d\theta}{4\pi R^2} = -\frac{1}{2} F_s E_3(\tau_v), \qquad (B.10)$$

where $E_n(x) = \int_1^\infty \frac{e^{-xt}}{t^n} dt = \int_x^\infty \frac{x^{n-1}e^{-t}}{t^n} dt$ is the exponential integral. When $\tau_s = 0$ (TOA), $\overline{F^-}(\tau_v) = F_s/4$. The radiative equilibrium thermal flux $F_{IR} = -F_{heat} = F_\oplus + \frac{1}{2} F_s E_3(\alpha\tau)$.

From equation (B.2), we solve the $B(\tau)$:

$$B(\tau) = \frac{3F_\oplus}{4\pi}\left(\frac{2}{3} + \tau\right) + \frac{3F_s}{4\pi}\left[\frac{1+\alpha}{6\alpha} + \frac{\alpha}{6} E_2(\alpha\tau) - \frac{1}{2\alpha} E_4(\alpha\tau)\right]. \qquad (B.11)$$

B.1.2. Analytical Solutions for Radiance, Flux, Heating and Cooling Rate

Based on the radiative equilibrium IR source functions above, we derive analytical solutions for the TOA radiance, upward and downward fluxes for each layer, and solar heating and thermal cooling rates for each layer. The source function $B(\tau)$ could have one of the following expressions, corresponding to the above cases (a) and (b), respectively:

1. $B(\tau) = B_0 + B_1\tau + B_2 e^{-\alpha\tau}$,
2. $B(\tau) = B_0 + B_1\tau + B_2 E_2(\alpha\tau) + B_3 E_4(\alpha\tau)$.

We will focus on expression 1 because it is less complicated than expression 2 and therefore the analytical solutions can be obtained through integrations. Expression 1 can describe the typical tropospheric temperature and stratospheric temperature with or without inversion. In the following notation, we will ignore the wavenumber index in the lower subscript but all the formulae should be considered monochromatic and can be used for testing the numerical line-by-line (LBL) radiative transfer models. Please see section B.4 for the details of the integration derivations.

TOA Radiance

The IR upward radiance at emission angle θ at τ_i:

$$I^+(\tau_i,\mu) = B(\tau_s)e^{-\frac{\tau_s-\tau_i}{\mu}} + \int_{\tau_i}^{\tau_s} B(t)e^{-\frac{t-\tau_i}{\mu}}\frac{dt}{\mu}, \qquad (B.12)$$

where τ_s is the total optical depth from the upper to the lower boundary. $\mu = cos\theta$.

IR downward radiance at τ_i:

$$I^-(\tau_i,\mu) = \int_0^{\tau_i} B(t)e^{\frac{t-\tau_i}{\mu}}\frac{dt}{\mu}. \qquad (B.13)$$

We are more interested the TOA IR radiance ($\tau_i = 0$) that can be measured by the satellite. The TOA IR radiance at emission angle θ:

$$I^+(0,\mu) = B(\tau_s)e^{-\frac{\tau_s}{\mu}} + \int_0^{\tau_s} B(t)e^{-\frac{t}{\mu}}\frac{dt}{.\mu} \qquad (B.14)$$

The global averaged TOA IR radiance:

$$\overline{I^+}(0,\mu) = \frac{\int_0^{\frac{\pi}{2}} I^+(0,\mu)\,2\pi R^2 sin\theta d\theta}{2\pi R^2} = B(\tau_s)E_2(\tau_s) + \int_0^{\tau_s} B(t)E_1(t)dt. \quad (B.15)$$

Plug in the source function $B(\tau) = B_0 + B_1\tau + B_2e^{-\alpha\tau}$, we obtain

$$I^+(0,\mu) = (B_0 + B_1\tau_s + B_2e^{-\alpha\tau_s})e^{-\frac{\tau_s}{\mu}} + \int_0^{\tau_s}(B_0 + B_1t + B_2e^{-\alpha t})e^{-\frac{t}{\mu}}\frac{dt}{\mu}$$

$$= B_0 + B_1\mu(1 - e^{-\frac{\tau_s}{\mu}}) + \frac{B_2}{\alpha\mu+1}(1 + \alpha\mu e^{-\left(\alpha+\frac{1}{\mu}\right)\tau_s}), \qquad (B.16)$$

and

$$\overline{I^+}(0,\mu) = (B_0 + B_1\tau_s + B_2e^{-\alpha\tau_s})E_2(\tau_s) + \int_0^{\tau_s}(B_0 + B_1t + B_2e^{-\alpha t})E_1(t)dt$$

$$= B_0 + B_1\left(\frac{1}{2} - E_3(\tau_s)\right)$$

$$+ \frac{B_2}{\alpha}\left[\ln(1+\alpha) - e^{-\alpha\tau_s}E_1(\tau_s) + E_1\big((1+\alpha)\tau_s\big)\right.$$

$$\left. + \alpha e^{-\alpha\tau_s}E_2(\tau_s)\right]. \qquad (B.17)$$

Upward and Downward Fluxes

From the downward solar flux in equation (B.8), the global-averaged solar flux at τ_v is

$$\overline{F^-}(\tau_v) = \frac{\int_0^{\frac{\pi}{2}} F_v^-(\mu, \tau_v)\, 2\pi R^2 sin\theta d\theta}{4\pi R^2} = -\frac{1}{2} F_s E_3(\tau_v). \qquad (B.18)$$

From equation (B.12), the IR upward flux at layer τ_i is

$$F^+(\tau_i) = \int_0^1 \mu I^+(\tau_i, \mu)\, d\mu d\omega = 2\pi B(\tau_s) E_3(\tau_s - \tau_i) + 2\pi \int_{\tau_i}^{\tau_s} B(t) E_2(t - \tau_i) dt. \qquad (B.19)$$

From equation (B.13), the IR downward flux at layer τ_i:

$$F^-(\tau_i) = \int_0^1 \mu I^-(\tau_i, \mu)\, d\mu d\omega = 2\pi \int_0^{\tau_i} B(t) E_2(\tau_i - t) dt. \qquad (B.20)$$

Plug in the source function $B(\tau) = B_0 + B_1\tau + B_2 e^{-\alpha\tau}$, we obtain

$$F^+(\tau_i) = \pi B_0 + 2\pi B_1 \left(\frac{1}{3} + \frac{\tau_i}{2} - E_4(\tau_s - \tau_i)\right)$$
$$+ \frac{2\pi B_2 e^{-\alpha\tau_i}}{\alpha^2}\{e^{-\alpha(\tau_s - \tau_i)}[(E_1(\tau_s - \tau_i) - \alpha E_2(\tau_s - \tau_i) + \alpha^2 E_3(\tau_s - \tau_i)]$$
$$-E_1\big((1+\alpha)(\tau_s - \tau_i)\big) - \ln(1+\alpha) + \alpha\}. \qquad (B.21)$$

and

$$F^-(\tau_i) = 2\pi B_0 \left(\frac{1}{2} - E_3(\tau_i)\right) + 2\pi B_1 \left(-\frac{1}{3} + \frac{\tau_i}{2} + E_4(\tau_i)\right)$$
$$+ \frac{2\pi B_2 e^{-\alpha\tau_i}}{\alpha^2}\big\{e^{\alpha\tau_i}\,[(E_1(\tau_i) + \alpha E_2(\tau_i)] - E_1\big((1-\alpha)\tau_i\big) - \ln(|\alpha - 1|) - \alpha\big\}. \qquad (B.22)$$

Solar Heating Rate

The Solar heating Rate at τ_v is

$$H_{heat}(\tau_v) = \frac{dF_s^-(\mu, \tau_v)}{d\tau} = F_s\, e^{-\frac{\tau_v}{\mu}}. \qquad (B.23)$$

And the global-averaged solar heating rate at τ_v:

$$\overline{H_{heat}}(\tau_v) = \frac{d\overline{F^-}(\tau_v)}{d\tau} = \frac{1}{2}F_s E_2(\tau_v). \quad (B.24)$$

But the zonally averaged solar heating rate at τ_v is not integrable.

Thermal Cooling Rate

The IR Cooling Rate at τ_i:

$$H_{cool} = \frac{dF(\tau_i)}{d\tau} = 2\pi[-B(\tau_i)E_2(\tau_i) + (B(\tau_s) - B(\tau_i))E_2(\tau_s - \tau_i) + I_1 + I_2], \quad (B.25)$$

where

$$I_1 = \int_{\tau_i}^{\tau_s} \big(B(t) - B(\tau_i)\big)E_1(t - \tau_i)dt,$$

$$I_2 = \int_{0}^{\tau_i} \big(B(t) - B(\tau_i)\big)E_1(\tau_i - t)dt.$$

Plug in the source function $B(\tau) = B_0 + B_1\tau + B_2 e^{-\alpha\tau}$, we obtain

$$\begin{aligned} H_{cool} &= \frac{dF(\tau_i)}{d\tau} \\ &= -2\pi B_0 E_2(\tau_i) + 2\pi B_1\big(E_3(\tau_i) - E_3(\tau_s - \tau_i)\big) \\ &+ \frac{2\pi B_2 e^{-\alpha\tau_i}}{\alpha}\{\alpha e^{-\alpha(\tau_s - \tau_i)}E_2(\tau_s - \tau_i) + e^{\alpha\tau}E_1(\tau_i) \\ &- E_1\big((1-\alpha)\tau_i\big) - e^{-\alpha(\tau_s - \tau_i)}E_1(\tau_s - \tau_i) + E_1\big((1+\alpha)(\tau_s - \tau_i)\big) \\ &+ \ln(1+\alpha) - \ln(|\alpha - 1|) - 2\alpha\}. \end{aligned} \quad (B.26)$$

B.2. Numerical Schemes for Flux and Cooling Rate Calculations

B.2.1. Numerical Schemes

We consider two numerical schemes for the calculations of upward and downward intensities, fluxes and cooling rate. The first method is the direct integral with Gaussian

Quadrature method. But usually it needs larger number of Gaussian points to achieve the satisfactory accuracy. Our second method is the finite difference scheme. In the following notation, we ignore the wavenumber index in the lower subscript but all the formulae should be considered monochromatic and line-by-line (LBL) radiative transfer calculations. Using optical depth as the vertical coordinate, We divide the atmosphere into N layers with $N+1$ atmospheric levels as layer boundaries, noted by τ_i, where $i = 1, \dots, N+1$. The source function $B_i = B(\tau_i)$ is defined on the levels. Within each layer $[\tau_i, \tau_{i+1}]$, we approximate the source function linearly as function of optical depth: $B_i(t) = B_i + B_i'(t - \tau_i)$, where $\tau_i \le t \le \tau_{i+1}$, where $B_i' = (B(\tau_{i+1}) - B(\tau_i))/\Delta i$ and $\Delta i = \tau_{i+1} - \tau_i$.

The upward intensity $\boldsymbol{I_v^+(\tau_i, \mu)}$:

$$I^+(\tau_i, \mu) = B_{N+1} e^{-\frac{\tau_{N+1} - \tau_i}{\mu}} + \sum_{j=1}^{N} \int_{\tau_j}^{\tau_{j+1}} B_j(t) e^{-\frac{t-\tau_i}{\mu}} \frac{dt}{\mu}$$

$$= B_{N+1} e^{-(\tau_{N+1} - \tau_i)/\mu} + \sum_{j=1}^{N} e^{-(\tau_j - \tau_i)/\mu} \left[\left(B_j + B_j' \mu\right)(1 - e^{-\Delta j/\mu}) - B_j' \Delta j e^{-\Delta j/\mu} \right]. \quad (B.27)$$

Specifically, the TOA emission is

$$I^+(0, \mu) = B_s e^{-\tau_s/\mu} + \sum_{j=1}^{N} e^{-\tau_j/\mu} \left[\left(B_j + B_j' \mu\right)(1 - e^{-\Delta j/\mu}) - B_j' \Delta j e^{-\Delta j/\mu} \right]. \quad (B.28)$$

The downward intensity $\boldsymbol{I_v^-(\tau_i, \mu)}$:

$$I^-(\tau_i, \mu) = \sum_{j=1}^{i-1} e^{-(\tau_j - \tau_i)/\mu} \left[B_j (e^{\Delta j/\mu} - 1) + B_j' \mu \left(\frac{\Delta j}{\mu} e^{\Delta j/\mu} - e^{\Delta j/\mu} + 1 \right) \right]. \quad (B.29)$$

The upward flux $\boldsymbol{F^{\uparrow}(\tau_i)}$:

$$F^{\uparrow}(\tau_i) = 2\pi B_{N+1} E_3(\tau_{N+1} - \tau_i) + 2\pi \sum_{j=i}^{N} I_{ij}^{\uparrow}, \quad (B.30)$$

where $I_{ij}^{\uparrow} = B_j\left[E_3(\tau_j - \tau_i) - E_3(\tau_{j+1} - \tau_i)\right] - B_j'\left[(\tau_{j+1} - \tau_j)E_3(\tau_{j+1} - \tau_j) - E_4(\tau_j - \tau_i) + E_4(\tau_{j+1} - \tau_i)\right]$.

If $\Delta j < 10^{-4}$, we use an approximated formula to minimize the numerical errors

$$I_{ij}^{\uparrow} = \frac{3B_j - B_{j+1}}{2} E_2(\tau_{j+1} - \tau_i)\Delta j.$$

The downward flux $F^{\downarrow}(\tau_i)$:

$$F^{\downarrow}(\tau_i) = 2\pi \sum_{j=1}^{i-1} I_{ij}^{\downarrow}, \qquad (B.31)$$

where $I_{ij}^{\downarrow} = B_j\left[E_3(\tau_j - \tau_{j+1}) - E_3(\tau_i - \tau_j)\right] + B_j'\left[(\tau_{j+1} - \tau_j)E_3(\tau_i - \tau_{j+1}) + E_4(\tau_i - \tau_j) - E_4(\tau_i - \tau_{j+1})\right]$.

If $\Delta j < 10^{-4}$, we use

$$I_{ij}^{\downarrow} = \frac{B_j + B_{j+1}}{2} E_2(\tau_i - \tau_{j+1})\Delta j.$$

The **cooling rate** can be calculated in two ways.

(1) The cooling rate defined at level τ_i is

$$H_{cool} = \frac{dF(\tau_i)}{d\tau} = 2\pi \left[B_{N+1}E_2(\tau_{N+1} - \tau_i) - 2B_i + \sum_{j=i}^{N} I_1 + \sum_{j=1}^{i-1} I_2 \right], \qquad (B.32)$$

where $I_1 = B_j\left[E_2(\tau_j - \tau_i) - E_2(\tau_{j+1} - \tau_i)\right] - B_j'\left[(\tau_{j+1} - \tau_j)E_2(\tau_{j+1} - \tau_j) - E_3(\tau_j - \tau_i) + E_3(\tau_{j+1} - \tau_i)\right]$.

If $\Delta j < 10^{-4}$ (and $j \neq i - 1$), we use

$$I_1 = \frac{3B_j - B_{j+1}}{2} E_1(\tau_{j+1} - \tau_i)\Delta j,$$

and $I_2 = B_j\left[E_2(\tau_j - \tau_{j+1}) - E_2(\tau_i - \tau_j)\right] + B_j'\left[(\tau_{j+1} - \tau_j)E_2(\tau_i - \tau_{j+1}) + E_3(\tau_i - \tau_j) - E_3(\tau_i - \tau_{j+1})\right]$.

If $\Delta j < 10^{-4}$ (and $j \neq i - 1$), we use

$$I_2 = \frac{B_j + B_{j+1}}{2} E_1(\tau_i - \tau_{j+1})\Delta j.$$

(2) The averaged cooling rate within layer $[\tau_i, \tau_{i+1}]$ is

$$H_{cool} = \frac{dF(\tau_i)}{d\tau} = [F^{\downarrow}(\tau_i) + F^{\uparrow}(\tau_{i+1}) - F^{\downarrow}(\tau_{i+1}) - F^{\uparrow}(\tau_i)]/(\tau_{i+1} - \tau_i). \quad (B.33)$$

B.2.2. Comparison Between Analytical and Numerical Calculations

In order to test the accuracy of the two numerical schemes, we applied three typical source function profiles to the models:

(1) $B(\tau) = 3 + 0.2\,\tau$,

(2) $B(\tau) = 5 + 0.05\,\tau + 5\exp(-0.5\,\tau)$,

(3) $B(\tau) = 1 + 0.01\,\tau + 15\exp(-0.9\,\tau)$.

For the Gaussian Quadrature method we use 100 Gaussian points. The model has 72 levels with optical depth evenly distributed logarithmically from 10^{-5} to 10^{2}. Figure B1 shows the three source function profiles and the corresponding averaged IR cooling rates within each layer, indicated by the middle point of the vertical grid. The comparisons with analytical solutions show that the two integration methods are roughly comparably accurate and the relative errors compared with the analytical solutions are generally less than 1 percent. The differences are larger in the larger optical depth region because (1) the cooling rate is approaching zero, thus limited by the computational precision; (2) the optical grid is coarser, leading to larger numerical errors. For instance, the 720-level model agrees much better than the 72-level model. The cooling rate for case (1) has the least errors because the source function is linear in τ, in consistent with the assumption in our numerical methods within each grid box. When the nonlinear terms are more significant, the relative errors

become larger. Figure B.2 shows the averaged IR cooling rates defined at levels and the associated errors. Figs. B.3 and B.4 are showing the upward and downward thermal fluxes at each level, respectively. The relative difference of the numerical values and analytical solutions are generally within 1 percent.

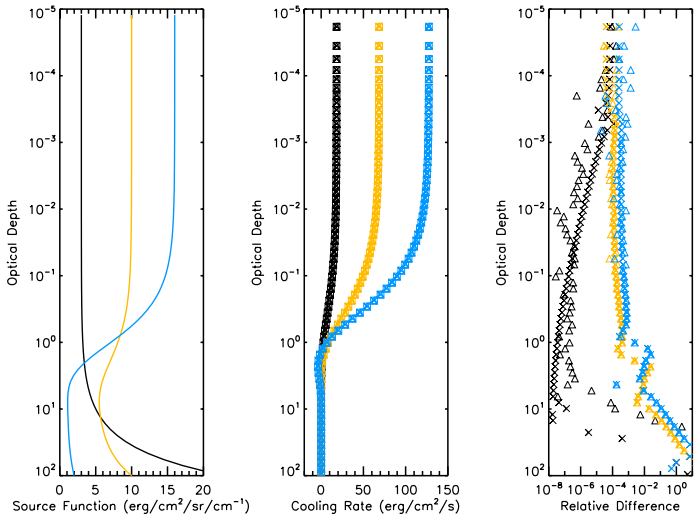

Figure B.1. Test cases (1: black; 2: orange; 3: blue) for averaged cooling rates within each layer from different numerical schemes. Three symbols indicate three solutions. Squares are analytical solutions; triangles are from the Gaussian Quadrature method; crosses are from the finite difference scheme. The relative difference is defined as the absolute value of (numerical-analytical)/analytical.

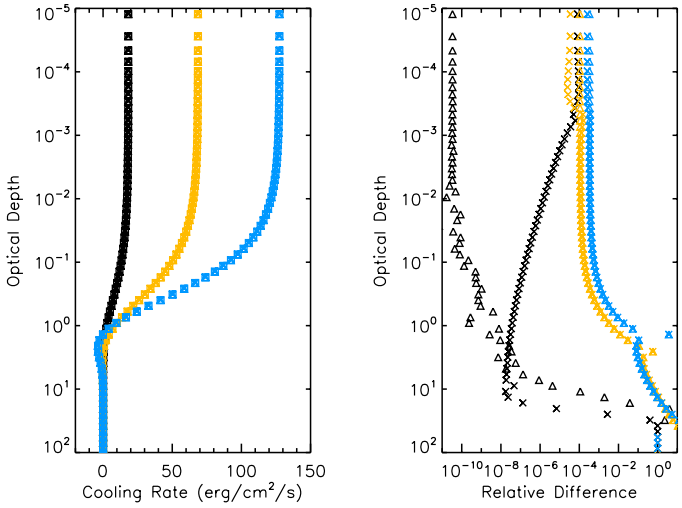

Figure B.2. Same as Figure B.1, but for the cooling rates defined at levels.

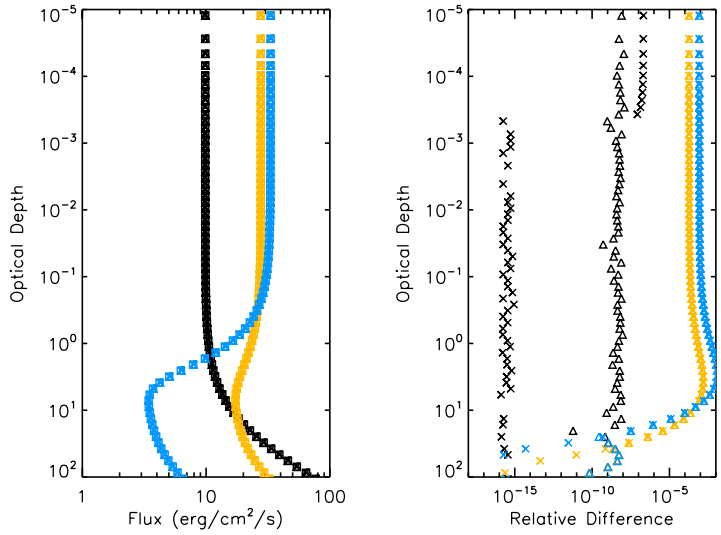

Figure B.3. Test cases of upward IR fluxes $F^{\uparrow}(\tau)$ from different numerical schemes and compared with the analytical solutions. The symbols and colors follow Figure B.1.

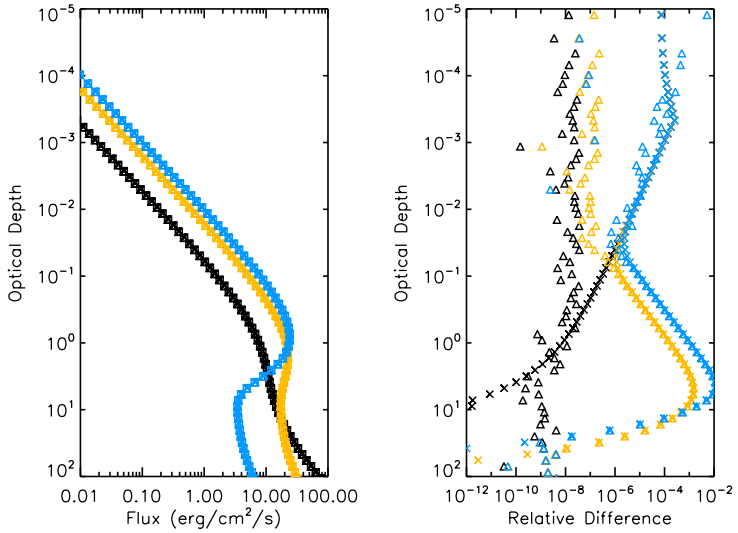

Figure B.4. Test cases of downward IR fluxes $F^{\downarrow}(\tau)$ from different numerical schemes and compared with the analytical solutions. The symbols and colors follow Figure B.1.

B.3. Non-LTE Formulism

In this study we consider a simple two-level non-LTE radiative transfer between a vibrational level and the ground level. We ignore the interaction between the vibrational

levels, especially the excitation of the low-lying fundamentals (e.g., in the thermal IR wavelength) by the higher vibrational levels (i.e., the vibrational-vibration transfer, or "V-V transfer"). In the absence of the vibrational chemistry, collisions will be the only cause of the departure of the source function from LTE through the vibrational-translational transfer ("V-T transfer"). The non-LTE source function, J_ν at wavenumber ν, can be formulated as (see Appleby 1990; Yelle 1991; Goody and Yung 1995; López-Puertas and Taylor 2001):

$$J_\nu(\tau) = \frac{\bar{I}(\tau) + \varepsilon(\tau)B_\nu(\tau)}{1 + \varepsilon(\tau)}, \qquad (B.34)$$

where $\varepsilon \equiv C_{10}/A_{10}$, C_{10} is the de-activation rates due to thermal collisions and A_{10} is the Einstein coefficient of the vibrational band. B_ν is the LTE source function (Planck function). $\bar{I}$ is the mean radiation field averaged in the vibrational band:

$$\bar{I}(\tau) = \frac{\int \bar{I}_\nu(\tau)k_\nu d\nu}{\int k_\nu d\nu}, \qquad (B.35)$$

where $\bar{I}_\nu(\tau)$ is the mean intensity averaged for all the emission angles (Goody and Yung, equation 2.103):

$$\bar{I}_\nu(\tau) = \frac{1}{2}B_\nu(\tau_s)E_2(\tau_s - \tau) + \frac{1}{2}\int_0^{\tau_s} J_\nu(t)E_1(|t-\tau|)dt, \qquad (B.36)$$

where τ is the optical depth. $E_1(x)$ and $E_2(x)$ are exponential integral functions. For gas giant planets, we need to include the continuum effect from H_2-H_2 and H_2-He CIA that is assumed to be always in LTE. The source function is modified to include this partitioning:

$$J_\nu(\tau) = \frac{1 - r(\tau)}{1 + \varepsilon(\tau)}\left[\bar{I}(\tau) + \varepsilon(\tau)B_\nu(\tau)\right] + r(\tau)B_\nu(\tau), \qquad (B.37)$$

where $r(\tau) = \tau_{H_2-H_2}/(\tau_{gas} + \tau_{H_2-H_2})$ is the ratio of the continuum optical depth to the total optical depth.

Substituted in equation (B.36) and we obtain the equation for the mean radiation field:

$$\bar{I}_\nu(\tau) = \frac{1}{2}B_\nu(\tau_s)E_2(\tau_s - \tau)$$
$$+\frac{1}{2}\int_0^{\tau_s}\left\{\frac{1 - r(t)}{1 + \varepsilon(t)}\left[\frac{\int \bar{I}_\nu(t)k_\nu d\nu}{\int k_\nu d\nu} + \varepsilon(t)B_\nu(t)\right] + r(t)B_\nu(t)\right\}E_1(|t - \tau|)dt. \qquad (B.38)$$

Once we solve $\bar{I}_\nu(\tau)$, and the source function $J_\nu(\tau)$ can be derived. We now introduce two numerical schemes to solve $\bar{I}_\nu(\tau)$.

B.3.1. Iteration Method

In the iteration method, first we write the equations in the discretized format:

$$\begin{cases} J_\nu(\tau) = \dfrac{1-r(\tau)}{1+\varepsilon(\tau)}\left[\dfrac{\sum \bar{I}_\nu(\tau)k_\nu\Delta\nu}{\sum k_\nu\Delta\nu} + \varepsilon(\tau)B_\nu(\tau)\right] + r(\tau)B_\nu(\tau), & (B.39a) \\ \bar{I}_\nu(\tau) = \dfrac{1}{2}B_\nu(\tau_N)E_2(\tau_N-\tau) + \dfrac{1}{2}\sum_{j=1}^{N}\dfrac{J_\nu(\tau_j)+J_\nu(\tau_{j+1})}{2}\left|E_2\left(\left|\tau-\tau_j\right|\right) - E_2\left(\left|\tau-\tau_{j+1}\right|\right)\right|. & (B.39b) \end{cases}$$

Start from $\overline{I_\nu}(\tau) = \int B_\nu(\tau)k_\nu d\nu \,/\, \int k_\nu d\nu$ and iterate the above two following equations. Usually $\overline{I_\nu}(\tau)$ converges after four or five iterations.

B.3.2. Matrix Inversion Method

We can also directly solve $\overline{I_\nu}(\tau)$ by the Matrix Inversion Method. Discretize the equation:

$$\begin{aligned} \bar{I}_\nu(\tau_i) = {} & \frac{1}{2}B_\nu(\tau_N)E_2(\tau_N-\tau_i) \\ & + \frac{1}{2}\sum_{j=1}^{N}\left[\left(1-r_j\right)J_{gj} + r_jJ_{cj}\right]\left|E_2\left(\left|\tau_i-\tau_j\right|\right) - E_2\left(\left|\tau_i-\tau_{j+1}\right|\right)\right|, \end{aligned} \qquad (B.40)$$

where J_{gj} and J_{cj} are the continuum and gas band contribution:

$$J_{cj} = \frac{(B_j + B_{j+1})}{2}, \qquad (B.41a)$$

and

$$J_{gj} = \frac{1}{2}\left[\frac{\bar{I}_j + \varepsilon_j B_j}{1+\varepsilon_j} + \frac{\overline{I_{j+1}} + \varepsilon_{j+1}B_{j+1}}{1+\varepsilon_{j+1}}\right]. \qquad (B.41b)$$

Therefore,

$$\bar{I}_\nu(\tau_i)$$
$$= \frac{1}{2}B_N E_2(\tau_N - \tau_i) + \frac{1}{4}\sum_{j=1}^{N}[\frac{r_j + \varepsilon_j}{1+\varepsilon_j}B_j + \frac{r_j + \varepsilon_{j+1}}{1+\varepsilon_{j+1}}B_{j+1}]\ \left|E_2(|\tau_i - \tau_j|) - E_2(|\tau_i - \tau_{j+1}|)\right|$$
$$+\frac{1}{4}\sum_{j=1}^{N}(|E_2(|\tau_i - \tau_j| - E_2(|\tau_i - \tau_{j+1}|)|)[\frac{(1-r_j)\bar{I}_j}{1+\varepsilon_j} + \frac{(1-r_j)\overline{I_{j+1}}}{1+\varepsilon_{j+1}}]. \qquad (B.42)$$

Using Einstein notation, $\bar{I}_\nu(\tau_i) \equiv \alpha_i + \beta_{ik}\bar{I}_k$, where:

$$\alpha_i = \frac{1}{2}B_\nu(\tau_N)E_2(\tau_N - \tau_i)$$
$$+\frac{1}{4}\sum_{j=1}^{N}\left(\frac{r_j + \varepsilon_j}{1+\varepsilon_j}B_j + \frac{r_j + \varepsilon_{j+1}}{1+\varepsilon_{j+1}}B_{j+1}\right)|E_2(|\tau_i - \tau_j|) - E_2(|\tau_i - \tau_{j+1}|)|,$$

$$\beta_{i,1} = \frac{1}{4}(|E_2(|\tau_i - \tau_1|) - E_2(|\tau_i - \tau_2|)|)\left(\frac{1-r_1}{1+\varepsilon_1}\right),$$
$$\beta_{i,k}(k = 2 \ldots N) = \frac{1}{4}|E_2(|\tau_i - \tau_{k-1}|) - E_2(|\tau_i - \tau_k|)|\left(\frac{1-r_{k-1}}{1+\varepsilon_k}\right)$$
$$+\frac{1}{4}|E_2(|\tau_i - \tau_k|) - E_2(|E_i - \tau_{k+1}|)|\left(\frac{1-r_k}{1+\varepsilon_k}\right),$$
$$\beta_{i,N+1} = \frac{1}{4}(|E_2(|\tau_i - \tau_N|) - E_2(|\tau_i - \tau_{N+1}|)|)\left(\frac{1-r_N}{1+\varepsilon_{N+1}}\right).$$

Take the band average ("~" stands for the matrix form):

$$\tilde{\bar{I}} = \frac{\int \tilde{\alpha}\, k_\nu d\nu}{\int k_\nu d\nu} + \frac{\int \tilde{\beta}\, k_\nu d\nu}{\int k_\nu d\nu}\bar{I} = \tilde{\bar{\alpha}} + \tilde{\bar{\beta}}\,\bar{I}. \qquad (B.43)$$

Therefore the final solution is $\tilde{\bar{I}} = \left(\tilde{\boldsymbol{I}} - \tilde{\bar{\beta}}\right)^{-1}\tilde{\bar{\alpha}}$, where $\tilde{\boldsymbol{I}}$ is the identity matrix. For the LTE situation ($\varepsilon \to \infty$), $\tilde{\bar{\beta}} \to \tilde{0}$, $\tilde{\bar{I}} \to \tilde{\bar{\alpha}}$.

Our calculations show that the matrix inversion method is less accurate than the iteration method. Therefore in this study we adopt the latter method.

B.4. Derivations for the Integral Involving Exponential Integral Functions

The general properties of the exponential integral functions are

$$E_n(0) = \frac{1}{n-1}\ (n \geq 2),$$

$$\int E_n(x)dx = -E_{n+1}(x).$$

Therefore, we obtain

$$\int_0^\tau tE_n(t)dt\ = -\tau E_{n+1}(\tau) + \int_0^\tau E_{n+1}(t)dt = \frac{1}{n+1} - \ E_{n+2}(\tau) - \tau E_{n+1}(\tau).$$

B.4.1. Derivation of $\boldsymbol{F_n = \int_\tau^{\tau_s} e^{-\alpha t} E_n(t-\tau)dt}$

$$F_n = e^{-\alpha\tau}\int_0^{\tau_s-\tau} e^{-\alpha t}E_n(t)dt$$

$$= -\frac{e^{-\alpha\tau}}{\alpha}\left[e^{-\alpha(\tau_s-\tau)}E_n(\tau_s-\tau) - \frac{1}{n-1} + e^{\alpha\tau}F_{n-1}\right].$$

Therefore,

$$F_n = \left(-\frac{1}{\alpha}\right)^{n-1}F_1 + \sum_{m=2}^{n}\left(-\frac{1}{\alpha}\right)^{n-m+1}[e^{-\alpha\tau_s}E_m(\tau_s-\tau) - \frac{e^{-\alpha\tau}}{m-1}], \qquad (B.44)$$

where,

$$F_1 = \int_\tau^{\tau_s} e^{-\alpha t}E_1(t-\tau)dt\ = e^{-\alpha\tau}\int_0^{\tau_s-\tau} e^{-\alpha t}dt\int_1^\infty \frac{e^{-tz}}{z}dz$$

$$= e^{-\alpha\tau}\int_{1+\alpha}^\infty \frac{1-e^{-(\tau_s-\tau)x}}{x(x-\alpha)}dx = \frac{e^{-\alpha\tau}}{\alpha}\int_{1+\alpha}^\infty \left(\frac{1}{x-\alpha} - \frac{1}{x}\right)(1-e^{-(\tau_s-\tau)x})\,dx$$

$$= \frac{e^{-\alpha\tau}}{\alpha}\ln(1+\alpha) + \frac{e^{-\alpha\tau}}{\alpha}\int_{1+\alpha}^\infty (\frac{e^{-(\tau_s-\tau)x}}{x} - \frac{e^{-(\tau_s-\tau)x}}{x-\alpha})dx$$

$$= \frac{e^{-\alpha\tau}}{\alpha}\left[-e^{-\alpha(\tau_s-\tau)}E_1(\tau_s-\tau) + E_1\big((1+\alpha)(\tau_s-\tau)\big) + \ln(1+\alpha)\right], \qquad (B.45)$$

when n=2,

$$F_2 = \int_{\tau}^{\tau_s} e^{-\alpha t}E_2(t-\tau)dt =$$

$$-\frac{e^{-\alpha\tau}}{\alpha^2}\{e^{-\alpha(\tau_s-\tau)}(\alpha E_2(\tau_s-\tau) - E_1(\tau_s-\tau)) + E_1\big((1+\alpha)(\tau_s-\tau)\big) + \ln(1+\alpha) - \alpha\}. \qquad (B.46)$$

B.4.2. Derivation of $\boldsymbol{K_n = \int_0^{\tau} e^{-\alpha t}E_n(\tau - t)dt}$

$$K_n = e^{-\alpha\tau}\int_0^{\tau} e^{\alpha t}E_n(t)dt = \frac{1}{\alpha}[E_n(\tau) - \frac{e^{-\alpha\tau}}{n-1} + K_{n-1}].$$

Therefore,

$$K_n = \frac{K_1}{\alpha^{n-1}} + \sum_{m=2}^{n}\left(\frac{1}{\alpha}\right)^{n-m+1}\left[E_m(\tau) - \frac{e^{-\alpha\tau}}{m-1}\right], \qquad (B.47)$$

where,

$$K_1 = \int_0^{\tau} e^{-\alpha t}E_1(\tau-t)dt = e^{-\alpha\tau}\int_0^{\tau} e^{\alpha t}dt\int_1^{\infty}\frac{e^{-tz}}{z}dz$$

$$= e^{-\alpha\tau}\int_{1-\alpha}^{\infty}\frac{1-e^{-\tau x}}{x(x+\alpha)}dx = \frac{e^{-\alpha\tau}}{\alpha}\int_{1-\alpha}^{\infty}\left(\frac{1}{x} - \frac{1}{x+\alpha}\right)(1-e^{-\tau x})dx. \qquad (B.48)$$

Note that if $\alpha > 1$, there is a singularity at $x = 1$. But the Cauchy principal value still exists. For example, if $\alpha > 1$,

$$\int_{1-\alpha}^{\infty}\frac{1}{x(x+\alpha)}\,dx = \lim_{\epsilon\to 0}\left(\int_{1-\alpha}^{-\epsilon}\frac{1}{x(x+\alpha)}\,dx + \int_{\epsilon}^{\infty}\frac{1}{x(x+\alpha)}\,dx\right)$$

$$= \lim_{\epsilon\to 0}\frac{\ln\left(\frac{\alpha+\epsilon}{\alpha-\epsilon}\right) - \ln(\alpha-1)}{\alpha}$$

$$= -\frac{\ln(\alpha-1)}{\alpha},$$

if $\alpha < 1$,

$$\int_{1-\alpha}^{\infty} \frac{1}{x(x+\alpha)}\, dx = -\frac{\ln(1-\alpha)}{\alpha}.$$

Therefore,

$$K_1 = \frac{-e^{-\alpha\tau}}{\alpha}\ln(|\alpha-1|) + \frac{e^{-\alpha\tau}}{\alpha}\int_{1-\alpha}^{\infty}\left(\frac{e^{-\tau x}}{x+\alpha} - \frac{e^{-\tau x}}{x}\right) dx$$

$$= \frac{e^{-\alpha\tau}}{\alpha}\left[e^{\alpha\tau}E_1(\tau) - E_1\big((1-\alpha)\tau\big) - \ln(|\alpha-1|)\right]. \qquad (B.49)$$

when n=2,

$$K_2 = \int_0^{\tau} e^{-\alpha t}E_2(\tau-t)dt$$

$$= \frac{e^{-\alpha\tau}}{\alpha^2}\left\{e^{\alpha\tau}\left[(E_1(\tau) + \alpha E_2(\tau)\right] - E_1\big((1-\alpha)\tau\big) - \ln(|\alpha-1|) - \alpha\right\}. \qquad (B.50)$$

Note that there is no singularity at $\alpha = 1$, since:

$$-E_1\big((1-\alpha)\tau\big) - \ln(|\alpha-1|) = \gamma + \ln(|\alpha-1|\tau) - \ln(|\alpha-1|) = \gamma + \ln(\tau),$$

where γ is the Euler–Mascheroni constant.

BIBLIOGRAPHY

Andrews, D.G., Holton, J.R., Leovy, C.B., Middle Atmosphere Dynamics, Academic Press, 1987.

Appleby, J.F., 1990. CH_4 nonlocal thermodynamic equilibrium in the atmospheres of the giant planets. Icarus 85, 355-379.

Appleby, J.F., Hogan, J.S., 1984. Radiative-convective equilibrium models of Jupiter and Saturn. Icarus 59, 336-366.

Arnold, F., 2006. Atmospheric aerosol and cloud condensation nuclei formation: A possible influence of cosmic rays? Space Science Review 125, 169-186.

Atkinson, R., Baulch, D.L., Cox, R.A., Crowley, J.N., Hampson, R.F., Hynes, R.G., Jenkin, M.E., Rossi, M.J., Troe, J., 2004. Evaluated kinetic and photochemical data for atmospheric chemistry: Volume I-gas phase reactions of O_x, HO_x, NO_x and SO_x species. Atmospheric Chemistry and physics 4, 1461-1738.

Atkinson, R., Baulch, D.L., Cox, R.A., Hampson Jr., R.F., Kerr, J.A., Troe, J., 1989, Evaluated kinetic and photochemical data for atmospheric chemistry: Supplement III, Journal of Physical and Chemical Reference Data 18, 3, 881-1097.

Ayers, G.P., Gillett, R.W., Gras, J.L., 1980. On the vapor pressure of sulfuric acid. Geophysics Research Letter 7, 433-436.

Bahou, M., Chung, C.Y., Lee, Y.P., Cheng, B.M., Yung, Y.L., Lee, L.C., 2001. Absorption cross sections of HCl and DCl at 135-232 nanometers: Implications for photodissociation on Venus. The Astrophysical Journal Letters 559, L179-L182.

Bailey, J., Ahlsved, L., Meadows, V., 2011. The near-IR spectrum of Titan modeled with an improved methane line list. Icarus 213, 218-232.

Baines, K.H., West, R.A., Giver, L.P., Moreno, F., 1993. Quasi-random narrow-band model fits to near-infrared low-temperature laboratory methane spectra and derived exponential-sum absorption coefficients. Journal of Geophysical Research 98, 5517-5529.

Banfield, D., Gierasch, P., Bell, M., Ustinov, E., Ingersoll, A., Vasavada, A., West, R.A., Belton, M., 1998. Jupiter's cloud structure from Galileo imaging data. Icarus 135, 230-250.

Banfield, D., Gierasch, P.J., Squyres, S.W., Nicholson, P.D., Conrath, B.J., Matthews, K., 1996. 2 μm spectrophotometry of Jovian stratospheric aerosols-scattering opacities, vertical distributions, and wind speeds. Icarus 121, 389-410.

Barrado-Izagirre, N., Sánchez-Lavega, A., Pérez-Hoyos, S., Hueso, R., 2008. Jupiter's polar clouds and waves from Cassini and HST images: 1993-2006. Icarus 194, 173-185.

Baulch, D.L., Cobos, C.J., Cox, R.A., Esser, C., Frank, P., Just, T., Kerr, J.A., Pilling, M.J., Troe, J., Walker, R.W., Warnatz, J., 1992. Evaluated kinetic data for combustion modelling. Journal of Physical and Chemical Reference Data 21, 411-734.

Baulch, D.L., Duxbury, J., Grant, S.J., Montague, D.C., 1981. Evaluated kinetic data for high temperature reactions volume 4 homogeneous gas phase reactions of halogen- and cyanide-containing species. Journal of Physical and Chemical Reference Data 1-721.

Baumgärtner, E., Hess, P., 1974. Ultrasonic absorption in mixtures of methane with hydrogen, deuterium, and helium. Acustica 30, 281-285.

Belyaev, D., Korablev, O., Fedorova, A., Bertaux, J.L., Vandaele, A.C., Montmessin, F., Mahieux, A., Wilquet, V., Drummond, R., 2008. First observations of SO_2 above Venus' clouds by means of solar occultation in the Infrared. Journal of Geophysical Research 113, E00B25, doi:10.1029/2008JE003143.

Belyaev, D., Montmessin, F., Bertaux, J.L., Mahieux, A., Fedorova, A., Korablev, O., Marcq, E., Yung, Y.L., Zhang, X., 2011. Vertical profiling of SO_2 and SO above Venus' clouds by SPICAV/SOIR solar occultations. Icarus 217, 740-751.

Bertaux, J.L., Vandaele, A.C., Korablev, O., Villard, E., Fedorova, A., Fussen, D., Quemerais, E., Belyaev, D., Mahieux, A., Montmessin, F., Muller, C., Neefs, E., Nevejans, D., Wilquet, V., Dubois, J.P., Hauchecorne, A., Stepanov, A., Vinogradov, I., Rodin, A., Team, S.S., 2007. A warm layer in Venus' cryosphere and high-altitude measurements of HF, HCl, H_2O and HDO. Nature 450, 646-649.

Bézard, B., Griffith, C.A., Lacy, J., Owen, T., 1995. Non-detection of hydrogen cyanide on Jupiter. Icarus 118, 384-391.

Bézard, B., Griffith, C.A., Kelly, D.M., Lacy, J.H., Greathouse, T., Orton, G., 1997. Thermal infrared imaging spectroscopy of Shoemaker-Levy 9 impact sites: temperature and HCN retrievals. Icarus 125, 94-120.

Borysow, J., Frommhold, L., Birnbaum, G., 1988. Collison-induced rototranslational absorption spectra of H_2-He pairs at temperatures from 40 to 3000 K. The Astrophysical Journal 326, 509-515.

Borysow, A., Frommhold, L., 1989a. Collision-induced infrared spectra of H_2-He pairs at temperatures from 18 to 7000 K. II-Overtone and hot bands. The Astrophysical Journal 341, 549-555.

Borysow, A., Frommhold, L., Moraldi, M., 1989b. Collision-induced infrared spectra of H_2-He pairs involving 0-1 vibrational transitions and temperatures from 18 to 7000 K. The Astrophysical Journal 336, 495-503.

Borysow, A., 1992. New model of collision-induced infrared absorption spectra of H_2-He pairs in the 2-2.5 μm range at temperatures from 20 to 300 K: An update. Icarus 96, 169-175.

Borysow, A., 2002. Collision-induced absorption coefficients of H_2 pairs at temperatures from 60 K to 1000 K. Astronomy and Astrophysics 390, 779-782.

Brune, W.H., Schwab, J.J., Anderson, J.O., 1983. Laser magnetic resonance, resonance fluorescence, and resonance absorption studies of the reaction kinetics of $O+OH \rightarrow H+O_2$, $O+HO_2 \rightarrow OH+O_2$, $N+OH \rightarrow H+NO$, and $N+HO_2 \rightarrow$ Products at 300 K between 1 and 5 Torr. The Journal of Physical Chemistry A 87, 4503-4514.

Bryukov, M.G., Kachanov, A.A., Timonnen, R., Seetula, J., Vandoren, J., Sarkisova, O.M., 1993. Kinetics of HNO reactions with O_2 and HNO. Chemical Physics Letters 208, 392-398.

Burkholder, J.B., McKeen, S., 1997. UV absorption cross sections for SO_3. Geophysical Research Letters 24, 3201-3204.

Burkholder, J.B., Mills, M., McKeen, S., 2000. Upper Limit for the UV Absorption Cross Sections of H_2SO_4. Geophysical Research Letters 27, 2493-2496.

Campbell, I.M., Thrush, B.A., 1967. The recombination of nitrogen atoms and the nitrogen afterglow. Proceedings of the Royal Society A 296, 201-221.

Cappa, C.D., Wilson, K.R., 2011. Evolution of organic aerosol mass spectra upon heating: implications for OA phase and partitioning behavior. Atmospheric Chemistry and Physics 11, 1895-1911.

Carlson, R.W., 2010. Venus' Ultraviolet Absorber and Sulfuric Acid Droplets. International Venus Conference, Aussois, France, 4-4.

Cess, R., Chen, S., 1975. The influence of ethane and acetylene upon the thermal structure of the Jovian atmosphere. Icarus 26, 444-450.

Cess, R., Khetan, S., 1973. Radiative transfer within the atmospheres of the major planets. Journal of Quantitative Spectroscopy and Radiative Transfer 13, 995-1009.

Chamberlain, T.P., Hunten, D.M., 1989. Theory of planetary atmospheres: an introduction to their physics and chemistry, Academic Press.

Chan, Y., Dalgarno, A., 1965. The refractive index of helium. Proceedings of the Physical Society 85, 227, doi:10.1088/0370-1328/85/2/304

Chase, M.W., Davies, C.A., Downey, J.R., Frurip, D.J., McDonald, R.A., Syverud, A. N., 1985. JANAF Thermochemical Tables. Third Edition. I, Al--Co. II, Cr--Zr. Journal of Physical and Chemical Reference Data 14 (Suppl.), 1-1856.

Clancy, R.T., Sandor, B., Moriarty-Schieven, G., 2008. Venus upper atmospheric CO, temperature, and winds across the afternoon/evening terminator from June 2007 JCMT sub-millimeter line observations. Planetary and Space Science 56, 1344-1354.

Clegg, S.L., Brimblecombe, P., 1995. Application of a multicomponent thermodynamic model to activities and thermal properties of 0-40 mol kg^{-1} aqueous sulfuric acid from less than 200 K to 328 K. Journal of Chemical and Engineering Data 40, 43-64.

Connes, P., Connes, J., Benedict, W.S., Kaplan, L.D., 1967. Traces of HCl and HF in atmosphere of Venus. The Astrophysical Journal 147, 1230-1237.

Conrath, B.J., Gierasch, P.J., Leroy, S.S., 1990. Temperature and circulation in the stratosphere of the outer planets. Icarus 83, 255-281.

Conrath, B.J., Gautier, D., 2000. Saturn helium abundance: A reanalysis of Voyager measurements. Icarus 144, 124-134.

Crisp, D., 1986. Radiative forcing of the Venus mesosphere .1. Solar fluxes and heating rates. Icarus 67, 484-514.

Dahneke, B., 1983. Simple kinetic theory of Brownian diffusion in vapors and aerosols. Theory of Dispersed Multiphase Flow, 97-133.

Dahneke, B., 1983. Simple kinetic theory of Brownian diffusion in vapors and aerosols, in: R.E. Meyer, (Ed.), Theory of Dispersed Multiphase Flow. Academic Press, New York, 97-133.

de Pater, I., Roe, H., Graham, J.R., Strobel, D.F., Bernath, P., 2002. Detection of the Forbidden SO $a^1\Delta \rightarrow X^3\sum^-$ Rovibronic Transition on Io at 1.7 μm. Icarus 156, 296-301.

DeMore, W.B., Golden, D.M., Hampson, R.F., Howard, C.J., Kurylo, M.J., Molina, M.J., Ravishankara, A.R., Sander, S.P., 1994. Chemical kinetics and photochemical data for use in stratospheric modeling: Evaluation number 11.

DeMore, W.B., Sander, S.P., Golden, D.M., Hampson, R.F., Kurylo, M.J., Howard, C.J., Ravishankara, A.R., Kolb, C.E., Molina, M.J., 1997. Chemical kinetics and photochemical data for use in stratospheric modeling: Evaluation number 12.

Dodonov, A., Zelenov, V., Strunin, V., Talroze, V., 1981. Mass-spectrometric determination of rate constants of reaction steps 7. Flow-rate and contact time in the mass-spectrometric probing of a diffusional cloud in a flow. Kinetics and Catalysis 22, 689-697.

Drossart, P., Fouchet, Th., Crovisier, J., Lellouch, E., Encrenaz, Th., Feuchtgruber, H., Champion, J.-P., 1999. Fluorescence in the 3 micron bands of methane on Jupiter and Saturn from ISO/SWS observations. ESA SP-427, 169–172.

Drossart, P., Maillard, J.P., Caldwell, J., Rosenqvist, J., 1993. Line-resolved spectroscopy of the Jovian H_3^+ auroral emission at 3.5 micrometers. The Astrophysical Journal 402, L25-L28.

Feierabend, K.J., Havey, D.K., Brown, S.S., Vaida, V., 2006. Experimental absolute intensities of the $4\nu_9$ and $5\nu_9$ O-H stretching overtones of H_2SO_4. Chemical Physics Letters 420, 438-442.

Festou, M., Atreya, S., Donahue, T., Sandel, B., Shemansky, D., Broadfoot, A., 1981. Composition and thermal profiles of the Jovian upper atmosphere determined by the

Voyager ultraviolet stellar occultation experiment. Journal of Geophysical Research 86, 5715-5725.

Fouchet, T., Lellouch, E., Bézard, B., Feuchtgruber, H., Drossart, P., Encrenaz, T., 2000. Jupiter's hydrocarbons observed with ISO-SWS: vertical profiles of C_2H_6 and C_2H_2, detection of CH_3C_2H. arXiv preprint astro-ph/0002273.

Friedson, A.J., West, R.A., Hronek, A.K., Larsen, N.A., Dalal, N., 1999. Transport and mixing in Jupiter's stratosphere inferred from Comet SL-9 dust migration. Icarus 138, 141-156.

Froidevaux, L., Yung, Y.L., 1982. Radiation and chemistry in the stratosphere: Sensitivity to O_2 absorption cross sections in the Herzberg continuum. Geophysical Research Letters 9, 854-857.

Giauque, W.F., Hornung, E.W., Kunzler, J.E., Rubin, T.R., 1960. The thermodynamic properties of aqueous sulfuric acid solutions and hydrates from 15-degrees K to 300-degrees K. Journal of the American Chemical Society 82, 62-70.

Gierasch, P.J., Conrath, B.J., Magalhães, J.A., 1986. Zonal mean properties of Jupiter's upper troposphere from Voyager infrared observations. Icarus 67, 456-483.

Gladstone, G.R., Allen, M., Yung, Y., 1996. Hydrocarbon photochemistry in the upper atmosphere of Jupiter. Icarus 119, 1-52.

Gladstone, G.R., Yung, Y.L., 1983. An analysis of the reflection spectrum of Jupiter from 1500 A to 1740 A. The Astrophysical Journal 266, 415-424.

Glaze, L.S., Baloga, S.M., Wimert, J., 2010. Volcanic Eruptions from Linear Vents on Earth, Venus and Mars: Comparisons with Central Vent Eruptions. 41st Lunar and Planetary Science Conference, 1147-1148.

Gmitro, J.I., Vermeulen, T., 1964. Vapor-liquid equilibria for aqueous sulfuric acid. AIChE Journal 10, 740-746.

Goody, R.M., Yung, Y.L., Atmospheric radiation: theoretical basis, Oxford University Press, USA, 1995.

Greathouse, T.K., Gladstone, G., Moses, J., Stern, S., Retherford, K., Vervack Jr, R., Slater, D., Versteeg, M., Davis, M., Young, L., 2010. New Horizons Alice ultraviolet observations of a stellar occultation by Jupiter’s atmosphere. Icarus 208, 293-305.

Greathouse, T., Orton, G., Richter, M., Dowling, T., 2011. The thermal response to waves propagating through Jupiter's middle atmosphere, EPSC-DPS Joint Meeting 2011, held 2-7 October 2011 in Nantes, France. 893.

Grillo, A., Reed, R., Slack, M.W., 1979. Infrared measurements of sulfur-dioxide thermal-decomposition rate in shock-waves. Journal of Chemical Physics 70, 1634-1636.

Häger, J., Krieger, W., Pfab, J., 1981. Collisional deactivation of laser-excited acetylene by H_2, HBr, N_2 and CO. Journal of the Chemical Society 2 77, 469-476.

Halthore, R.N., Allen Jr, J., Decola, P.L., 1994. A non-LTE model for the Jovian methane infrared emissions at high spectral resolution. The Astrophysical Journal 424, L61-L64.

Hanel, R., Conrath, B., Herath, L., Kunde, V., Pirraglia, J., 1981. Albedo, internal heat, and energy balance of Jupiter: Preliminary results of the Voyager infrared investigation. Journal of Geophysical Research 86, 8705-8712.

He, Y., Liu, X., Lin, M.C., Melius, C.F., 1993. Thermal reaction of HNCO with NO2 at moderate temperatures. International Journal of Chemical Kinetics 25, 845-863.

Hermans, C., Vandaele, A.C., Fally, S., 2009. Fourier transform measurements of SO2 absorption cross sections: I. Temperature dependence in the 24000-29000 cm-1 (345-420 nm) region. Journal of Quantitative Spectroscopy and Radiative Transfer 110, 756-765.

Hintze, P.E., Kjaergaard, H.G., Vaida, V., Burkholder, J.B., 2003. Vibrational and electronic spectroscopy of sulfuric acid vapor. The Journal of Physical Chemistry A 107, 1112-1118.

Hord, C.W., West, R.A., Simmons, K.E., Coffeen, D.L., Sato, M., Lane, A.L., Bergstralh, J., 1979. Photometric observations of Jupiter at 2400 angstroms. Science 206, 956-959.

Hubbard, W., Haemmerle, V., Porco, C., Rieke, G., Rieke, M., 1995. The occultation of SAO 78505 by Jupiter. Icarus 113, 103-109.

Imanaka, H., Khare, B.N., Elsila, J.E., Bakes, E.L.O., McKay, C.P., Cruikshank, D.P., Sugita, S., Matsui, T., Zare, R.N., 2004. Laboratory experiments of Titan tholin

formed in cold plasma at various pressures: implications for nitrogen-containing polycyclic aromatic compounds in Titan haze. Icarus 168, 344-366.

Irwin, P., Calcutt, S., Taylor, F., Weir, A., 1996. Calculated k distribution coefficients for hydrogen-and self-broadened methane in the range 2000 cm^{-1}-9500 cm^{-1} from exponential sum fitting to band-modelled spectra. Journal of Geophysical Research 101, 26137-26154.

Irwin, P., Parrish, P., Fouchet, T., Calcutt, S., Taylor, F., Simon-Miller, A., Nixon, C., 2004. Retrievals of Jovian tropospheric phosphine from Cassini/CIRS. Icarus 172, 37-49.

Irwin, P., Sromovsky, L., Strong, E., Sihra, K., Teanby, N., Bowles, N., Calcutt, S., Remedios, J., 2006. Improved near-infrared methane band models and *k-distribution* parameters from 2000 cm^{-1}-9500 cm^{-1} and implications for interpretation of outer planet spectra. Icarus 181, 309-319.

Irwin, P., Teanby, N., de Kok, R., Fletcher, L., Howett, C., Tsang, C., Wilson, C., Calcutt, S., Nixon, C., Parrish, P., 2008. The NEMESIS planetary atmosphere radiative transfer and retrieval tool. Journal of Quantitative Spectroscopy and Radiative Transfer 109, 1136-1150.

Karkoschka, E., Tomasko, M.G., 2010. Methane absorption coefficients for the Jovian planets from laboratory, Huygens, and HST data. Icarus 205, 674-694.

Kaye, J.A., Strobel, D.F., 1983. HCN formation on Jupiter: The coupled photochemistry of ammonia and acetylene. Icarus 54, 417-433.

Kedziora-Chudczer, L., Bailey, J., 2011. Modelling the near-IR spectra of Jupiter using line-by-line methods. Monthly Notices of the Royal Astronomical Society 414, 1483-1492.

Khare, B., Sagan, C., Thompson, W., Arakawa, E., Votaw, P., 1987. Solid hydrocarbon aerosols produced in simulated Uranian and Neptunian stratospheres. Journal of Geophysical Research 92, 15067-15082.

Khare, B.N., Sagan, C., Arakawa, E., Suits, F., Callcott, T., Williams, M., 1984. Optical constants of organic tholins produced in a simulated titanian atmosphere: from soft X-ray to microwave frequencies. Icarus 60, 127-137.

Knollenberg, R.G., Hunten, D.M., 1980. The microphysics of the clouds of Venus: Results of the Pioneer Venus particle size spectrometer experiment. Journal of Geophysical Research 85, 8039-8058.

Knutson, H.A., Charbonneau, D., Allen, L.E., Fortney, J.J., Agol, E., Cowan, N.B., Showman, A.P., Cooper, C.S., Megeath, S.T., 2007. A map of the day-night contrast of the extrasolar planet HD 189733b. Nature 447, 183-186.

Kostiuk, T., Espenak, F., Mumma, M.J., Deming, D., Zipoy, D., 1987. Variability of ethane on Jupiter. Icarus 72, 394-410.

Kostiuk, T., Romani, P., Espenak, F., Livengood, T.A., Goldstein, J.J., 1993. Temperature and abundances in the Jovian auroral stratosphere 2. Ethylene as a probe of the microbar region. Journal of Geophysical Research 98, 18823-18818,18830.

Krasnopolsky, V.A., 2006. A sensitive search for nitric oxide in the lower atmospheres of Venus and Mars: Detection on Venus and upper limit for Mars. Icarus 182, 80-91.

Krasnopolsky, V.A., 2008. High-resolution spectroscopy of Venus: Detection of OCS, upper limit to H_2S, and latitudinal variations of CO and HF in the upper cloud layer. Icarus 197, 377-385.

Krasnopolsky, V.A., 2010a. Spatially-resolved high-resolution spectroscopy of Venus 1. Variations of CO_2, CO, HF, and HCl at the cloud tops. Icarus 208, 539-547.

Krasnopolsky, V.A., 2010b. Spatially-resolved high-resolution spectroscopy of Venus 2. Variations of HDO, OCS, and SO_2 at the cloud tops. Icarus 209, 314-322.

Krasnopolsky, V.A., 2010c. Venus night airglow: Ground-based detection of OH, observations of O_2 emissions, and photochemical model. Icarus 207, 17-27.

Krasnopolsky, V.A., Pollack, J.B., 1994. H_2O-H_2SO_4 system in Venus' clouds and OCS, CO, and H_2SO_4 profiles in Venus' troposphere. Icarus 109, 58-78.

Kulmala, M., Laaksonen, A., 1990. Binary nucleation of water-sulphuric acid system: comparison of classical theories with different H_2SO_4 saturation vapour pressures. Journal of Chemical Physics 93, 696-701.

Landau, L., Teller, E., 1936. On the theory of sound dispersion. Physikalische zeitschrift der Sowjetunion 10, 34.

Lane, J.R., Kjaergaard, H.G., 2008. Calculated electronic transitions in sulfuric acid and implications for its photodissociation in the Atmosphere. The Journal of Physical Chemistry A 112, 4958-4964.

Lane, T.E., Donahue, N.M., Pandis, S.N., 2008. Simulating secondary organic aerosol formation using the volatility basis-set approach in a chemical transport model. Atmospheric Environment 42, 7439-7451.

Lellouch, E., Bézard, B., Strobel, D., Bjoraker, G., Flasar, F., Romani, P., 2006. On the HCN and CO_2 abundance and distribution in Jupiter's stratosphere. Icarus 184, 478-497.

Lellouch, E., Hunten, D.M., Kockarts, G., Coustenis, A., 1990. Titan's thermosphere profile. Icarus 83, 308-324.

Levenberg, K., 1944. A method for the solution of certain problems in least squares. Quarterly of Applied Mathematics 2, 164-168.

Li, L., Baines, K.H., Smith, M.A., West, R.A., Pérez-Hoyos, S., Trammell, H.J., Simon-Miller, A.A., Conrath, B.J., Gierasch, P.J., Orton, G.S., 2012. Emitted power of Jupiter based on Cassini CIRS and VIMS observations. Journal of Geophysical Research 117, E11002.

Liang, M.C., Shia, R.L., Lee, A.Y.T., Allen, M., Friedson, A.J., Yung, Y.L., 2005. Meridional transport in the stratosphere of Jupiter. The Astrophysical Journal Letters 635, L177-L180.

Liang, M.C., Yung, Y.L., 2009. Modeling the distribution of H_2O and HDO in the upper atmosphere of Venus. Journal of Geophysical Research-Planets 114, E00B28.

Lide, D.R., ed., 2005. CRC Handbook of Chemistry and Physics, Internet Version 2005, http://www.hbcpnetbase.com, CRC Press, Boca Raton, FL.

Lin, J.S., Hildemann, L.M., 1997. A generalized mathematical scheme to analytically solve the atmospheric diffusion equation with dry deposition. Atmospheric Environment 31, 59-71.

Lindzen, R.S., 1981. Turbulence and stress owing to gravity-wave and tidal breakdown. Journal of Geophysical Research-Oceans and Atmosphere 86, 9707-9714.

Livengood, T., Kostiuk, T., Espenak, F., Goldstein, J., 1993. Temperature and Abundances in the Jovian Auroral Stratosphere, 1, Ethane as a Probe of the Millibar Region. Journal of Geophysical Research 98, 18813-18822.

López-Puertas, M., Taylor, F.W., Non-LTE radiative transfer in the atmosphere, World Scientific Publishing Company Incorporated, 2001.

Lovejoy, E.R., Hanson, D.R., Huey, L.G., 1996. Kinetics and products of the gas-phase reaction of SO_3 with water. The Journal of Physical Chemistry 100, 19911-19916.

Lu, C.W., Wu, Y.J., Lee, Y.P., Zhu, R.S., Lin, M.C., 2003. Experiments and calculations on rate coefficients for pyrolysis of SO_2 and the reaction O+SO at high temperatures. The Journal of Physical Chemistry A 107, 11020-11029.

Lu, C.W., Wu, Y.J., Lee, Y.P., Zhu, R.S., Lin, M.C., 2006. Experimental and theoretical investigation of rate coefficients of the reaction $S(^3P)$+ OCS in the temperature range of 298-985 K. The Journal of Physical Chemistry 125, 164329, 10.1063/1.2357739.

Lyons, J.R., 2008. An estimate of the equilibrium speciation of sulfur vapor over solid sulfur and implications for planetary atmospheres. Journal of Sulfur Chemistry 29, 269-279.

Mackowski, D., Mishchenko, M., 2011. A multiple sphere T-matrix Fortran code for use on parallel computer clusters. Journal of Quantitative Spectroscopy and Radiative Transfer 112, 2182-2192.

Marcq, E., Belyaev, D., Montmessin, F., Fedorova, A, Bertaux, J.-L., Vandaele, A.C., Neefs, E., 2011a. An investigation of the SO_2 content of the venusian mesosphere using SPICAV-UV in nadir mode. Icarus 211, 58–69.

Marcq, E., Belyaev, D., Bertaux, J.-L., Fedorova, A, Montmessin, F., 2011b. Long-term monitoring SO_2 above the clouds of Venus using SPICAV-UV in nadir mode. EGU General Assembly 13, EGU2011-2603.

Marcq, E., Bézard, B., Drossart, P., Piccioni, G., Reess, J.M., Henry, F., 2008. A latitudinal survey of CO, OCS, H_2O, and SO_2 in the lower atmosphere of Venus: Spectroscopic studies using VIRTIS-H. Journal of Geophysical Research-Planets 113, E00B07, doi:10.1029/2008JE003074.

Marcq, E., Bézard, B., Encrenaz, T., Birlan, M., 2005. Latitudinal variations of CO and OCS in the lower atmosphere of Venus from near-infrared nightside spectro-imaging. Icarus 179, 375-386.

Marcq, E., Encrenaz, T., Bézard, B., Birlan, M., 2006. Remote sensing of Venus' lower atmosphere from ground-based IR spectroscopy: Latitudinal and vertical distribution of minor species. Planetary and Space Science 54, 1360-1370.

Markiewicz, W.J., Titov, D.V., Limaye, S.S., Keller, H.U., Ignatiev, N., Jaumann, R., Thomas, N., Michalik, H., Moissl, R., Russo, P., 2007. Morphology and dynamics of the upper cloud layer of Venus. Nature 450, 633-636.

Markwardt, C.B., 2008. Non-Linear Least Squares Fitting in IDL with MPFIT. in proc. Astronomical Data Analysis Software and Systems XVIII, Quebec, Canada, ASP Conference Series, 411, eds. D. Bohlender, P. Dowler & D. Durand (Astronomical Society of the Pacific: San Francisco), 251-254.

Marquardt, D.W., 1963. An algorithm for least-squares estimation of nonlinear parameters. Journal of the Society for Industrial and Applied Mathematics 11, 431-441.

McGouldrick, K., Toon, O.B., Grinspoon, D.H. 2010, Sulfuric acid aerosols in the atmospheres of the terrestrial planets. Planetary and Space Science 59, 10, 934-941, doi:10.1016/j.pss.2010.05.020.

McGrath, M., Feldman, P., Ballester, G., Moos, H., 1989. IUE observations of the Jovian dayglow emission. Geophysical Research Letters 16, 583-586.

Meng, Z., Seinfeld, J.H., 1996. Timescales to achieve atmospheric gas-aerosol equilibrium for volatile species. Atmospheric Environment 30, 2889-2900.

Miller, Y., Gerber, R.B., 2006. Dynamics of vibrational overtone excitations of H_2SO_4, H_2SO_4-H_2O: Hydrogen hopping and photodissociation processes. Journal of the American Chemical Society 128, 9594-9595.

Miller, Y., Gerber, R.B., Vaida, V., 2007. Photodissociation yields for vibrationally excited states of sulfuric acid under atmospheric conditions. Geophysical Research Letters 34, L16820, doi:10.1029/2007GL030529.

Mills, F.P., 1998. I. Observations and Photochemical Modeling of the Venus Middle Atmosphere. II. Thermal Infrared Spectroscopy of Europa and Callisto. Ph. D. thesis, California Institute of Technology 1-277.

Mills, F.P., Allen, M., 2007. A review of selected issues concerning the chemistry in Venus' middle atmosphere. Planetary and Space Science 55, 1729-1740.

Mills, F.P., Esposito, L.W., Yung, Y.L., 2007. Atmospheric Composition, Chemistry, and Clouds, in: L.W. Esposito, E.R. Stofan, T.E. Cravens, (Eds.), Exploring Venus as a Terrestrial Planet. American Geophysical Union, Washington, DC, 73-100.

Mills, M.J., Toon, O.B., Vaida, V., Hintze, P.E., Kjaergaard, H.G., Schofield, D.P., Robinson, T.W., 2005. Photolysis of sulfuric acid vapor by visible light as a source of the polar stratospheric CN layer. Journal of Geophysical Research 110, D08201, doi:10.1029/2004JD005519.

Moré, J. 1978. The Levenberg-Marquardt Algorithm: Implementation and Theory. in Numerical Analysis 630, ed. G. A. Watson, Springer-Verlag: Berlin.

Moreno, F., 1996. The structure of the stratospheric aerosol layer in the equatorial and south polar regions of Jupiter. Icarus 124, 632-644.

Moreno, F., Sedano, J., 1997. Radiative balance and dynamics in the stratosphere of Jupiter: Results from a latitude-dependent aerosol heating model. Icarus 130, 36-48.

Morrissey, P.F., Feldman, P.D., McGrath, M.A., Wolven, B.C., Moos, H.W., 1995. The ultraviolet reflectivity of Jupiter at 3.5Å resolution from Astro-1 and Astro-2. The Astrophysics Journal 454, L65–L68.

Moses, J.I., Fouchet, T., Bézard, B., Gladstone, G., Lellouch, E., Feuchtgruber, H., 2005. Photochemistry and diffusion in Jupiter's stratosphere: Constraints from ISO observations and comparisons with other giant planets. Journal of Geophysical Research 110, E08001.

Moses, J.I., Bézard, B., Lellouch, E., Gladstone, G.R., Feuchtgruber, H., Allen, M., 2000. Photochemistry of Saturn's atmosphere-II. Effects of an influx of external oxygenI. Icarus 145, 166-202.

Moses, J.I., Fouchet, T., Yelle, R.V., Friedson, A.J., Orton, G.S., Bézard, B., Drossart, P., Gladstone, G.R., Kostiuk, T., Livengood, T.A., 2004. The stratosphere of Jupiter. in

Jupiter-The planet, satellites and magnetosphere. F. Bagenal, T. Dowling and W. McKinnon, Eds., Cambridge University Press.

Moses, J.I., Zolotov, M.Y., Fegley, B., 2002. Photochemistry of a volcanically driven atmosphere on Io: Sulfur and oxygen species from a Pele-type eruption. Icarus 156, 76-106.

Niemann, H., Atreya, S., Carignan, G., Donahue, T., Haberman, J., Harpold, D., Hartle, R., Hunten, D., Kasprzak, W., Mahaffy, P., 1998. The composition of the Jovian atmosphere as determined by the Galileo probe mass spectrometer. Journal of Geophysical Research 103, 22, 831-845.

Nixon, C.A., Achterberg, R.K., Conrath, B.J., Irwin, P.G.J., Teanby, N.A., Fouchet, T., Parrish, P.D., Romani, P.N., Abbas, M., LeClair, A., Strobel, D., Simon-Miller, A.A., Jennings, D.J., Flasar, F.M., Kunde, V.G., 2007. Meridional variations of C2H2 and C_2H_6 in Jupiter's atmosphere from Cassini CIRS infrared spectra. Icarus 188, 47-71.

Nixon, C.A., Achterberg, R.K., Romani, P.N., Allen, M., Zhang, X., Teanby, N.A., Irwin, P.G.J., Flasar, F.M., 2010. Abundances of Jupiter's trace hydrocarbons from Voyager and Cassini. Planetary and Space Science 58, 1667-1680.

Noll, K., Knacke, R., Tokunaga, A., Lacy, J., Beck, S., Serabyn, E., 1986. The abundances of ethane and acetylene in the atmospheres of Jupiter and Saturn. Icarus 65, 257-263.

Orton, G.S., Gustafsson, M., Burgdorf, M., Meadows, V., 2007. Revised ab initio models for H_2-H_2 collision-induced absorption at low temperatures. Icarus 189, 544-549.

Orton, G.S., Yanamandra-Fisher, P.A., Fisher, B.M., Friedson, A.J., Parrish, P.D., Nelson, J.F., Bauermeister, A.S., Fletcher, L., Gezari, D.Y., Varosi, F., 2008. Semi-annual oscillations in Saturn’s low-latitude stratospheric temperatures. Nature 453, 196-199.

Park, S., Lee, K., 2000. Condensational growth of polydisperse aerosol for the entire particle size range. Aerosol Science and Technology 33, 222-227.

Pätzold, M., B. Häusler, M. K. Bird, Tellmann, S., Mattei, R., Asmar, S.W., Dehant, V., Eidel, W., T. Imamura, Simpson, R.A., Tyler, G.L., 2007. The structure of Venus' middle atmosphere and ionosphere. Nature 450, 657-660.

Pernice, H., Garcia, P., Willner, H., Francisco, J.S., Mills, F.P., Allen, M., Yung, Y.L., 2004. Laboratory evidence for a key intermediate in the Venus atmosphere:

Peroxychloroformyl radical. Proceedings of the National Academy of Sciences 101, 14007-14010.

Perraud, V., Bruns, E.A., Ezell, M.J., Johnson, S.N., Yu, Y., Alexander, M.L., Zelenyuk, A., Imre, D., Chang, W.L., Dabdub, D., 2012. Nonequilibrium atmospheric secondary organic aerosol formation and growth. Proceedings of the National Academy of Sciences 109, 2836-2841.

Piccialli, A., Titov, D.V., Grassi, D., Khatuntsev, I., Drossart, P., Piccioni, G., Migliorini, A., 2008. Cyclostrophic winds from the Visible and Infrared Thermal Imaging Spectrometer temperature sounding: A preliminary analysis. Journal of Geophysical Research-Planets 113, E00B11, doi:10.1029/2008JE003127.

Pollack, J.B., Dalton, J.B., Grinspoon, D., Wattson, R.B., Freedman, R., Crisp, D., Allen, D.A., Bézard, B., Debergh, C., Giver, L.P., Ma, Q., Tipping, R., 1993. Near-infrared light from venus nightside - a spectroscopic analysis. Icarus 103, 1-42.

Polyanin, A.D., Zaitsev, V.F., Handbook of exact solutions for ordinary differential equations, Chapman and Hall/CRC, 2002.

Porco, C.C., West, R.A., McEwen, A., Del Genio, A.D., Ingersoll, A.P., Thomas, P., Squyres, S., Dones, L., Murray, C.D., Johnson, T.V., 2003. Cassini imaging of Jupiter's atmosphere, satellites, and rings. Science 299, 1541-1547.

Prather, M.J., 1986. Numerical advection by conservation of second-order moments. Journal of Geophysical Research 91, 6671-6681.

Prinn, R.G., 1975. Venus - chemical and dynamical processes in stratosphere and mesosphere. Journal of the Atmospheric Sciences 32, 1237-1247.

Pryor, W.R., Hord, C.W., 1991. A study of photopolarimeter system UV absorption data on Jupiter, Saturn, Uranus, and Neptune: Implications for auroral haze formation. Icarus 91, 161-172.

Rages, K., Beebe, R., Senske, D., 1999. Jovian stratospheric hazes: The high phase angle view from Galileo. Icarus 139, 211-226.

Riipinen, I., Pierce, J., Yli-Juuti, T., Nieminen, T., Häkkinen, S., Ehn, M., Junninen, H., Lehtipalo, K., Petäjä, T., Slowik, J., 2011. Organic condensation: a vital link

connecting aerosol formation to cloud condensation nuclei (CCN) concentrations. Atmospheric Chemistry and Physics 11, 3865-3878.

Riley, P.S., Cosic, B., Fontijn, A., 2003. The H+NO recombination reaction over a wide temperature range. International Journal of Chemical Kinetics 35, 374-380.

Rodgers, C.D., Inverse methods for atmospheric sounding, World Scientific, 2000.

Sada, P.V., Bjoraker, G.L., Jennings, D.E., McCabe, G.H., Romani, P.N., 1998. Observations of CH_4, C_2H_6, and C_2H_2 in the Stratosphere of Jupiter. Icarus 136, 192-201.

Sander, S.P., Friedl, R.R., Golden, D.M., Kurylo, M.J., Huie, R.E., Orkin, V.L., Moortgat, G.K., Ravishankara, A.R., Kolb, C.E., Molina, M.J., Finlayson-Pitts, B.J., 2002. Chemical kinetics and photochemical data for use in atmospheric studies: evaluation number 14, Jet Propulsion Laboratory, California Institute of Technology, Pasadena, CA.

Sander, S.P., Golden, D.M., Kurylo, M.J., Moortgat, G.K., Wine, P.H., Ravishankara, A.R., Kolb, C.E., Molina, M.J., Finlayson-Pitts, B.J., Huie, R.E., Orkin, V.L., Friedl, R.R., Keller-Rudek, H., 2006. Chemical kinetics and photochemical data for use in atmospheric studies: evaluation number 15, Jet Propulsion Laboratory, California Institute of Technology, Pasadena, CA.

Sandor, B.J., Clancy, R.T., Moriarty-Schieven, G., Mills, F.P., 2010. Sulfur chemistry in the Venus mesosphere from SO2 and SO microwave spectra. Icarus 208, 49-60.

Sandor, B.J., Clancy, R.T., Moriarty-Schieven, G.H., 2011, Upper limits for H_2SO_4 in the mesosphere of Venus, Icarus, in press, doi:10.1016/j.icarus.2011.03.032.

Schwartz, R., Slawsky, Z.I., Herzfeld, K., 1952. Calculation of vibrational relaxation times in gases. The Journal of Chemical Physics 20, 1591.

Seiff, A., Models of Venus's Atmosphreic Structure, in: Venus, D.M. Hunten, L. Colin, T.M. Donahue, V.I. Moroz, (Eds.), 1983. University of Arizona Press, Tucson, Arizona, 1045-1048.

Seiff, A., Kirk, D.B., Knight, T.C.D., Young, R.E., Mihalov, J.D., Young, L.A., Milos, F.S., Schubert, G., Blanchard, R.C., Atkinson, D., 1998. Thermal structure of Jupiter's

atmosphere near the edge of a 5 μm hot spot in the north equatorial belt. Journal of Geophysical Research 103, 22857-22822,22889.

Seinfeld, J.H., Pandis, S.N., 2006. Atmospheric Chemistry and Physics: From Air Pollution to Climate Change, John Wiley & Sons, Inc., New York.

Shia, R., Ha, Y.L., Wen, J.S., Yung, Y.L., 1990. Two-dimensional atmospheric transport and chemistry model- Numerical experiments with a new advection algorithm. Journal of Geophysical Research 95, 7467-7483.

Simon-Miller, A.A., Conrath, B.J., Gierasch, P.J., Orton, G.S., Achterberg, R.K., Flasar, F.M., Fisher, B.M., 2006. Jupiter's atmospheric temperatures: From Voyager IRIS to Cassini CIRS. Icarus 180, 98-112.

Simon-Miller, A.A., Poston, B.W., Orton, G.S., Fisher, B., 2007. Wind variations in Jupiter's equatorial atmosphere: A QQO counterpart? Icarus 186, 192-203.

Singleton, D.L., Cvetanovic, R.J., 1988. Evaluated chemical kinetic data for the reactions of atomic oxygen O(^{3}P) with sulfur-containing-compounds, Journal of Physical and Chemical Reference Data 17, 1377-1437.

Smith, P.H., 1986. The vertical structure of the Jovian atmosphere. Icarus 65, 264-279.

Smrekar, S.E., Stofan, E.R., Mueller, N., Treiman, A., Elkins-Tanton, L., Helbert, J., Piccioni, G., Drossart, P., 2010. Recent Hot-Spot Volcanism on Venus from VIRTIS Emissivity Data. Science 328, 605-608.

Sonnabend, G., Schmuelling, F., Kostiuk, T., Livengood, T.A., Annen, J.N., Buhl, D., Fast, K.E., Delgado, J.D., Hewagama, T., 2005. A New Search for OCS in the Middle Atmosphere of Venus. Bulletin of the American Astronomical Society 37, 750.

Spracklen, D.V., Carslaw, K.S., Merikanto, J., Mann, G.W., Reddington, C.L., Pickering, S., Ogren, J.A., Andrews, E., Baltensperger, U., Weingartner, E., 2010. Explaining global surface aerosol number concentrations in terms of primary emissions and particle formation. Atmospheric Chemistry and Physics 10, 4775-4793.

Stamnes, K., Tsay, S.C., Jayaweera, K., Wiscombe, W., 1988. Numerically stable algorithm for discrete-ordinate-method radiative transfer in multiple scattering and emitting layered media. Applied Optics 27, 2502-2509.

Strobel, D., 1974. Hydrocarbon abundances in the Jovian atmosphere. The Astrophysical Journal 192, L47-L49.

Strobel, D.F., Apruzese, J.P., Schoeberl, M.R., 1985. Energy balance constraints on gravity wave induced eddy diffusion in the mesosphere and lower thermosphere. Journal of Geophysical Research 90, 13067-13013,13072.

Stull, D.R., 1947. Vapor pressure of pure substances—Inorganic compounds. Industrial and Engineering Chemistry 39, 540-550.

Sun, F., DeSain, J.D., Scott, G., Hung, P.Y., Thompson, R.I., Glass, G.P., Curl, R.F., 2001. Reactions of NH_2 with NO_2 and of OH with NH_2O. The Journal of Physical Chemistry A 105, 6121-6128.

Sundaram, M.S., Mills, F.P., Allen, M., and Yung, Y.L., 2011, An initial model assessment of NO_x photochemistry on Venus with heterogeneous oxidation of CO. In: Proceedings of the 10th Australian Space Science Conference, Brisbane, Australia, 119-132.

Tabazadeh, A., Toon, O.B., Clegg, S.L., Hamill, P., 1997. A new parameterization of H_2SO_4/H_2O aerosol composition: Atmospheric implications. Geophysical Research Letters 24, 1931-1934.

Tomasko, M., Doose, L., Engel, S., Dafoe, L., West, R., Lemmon, M., Karkoschka, E., See, C., 2008. A model of Titan's aerosols based on measurements made inside the atmosphere. Planetary and Space Science 56, 669-707.

Tomasko, M., Karkoschka, E., Martinek, S., 1986. Observations of the limb darkening of Jupiter at ultraviolet wavelengths and constraints on the properties and distribution of stratospheric aerosols. Icarus 65, 218-243.

Tomasko, M., West, R., Castillo, N., 1978. Photometry and polarimetry of Jupiter at large phase angles: I. Analysis of imaging data of a prominent belt and a zone from pioneer 10. Icarus 33, 558-592.

Vaden, T.D., Imre, D., Beranek, J., Shrivastava, M., Zelenyuk, A., 2011. Evaporation kinetics and phase of laboratory and ambient secondary organic aerosol. Proceedings of the National Academy of Sciences 108, 2190-2195.

Vaida, V., Kjaergaard, H.G., Hintze, P.E., Donaldson, D.J., 2003. Photolysis of sulfuric acid vapor by visible solar radiation. Science 299, 1566-1568.

Vandaele, A.C., De Maziere, M., Drummond, R., Mahieux, A., Neefs, E., Wilquet, V., Korablev, O., Fedorova, A., Belyaev, D., Montmessin, F., Bertaux, J.L., 2008. Composition of the Venus mesosphere measured by Solar Occultation at Infrared on board Venus Express. Journal of Geophysical Research 113, E00B23, doi:10.1029/2008JE003140.

Vandaele, A.C., Hermans, C., Fally, S., 2009. Fourier transform measurements of SO2 absorption cross sections: II. Temperature dependence in the 29000-44000 cm^{-1} (227-345 nm) region. Journal of Quantitative Spectroscopy and Radiative Transfer110, 2115-2126.

Vander Auwera, J., Moazzen-Ahmadi, N., Flaud, J.M., 2007. Toward an accurate database for the 12 μm region of the ethane spectrum. The Astrophysical Journal 662, 750-757.

Varanasi, P., 1992. Intensity and linewidth measurement in the 13.7 μm fundamental bands of $12C_2H_2$ and $^{12}C^{13}CH_2$ at planetary atmospheric temperatures. Journal of Quantitative Spectroscopy and Radiative Transfer 47, 263-274.

Virtanen, A., Joutsensaari, J., Koop, T., Kannosto, J., Yli-Pirilä, P., Leskinen, J., Mäkelä, J.M., Holopainen, J.K., Pöschl, U., Kulmala, M., 2010. An amorphous solid state of biogenic secondary organic aerosol particles. Nature 467, 824-827.

Virtanen, A., Kannosto, J., Kuuluvainen, H., Arffman, A., Joutsensaari, J., Saukko, E., Hao, L., Yli-Pirilä, P., Tiitta, P., Holopainen, J., 2011. Bounce behavior of freshly nucleated biogenic secondary organic aerosol particles. Atmospheric Chemistry and Physics 11, 8759-8766.

Von Zahn, U., Hunten, D., Lehmacher, G., 1998. Helium in Jupiter's atmosphere: Results from the Galileo probe helium interferometer experiment. Journal of Geophysical Research 103, 22815-22822,22829.

Von Zahn, U., Krankowsky, D., Mauersberger, K., Nier, A.O., Hunten, D.M., 1979. Venus thermosphere-in situ composition measurements, the temperature profile, and the homopause altitude. Science 203, 768-770.

Wagener, R., Caldwell, J., Owen, T., Kim, S.J., Encrenaz, T., Combes, M., 1985. The jovian stratosphere in the ultraviolet. Icarus 63, 222-236.

Wallace, L., Prather, M., Belton, M.J.S., 1974. The thermal structure of the atmosphere of Jupiter. The Astrophysical Journal 193, 481-493.

West, R.A., 1979. Spatially resolved methane band photometry of Jupiter: II. Analysis of the South Equatorial Belt and South Tropical Zone reflectivity. Icarus 38, 34-53.

West, R.A., 1988. Voyager 2 imaging eclipse observations of the Jovian high altitude haze. Icarus 75, 381-398.

West, R.A., Smith, P.H., 1991. Evidence for aggregate particles in the atmospheres of Titan and Jupiter. Icarus 90, 330-333.

West, R., Friedson, A., Appleby, J., 1992. Jovian large-scale stratospheric circulation. Icarus 100, 245-259.

West, R.A., Baines, K.H., Friedson, A.J., Banfield, D. Ragent, B., Taylor, F., 2004. Jovian Clouds and Haze. In Jupiter - The Planet, Satellites and Magnetosphere. F. Bagenal, T. Dowling and W. McKinnon, Eds., Cambridge University Press.

West, R., Knowles, B., Birath, E., Charnoz, S., Di Nino, D., Hedman, M., Helfenstein, P., McEwen, A., Perry, J., Porco, C., 2010. In-flight calibration of the Cassini imaging science sub-system cameras. Planetary and Space Science 58, 1475-1488.

Wilquet, V., Fedorova, A., Montmessin, F., Drummond, R., Mahieux, A., Vandaele, A.C., Villard, E., Korablev, O., Bertaux, J.L., 2009. Preliminary characterization of the upper haze by SPICAV/SOIR solar occultation in UV to mid-IR onboard Venus Express. Journal of Geophysical Research 114, E00B42, doi:10.1029/2008JE003186.

Wong, A.S., Yung, Y.L., Friedson, A.J., 2003. Benzene and haze formation in the polar atmosphere of Jupiter. Geophysical Research Letters 30, 1447.

Woo, R., Ishimaru, A., 1981. Eddy diffusion-coefficient for the atmosphere of venus from radio scintillation measurements. Nature 289, 383-384.

Yardley, J.T., Fertig, M.N., Moore, C.B., 1970. Vibrational deactivation in methane mixtures. The Journal of Chemical Physics 52, 1450.

Yelle, R.V., 1991. Non-LTE models of Titan's upper atmosphere. The Astrophysical Journal 383, 380-400.

Yelle, R.V., Griffith, C.A., Young, L.A., 2001. Structure of the Jovian stratosphere at the Galileo probe entry site. Icarus 152, 331-346.

Yelle, R.V., Young, L.A., Vervack, R.J., Young, R., Pfister, L., Sandel, B.R., 1996. Structure of Jupiter's upper atmosphere: Predictions for Galileo. Journal of Geophysical Research-All Series 101, 2149-2161.

Young, L.A., Yelle, R.V., Young, R., Seiff, A., Kirk, D.B., 1997. Gravity waves in Jupiter's thermosphere. Science 276, 108-111.

Young, L.A., Yelle, R.V., Young, R., Seiff, A., Kirk, D.B., 2005. Gravity waves in Jupiter's stratosphere, as measured by the Galileo ASI experiment. Icarus 173, 185-199.

Yung, Y.L., DeMore, W.B., 1982. Photochemistry of the stratosphere of Venus: Implications for Atmospheric Evolution. Icarus 51, 199-247.

Yung, Y.L., Liang, M.C., Jiang, X., Shia, R.L., Lee, C., Bézard, B., Marcq, E., 2009. Evidence for carbonyl sulfide (OCS) conversion to CO in the lower atmosphere of Venus. Journal of Geophysical Research 114, E00B34, doi:10.1029/2008JE003094.

Zhang, X., Liang, M.C., Montmessin, F., Bertaux, J.L., Parkinson, C., Yung, Y.L., 2010. Photolysis of sulphuric acid as the source of sulphur oxides in the mesosphere of Venus. Nature Geoscience 3, 834-837.